# THÈSE POUR OBTENIR LE GRADE DE DOCTEUR DE L'UNIVERSITÉ DE MONTPELLIER

**En Physique**

**École doctorale Information, Structures et Systèmes (I2S)**

**Unité de recherche UMR5221**

# The negatively charged boron vacancy center in hexagonal boron nitride: toward an atomically thin quantum sensor


**Présentée par Tristan CLUA PROVOST**

**le 05/12/2025**

**Sous la direction de Vincent JACQUES**


**Devant le jury composé de**

| | |
|---|---|
| Olivier ARCIZET, directeur de recherche, CNRS, Institut Néel, Grenoble | Président du jury |
| Diana SERRANO, chargé de recherche, CNRS, Institut de recherche de chimie de Paris, Paris | Rapporteur |
| Jean-Sebastien LAURET, professeur des universités, ENS-Paris-Saclay, Gif-sur-Yvette | Rapporteur |
| Patrice BERTET, directeur de recherche, CEA Paris-Saclay, Gif-sur-Yvette | Examinateur |
| Gabriel HETET, maître de conférences, ENS-Paris, Paris | Examinateur |
| Vincent JACQUES, directeur de recherche, CNRS, L2C, Montpellier | Directeur de thèse |
| Cédric ROBERT, chargé de recherche, CNRS, LPCNO, Toulouse | Invité |

UNIVERSITÉ DE MONTPELLIER

# Table of Contents

**Remerciements** **5**

**Introduction** **9**

**1 A quantum sensor in a van der Waals material** **21**

1.1 Optical and spin properties of the $V_B^-$ center in hBN . . . . . 21

1.1.1 From the electronic structure to the optical properties . . . . . 21

1.1.2 Optically-detected magnetic resonance . . . . . 26

1.2 Spin Hamiltonian . . . . . 29

1.2.1 Electron spin-spin interaction . . . . . 30

1.2.2 Stress and electric-field couplings . . . . . 32

1.2.3 Zeeman effect . . . . . 36

1.2.4 Hyperfine interaction . . . . . 37

1.3 Coherent control and spin relaxation times . . . . . 40

1.3.1 Initialization and readout . . . . . 41

1.3.2 Coherent spin control and rabi Sequence . . . . . 42

1.3.3 Longitudinal spin relaxation time $T_1$ . . . . . 45

1.3.4 Inhomogeneous coherence time $T_2^*$ . . . . . 47

1.3.5 Spin echo coherence time $T_2$ . . . . . 49

1.4 Magnetic imaging with $V_B^-$ centers in hBN: proof of concept . . . . . 51

1.4.1 Sensor engineering . . . . . 52

1.4.2 Sensitivity characterization . . . . . 55

1.4.3 Magnetic imaging . . . . . 56

1.5 Conclusion . . . . . 58

**2 Spin-dependent photodynamics of the $V_B^-$ center** **61**

2.1 Photodynamics modelling . . . . . 62

2.1.1 Seven-level model . . . . . 62

2.1.2 Practical examples . . . . . 66

2.2 Photodynamics at room temperature . . . . . 69

2.2.1 Excited state lifetime measurements . . . . . 71

2.2.2 PL time traces under continuous optical excitation . . . . . 74
2.2.3 Discussion . . . . . 77
2.3 Photodynamics at liquid-helium temperature . . . . . 81
2.3.1 Measurements . . . . . 81
2.3.2 Comments . . . . . 83
2.4 Photodynamics in an external magnetic field . . . . . 84
2.4.1 Seven-level model in a magnetic field . . . . . 84
2.4.2 Dependence on magnetic field orientation . . . . . 86
2.4.3 Level anti-crossings . . . . . 88
2.4.4 PL versus magnetic-field: the complete picture . . . . . 90
2.5 Conclusion . . . . . 91

**3 Engineering the $V_B^-$ center nuclear spin environment 95**
3.1 Isotopic purification of hBN . . . . . 98
3.1.1 Metal-flux growth of bulk monoisotopic hBN crystals . . . . . 98
3.1.2 Raman characterization . . . . . 99
3.1.3 Nitrogen ion implantation . . . . . 101
3.2 ODMR spectroscopy of the $V_B^-$ center in isotopically purified hBN flakes . . . . . 101
3.2.1 From $^{14}$N to $^{15}$N isotope . . . . . 103
3.2.2 From $^{11}$B to $^{10}$B isotope . . . . . 105
3.2.3 Simulations of the $V_B^-$ center hyperfine Structure . . . . . 105
3.2.4 Discussion . . . . . 107
3.3 Optically-induced nuclear spin polarization . . . . . 108
3.3.1 Experimental observation . . . . . 109
3.3.2 Toy model . . . . . 111
3.3.3 Magnetic field dependence . . . . . 116
3.4 Conclusion . . . . . 119

**4 Neutron irradiation for $V_B^-$ centers generation 123**
4.1 Working principle of neutron irradiation: a $^{10}$**B** advantage . . . . . 124
4.2 First iteration: early steps with neutron irradiation . . . . . 126
4.2.1 Optical characterization: $^{10}$**B** versus $^{11}$**B** isotopes . . . . . 127
4.2.2 Orthorhombic splitting $E$ and charge model . . . . . 129
4.3 Second iteration: optimizing the sensitivity . . . . . 132
4.3.1 PL signal optimization . . . . . 133

4.3.2 ODMR spectroscopy of neutron irradiated $h^{10}B^{15}N$ crystals . 135
4.3.3 Impact of neutron irradiation on spin relaxation times . . . . 138
4.3.4 Cross-relaxation relaxometry . . . . . 140
4.4 Toward an atomically-thin sensor . . . . . 144
4.5 Conclusion . . . . . 146

**5 Optical and spin properties of $V_B^-$ centers in atomically-thin hBN flakes 149**
5.1 Flake thickness-dependent optical response of a $V_B^-$ centers . . . . . 150
5.1.1 Modelling of the PL signal thickness-dependence . . . . . 151
5.1.2 Optical absorption . . . . . 153
5.1.3 Emission thickness-dependence . . . . . 157
5.1.4 Overall modelling and large scale study . . . . . 160
5.2 Orthorhombic splitting **E** in the few-layer limit . . . . . 162
5.2.1 Zero-field ODMR spectra in few-layer $h^{10}B^{14}N$ flakes . . . . . 162
5.2.2 ODMR spectroscopy versus field in $h^{\mathbf{10}}B^{\mathbf{15}}N$ flakes . . . . . 164
5.3 Thickness dependence of the longitudinal spin relaxation time $\mathbf{T_1}$ . . 168
5.4 Spin coherence of $V_B^-$ centers in atomically-thin hBN flakes . . . . . 171
5.4.1 Few-layer flake from $S_1$ sample . . . . . 171
5.4.2 Few-layer flakes from $S_{10}$ sample . . . . . 173
5.4.3 Qualitative explanation . . . . . 175
5.5 Conclusion . . . . . 177

**Conclusion 181**

**List of Publications 187**

**Bibliography 191**

**Résumé 223**

# Remerciements

Il est bien difficile de se faire une idée précise de ce que représente réellement une thèse avant d'en avoir soi-même commencé une. S'il est un point crucial, souvent sous-évalué par les jeunes étudiants, c'est bien le rôle de premier plan joué par l'ensemble des personnes qui entourent le doctorant : encadrants, collègues doctorants et post-doctorants, équipes techniques et administratives du laboratoire, collaborateurs, ainsi que proches. Après trois années de thèse, je peux aisément affirmer que ces derniers ont au moins autant d'impact sur le rendu final de ce travail que le doctorant lui-même. Je dirais même que c'est bien souvent la qualité de cet environnement humain qui fait la différence entre une thèse réussie, scientifiquement et humainement, et une thèse moins satisfaisante et plus éprouvante. Si je laisse au lecteur le soin d'évaluer la qualité scientifique de ce manuscrit, je peux d'ores et déjà affirmer que ces trois dernières années de thèse furent pour moi une expérience particulièrement enrichissante et agréable. Je me dois donc de remercier ici l'ensemble des personnes qui y ont contribué.

Je peux d'abord commencer par souligner la qualité de l'encadrement prodigué par mon directeur de thèse. Discussions quotidiennes sur l'état d'avancement des expériences, mise en place de collaborations pertinentes, participation régulière à des conférences, vision claire et planifiée du projet scientifique de ma thèse : je te remercie, *Vincent*, de m'avoir fait évoluer dans cet environnement particulièrement stimulant et rassurant pour un jeune thésard. Dans les salles sombres des expériences d'optique, ce fut ensuite Alrik Durand qui prolongea ma formation sur les détails techniques de la manip. Merci à toi, Alrik, pour cette première année de thèse passée à me former, ainsi que pour ta faculté impressionnante à toujours avoir une réponse détaillée à chacune de mes questions, aussi diverses que variées. I would also like to thank you, Zhao, for the years we shared in the hBN team, and for your deep understanding and inspiring knowledge of the literature. Je voudrais également remercier les membres de mon jury : Mme Diana Serrano, M. Patrice Bertet, M. Olivier Arcizet, M. Jean-Sébastien Lauret et M. Gabriel Hétet. Merci à vous d'avoir pris le temps de lire avec attention ce manuscrit et de m'avoir fait part, lors de la

soutenance, de vos commentaires, questions et critiques pertinentes.

Comme il apparaîtra clair à la lecture de ce manuscrit, les résultats obtenus dans ce travail de thèse reposent en grande partie sur la qualité des échantillons étudiés. Ces derniers sont le fruit d'un réseau de collaborations impliquant des chercheurs américains de l'université du Kansas, responsables de la croissance du nitrure de bore hexagonal, ainsi que des chercheurs toulousains du LPCNO et du CEMES, responsables respectivement de l'exfoliation et de l'implantation ionique des cristaux. Je tiens tout particulièrement à remercier Cédric Robert et Jules Fraunié du LPCNO à Toulouse. Grand merci à vous deux, pour votre qualité scientifique d'abord, puis pour votre gentillesse et disponibilité. Ce fut toujours un plaisir de venir vous rendre visite à Toulouse. Merci également à Grégory Seine et Alain Claverie du CEMES pour leur connaissance approfondie des processus de création de défauts et pour la mise en œuvre, pas toujours aisée, de l'implanteur ionique. Finally, I wish to thank Professor James H. Edgar and his student Thomas Poirier for providing state-of-the-art crystal quality.

Ensuite vient l'équipe S2QT dans son ensemble. Merci à toi, Isabelle, pour ton partage constant de connaissances sur les subtilités du monde académique, ainsi que pour ton inégalable serviabilité ; merci à toi, Guillaume, pour ta précieuse expertise sur le nitrure de bore et ton attitude toujours chaleureuse ; merci à toi, Aurore, pour ton aide régulière en informatique, ton engagement dans la vie de l'équipe et le soin que tu as apporté à mon ennuyeux régime sans gluten ; merci à toi, Pierre, d'avoir pris en charge le déménagement de l'équipe dans le nouveau bâtiment, ainsi que les nombreuses interventions qui ont suivi ; merci à toi, Anaïs, pour ton dynamisme et ton application au sein de la communauté du quantique en France, tous deux inspirants ; merci à toi, Bernard, pour tes conseils avisés et tes encouragements.

Après les permanents viennent tous les collègues doctorants et post-doctorants avec lesquels j'ai partagé ces années de thèse, à commencer par la première génération composée de Florentin, Maxime, Adrien et Yoann. Caractérisés par un humour prononcé, je vous remercie pour votre accueil chaleureux au sein de l'équipe, ainsi que pour la transmission des connaissances. Vient ensuite ma génération, ou plutôt notre génération, avec Elias, Félix et Juliette. Merci, et encore félicitations à vous pour ces trois belles années de thèse. Je te remercie particulièrement, Elias, pour

nos discussions enrichissantes et le soutien mutuel que nous nous sommes apporté. Enfin, merci à ceux qui nous ont rejoint en cours de route, Krithika, Jessica, Florie ainsi que Carolin, Alexandra, Roméo et Elijah, qui ont ramené un vent de fraîcheur et ont contribué à une certaine augmentation de ma vie sociale. Est-ce que j'oublie quelqu'un... ? Ah oui, merci Alicia d'avoir bousculé mon quotidien avec ton énergie sans pareille. Je voudrais également remercier les deux stagiaires de master qui ont contribué aux travaux présentés dans ce manuscrit. Théo et Lili, je vous souhaite le meilleur dans la poursuite de vos études ou de votre carrière professionnelle.

Je voudrais également souligner les contributions d'autres services du laboratoire, tels que le service de mécanique. Merci Thomas pour ton travail de qualité et ta jovialité. Merci aux ressources humaines, Dominique Diamante et Béatrice Tomberli, pour leur réactivité, merci à Jean-Christophe Art, Stéphanie Martegouttes et Audrey Combe, pour la gestion efficace des missions et autres livraisons. Merci à Christelle Eve pour l'organisation des conférences et des bons repas qui vont avec.

Il me faut maintenant remercier celles et ceux qui n'ont pas tant contribué à ce travail de thèse qu'à mon développement personnel, et donc à ma présence jusqu'ici. Merci à ma mère d'avoir su trouver le juste équilibre entre rigueur et douceur ; merci à mon père d'avoir cultivé ma curiosité et mon ouverture d'esprit ; et à ma sœur d'avoir toujours constitué un exemple de réussite, jusqu'à soutenir sa thèse trois mois avant la mienne. Merci à mes grand-parents et à tout le reste de la famille pour leur présence toujours bienveillante.

Pour finir, j'aimerais ne pas oublier le rôle crucial qu'une université quasi gratuite a pu jouer dans mon parcours. Loin d'être une passion depuis l'enfance, la physique n'a commencé à attirer ma curiosité que durant mes années de lycée. C'est précisément parce que je savais mon choix sans graves conséquences que je me suis permis de me lancer dans cette discipline encore nouvelle pour moi. Qu'il en reste ainsi le plus longtemps possible.

# Introduction

Quantum physics is often praised for its strangeness and its fascinating principles that seem to defy common sense. It is no exaggeration to say that it has revolutionized our perception of the world, a world in which a physical quantity is not always well defined a priori, but acquires a precise value only upon measurement. A world where two objects can remain intimately correlated, even when separated by arbitrarily large distances. A world where particles behave as waves, interfering with others and even with themselves. Turning these truly astonishing concepts into practical devices is the challenge, and the promise, of *Quantum Technologies*.

Four distinct goals are commonly distinguished. Developing quantum algorithms and experimental platforms capable of outperforming classical computers defines the field of *Quantum Computing*. Transferring quantum states across large distance to provide ultimate security in telecommunication is the challenge of *Quantum Communication*. Engineering a highly tunable quantum platform that can reproduce the behavior of complex quantum system, such as strongly correlated materials or chemical processes, is the aim of *Quantum Simulation*. And finally, the one pursued in this present work, exploiting the remarkable sensitivity of quantum systems to their environment to develop ultra-high-performance sensors is the objective of **Quantum Sensing**.

In a reference review, Degen et al. [1] proposed three different degrees of quantum sensors, with increasing levels of quantumness: (i) a quantum system, i.e, a system composed of discrete energy levels, (ii) a quantum system operated in a quantum state, i.e, a coherent superposition, and (iii) an entangled quantum system that demonstrates a genuine quantum advantage compared to its classical counterparts. Hence, in contrast to quantum computers, a quantum sensor does not necessarily have to demonstrate a quantum advantage to be relevant.

A wide variety of quantum sensing platform are currently developed. As most prominent examples one can cite magnetometers based on atomic vapor cells [2],

atomic gravimeters [3], superconducting quantum interference devices (SQUIDs) for magnetic-field sensing [4], and *optically-active spin defects* for magnetic-field, electric-field, pressure and temperature sensing [5–12]. In this manuscript, we focus our attention on this latter category.

## Optically Active Spin Defects

While a crystal is characterized by a well-ordered and symmetric structure, it may also host localized imperfections such as substitutional impurities, interstitial atoms, or vacancies [Fig. 1(a)]. By breaking the translational symmetry of the crystal lattice, these point defects produce localized electronic states with discrete energy levels [Fig. 1 (b)]. When these states lie within the material's band gap and are coupled through electric-dipole-allowed transitions, one recovers an atomic-like quantum system with ground and excited states connected by photon absorption and emission. In this regard, point defects in wide-bandgap materials can be viewed as artificial atoms, embedded within a solid-state matrix.

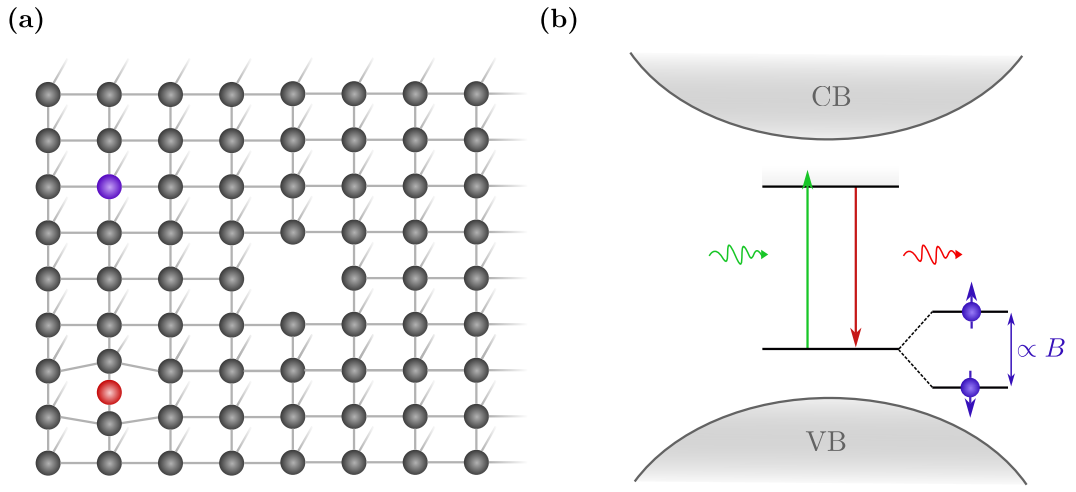


**Figure 1:** Optically active spin defects. (a) Illustration of a crystal lattice with point defects. (b) Sketch of the discrete energy levels of a spin defect lying in between the valence band (VB) and conduction band (CB) of a host material. Green and red arrows depict photon absorption and emission between the ground and excited state. The presence of magnetic-field $B$ lifts the degeneracy between the spin states.

Like atoms, some point defects possess a non-zero electron spin and are thus referred to as **spin defects**. This additional degree of freedom becomes particularly interesting when it couples to the optical properties of the defect, making it possible

to initialize and read out the spin state by optical means, a technique known as *optically detected magnetic resonance* (ODMR). The latter is especially important because it enables spectroscopy of the spin-state transitions. Since the electron spin couples to various types of perturbations such as magnetic and electric fields, temperature, or mechanical stress, one can then use ODMR spectroscopy to operate optically active spin defects as sensors [Fig. 1 (b)]. Although different spin-defect-based sensing platforms are under investigation [13], one system in particular has long dominated, and still dominates, the literature: the $NV^-$ center in diamond.

## The $NV^-$ Center in Diamond

The negatively charged nitrogen-vacancy ($NV^-$) center in diamond is the archetype of an optically active spin defect [14]. Its spin triplet ($S = 1$) ground state, can be initialized and read out optically at room temperature [15, 16], unlocking by the same occasion the ODMR spectroscopy of its spin sublevels. With spin-coherence times reaching the millisecond, the $NV^-$ center has held for several years the record of coherence among solid-state quantum systems [17]. Combined with fast coherent control in the gigahertz regime [18], its outstanding spin properties have established the $NV^-$ center as a candidate for a solid-state qubit platform [19]. In addition to its remarkable spin properties, the $NV^-$ center also exhibits exceptional optical characteristics. Bright enough to be detected at the single-defect level [15], it is a photostable single-photon emitter operating at room temperature [20, 21]. Sitting at the crossroads of excellent optical and spin properties, the $NV^-$ center has also been explored for the realization of a spin–photon interface, an essential ingredient for future quantum communication networks [22, 23].

However, over the past years, the $NV^-$ center has primarily demonstrated its unique potential as a quantum sensor. Two main architectures have been developed: scanning $NV^-$ microscopy and widefield $NV^-$ microscopy [10, 24–28]. In the former, a single $NV^-$ center is integrated into a nanometric diamond tip that scans the sample surface while being probed by a confocal microscope [Fig. 2(a)]. In this configuration, the spatial resolution is limited by the tip stand-off distance, typically $\sim$ 30–100 nm. Conversely, in widefield $NV^-$ microscopy, a dense ensemble of $NV^-$ centers hosted in a bulk diamond is probed through a widefield optical microscope [Fig. 2(b)]. In this case, one benefits from a much stronger signal at the cost of a

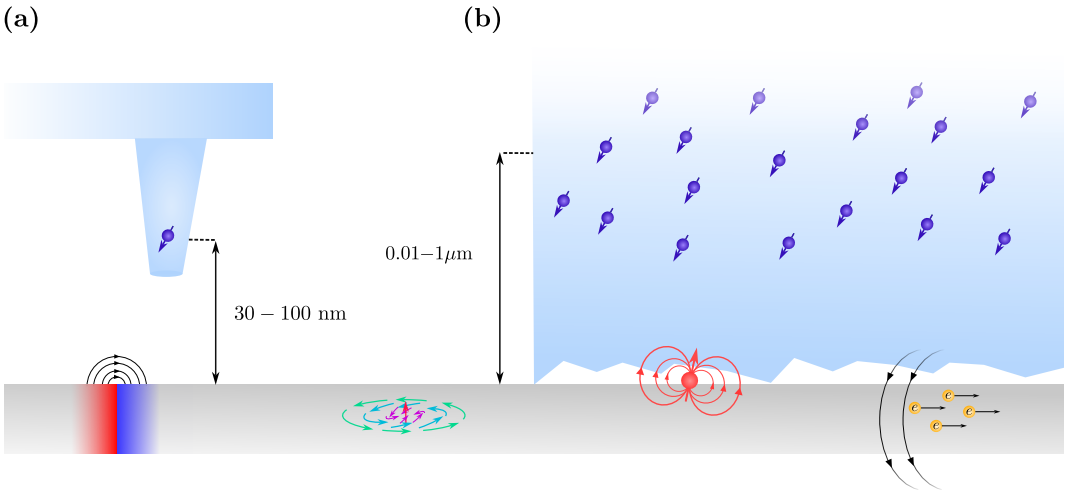


**Figure 2:** The two main architectures of quantum sensors based on $NV^-$ center. (a) Scanning $NV^-$ microscopy. (b) Widefield $NV^-$ microscopy.

spatial resolution limited by optical diffraction to the micron scale. A wide variety of applications have been demonstrated for these sensors, ranging from biosensing [9, 29, 30], micro- and nanoscale nuclear magnetic resonance [31, 32], and geology [33], to condensed-matter physics [34]. In this latter field, $NV^-$ center–based sensors have proven especially powerful as magnetic-field imagers, enabling the real-space imaging of domain walls in ferromagnets [35], magnetic vortices in superconductors [36, 37], magnetic cycloids in multiferroic materials [38], and current flow in graphene [39], among others.

While $NV^-$ center–based quantum sensors offer state-of-the-art capabilities and continue to attract growing interest, the perpetual quest for improvement that drives the scientific community naturally raises the question of how the limits of spin-defect-based quantum sensors could be pushed even further. Two main aspects in particular could benefit improvements, the sensor to sample distance and the flexibility of the sensor.

1. **Sensor sample proximity.** In scanning $NV^-$ microscopy, the sensor to sample distance is typically on the order of 30–100 nm [40]. In ensemble-based $NV^-$ sensors, the sensor–sample proximity is more variable, as it depends on the thickness of the $NV^-$-doped layer. Typical values range from about 10 nm to 1 µm [39, 41, 42]. Although the sensor–sample distance is constrained by different parameters in the two techniques, its fundamental limitation is common to both: the three-dimensional (3D) nature of diamond. As a bulk

3D material, diamond sensors inevitably exhibit a certain surface roughness or curvature that prevents perfect contact with the sample. In addition, the spin defect cannot be positioned exactly at the surface, as near-surface $NV^-$ centers suffer from charge-state instability and degraded spin properties when approaching the diamond surface [43–51].A shorter sensor–sample distance would directly increase the field experienced by the probe. For instance, a dipolar magnetic field decays as $B \propto 1/r^3$, where $r$ is the distance between the magnetic source and the sensor. Further reducing the distance between the spin defect and the sample is therefore essential.

2. **Sensor flexibility.** A second drawback of a 3D matrix such as diamond lies in its mechanical rigidity, which prevents the sensor from adapting to complex architectures or nontrivial topographies such as patterned surfaces, multilayered structures, or curved geometries.

To mitigate these limitations, which, beyond diamond, are inherent to all 3D materials, the community has turned its attention to a new class of materials: the van der Waals materials.

## From a 3D to a 2D Sensor

Van der Waals (vdW) materials are characterized by a layered crystal structure, in which strong in-plane covalent bonds hold the atoms together within each layer, while adjacent layers are only weakly coupled through van der Waals forces. Owing to this inherently two-dimensional (2D) nature, a bulk vdW crystal can be mechanically exfoliated into atomically thin flakes, down to a few or even a single layer [52]. In this regard, van der Waals material constitute an ideal material platform for a quantum sensor. In this alternative architecture, the sensor itself would take the form of a **flexible atomic foil** hosting optically-active spin defect that could be placed directly on top of the sample to achieve an **atomic-scale proximity** [Fig. 3].

Moreover, following the landmark discovery of graphene [53], this new class of materials rapidly expanded to encompass almost the entire bestiary of condensed-matter physics, including magnets [54], superconductors [55], and topological insulators [56]. These materials can be also stacked vertically to form so-called van der Waals heterostructures [57]. By combining layers with distinct properties, one can engineer artificial materials with tailored functionalities. This has been elegantly

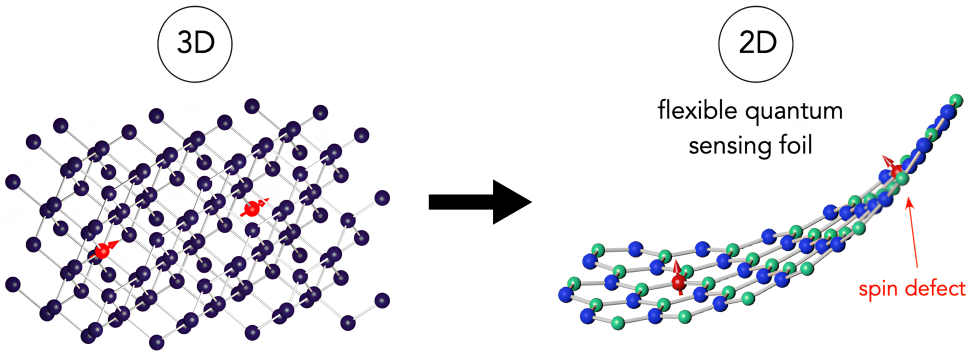


**Figure 3:** From a 3D to a 2D sensor.

demonstrated by Kezilebieke *et al.*, who achieved topological superconductivity by stacking a vdW superconductor with a vdW ferromagnet [58]. In such heterostructures, the relative twist angle between adjacent layers also becomes a tunable parameter, giving rise to emergent phenomena such as magic-angle superconductivity in twisted bilayer graphene [59]. A van der Waals quantum sensor would thus be particularly well suited to probe the rich physics of this new class of materials, by being directly integrated within such heterostructure.

Motivated by these promises, part of the community has begun to investigate potential candidates for this new 2D sensing platform [60]. The first crucial step was the choice of the host material, a van der Waals crystal, of course, but which one? The primary criterion is the bandgap: it should be wide enough to maximize the likelihood of hosting optically active defects. Chemical stability under ambient conditions is also essential to keep the sensing apparatus as accessible and simple as possible. Although several candidates fulfill these requirements, one material clearly stands out: hexagonal boron nitride.

## hexagonal Boron Nitride

Hexagonal boron nitride (hBN) is a polymorph of boron nitride in which each boron atom is connected to three nitrogen atoms through in-plane $\sigma$ bonds, and vice versa. This arrangement gives rise to the characteristic honeycomb lattice shown in Figure 4(a). In contrast to the strong in-plane covalent bonds, the interlayer bonding arises solely from weak van der Waals interactions, making hBN a member

of the van der Waals crystal family. Several stacking sequences, known as polytypes, are possible for these layers. The most stable one, denoted $AA'$, is depicted in Figure4(b) [61]. In this configuration, the atomic specie alternates between boron and nitrogen along the out-of-plane lattice vector $\vec{c}$. As a result, the out-of-plane periodicity is recovered every three layers and corresponds to twice the interlayer spacing, $|c| \approx 6.6$ Å.

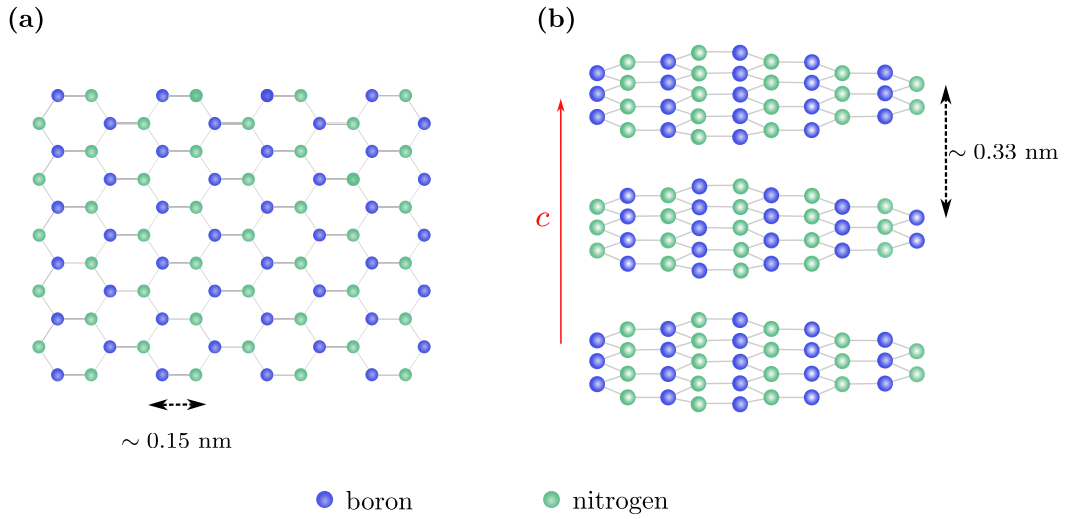


**Figure 4:** Schematic of the hBN crystal lattice (a) in-plane (b) out-of-plane with a $AA'$ stacking order.

hBN is an insulating material with a wide bandgap of approximately 6 eV. It is especially well known in the van der Waals materials community for its excellent capping capabilities. Almost insensitive to oxidation [62] and even acting as a corrosion inhibitor [63], hBN is chemically stable down to the single layer [64] and all the way up to temperatures as high as 1000°C [65]. This robustness, combined with its oustanding dielectric properties, has made hBN a go-to protective layer in the vdW materials community [57]. Hence, graphene placed on an hBN substrate famously shows enhanced carrier mobility and improved charge stability [66–68], while hBN encapsulation shields unstable transition metal dichalcogenides (TMDs) from oxidation for months [69] and even enhanced their optical properties [70, 71]. Far from being just a simple capping layer, hBN also stands out among the vdW material as featuring ferroelectric domains in twisted or self-folded structures [72, 73], as well as producing large magnetoresistance in magnetoresistive heterojunctions [74, 75].

hBN thus emerges as an ideal host for a sensing platform capable of both pro-

tecting and probing the sample of interest. Moreover, its large bandgap offers ample room to host optically active spin defects.

## A Zoology of Color Centers

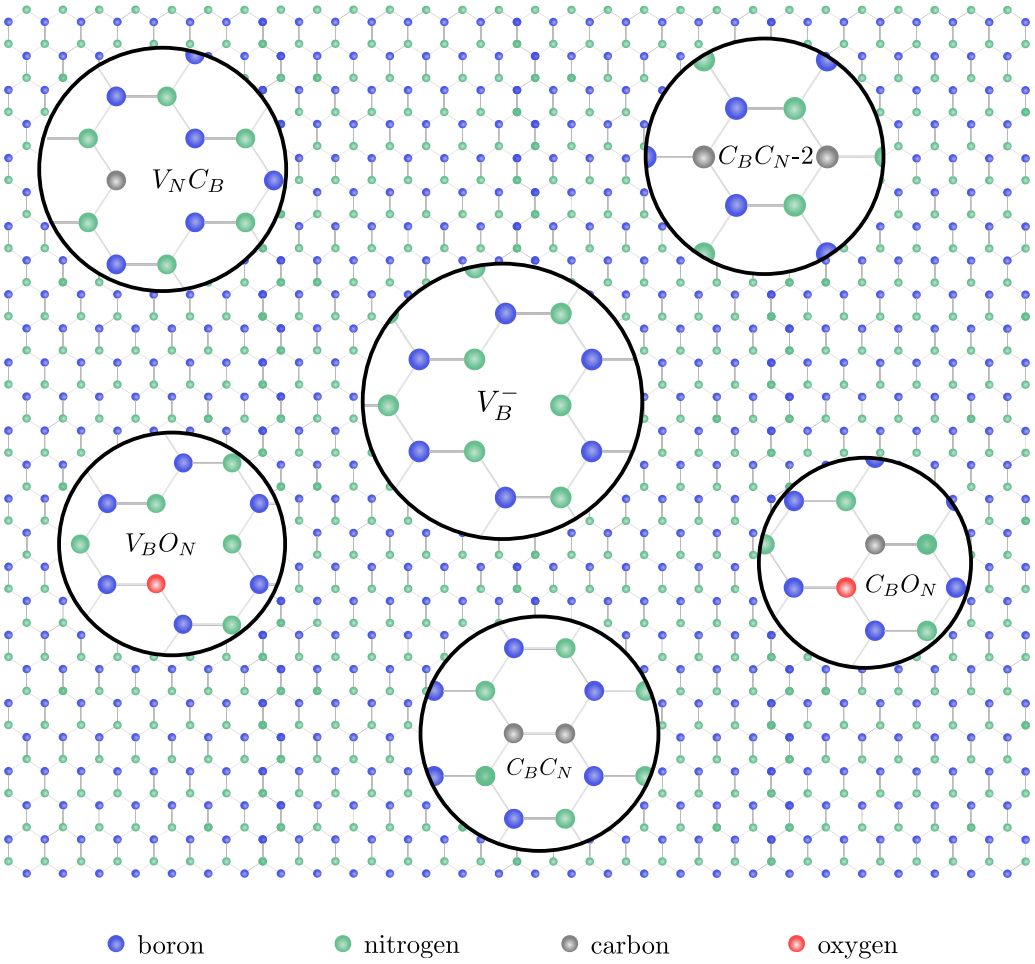


**Figure 5:** Non-exhaustive schematic of different point defects in hBN: $V_N C_B$ [76], $C_B C_N$ [77], $C_B O_N$ [78], $V_B O_N$ [79], $C_B C_N$-2 [77, 78], $V_B^-$ [80, 81].

Although defect-related photoluminescence in hBN has been known for decades [82, 83], the recent burst of interest in color centers in hBN was ignited by the report of Tran *et al.*, who in 2016 demonstrated single-photon emission in the optical range at room temperature [84]. That same year, this result was reproduced by numerous research groups worldwide [85–89]. Since then, single-photon emitters (SPEs) in hBN have given rise to a plethora of studies reporting UV emitters [90], blue emitters [91, 92], yellow emitters [93, 94], green emitters [95], and a broad diversity of emitters between 600 and 700 nm [96–99]. While the UV emission has recently

been attributed to a carbon dimer [100], the microscopic origin of most other defects remains unknown. Figure 5 illustrates potential candidates: blue and green emission could involve oxygen impurities [79, 95], whereas the broad family of emitters around 600 nm is most likely associated with carbon-related defects [76, 101, 102]. However, our sensor design relies on spin properties rather than quantum emission, in this regard the literature has been far less abundant.

One can trace back to the 1970s to find the first reports of paramagnetic centers in hBN [82, 103]. However, it was only in recent years that these signals could be correlated with specific optical emission lines. It was first confirmed that certain defects in the group emitting near 600 nm exhibited spin properties, albeit with wide variability [104, 105]. Then, in 2020, Gottscholl *et al.* demonstrated room-temperature optical initialization and readout of an ensemble of spin defects in neutron-irradiated hBN [81]. Remarkably, the study also unveiled the microscopic structure of the defect: a boron vacancy, more precisely its negatively charged state ($V_B^-$) [80]. Not only did this defect carried a spin, but its spin-dependent optical properties closely resembled those of the $NV^-$ center in diamond, the benchmark spin defect. This pioneering study initiated a new research line, within which the present work finds its place.

## Thesis Scope and Manuscript Outline

The main objective of this thesis is to assess the potential and viability of the negatively charged boron vacancy in hexagonal boron nitride as a 2D quantum sensor. This goal encompasses several key aspects: demonstrating quantum sensing with this new platform, identifying the main obstacles that currently limit its performance, engineering the defect environment, and optimizing the defect creation process. Crucially, all these efforts rely on a central claim: the operability of the sensor down to the few-layer limit. Far from being a given, this must be demonstrated. This manuscript is organized into five chapters, each developing further one of these aspects.

In the **first chapter**, we formally introduce the negatively charged boron vacancy center. Based on ab initio predictions from the literature, we begin by describing its electronic structure and optical properties, and then introduce the principles

of ODMR spectroscopy. We express the spin Hamiltonian of the defect's ground state and show how its spin couples to magnetic and electric fields, as well as to mechanical stress. Building on this foundation, we demonstrate optically induced spin-state initialization, time-resolved readout, and coherent control, and use these key tools to measure the spin relaxation times. Finally, the chapter concludes with a proof-of-principle demonstration of magnetic-field imaging of a van der Waals magnet using a $V_B^-$ center embedded in an hBN flake. This first chapter sets the stage for the rest of the thesis and helps identify the main obstacles currently limiting the sensor's sensitivity: its dim optical emission and the dense surrounding nuclear-spin bath.

In the **second chapter**, we present a comprehensive study of the spin-dependent photodynamics of the $V_B^-$ center. We first introduce a seven-level rate-equation model and show that it can capture the essential of the $V_B^-$ center photodynamics. We then perform a series of time-resolved photoluminescence measurements and extract all parameters of the model at room temperature. We show that all measurement can be well reproduced by assuming a low radiative decay. The same analysis is then carried out under cryogenic conditions, revealing a nearly unchanged photodynamics. In the final part, we use the complete model to reproduce the behavior of the spin-dependent photodynamics of the $V_B^-$ center under applied magnetic fields, achieving an excellent agreement with the experimental data.

In the **third chapter**, we explore two complementary strategies to engineer the nuclear-spin bath intrinsic to the hBN lattice and thereby improve the sensor's magnetic sensitivity: isotopic purification and optically induced nuclear-spin polarization. By enriching the hBN lattice with $^{10}B$ and $^{15}N$ isotopes, we obtain a sharper magnetic resonance and achieve a fourfold enhancement in magnetic-field sensitivity. In a second approach, we harness the hyperfine coupling between the electronic and nuclear spins to transfer the electron-spin polarization to the surrounding nitrogen nuclei, reaching a nuclear-spin polarization of nearly 30%.

In the **fourth chapter**, we investigate neutron irradiation as a means to generate $V_B^-$ centers in hBN. This technique, which relies on nuclear transmutation, offers a promising route to fabricate atomically thin quantum sensors by irradiating the bulk material first and exfoliating it only afterward. In a first batch of samples,

we demonstrate the crucial role of isotopic purification with $^{10}$B for efficient $V_B^-$ centers creation. In a second batch, we identify the optimal irradiation duration that maximizes the sensor's magnetic sensitivity. Finally, we conclude this chapter by performing ODMR spectroscopy on few-layer neutron-irradiated flakes, showing that the defect spin can still be initialized and read out down to the atomic-scale limit. We further estimate the magnetic-field sensitivity of this atomically thin sensor and find that it remains competitive with that of state-of-the-art solid-state quantum sensors, thereby validating the potential of neutron irradiation for $V_B^-$ center engineering in hBN.

In the **fifth and final chapter** of this manuscript, we explore the physics of this new platform composed of optically active spin defects embedded in atomically thin flakes of a van der Waals material. We first study the evolution of the photoluminescence signal with flake thickness, both experimentally and theoretically, and demonstrate that $V_B^-$ centers in thin hBN flakes exhibit enhanced optical absorption and improved collection efficiency compared to $V_B^-$ centers in thick flakes. In the second part, we investigate the impact of atomic-scale proximity to the surface on the spin relaxation times. Our results reveal that spin coherence is remarkably preserved despite the surface proximity, and can even be enhanced in the few-layer limit, depending on the nature of the spin bath governing decoherence. Altogether, this final chapter highlights the robustness of $V_B^-$ spin defects in embedded in atomically-thin hBN flakes and establishes this new system as a promising platform for next-generation quantum sensing.

# 1 A quantum sensor in a van der Waals material

The aim of this first chapter is to introduce the main properties of the negatively charged boron vacancy ($V_B^-$) in hexagonal boron nitride (hBN) and the experimental methods, while at the same time providing the reader with an overview of the current state of the literature. In Section 1.1, we begin by introducing the electronic structure of the $V_B^-$ center and describe the dynamics of its optical cycles. This will lead us to introduce the spin-dependent optical properties of the defect that enable optically detected magnetic resonance (ODMR) spectroscopy. This technique allows to interrogate the frequencies of the spin transitions, opening the way to use the $V_B^-$ center as a sensitive probe of external perturbations. We then explore in Section 1.2 the various perturbations that couple to the electron spin of the $V_B^-$ center through their respective contributions to the spin Hamiltonian. The spin properties of the $V_B^-$ center are further investigated in Section 1.3, where, using coherent spin control and time-resolved readout, we measure its spin relaxation times. Finally, we close this first chapter by demonstrating, in Section 1.4, magnetic imaging of a van der Waals magnet with $V_B^-$ centers embedded in a hBN flake.

## 1.1 Optical and spin properties of the $V_B^-$ center in hBN

### 1.1.1 From the electronic structure to the optical properties

When a boron atom is removed from the hBN lattice, the electrons of the three neighboring nitrogen atoms, ordinarily engaged in bonding, are left dangling. The half-filled $\sigma$ bonds contribute one electron per nitrogen atom, while the fully occupied $\pi$ bonds, contribute two electrons per nitrogen. As a result, the neutral boron vacancy comprises nine electrons. To form the negatively-charged boron vacancy, an additional electron must be captured from the environment, bringing finally the total to ten electrons.

To predict the electronic structure of this system, one must combine a group theory analysis and advanced ab initio methods, such as density functional theory (DFT). I will not provide a detailed description of these theoretical techniques, which are rich in subtleties and out of my expertise, but instead summarize the results of three key studies: Abdi *et al.* [106], Reimers *et al.* [107], and Ivady *et al.* [80]. Together, these works offer valuable insight into the electronic structure and the photophysics of the $V_B^-$ center in hBN.

Beside being embedded in a solid-state matrix, this system of ten strongly localized electrons can be treated as a molecular-like entity. Hence, a convenient starting point is to construct molecular orbitals (MOs) from linear combinations of the $\sigma_n$ and $\pi_n$ bonds of the three neighboring nitrogen atoms, with $n = \{1, 2, 3\}$ denoting the nitrogen atom index. This construction must be carried out within a group-theoretical framework, ensuring that the MOs transform as irreducible representations of the defect's point group symmetry, namely $D_{3h}$. Following the derivation of Abdi *et al.* [106], this procedure yields a set of six MOs:

$$a_1' = \frac{1}{\sqrt{3}}(\sigma_1 + \sigma_2 + \sigma_3), \tag{1.1}$$

$$a_2'' = \frac{1}{\sqrt{3}}(\pi_1 + \pi_2 + \pi_3), \tag{1.2}$$

$$e_x' = \frac{1}{\sqrt{6}}(2\sigma_1 - \sigma_2 + \sigma_3), \tag{1.3}$$

$$e_y' = \frac{1}{\sqrt{2}}(\sigma_2 - \sigma_3), \tag{1.4}$$

$$e_x'' = \frac{1}{\sqrt{6}}(2\pi_1 - \pi_2 + \pi_3), \tag{1.5}$$

$$e_y'' = \frac{1}{\sqrt{2}}(\pi_2 - \pi_3). \tag{1.6}$$

Here, the MOs are labeled using Mulliken notation. In particular, the symbol $e$ denotes a doubly degenerate orbital, such as the pairs $\{e_x', e_y'\}$ and $\{e_x'', e_y''\}$. Following Abdi *et al.*, I adopt a simplified notation, referring to these pairs simply as $e'$ and $e''$, respectively.

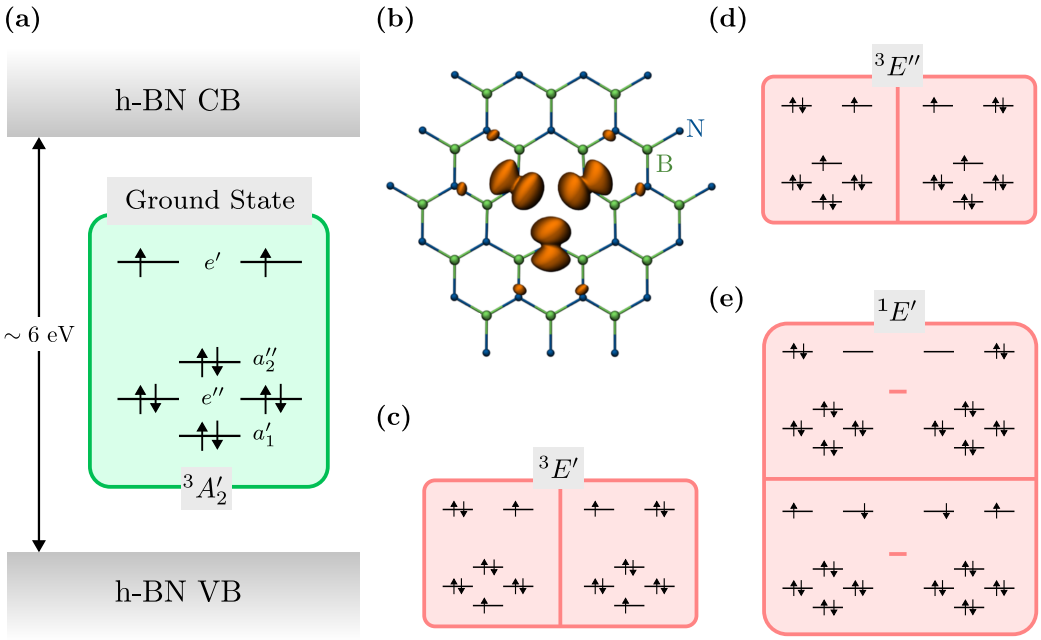


**Figure 1.1:** Electronic configurations of the $V_B^-$ center. (a) Molecular orbital diagram of the $V_B^-$ center GS. The arrows represents the ten electron spins. The position of the MOs in the hBN bandgap is not at scale. (b) Electron spin density of the GS obtained by DFT, reproduced from Ref. [80]. (c-d) Molecular orbital diagram of the two triplet excited states $^3E'$ and $^3E''$(d,c) and the singlet excited state $^1E'$ (e).

The ground state (GS) of the $V_B^-$ center is obtained when MOs $a_1'$, $a_2''$ and $e''$ are fully occupied, while both $e'$ remain half-filled. This configuration, labelled $^3A_2'$, is depicted in Figure 1.1(a). In this state, the two unpaired electrons form a symmetric spin configuration with total spin $S = 1$. The GS of the $V_B^-$ center is therefore a **spin-triplet**. Its spatial distribution can be visualized through the electron spin density, defined as the difference between spin-up and spin-down densities. Depicted in Figure 1.1(b), it is predominantly localized on the three nitrogen atoms surrounding the vacancy and confined within a single hBN layer. This observation is consistent with the fact that the unpaired electrons occupy the $e'$ orbitals, which are linear combinations of the in-plane $\sigma$ bonds [Eq. (1.3, 1.4)].

Starting from this ground-state configuration, several excitation pathways are possible. One possibility is the promotion of a spin-down electron from $a_1'$ or $a_2''$ into $e'$, giving rise to the excited states $^3E'$ and $^3E''$, respectively [Fig. 1.1(c,d)]. Because these excitations still leave two unpaired spin-up electrons, both correspond

to spin-triplet states [1]. Alternatively, the two unpaired electrons in $e'$ can be paired into an antisymmetric combination of spin-up and spin-down, yielding a singlet state ($S = 0$), denoted $^1E'$ [Fig. 1.1(e)].

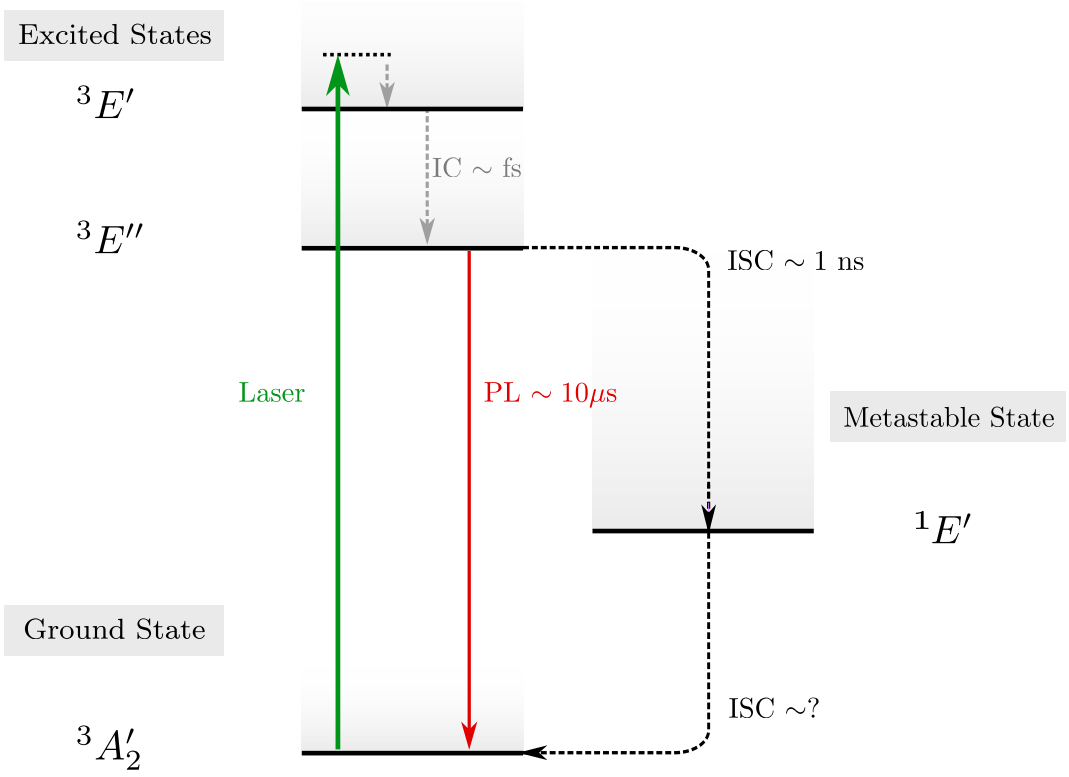


**Figure 1.2:** Schematic of the $V_B^-$ center photodynamics. The green and red arrows represents the optical excitation at 532 nm and the radiative recombination toward the GS, respectively. The dashed arrows depict non-radiative processes. The grey arrows represent internal conversion (IC) within the spin triplet manifold while the black arrows represent intersystem crossing (ISC) through the spin singlet. The state labels correspond to the $D_{3h}$ symmetry representation.

The ordering of these excited states, not to scale, is illustrated in Figure 1.2: the excited state (ES) $^3E'$ lies highest in energy, followed by $^3E''$, while the singlet state $^1E'$ is located between the GS and the two triplet ES. To distinguish the singlet state from the two triplet ones, we will refer to $^1E'$ as the metastable state. This energy diagram provides a convenient basis to discuss the photophysics of the defect under optical excitation. Owing to the selection rules governing electric-dipole transitions, optical excitation must conserve the spin state. Consequently, from the GS the defect can only be excited within the spin-triplet manifold $\left\{^3E', ^3E''\right\}$.

[1] Note that a third triplet excited state, originating from the promotion of an electron from the $e''$ to the $e'$ orbitals, also exists but is neglected here for simplicity.

With the excitation wavelength used in this work, 532 nm ($\approx$ 2.3 eV), the defect is expected to be promoted close to the $^3E'$ state, i.e, the triplet state with highest energy. Notably, this is also the state for which the absorption is predicted to be the strongest [107]. However, the defect does not remain in this first ES for long. Through a phonon-mediated relaxation process, known as internal conversion, the system undergoes an ultrafast and radiationless relaxation within the spin-triplet manifold. Within only a few femtoseconds, it reaches the lowest-energy spin triplet ES, $^3E''$ [107].

From the $^3E''$ level, the defect can relax to the GS via two distinct channels: either through direct *radiative* decay, giving rise to a photoluminescence (PL) signal around 800 nm, or via a *non-radiative* pathway through the metastable singlet state, $^1E'$ [Fig. 1.2]. The latter process, known as intersystem crossing (ISC), is enabled by spin–orbit coupling, which allows the otherwise forbidden transition between triplet and singlet manifolds.

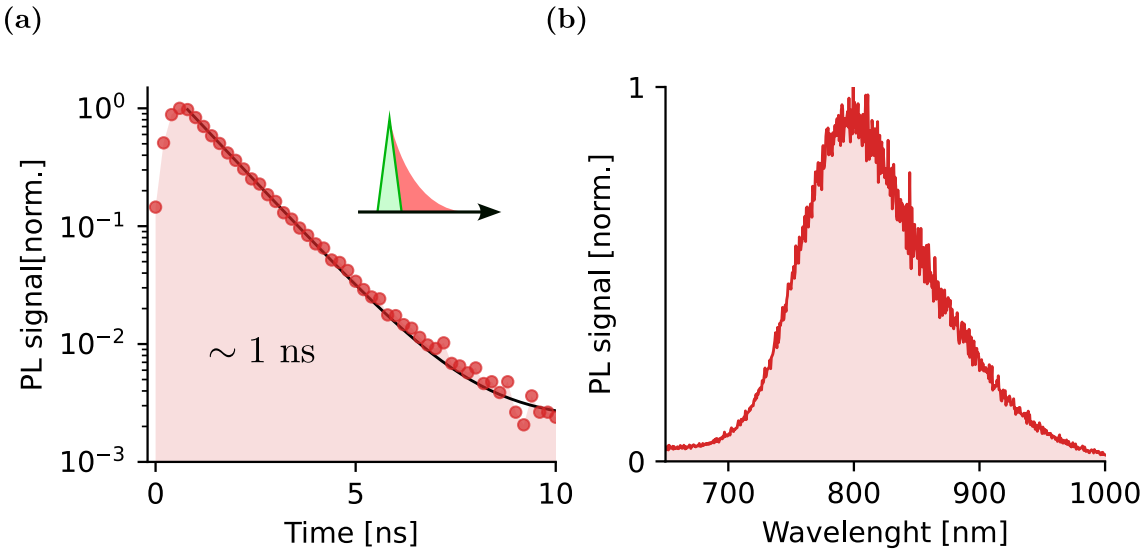


**Figure 1.3:** Optical properties of the $V_B^-$ center. (a) PL decay obtained under a picosecond optical excitation. The decay is fitted with a mono-exponential decay (solid line) to obtain an estimation of the ES lifetime, $\tau_{ES} = 1.20(1)$ ns. (b) Photoluminescence spectrum of $V_B^-$ centers, measured at room temperature under a green (532 nm) laser excitation.

An important aspect of $V_B^-$ photophysics must be emphasized here: the direct dipole transition $^3E'' \rightarrow {}^3A_2'$ is symmetry-forbidden [80, 106, 107]. As a consequence the radiative relaxation is predicted to be slow, with a characteristic timescale of around 10 µs. In contrast, the non-radiative ISC process is expected to occur within

only one nanosecond [107]. As a direct consequence, ab initio studies predict an extremely low quantum efficiency for the $V_B^-$ center, on the order of $10^{-4}$. This point is still a matter of debate in the community and will be discussed in more details in Chapter 2. Without expanding too much the discussion here, it is worth noting that the predicted timescale of the non-radiative ISC process is consistent with the experimentally measured ES lifetime: $\tau_{ES} = 1.20(1)$ ns [Fig. 1.3(a)]. Furthermore, it is empirically known that the $V_B^-$ center exhibits a dim emission, with **no optical isolation of a single center** reported to date. For these reasons, our group tends to agree with the theoretical prediction that the ES lifetime is largely dominated by the non-radiative decay channel through the metastable singlet state mediated.

According to a recent study, the observed PL signal can only be explained by the involvement of phonons, which slightly perturb the defect symmetry and thereby render the transition weakly allowed [108]. This mechanism accounts for the broad PL spectrum of the $V_B^-$ center, plotted in Figure 1.3(b), which does not show trace of a zero-phonon line (ZPL). Such remarkably poor optical properties would certainly have ruled out any interest of the community in the $V_B^-$ center, if the latter did not host an optically-detectable electron spin.

### 1.1.2 Optically-detected magnetic resonance

The $V_B^-$ center GS and ES are spin triplets ($S = 1$). As the name suggests, in such configuration the two unpaired spins can be arranged in three different states:

$$|m_s = 0\rangle = \frac{1}{\sqrt{2}}(|\uparrow\downarrow\rangle + |\downarrow\uparrow\rangle) \quad , \quad |m_s = -1\rangle = |\downarrow\downarrow\rangle \quad , \quad |m_s = +1\rangle = |\uparrow\uparrow\rangle \,, \tag{1.7}$$

where $m_s$ denotes the spin projection along the $z$ axis. As we will see in the next section, the spin–spin interaction between the two unpaired electrons lifts the degeneracy between $|m_s = 0\rangle$ and $|m_s = \pm 1\rangle$, and simultaneously defines the out-of-plane $c$ axis of the hBN lattice, as the natural quantization axis. It is therefore natural to choose the laboratory frame such that the $z$ axis is aligned with the crystal $c$ axis of the hBN crystal, which we will systematically do throughout this manuscript. The energy splitting between the spin state is about six orders of magnitude smaller than the electric-dipole transitions discussed so far. For this reason, it is referred to as the *fine structure*.

As mentioned in the general introduction of this manuscript, the spin and optical properties of this defect are deeply connected. To illustrate this central point, we simplify the electronic structure described in the previous section and consider a single triplet ES. Accounting for the fine structure, we are thus dealing with a seven-level system: three states in the GS, $\{|m_s = 0\rangle, |m_s = -1\rangle, |m_s = +1\rangle\}$, three in the ES, $\{|m_s = 0\rangle', |m_s = -1\rangle', |m_s = +1\rangle'\}$, and one metastable state, $|m\rangle$. This model is sketched in Figure 1.4(a).

Under optical excitation, the spin projection $m_s$ is conserved ($\Delta m_s = 0$), owing again to the selection rules of the electric-dipole interaction. The same applies to the radiative decay, responsible for the photoluminescence signal. The key aspect of the photodynamics then lies in the ISC rates coupling the triplet states with the metastable singlet state. Because these processes are mediated by spin–orbit coupling, they are inherently spin dependent. In other words, the coupling to the non-radiative pathway depends on the spin projection $m_s$. From the ES, the imbalance favors $|m_s = \pm 1\rangle'$ sublevels, which are more strongly coupled to the metastable state. Conversely, from the metastable state, the coupling is stronger toward $|m_s = 0\rangle$ than toward $|m_s = \pm 1\rangle$. These asymmetries in the coupling to the metastable state give rise to two key features:

1. Because the metastable state preferentially relaxes into $|m_s = 0\rangle$, the defect is efficiently pumped into this state during an optical cycle. As a result, optical excitation alone can initialize the defect into $|m_s = 0\rangle$, at room temperature and without any external magnetic field.

2. Because $|m_s = \pm 1\rangle'$ couples more strongly to the non-radiative channel, the defect emits more PL when it is in $|m_s = 0\rangle$. For this reason, $|m_s = 0\rangle$ is commonly referred to as the bright state, whereas $|m_s = \pm 1\rangle$ are called dark states. Crucially, it implies that one can readout the spin state by monitoring the PL signal intensity.

The significance of these two properties can hardly be overstated, as nearly all measurements in this manuscript rely on them, either directly or indirectly. They are particularly central, as they enable the probing of the defect's fine structure through optically detected magnetic resonance (ODMR) spectroscopy. The principle is as follows: a laser continuously pumps the defect into the bright spin state

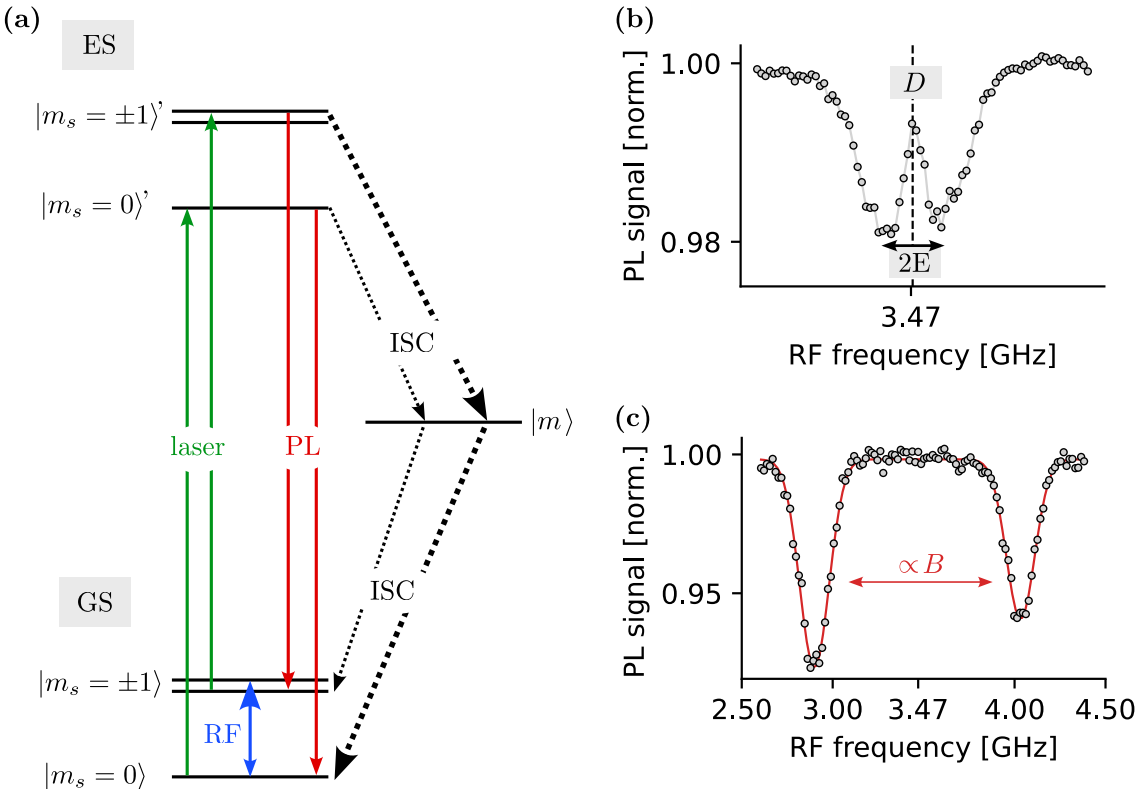


**Figure 1.4:** Spin-dependent photodynamics and optically-detected magnetic resonance (ODMR) spectroscopy. (a) Simplified scheme of the spin-dependent photodynamics of the $V_B^-$ center. Dotted arrows depict non-radiative pathways. (b-c) ODMR spectra of the $V_B^-$ center GS, at (b) zero magnetic field and (c) $B = 20$ mT.

$|m_s = 0\rangle$, while at the same time, the frequency of a radiofrequency (RF) signal is swept across the spin transition resonance. When the RF frequency matches the resonance, the defect absorbs a RF photon and jumps from $|m_s = 0\rangle$ to $|m_s = \pm 1\rangle$, resulting in a drop of PL. By plotting the averaged PL signal as a function of the RF frequency one obtains an ODMR spectrum, a direct spectroscopic measurement of the defect's fine structure.

A typical ODMR spectrum of the $V_B^-$ center GS is shown in Figure 1.4(b). A PL drop of a few percent is observed at approximately 3.47 GHz. This frequency is commonly referred to as the axial zero-field-splitting (ZFS) parameter $D$. It corresponds to the frequency separation between $|m_s = 0\rangle$ and $|m_s = \pm 1\rangle$ in the absence of an external field. To illustrate the key role of ODMR spectroscopy for sensing, we now apply a magnetic field $B$ along the $z$ axis and record a second ODMR spectrum, displayed in Figure 1.4(c). Due to the well-known Zeeman effect, the applied magnetic field lifts the degeneracy between $|m_s = -1\rangle$ and $|m_s = +1\rangle$ sublevels, with a splitting directly proportional to the field magnitude. Measuring the Zeeman

shift through ODMR therefore provides a direct quantitative measurement of the magnetic field, constituting the basic principle of magnetometry with spin defects.

The reader may have noticed that a residual splitting remains even at zero external magnetic field in Figure 1.4(b). This splitting is known as the orthorhombic splitting $E$. As we will see in the next section, it originates from an other kind of perturbations. In fact, the fine structure of the defect encodes a wealth of information about its environment: it is sensitive not only to magnetic fields, but also to electric fields, temperature, and mechanical stress. The ability to precisely probe the spin transitions is therefore a powerful asset for sensing. To clarify how the $V_B^-$ spin couples to these different perturbations, and to identify the one responsible for the orthorhombic splitting $E$, we now introduce the spin Hamiltonian of the $V_B^-$ center.

## 1.2 Spin Hamiltonian

Owing to the short lifetime of the ES, we restrict our analysis to the GS spin Hamiltonian. Since it will be probed through ODMR spectroscopy, we express it in frequency units.

In classical electromagnetism, a particle with charge $q$ and angular momentum $\mathbf{L}$ carries a magnetic moment $\boldsymbol{\mu} = \gamma\mathbf{L}$, where $\gamma$ is the particle's gyromagnetic ratio, $\gamma = \frac{q}{2m}$. In the quantum realm, the spin $\mathbf{S}$ of a particle acts as an intrinsic angular momentum. Consequently, an electron has an associated magnetic moment given by $\boldsymbol{\mu_e} = \gamma_e\mathbf{S}$, where $\gamma_e = -\frac{1}{2\pi}\frac{g_e e}{2m_e} \approx -28$ GHz/T. Here, $g_e \approx 2$ is the Landé factor of the electron, which corrects the classical expression. The spin $\mathbf{S}$ is, however, a quantum quantity that can only take discrete values. Therefore, its components $\hat{S}_x$, $\hat{S}_y$ and $\hat{S}_z$ are not simple scalars but operators. The GS being a spin triplet, it is described by the Pauli $S = 1$ operators, which can be expressed as $3 \times 3$ matrices:

$$\hat{S}_x = \frac{1}{\sqrt{2}}\begin{pmatrix} 0 & 1 & 0 \\ 1 & 0 & 1 \\ 0 & 1 & 0 \end{pmatrix} \quad , \quad \hat{S}_y = \frac{1}{\sqrt{2}}\begin{pmatrix} 0 & -i & 0 \\ i & 0 & -i \\ 0 & i & 0 \end{pmatrix} \quad , \quad \hat{S}_z = \begin{pmatrix} -1 & 0 & 0 \\ 0 & 0 & 0 \\ 0 & 0 & 1 \end{pmatrix}. \tag{1.8}$$

Here, we have chosen $\hat{S}_z$ to be diagonal because of the natural definition of the

quantization axis. Its eigenvalues, are the three possible outcomes for a projection of the spin along the $z$ axis and the corresponding eigenvectors are $|m_s = 0\rangle$, $|m_s = -1\rangle$ and $|m_s = +1\rangle$. We note that in this manuscript $m_s$ will exclusively refer to the spin projection along the $z$ axis.

It is through its spin magnetic moment that the GS couples to the environment. As a result, all terms in the Hamiltonian will involve at least one spin-1 operator. These terms can be broadly categorized into two groups:

- Terms that commute with $\hat{S}_z$ (e.g, $\propto \hat{S}_z$, $\hat{S}_z^2$).
  When the Hamiltonian is expressed in the $|m_s\rangle$ basis, these terms contribute only to diagonal elements. They simply shift the respective energies of the spin states without mixing them. The axial Zeeman term is of this kind.

- Terms that do *not* commute with $\hat{S}_z$ (e.g, $\propto \hat{S}_x$, $\hat{S}_y^2$).
  In the $|m_s\rangle$ basis, these terms introduce off-diagonal elements. If their magnitude is small compared to the diagonal terms, their effect can be treated perturbatively. In this case, they induce transitions (or "jumps") between the $|m_s\rangle$ states. If their magnitude is now non-negligible to the diagonal terms, the full Hamiltonian must be diagonalized, and the new eigenstates become linear combinations of the original $|m_s\rangle$ basis. Additionally, an anticrossing appears between the new spin states. One can already anticipate that the orthorhombic splitting $E$ arises from such terms.

As we will see, both kind of terms appear in the GS Hamiltonian.

### 1.2.1 Electron spin-spin interaction

Even in the absence of any external perturbation, there exists an interaction intrinsic to the defect: the spin–spin interaction between the two unpaired electrons. It can be derived from the classical dipole–dipole interaction between two magnetic moments. In the quantum-mechanical formalism, it is written as

$$\hat{\mathcal{H}}_{SS} = \hat{\mathbf{S}}\bar{D}\hat{\mathbf{S}}.$$

Here, $D$ is not an operator but a $3 \times 3$ matrix:

$$\bar{D} = \begin{pmatrix} D_{xx} & D_{xy} & D_{xz} \\ D_{yx} & D_{yy} & D_{yz} \\ D_{zx} & D_{zy} & D_{zz} \end{pmatrix}.$$

The components of $\bar{D}$ arise from the magnetic dipole–dipole interaction, spatially averaged over the defect's spin density. As a consequence, $\bar{D}$ reflects the symmetry of the defect. Under $D_{3h}$ symmetry, with the $z$ axis aligned along the crystal $c$ axis, $\bar{D}$ reduces to a diagonal form [80, 106]:

$$\bar{D} = \begin{pmatrix} D_{\perp} & 0 & 0 \\ 0 & D_{\perp} & 0 \\ 0 & 0 & D_{zz} \end{pmatrix}.$$

Hence, the Hamiltonian describing the spin-spin interaction can be written:

$$\begin{aligned} \hat{\mathcal{H}}_{SS} &= D_{zz}\hat{S}_z^2 + D_{\perp}(\hat{S}_x^2 + \hat{S}_y^2), \\ &= D_{zz}\hat{S}_z^2 + D_{\perp}(\hat{S}_x^2 + \hat{S}_y^2 + \hat{S}_z^2 - \hat{S}_z^2), \\ &= D_{zz}\hat{S}_z^2 - D_{\perp}\hat{S}_z^2 + D_{\perp}S(S+1). \end{aligned}$$

Here we have used the identity $\hat{S}_x^2 + \hat{S}_y^2 + \hat{S}_z^2 = S(S+1)$. The last term only produces an overall shift of the spin states and can thus be neglected. The expression can then be further simplified to:

$$\hat{\mathcal{H}}_{SS} = D\hat{S}_z^2, \tag{1.9}$$

with $D = D_{zz} - D_{\perp}$ a scalar, known as the axial ZFS parameter. Its effect is straightforward: it induces a frequency shift $D$ between $|m_s = 0\rangle$ and $|m_s = \pm 1\rangle$ sublevels. Simultaneously, it fixes the $z$ axis ($c$ axis of the hBN lattice) as a natural quantization axis for the spin. In principle $D$ can be either positive or negative. In our case, the first report by Gottscholl *et al.* established that $D$ is positive, meaning that $|m_s = \pm 1\rangle$ sublevels lie higher in frequency than $|m_s = 0\rangle$ [81]. Regarding its value, both computational prediction [80] and experiment [Fig. 1.4(b)] agree on a value of $\sim 3.47$ GHz, at room-temperature.

Notably, the value of the axial ZFS parameter $D$ changes significantly with temperature, from 3.6 GHz at 5K to 3.25 GHz at 600K [109]. The first mechanism

is the modification of the lattice parameters. As the temperature decreases, the interatomic distances become shorter, leading to an enhancement of the spin–spin interaction, and consequently to an increase of the parameter $D$. Conversely, as the temperature rises, the lattice expands, reducing the spin–spin interaction and thus decreasing $D$. A second contribution to the temperature dependence of the axial splitting $D$ is the coupling to local phonon-modes. At finite temperature the vacancy vibrates around its equilibrium position which also affects the spin density. A report by Liu *et al.*, especially emphasized the role of this latter contribution for the $V_B^-$ center [110]. Because of this strong temperature dependence, the $V_B^-$ has been proposed as a temperature sensor [111, 112], and a first prove of principle has even been realized [113].

### 1.2.2 Stress and electric-field couplings

From Equation (1.9), it is clear that the spin-spin interaction cannot account for the orthorhombic splitting observed in in Figure 1.4(b). If neither magnetic field nor spin-spin interaction are involved, the usual suspects are stress and electric fields. To identify the culprit, we collaborated with Peter Udvarhelyi and Adam Gali, theorists and computational physicists working at the Wigner institute of Budapest, Hungary. They proceeded in two steps. First, they expressed the couplings of both kind of perturbations with the $V_B^-$ center's electronic spin using a group theory analysis. Then, they computed the strengths of these couplings using DFT on a single hBN flake containing 147 atoms. Here, I will briefly summarize their findings. For a more comprehensive overview, the reader may want to consult the related report, published in *Nature npj computational materials* [114].

#### Stress coupling

Analogously to temperature, mechanical stress may affect the ZFS parameters by reshaping the defect's spin density. According to the group symmetry analysis, the Hamiltonian describing the spin-stress coupling can be written as:

$$\hat{\mathcal{H}}_{\text{Stress}} = h_1(\sigma_{xx} + \sigma_{yy})\hat{S}_z^2 + h_2(\sigma_{xx} - \sigma_{yy})(\hat{S}_x^2 - \hat{S}_y^2). \tag{1.10}$$

Here, $\sigma_{xx}$ and $\sigma_{yy}$ denote the stress components along the $x$ and $y$ directions, defined in Figure 1.5, while $h_1$ and $h_2$ are their corresponding coupling constants. The stress along the $z$ axis is neglected, owning to the large interlayer spacing ($\sim 0.33$

nm) and the mostly planar spin density of the $V_B^-$ center [Fig. 1.1(b)]. In this expression, the two terms play very different roles. While the first one modify the splitting between $|m_s = 0\rangle$ and $|m_s = \pm 1\rangle$, and thus modify the axial ZFS parameter $D$, the second term mixes $|m_s = -1\rangle$ and $|m_s = +1\rangle$ sublevels. It is exactly the kind of term that we are looking for to account for the orthorhombic ZFS splitting $E$. However, the ab-initio calculations reveal a strong asymmetry between both effects, with $h_1 = -19.6 \pm 0.2$ MHz/GPa and $h_2 = 4 \pm 1.2$ MHz/GPa [2]. Stress have thus more impact on the $D$ parameter than on the orthorhombic ZFS parameter $E$. Moreover, while the first term relies on the sum of both spatial stress components and is therefore quite general, the second one requires an asymmetry between $\sigma_{xx}$ and $\sigma_{yy}$, a more restrictive condition.

These theoretical predictions have been recently tested by Mu Zhao, former postdoctoral fellow of the group, who realized a series of ODMR spectra under hydrostatic pressure, ranging from 0 to 3 GPa [115]. His analysis revealed a significant shift of the $D$ parameter, in very good quantitative agreement with the theoretical prediction of the coupling constant $h_1$. Under the same conditions, the orthorhombic parameter $E$ remained unchanged. To explain the zero-field splitting at zero-field, observed in Figure 1.4(b), we therefore need to turn to another kind of perturbation.

## Electric field

The interaction of the $V_B^-$ centers spin with an electric-field is described by the following Hamiltonian:

$$\hat{\mathcal{H}}_{\text{Elec}} = d_\perp[\mathcal{E}_y(\hat{S}_x^2 - \hat{S}_y^2) + \mathcal{E}_x(\hat{S}_x\hat{S}_y + \hat{S}_y\hat{S}_x)]. \tag{1.11}$$

where $\mathcal{E}_x$ and $\mathcal{E}_y$ are the electric field components along the $x$ and $y$ axis, while $d_\perp$ is the susceptibility of the $V_B^-$ center electron spin to a *transverse* electric field (perpendicular to the $z$ axis) . The DFT simulation yields $d_\perp = 20.72 \pm 0.02$ Hz.cm/V. Conversely, the group theory analysis reveals that $d_\parallel = 0$. In other words, an electric field parallel to the $z$ axis cannot couple to the $V_B^-$ center electron spin in the GS. It is clear from expression (1.11), that an electric-field cannot modify the $D$ parameter, but instead induces a mixing of $|m_s = \pm 1\rangle$ sublevels resulting in an orthorhombic splitting.

[2] The negative sign of $h_1$ indicates that $D$ decreases (increases) under tensile (compressive) stress.

To further highlight the distinct effects of stress and electric field on the spin Hamiltonian, Peter Udvarhelyi and Adam Gali, performed two last simulations. They computed the eigenvalues of the stress and electric-field Hamiltonians while progressively increasing the magnitude of each perturbation. For convenience, strain was used in place of stress, though the two are directly related through the elastic tensor. At each strain magnitude, 1000 random configurations of atomic displacements were generated, likewise, for each electric field magnitude, 1000 random configurations of positive and negative charges were considered. The resulting scatter plots are shown in Figure 1.5. They reveal a striking contrast. On one hand random strain yields random shifts of the parameter $D$ and so to an overall broadening of the magnetic resonance [Fig. 1.5(a)]. On the other hand, random charge distributions produce only an orthorhombic splitting $E$ [Fig. 1.5(b)]. We thus conclude that the orthorhombic splitting observed in the zero-field ODMR spectrum of Figure 1.4(b) results from the interaction of the $V_B^-$ electron spin with the transverse component of a local electric-field.

Notably, these findings closely resemble the physics of the $NV^-$ center in diamond [116]. We therefore draw on this similarity to explain the origin of the local electric field. As for the $NV^-$ center, we propose that each $V_B^-$ center is surrounded by a random distribution of charges: not only the $V_B^-$ centers themselves, but also positively charged defects, required to maintain the overall electrical neutrality of hBN. Locally, this random charge distribution creates an electric field at the $V_B^-$ center location, thereby producing an orthorhombic splitting $E$.

In this manuscript we will return several times to the orthorhombic splitting. It is therefore convenient to rewrite Equation (1.11) so that the orthorhombic parameter $E$ appears explicitly, rather than the electric field components. By a simple rotation of the $x$–$y$ basis by an angle $\phi$, defined through $\tan(2\phi) = \mathcal{E}_x/\mathcal{E}_y$, the spin-electric-field Hamiltonian takes the simpler form

$$\hat{\mathcal{H}}_{\text{Elec}} = E\left(\hat{S}_x^2 - \hat{S}_y^2\right), \tag{1.12}$$

where $E = d_\perp\sqrt{\mathcal{E}_x^2 + \mathcal{E}_y^2}$ is the so-called orthorhombic ZFS parameter. The fine-structure Hamiltonian can finally be written in its canonical form:

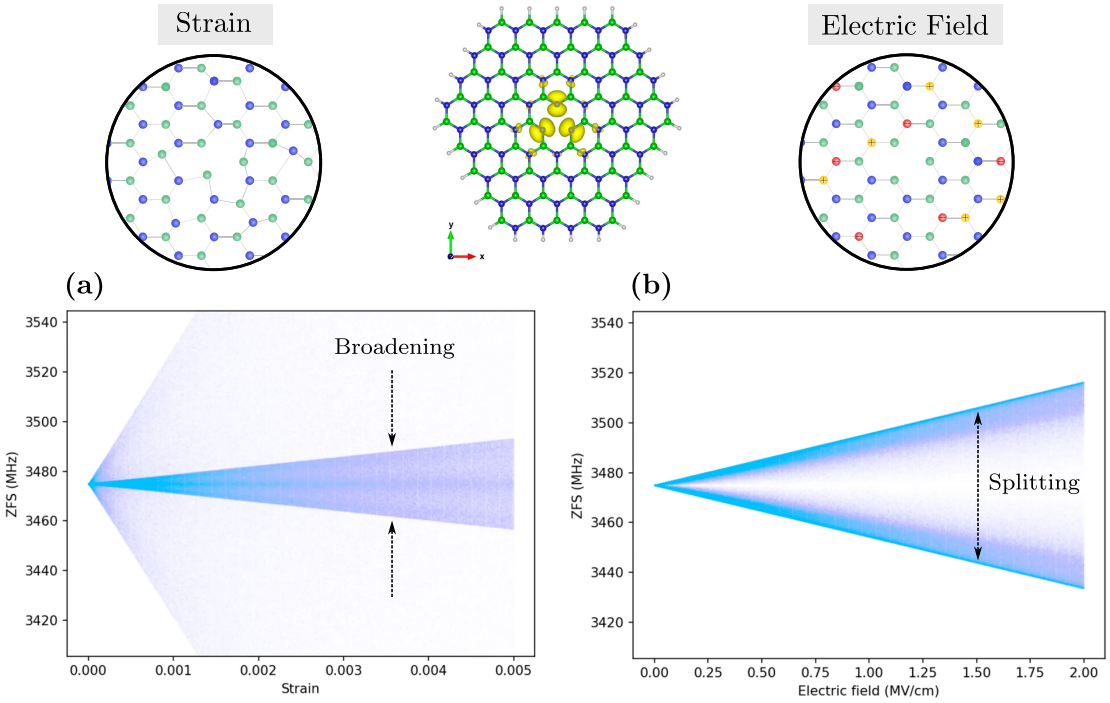


**Figure 1.5:** Impact of strain and electric field on the ZFS parameters. The top panels depict (left) local strain and (right) local charges around a $V_B^-$ center. The central illustration represents the hBN flake used in the DFT simulations. The green and red arrows define the $x$ and $y$ axis. (a) Eigenenergies of the spin-stress Hamiltonian expressed in Equation (1.10), as a function of strain magnitude. (b) Eigenenergies of the spin-electric-field Hamiltonian expressed in Equation (1.11) as a function of electric-field magnitude. Figures adapted from Ref. [114].

$$\hat{\mathcal{H}}_{\mathrm{FS}} = D\hat{S}_z^2 + E\left(\hat{S}_x^2 - \hat{S}_y^2\right). \tag{1.13}$$

This Hamiltonian accurately reproduces the behavior observed in Figure 1.4(b), predicting two eigenfrequencies, $f_\pm$, centered around the zero-field splitting parameter $D$ and separated by $2E$:

$$f_\pm = D \pm E. \tag{1.14}$$

If the orthorhombic parameter $E$ originates from local charges, as we have proposed, one could therefore extract the local charge density by measuring the splitting between $f_\pm$ at zero magnetic field. Such an analysis will be carried out in Chapters 4 and 5.

### 1.2.3 Zeeman effect

If the $V_B^-$ center electronic spin can couples to various perturbations, it is important to keep in mind that, as a spin, its remains predominantly sensitive to magnetic fields. The potential energy of a magnetic dipole in an external magnetic field $\mathbf{B}$, can be written as : $E_{\text{mag}} = -\boldsymbol{\mu}.\mathbf{B}$. Physically, this expression simply implies that the magnetic moment tends to align with the external magnetic field. By analogy with this classical expression, one can write the Zeeman Hamiltonian :

$$\hat{\mathcal{H}}_{\text{Zeeman}} = -\gamma_e \hat{\mathbf{S}} \cdot \mathbf{B} \tag{1.15}$$

Depending on the magnetic field orientation, different behaviours may be observed. Here, we only discuss the simplest one: a field aligned along the defect quantization axis ($|B| = B_z$). In this case, the total Hamiltonian becomes:

$$\hat{\mathcal{H}} = D\hat{S}_z^2 + E(\hat{S}_x^2 - \hat{S}_y^2) + |\gamma_e|\hat{S}_z B_z. \tag{1.16}$$

Two single quantum transitions ($\Delta m_s = \pm 1$) are possible, their frequencies being simply given by

$$f_\pm = D \pm \sqrt{E^2 + |\gamma_e|^2 B_z^2}. \tag{1.17}$$

In Figure 1.6(a), I plot $f_\pm$ as a function of $B_z$. When the magnetic field remains weak ($2\gamma_e B_z \approx E$), the orthorhombic ZFS parameter $E$ mixes the states $|m_s = \pm 1\rangle$, leading to two new eigenstates $|\pm\rangle = \frac{|m_s=+1\rangle \pm |m_s=-1\rangle}{\sqrt{2}}$. Being the superposition of two states with opposite spin projection along the $z$ axis, the latter are less sensitive to the external magnetic field. Consequently, $f_\pm$ do not scale linearly with $B_z$ [Fig. 1.6(b)]. Conversely, when $2\gamma_e B_z \gg E$, the orthorhombic term can be neglected, and a linear splitting emerges between $|m_s = -1\rangle$ and $|m_s = +1\rangle$:

$$f_\pm \approx D \pm |\gamma_e| B_z. \tag{1.18}$$

Crucially, this implies that the magnetic field component $B_z$ can be extracted by measuring the Zeeman shift in the ODMR spectrum. This is what is illustrated in Figure 1.6(c). By fitting the ODMR spectrum with two Gaussians functions, one can directly measure the magnetic field $B_z$ produced by a permanent magnet. This is the basic principle of magnetometry with spin defects.

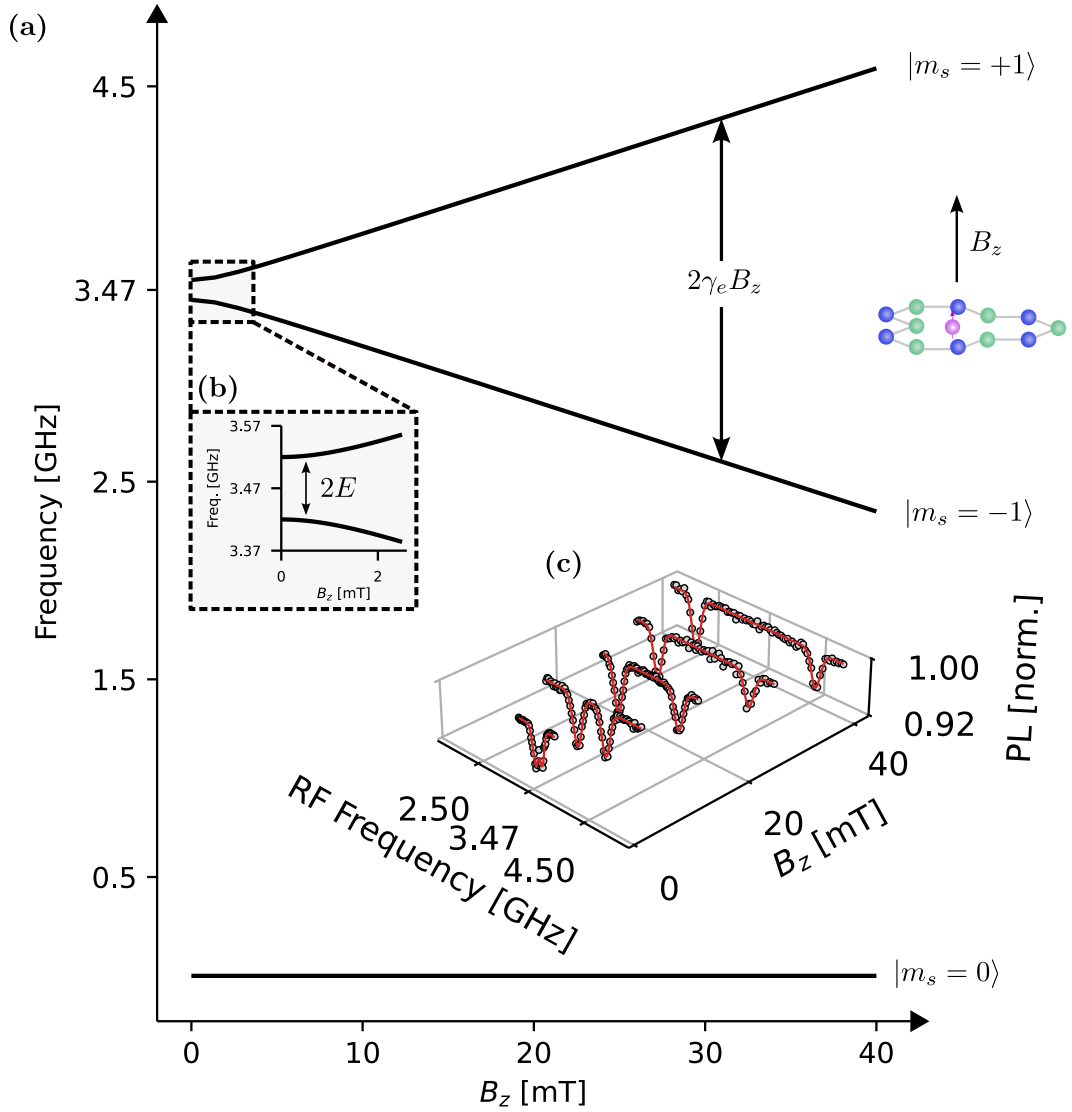


**Figure 1.6:** Zeeman effect. (a) Computed transition frequencies $f_\pm$ as a function of the magnetic field $B_z$. (b) Zoom on the low-field regime. (c) ODMR spectra recorded under various magnetic fields. The field is aligned along the defect quantization axis $z$ and its magnitude is increased from 0 to 40 mT. The magnetic field value is extracted by fitting the data with two Gaussian functions (solid red lines).

If the source of magnetic field can obviously be external, from a magnet or a magnetic sample of interest, it also exists an intrinsic source of magnetic field in a solid-state system : nuclear spins.

### 1.2.4 Hyperfine interaction

Like electrons, most nuclei carry a spin. The interaction between these nuclear spins and the central electron spin is known as the *hyperfine interaction*. It has a form analogous to the electron spin–spin interaction discussed previously:

$$H_{SI} = \hat{\mathbf{S}} A \hat{\mathbf{I}}, \tag{1.19}$$

except that now the Hamiltonian involves the nuclear spin vector $\hat{\mathbf{I}}$ and the hyperfine tensor $A$. The hyperfine tensor itself is made of two contributions:

$$A = A_{\mathrm{d}} + A_{\mathrm{c}}. \tag{1.20}$$

The term $A_{\mathrm{d}}$ accounts for the magnetic dipolar interaction between the two kinds of spins, averaged over the electron spin density. When the nucleus resides in a region of appreciable electron spin density, however, one must also include the Fermi contact term $A_{\mathrm{c}}$. This term corrects the classical dipole–dipole interaction, which assumes that the dipoles are spatially separated. It can be expressed as:

$$A_{\mathrm{c}} = \frac{2\mu_0}{3} \frac{h}{(2\pi)^2} \gamma_e \gamma_n |\psi(0)|^2 \mathbf{SI}, \tag{1.21}$$

where $\mu_0$ is the vacuum permittivity, $\psi(0)$ the electron spin density evaluated at the position of the nucleus, and $\gamma_n$ is the nuclear spin gyromagnetic ratio. Unlike the dipolar contribution, the Fermi contact term is isotropic, contributing equally to all three diagonal components of the hyperfine tensor. Since the $V_B^-$ center spin density is primarily localized on the three nearest-neighbor nitrogen atoms [cf. Fig. 1.1b], this contribution cannot be neglected. In fact, *ab initio* calculations show that for the first-neighbor nitrogen atoms the Fermi contact term dominates the dipolar one by nearly a factor of $\sim 30$ [80].

In natural hBN, the nitrogen sites are occupied with 99.6% probability by $^{14}$N, which carries a nuclear spin $I = 1$. To obtain the hyperfine interaction, one has thus to perform the sum over the three first nitrogen neighbors of the $V_B^-$ center:

$$\hat{\mathcal{H}}_{\mathrm{HF}} = \sum_{i=1}^{3} \hat{\mathbf{S}} A^i \hat{\mathbf{I}}^i. \tag{1.22}$$

As such, hyperfine interactions can add significant complexity to the Hamiltonian. Fortunately, under most experimental conditions, the ZFS and Zeeman terms far exceed the typical hyperfine coupling strength so that one can neglect all hyperfine terms that do not commute with $\hat{S}_z$ and $\hat{I}_z$, i.e, retain only the $A_{zz}$ components of each hyperfine tensor. This simplification, known as the secular approximation, yields:

$$\hat{\mathcal{H}}_{\text{HF}} = \sum_{i}^{3} A_{zz}^{i} \hat{S}_z \hat{I}_z^i. \tag{1.23}$$

These terms are easier to interpret: depending on the nuclear spin projection $m_I$, the electronic spin experiences a different effective magnetic field from the nuclei, resulting in a shift of $+A_{zz}$, $-A_{zz}$, or no shift when $m_I = 0$. Since there are three nitrogen atoms, the total number of possible nuclear spin configurations is however considerable: $(2I+1)^3 = 27$. Hopefully, under $D_{3h}$ symmetry, the three nitrogen atoms are equivalent, which implies that the hyperfine splitting $A_{zz}$ is identical for each nitrogen. As a result, many of these states are degenerate. In this case, sketched in Figure 1.7, it is convenient to define an effective total nuclear spin $I^{\text{eff}} = 3 \times I = 3$, yielding $2I^{\text{eff}} + 1 = 7$ effective hyperfine states, equally spaced by $A_{zz}$, and with respective degeneracies $\{1, 3, 6, 7, 6, 3, 1\}$.

This substructure is known as the *hyperfine structure*. To properly resolve it, a magnetic field must first be applied along the $z$ axis to avoid the state mixing induced by the orthorhombic parameter at zero field. Figure 1.7 shows an ODMR spectrum of the $V_B^-$ center focused on the electron spin resonance $|m_s = -1\rangle$. As expected, a substructure emerges. By fitting the ODMR spectrum with seven Gaussian functions, equally spaced and with amplitudes constrained by the expected degeneracies of each hyperfine sublevels, one obtains $A_{zz} = 47.5(3)$ MHz, in excellent agreement with the *ab initio* prediction of 48 MHz [80].

Unfortunately, since the linewidth of each peak is comparable to the axial hyperfine coupling$A_{zz}$, the seven hyperfine peaks are poorly resolved. This significant broadening arises from hyperfine interactions with more distant neighbors, in particular, the second-nearest neighbors: boron atoms. Boron atoms also carry a nuclear spin, although weakly coupled, they cause an additional subdivision of each resonance that we do not resolve. In consequence, the seven hyperfine sublebels of the first nitrogen shell can barely be distinguished, leading to a large electron spin resonance linewidth of $\sim 200$ MHz. As it will become clear by the end of this chapter, this large linewidth represents a major bottleneck for a sensor based on $V_B^-$ centers. In Chapter 3, we will see how isotopic control of both nitrogen and boron atoms can be employed to engineer the hyperfine structure and improve the situation. Yet, the key message remains: the dense nuclear spin bath intrinsic to the hBN lattice fundamentally limits the ODMR spectrum linewidth of the $V_B^-$ center.

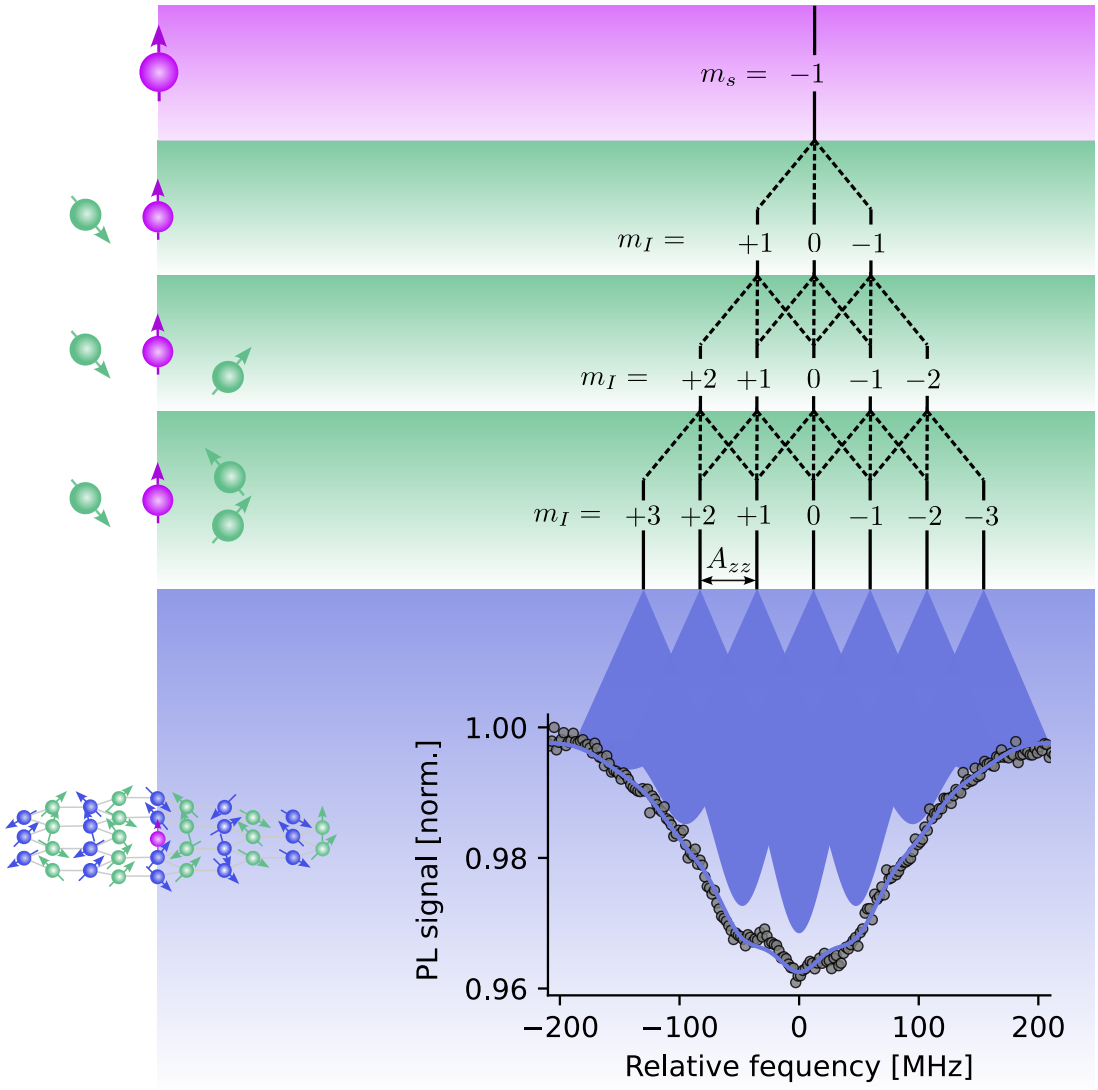


**Figure 1.7:** Hyperfine structure of the $V_B^-$ center surrounded by three equivalent $^{14}$N atoms. Top: schematic of the hyperfine structure of the $|m_s = -1\rangle$ electron spin sublevel while first $^{14}$N neighbors are progressively added. Bottom: ODMR spectrum focused on the electron spin resonance $|m_s = -1\rangle$ under a bias magnetic $B_z$ of few mT. The experimental curve is fitted with seven Gaussian functions (solid line), equally spaced and with amplitudes constrained by the corresponding level degeneracies.

## 1.3 Coherent control and spin relaxation times

While ODMR spectroscopy is particularly well suited for sensing static perturbations that remain constant over the course of a measurement, it is ineffective for probing dynamic perturbations. This is where pulse sequences come into play. By replacing continuous excitation with tailored sequences of laser and RF pulses, one can monitor the time evolution of the spin state and thereby access dynamic perturbations, such as magnetic or electric noise. Originally developed in the context

of electron paramagnetic resonance (EPR) and nuclear magnetic resonance(NMR), these pulse protocols have since been successfully adapted to optically active spin defects. The method relies on two key concepts: time-resolved spin-state readout and and RF-mediated spin coherent control. Equipped with these techniques, we can access the key quantities which characterize the spin dynamics: the spin relaxation times. Beyond providing valuable insights into the physics of the defect, these measurements can also be exploited in sensing experiments, a method known as relaxometry [1].

### 1.3.1 Initialization and readout

The principle of pulsed-sequences is depicted in Figure 1.8. A microsecond-long laser pulse first initialize the spin in $|m_s = 0\rangle$ through optical pumping. Then the spin is either left in the dark, free to interact with its environment, or manipulated with RF pulses. When the spin state needs to be readout, a second laser pulse, identical to the first, is applied. The readout method proceeds as follows:

1. The PL is averaged over a time window of a few hundred nanoseconds at the end of the pulse, when the spin is maximally polarized by optical pumping. This average defines a reference value $S_{\text{ref}}$.

2. The PL is averaged over a window at the very beginning of the pulse, when the spin-state information has not yet been erased by the optical polarization process. This yield a value $S_i$.

3. $S_i$ is normalized by the reference value $S_{\text{ref}}$, so that the normalized signal $S = \frac{S_i}{S_{\text{ref}}}$ equals 1 when the spin is maximally polarized in the $|m_s = 0\rangle$ state, and is less than 1 when part of the population has been transferred into the dark states $|m_s = \pm 1\rangle$ [see Fig. 1.8].

Since the readout laser pulse also repolarizes the system into $|m_s = 0\rangle$, the sequence can be immediately repeated with a parameter $\tau$, such as a delay or a pulse duration, incremented. The normalized PL signal $S$ is then measured for increasing values of $\tau$, yielding a time-resolved measurement of the spin state. To distinguish it from the continuous PL signal detected in ODMR spectroscopy, we will hereafter refer to $S$ as the readout PL signal (R-PL).

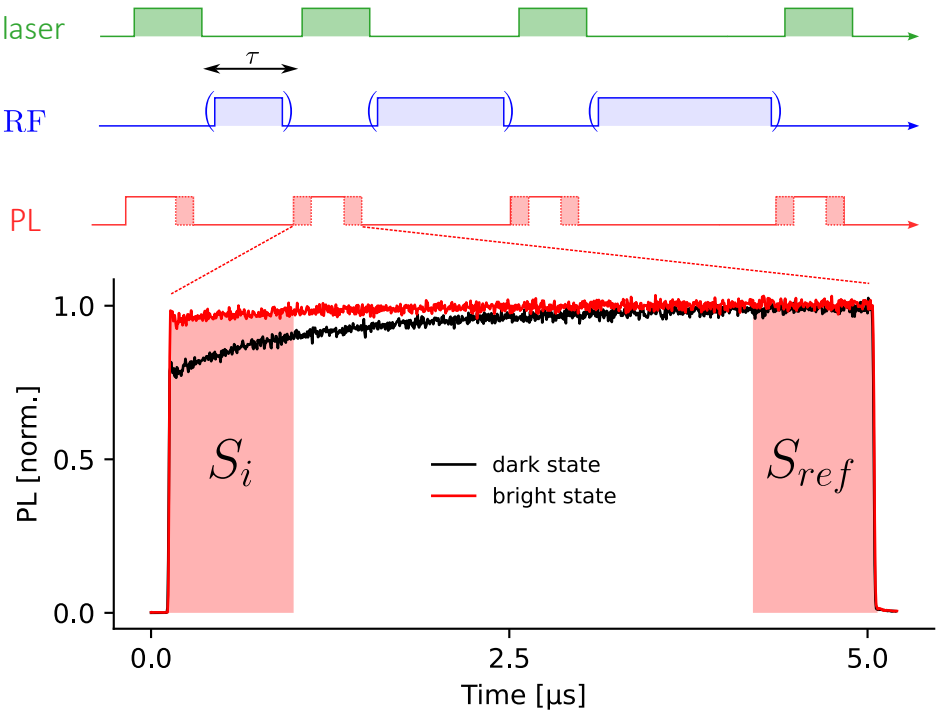


**Figure 1.8:** Pulsed sequence method. At the top: illustration of a pulse sequence combining laser and RF pulses. At the bottom: typical PL pulse for $V_B^-$ centers prepared in the bright state $|m_s = 0\rangle$ (red), or in the dark states $|m_s = \pm 1\rangle$ (black). The two time windows of interest, $S_i$ and $S_{ref}$, are highlighted in red.

### 1.3.2 Coherent spin control and rabi Sequence

With optical excitation alone, the spin can only be prepared in the $|m_s = 0\rangle$ state. To prepare the $|m_s = -1\rangle$ state, or more interestingly, a coherent superposition of $|m_s = 0\rangle$ and $|m_s = -1\rangle$, a pulsed RF drive is required. We begin by applying a magnetic field to isolate a specific electron spin transition, e.g $|m_s = 0\rangle \rightarrow |m_s = -1\rangle$, and reduce the system to an effective two-levels Hilbert space. In this case, the spin state can be written as:

$$|\Psi\rangle = \alpha\,|m_s = 0\rangle + \beta e^{-i\omega t}\,|m_s = -1\rangle\,, \tag{1.24}$$

where $\alpha$ and $\beta$ are real coefficients satisfying $\alpha^2 + \beta^2 = 1$, and $\omega$ is the Larmor angular frequency of the transition. To visualize such a spin state, one can use the Bloch-sphere representation. In this picture, sketched in Figure 1.9(a), the vertical axis is referred to as the population axis, as it reflects the relative occupation of the basis states: the north pole corresponds to full population in $|m_s = 0\rangle$ ($\alpha = 1$), and the south pole to full population in $|m_s = -1\rangle$ ($\beta = 1$). By contrast, the equatorial

plane is known as the coherence plane, where the azimuthal angle of the state is set by the phase $\phi(t) = \omega t$. Thus, in a coherent superposition the spin state precesses around the population axis at the Larmor angular frequency $\omega$.

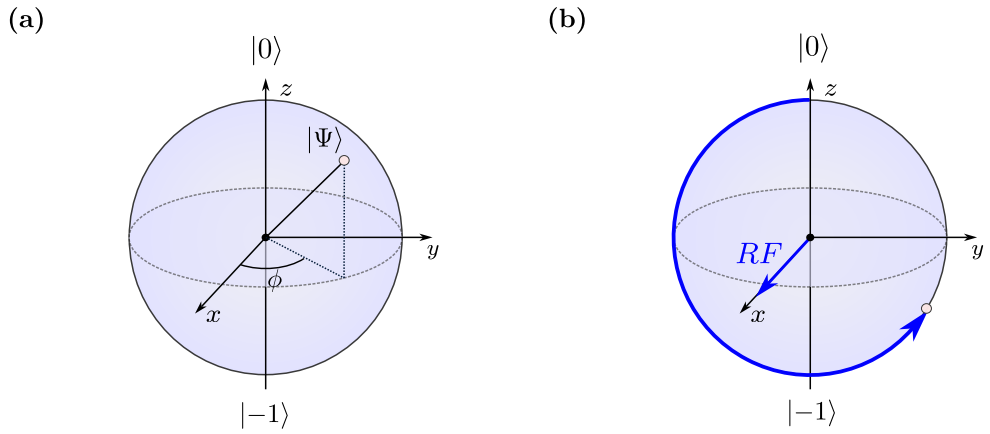


**Figure 1.9:** Bloch sphere and RF drive. (a) Bloch sphere representation of an arbitrary spin state $|\Psi\rangle$ (pink dot). (b) Rabi nutation visualized in a frame rotating at the Larmor frequency.

Since the Bloch sphere mirrors the physical spin components along $x$, $y$, and $z$, the axis of the RF drive can naturally be depicted on it. Starting from $|m_s = 0\rangle$, we apply a resonant RF drive oriented orthogonally to the $z$ axis. Being resonant, this RF field also rotates at the Larmor frequency. Under the influence of this transverse drive, the spin undergoes an additional precession, this time around the RF-field axis. The combination of both precessions gives rise to the well-known Rabi nutation. In the rotating frame, where the entire Bloch sphere itself rotates at the Larmor angular frequency $\omega$, the dynamics simplify: the spin state now undergoes simple oscillations between $|m_s = 0\rangle$ and $|m_s = -1\rangle$ [Fig. 1.9(b)]. Importantly, this type of spin manipulation is called *coherent*, meaning that the phase between the RF drive and the spin state remains well defined during the rotation. As a result, by applying an RF pulse of appropriate duration, the spin state can be placed at any desired latitude on the Bloch sphere. Two pulse durations are of particular importance:

- $\pi$ **pulse**: This corresponds to the RF pulse duration required to flip the spin from $|m_s = 0\rangle$ to $|m_s = -1\rangle$.

- $\frac{\pi}{2}$ **pulse**: This pulse creates a coherent superposition of the two spin states, with identical probability amplitudes. It is commonly used as the first step in

sequences designed to probe quantum coherence.

To calibrate the pulse duration, a Rabi sequence is performed [see Fig. 1.10(a)]. A radio-frequency (RF) pulse of variable length is applied between the initialization and readout laser pulses. The readout PL signal is then monitored as a function of the RF-pulse duration.

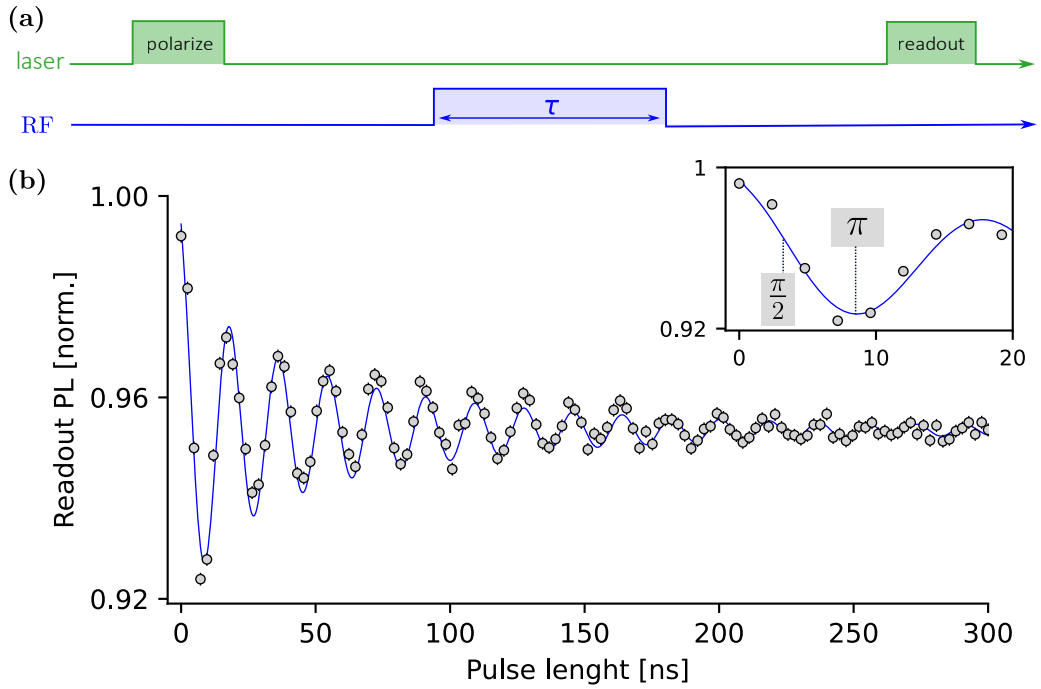


**Figure 1.10:** Coherent control of the $V_B^-$ center spin state. (a) Scheme of the Rabi sequence. (b) Readout PL signal as a function of the RF pulse length. The fit is performed using $f(\tau) = a\, e^{-(\tau/T_{rabi})^n} \cos\left(\frac{2\pi}{2\tau_\pi}\tau\right) + c$. The inserted panel is a zoom realized on the first Rabi period. Axis units are the same as the ones of the main plot.

A typical result is plotted in Figure 1.10(b). Clear monochromatic oscillations can be observed as the spin state is coherently transferred from the bright state ($|m_s = 0\rangle$) to the dark state ($|m_s = -1\rangle$). A typical $\pi$-pulse duration of $\tau_\pi \approx 8$ ns can be extracted. Notably, the Rabi oscillations show strong attenuation and vanish after only $\sim 200$ ns of RF driving. This behavior reflects the non-ideal nature of our two-level system: in reality, the transition involves a manifold of hyperfine states. As a result, perfect resonance cannot be guaranteed, and the actual driving may be slightly detuned. Because both the amplitude and the frequency of Rabi oscillations depend on detuning, the measured signal is effectively an average over several slightly different oscillations. Initially in phase, their frequency mismatch progressively leads to destructive interference and thus to damping of the oscillations. At this stage, the

spin is left in an incoherent superposition, and the information about its position on the coherence plane is completely lost. Fortunately, the Rabi drive is fast enough to enable reasonably efficient spin manipulation before the signal decays significantly. Now that we have unlocked coherent spin control and time-resolved readout, we proceed to measure the spin relaxation times.

### 1.3.3 Longitudinal spin relaxation time $T_1$

A fundamental limit to pulse-based spin control is set by population relaxation. The polarized state prepared by the first initialization pulse is an out-of-equilibrium state that cannot be preserved indefinitely. Once the laser is turned off, the spin interacts with its environment and progressively relaxes toward thermal equilibrium, where all spin states are equally populated. The characteristic timescale of this relaxation process defines the longitudinal spin relaxation time $T_1$.

The experimental sequence used to measure $T_1$ is illustrated in Figure 1.11(a). It is the simplest protocol, consisting of one laser pulse for initialization, a delay $\tau$ in the dark, and a second laser pulse for readout. When $\tau \ll T_1$, the $V_B^-$ electron spin remains polarized in $|m_s = 0\rangle$, and the readout PL signal stays bright. Conversely, when $\tau \gg T_1$, the spin relaxes toward the dark $|m_s = \pm 1\rangle$ states, causing the readout PL intensity to decrease. To verify that the variation of the readout PL signal arises solely from the loss of spin polarization, a differential measurement scheme can be employed: a $\pi$ pulse is applied at the end of the free-evolution interval to project the spin into the dark state. By subtracting the signals from sequences with and without applying the $\pi$ pulse, non–spin-related contributions to the PL signal are removed. In our case, however, no significant difference was observed, and we therefore rely primarily on the simpler, fully optical sequence.

Figure 1.11(b), shows the result of such sequence at room and low (4K) temperature. In both cases, the readout PL signal decays as the delay $\tau$ increases reflecting the progressive relaxation of the populations from a polarized state in $|m_s = 0\rangle$, to a thermal spin distribution. To extract $T_1$, the readout PL signal is then fitted with a mono-exponential decay. While at room temperature $T_1$ lies in the range of 15–20 µs, at 4 K it increases by nearly two orders of magnitude, reaching the millisecond timescale. This pronounced temperature dependence clearly indicates a phonon-mediated spin relaxation mechanism [117]. By combining measurements

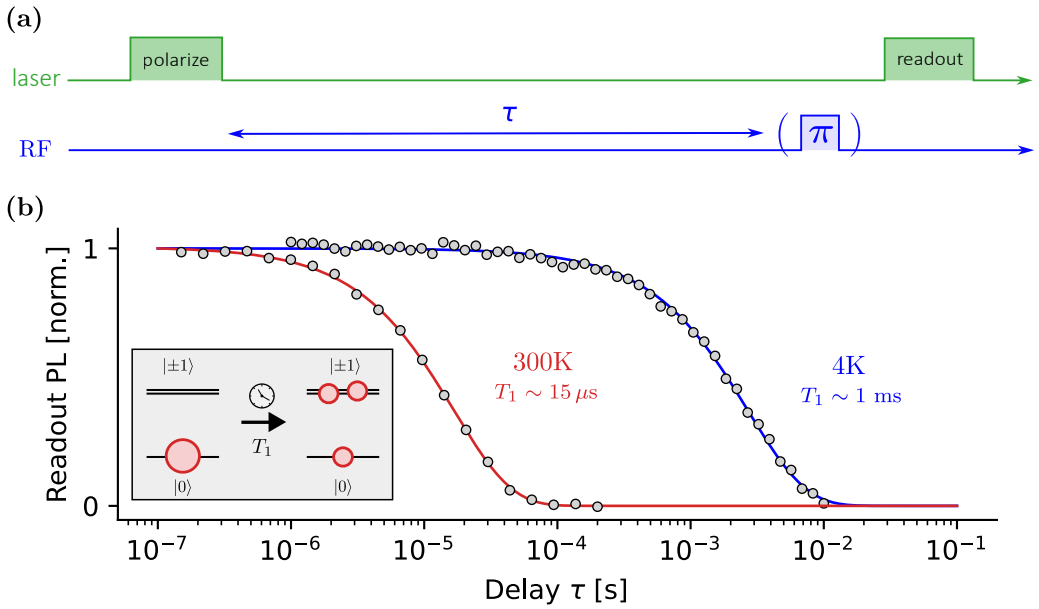


**Figure 1.11:** Longitudinal spin relaxation time $T_1$ of the $V_B^-$ center. (a) Scheme of the sequence used to measure $T_1$. The RF $\pi$ pulse is optional. (b) Experimental data obtained at room temperature (red) and 4 K (blue). The solid lines are mono-exponential decay fits. The signals have been artificially normalized between 0 and 1 for a better comparison. A typical contrast of 15% is observed between the polarized and thermal spin states. Inset: illustration of the spin relaxation process defining the longitudinal spin relaxation time $T_1$.

of the $T_1$ temperature dependence with *ab initio* simulations, Liu *et al.* identified a local out-of-plane vibrational mode at 18 meV as responsible for the $T_1$ relaxation [110]. This interpretation was further supported by recent theoretical work [118]. Since the energy of this phonon mode exceeds the spin transition by several orders of magnitude, a direct single-phonon process is unlikely. Instead, two-phonon Raman or Orbach processes are the most plausible relaxation pathways, similar to what is known for the $NV^-$ center in diamond [119].

Beyond spin–phonon relaxation, a $T_1$ sequence can also serve as a probe of magnetic noise. The principle is straightforward: if the noise has a transverse component, resonant with a spin transition, it can drive spin flips and thereby accelerate the relaxation of the spin population. This approach, known as $T_1$ relaxometry, has already been applied with $V_B^-$ centers to detect magnetic noise from paramagnetic ions in liquid solution [120, 121]. More recently, surface electric noise detection has also been reported [122].

### 1.3.4 Inhomogeneous coherence time $T_2^*$

After having probed the relaxation of the spin populations, we now turn to the spin coherence. A first approach to probe spin coherence is the Ramsey sequence, illustrated in Figure 1.12(a). After initialization in $|m_s = 0\rangle$ with a laser pulse, a first $\frac{\pi}{2}$ RF pulse projects the spin onto the coherence plane. The RF field is then switched off, allowing the spin to freely precess in the dark for a time $\tau$. Before the final optical readout of the spin state, a second $\frac{\pi}{2}$ pulse is applied to project the spin back onto the population axis.

For short delays $\tau$, the phase relationship between the spin and the RF field is preserved, since the internal clock of the RF generator provides a stable phase reference even during the free-evolution period. In this limit, the second $\frac{\pi}{2}$ pulse effectively completes a $\pi$ rotation, transferring the spin into the dark state and making the entire sequence equivalent to a $\pi$ pulse.

For longer timescales, however, the finite linewidth of the transition must again be taken into account. As illustrated in Figure 1.12(b), some spin states precess faster or slower than the targeted Larmor frequency because lying slightly higher or lower in energy. As a result, after free evolution the spin state is no longer represented by a single point on the Bloch sphere, but by a spread-out distribution. When the second RF $\frac{\pi}{2}$ pulse is applied, most of this distribution is not perfectly projected onto the dark state. Since the spreading increases with the free-precession time $\tau$, the effectiveness of the final projection decreases, causing the readout PL signal to rise. The characteristic timescale of this process defines the inhomogeneous coherence time, denoted $T_2^*$. Since the signal is usually less contrasted than for a $T_1$ measurement we prefer this time to implement a differential measurement scheme, i.e, the phase of the last $\frac{\pi}{2}$ pulse alternates between $x$ and $-x$ to project the spin either into the bright or the dark state. The differential readout signal ($\Delta$ readout PL signal) is obtained by taking the difference between the two sequences. In addition to removing non-spin related contributions to the PL signal, this scheme provides a proper definition of zero coherence, that is, when both the $\frac{\pi}{2}$ and $-\frac{\pi}{2}$ sequences yield the same readout PL signal. The typical result of such sequence applied to $V_B^-$ centers is shown in Figure 1.12(c). Within only a few nanoseconds both $\frac{\pi}{2}$ and $-\frac{\pi}{2}$ sequences merge and the differential readout PL signal reaches zero. By fitting this decay with a Gaussian decay profile, $ae^{-(t/T_2^*)^2} + c$, we extract $T_2^* =$

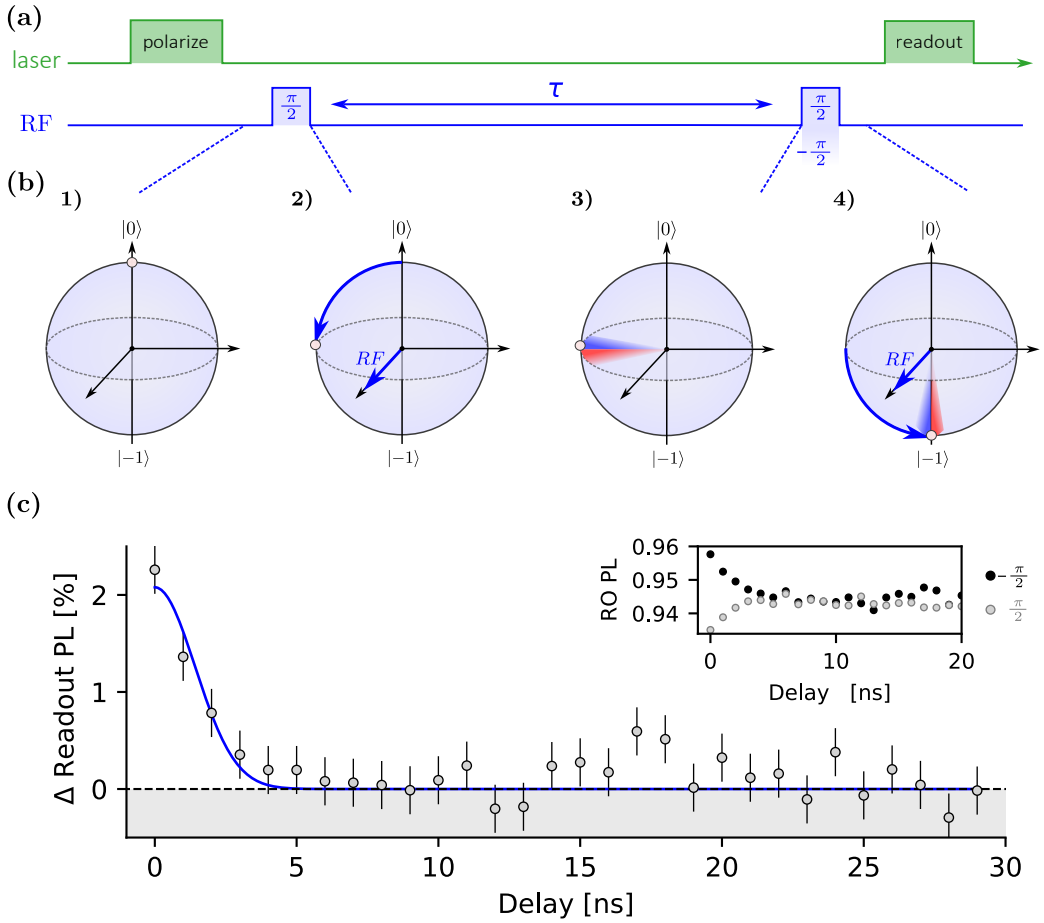


**Figure 1.12:** Inhomogeneous coherence time $T_2^*$ of the $V_B^-$ center. (a) Schematic of the Ramsey sequence. The last RF pulse alternates between $+\frac{\pi}{2}$ and $-\frac{\pi}{2}$ to perform a differential sequence. (b) Key steps of the sequence visualized on the Bloch sphere: 1) Initialization. 2) Projection on the coherence plane. 3) Free precession in the rotating frame. 4) Projection on the dark state. Blue (red) shade depicts states being blue(red)-shifted from the RF frequency. (d) Differential readout PL plotted as a function of the free precession time. The inserted panel depicts both $+\frac{\pi}{2}$ and $-\frac{\pi}{2}$ sequences individually.

1.8(2) ns. The inhomogeneous coherence time is directly related to the linewidth of the magnetic resonance. Assuming a Gaussian lineshape with full width at half maximum (FWHM) $\Gamma$, one finds

$$T_2^* = \frac{2\sqrt{\ln(2)}}{\pi\Gamma}, \tag{1.25}$$

which yields $\Gamma \approx 220$ MHz. Hence the extremely short value of $T_2^*$ is consistent with the hyperfine-broadened ODMR resonance presented in Section 1.2.4 [Fig. 1.7].

### 1.3.5 Spin echo coherence time $T_2$

The limitation of the Ramsey sequence lies in its sensitivity to the non-selectivity of the RF drive, which simultaneously excites multiple transitions with slightly different Larmor frequencies. However, since this dephasing is constant over the course of the measurement, one can exploit a simple trick to cancel it. This is precisely the aim of the spin-echo sequence, illustrated in Figure 1.13(a). It closely resembles the Ramsey sequence, except that a $\pi$ pulse is inserted midway between the two $\pi/2$ pulses. More precisely, the $\pi$ pulse is applied along the $y$-axis of the Bloch sphere, i.e, phase-shifted by 90° compared to the $\frac{\pi}{2}$ pulses. Without changing the principle of the sequence, this scheme is known to be more robust against pulse errors [123].

The role of the RF $\pi$ pulse is illustrated in Figure 1.13(b). After a first free-precession interval of duration $\tau/2$, the $\pi$ pulse reverses the phase which respect to the $y$ axis. As a result, states that were precessing faster now lag behind, while the slower states move ahead. If the system is allowed to evolve for another delay $\tau/2$, the dephasing is cancelled and all spin components refocus on the Bloch sphere. At this precise moment, the second $\pi/2$ pulse is applied, projecting all the coherence back onto the population axis. Hence, by simply adding a $\pi$ pulse one get rid of the static dephasing probed by the Ramsey sequence. However, this elegant trick only works if the spin accumulates exactly the same phase during both precession intervals, that is, if the Larmor frequency remains unchanged throughout the sequence. In reality, the spin environment exhibits some dynamics, e.g, nuclear spin flips, which eventually causes the Larmor frequency to fluctuate. When this happens, the spin fails to rephase completely, leading once again to a loss of coherence and to a decay of the signal. The characteristic time associated with this process is known as the spin echo coherence time, simply denoted $T_2$. Unlike $T_2^*$, which is sensitive to static or quasi-static noise, $T_2$ reflects only dynamical noise and therefore provides additional informations compare to ODMR spectroscopy.

Once again, we employ a differential scheme for more reliability. A typical result is shown in Figure 1.13(c). We fit it with a stretch exponential law to obtain the spin echo coherence time $T_2 = 99(9)$ ns. Although this represents an order-of-magnitude improvement compared to $T_2^*$, the value remains short. The culprit is, once again, the nuclear spins. The bath of nitrogen and nuclear spins surrounding the $V_B^-$ center is constantly crossed by spin flips, producing an effective fluctuating magnetic

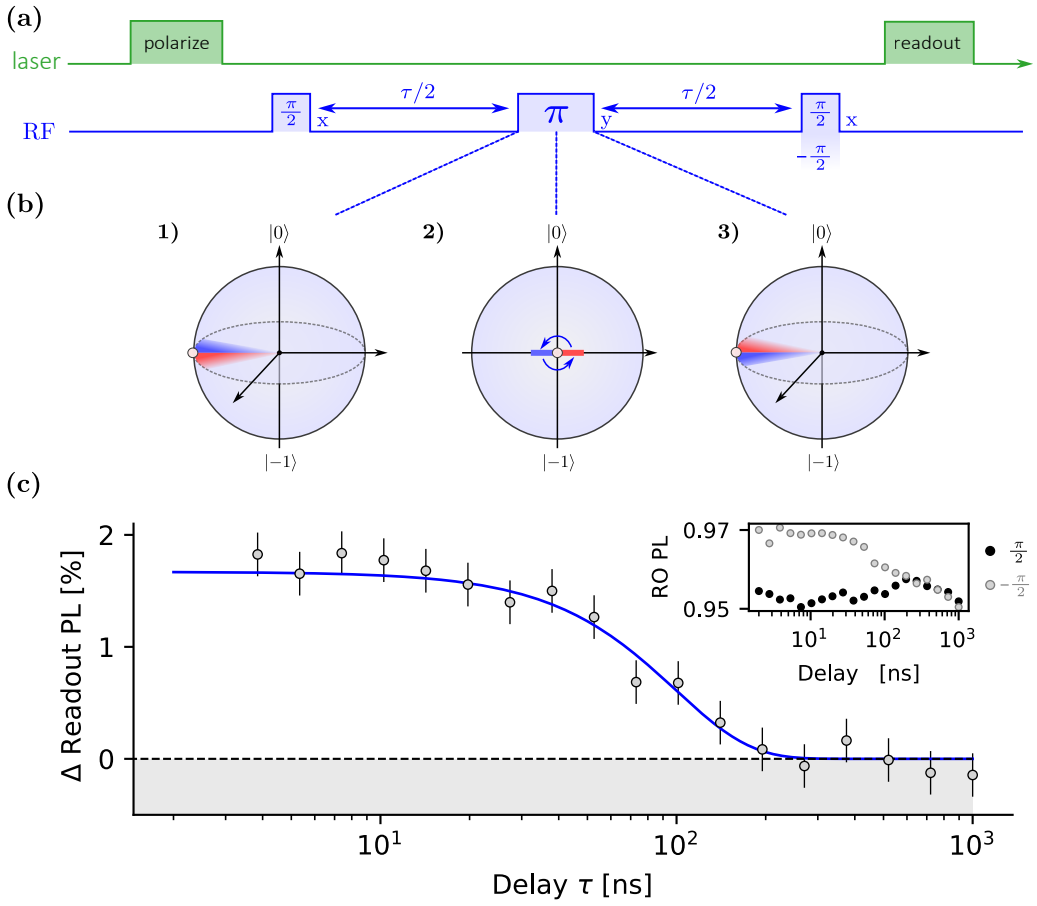


**Figure 1.13:** Spin echo coherence time $T_2$ of the $V_B^-$ center. (a) Scheme of the spin echo sequence. The RF $\pi$ pulse is applied along the $y$ axis of the Bloch sphere (rotating frame) while the $\frac{\pi}{2}$ are applied along the $x$ axis. The last RF pulse alternates between $+\frac{\pi}{2}$ and $-\frac{\pi}{2}$ to perform a differential sequence. (b) Key step of the sequence visualized on the Bloch sphere. 1) Phase distribution before the RF $\pi$ pulse. 2) Phase rotation during the RF $\pi$ pulse. 3) Phase distribution after the RF $\pi$ pulse. (c) Differential readout PL signal plotted as a function of the total free precession time $\tau$. The inserted panel depicts both $+\frac{\pi}{2}$ and $-\frac{\pi}{2}$ sequences individually.

field at the location of the $V_B^-$ center. Theoretical works predict that such noise limits the coherence time $T_2$ of $V_B^-$ center to about 100 ns in natural hBN [124], in full agreement with the presented data and others experimental reports [125–127].

It should be noted that this drastic limitation arises not only from the dense nuclear spin environment but also from the strong coupling between the electronic spin and the nuclear spin bath. As discussed in Section 1.2.4, the spin density of the $V_B^-$ center is largely localized around the three nearest-neighbor nitrogen atoms, leading to a large axial hyperfine splitting $A_{zz} \approx 48$ MHz, through the Fermi contact term. The magnitude of this hyperfine coupling is a critical factor for decoherence, as it determines the phase shift acquired by the electronic spin whenever a nitrogen

nuclear spin flips.

Finally, it should be noted that if an oscillating noise component is resonant with the interpulse delay, the spin echo will not only fail to suppress it but will actually enhance its contribution to dephasing. This property can be exploited for noise spectroscopy and AC-field sensing. The sensitivity and frequency range of this method are nonetheless constrained by the spin-echo time, which, as discussed, is relatively short for the $V_B^-$ center. To overcome this limitation, one can employ more sophisticated refinements of the basic spin-echo sequence, such as XY-8 or CPMG sequences. A preliminary proof-of-principle of AC magnetic-field sensing using this approach with $V_B^-$ centers has already been reported [126].

## 1.4 Magnetic imaging with $V_B^-$ centers in hBN: proof of concept

To conclude this first chapter, we aim to demonstrate a proof-of-concept of magnetic field imaging using $V_B^-$ centers embedded in an hBN flake. Since the promise of this sensor lies primarily in its ability to probe van der Waals (vdW) materials, we naturally selected a vdW magnet as the sample of interest. Specifically, we chose to investigate $1T$-$CrTe_2$, a vdW ferromagnet with in-plane magnetic anisotropy. In its bulk form, this crystal exhibits a Curie temperature ($T_c$) slightly above 300 K and a magnetization of approximately $M \sim 130$ kA/m under ambient conditions [128–131]. Importantly, this allows magnetic imaging to be performed directly at room temperature.

We begin by describing, step by step, the sample preparation process. We then characterize the sensor's sensitivity, constituting a first figure of merit and a baseline for subsequent improvements. Finally, we demonstrate imaging of the magnetic field produced by the $CrTe_2$ flake. This study was carried out during my Master's internship, and my personal contribution was therefore relatively modest. The main experimental work was carried out by Pawan Kumar and Florentin Fabre, former postdoctoral fellow and PhD student of the team, respectively.

### 1.4.1 Sensor engineering

This process consists of three main steps: hBN growth, $V_B^-$ center creation, and the exfoliation of the bulk crystals. It should be emphasized that all these steps are the result of collaborations, which will be explicitly acknowledged. The work carried out in Montpellier, focused exclusively on the sensing experiment.

#### hBN bulk crystal growth

The hBN crystals used in this work were grown by the group of James H. Edgar at Kansas State University. The growth method, known as the metal-flux technique, consists in melting metallic (Ni–Cr) precursors with boron powder while sustaining the mixture under a nitrogen flux [132]. This process yields large, high-quality bulk hBN crystals, reaching millimeter-scale dimensions in-plane. A photograph of a typical crystal obtained by this technique is shown in Figure 1.14(a). Importantly for thesis work, this method enables the growth of mono-isotopic hBN crystals. For this specific study, the hBN sample was isotopically enriched in $^{10}$B, with a purity exceeding 99 %, while the nitrogen isotope is naturally purified with $^{14}$N [133]. Since Chapter 3 is devoted to isotopic purification, a more detailed discussion of the crystal growth and isotopic control is postponed to that chapter. It is worth to say that all samples studied in my thesis work, where exclusively provided by James H. Edgar 's group and grown by the metal-flux technique.

#### $V_B^-$ centers creation

Since the $V_B^-$ center is a dim emitter, experiments can only be performed on ensembles. Hopefully, given its relatively simple structure, the $V_B^-$ center is particularly easy to create, and most conventional defect-creation techniques have proven effective: ion implantation [135–137], focused ion beam [138–141], electron irradiation [142, 143], femtosecond-laser writing [144], and neutron irradiation [81, 145]. In our group, two main approaches have been explored for defect creation: neutron irradiation and ion implantation. In this specific work we relied on neutron irradiation. A pristine bulk hBN crystal was irradiated with thermal neutrons at a dose of $2.6 \times 10^{16}$ neutron.cm$^{-2}$. This method produces a homogeneous defect distribution throughout the crystal depth, allowing irradiation to be performed directly on the bulk crystal. More details about this important point will be given in Chapter 4, which is devoted to the characterization of neutron irradiated crystals.

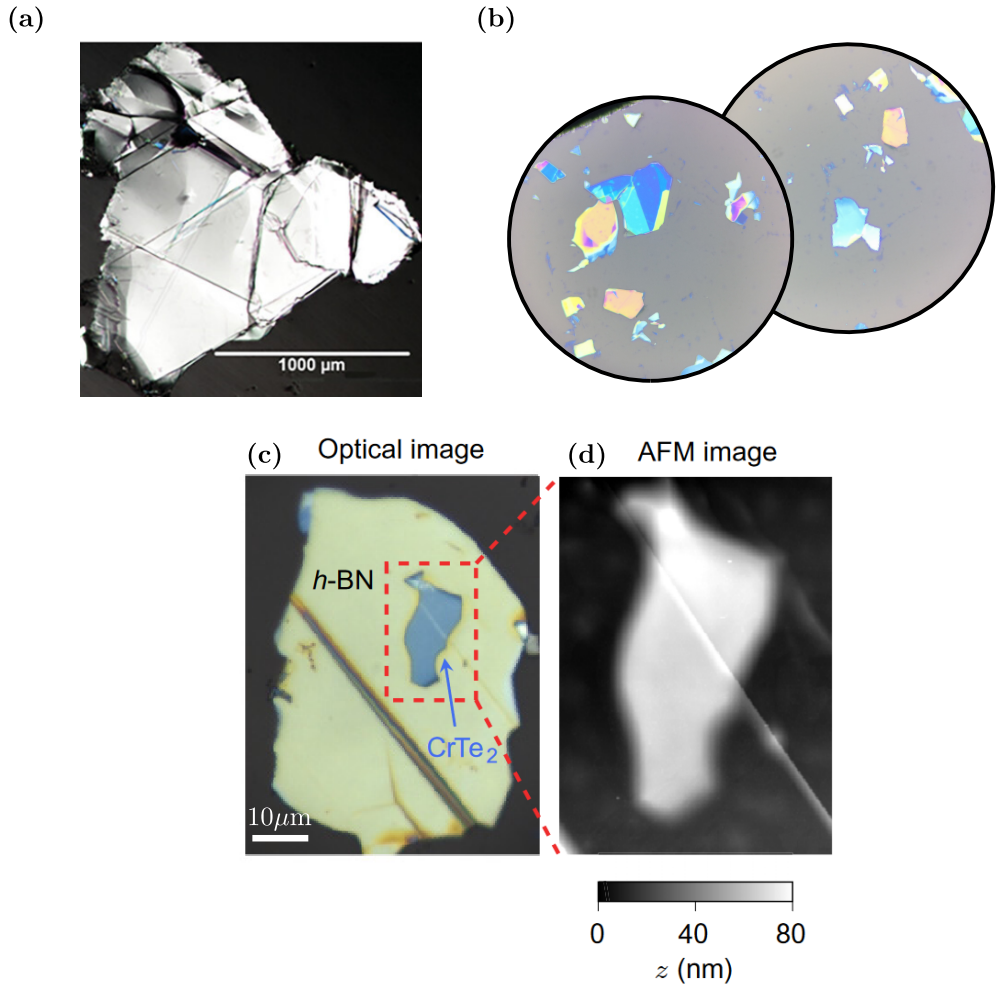


**Figure 1.14:** van der Waals heterostructure preparation. (a) Photograph of a bulk hBN crystal grown by James H. Edgar's group, reproduced from Ref. [134]. (b) Optical images of hBN flakes obtained by mechanical exfoliation of a bulk crystal. (c) Optical image of the $CrTe_2$(64 nm)/h-BN (85 nm) heterostructure. (d) AFM scan of the heterostructure.

## Exfoliation

To prepare the vdW heterostructure, we collaborated with Cédric Robert and Xavier Marie, at LPCNO in Toulouse. They relied on mechanical exfoliation, the technique that gave birth to the entire field of van der Waals materials [52]. The principle is straightforward: adhesive tape is used to peel off layers from a bulk crystal. Since the adhesive force of the tape exceeds the weak interlayer van der Waals forces, each removal detaches a few flakes from the surface. Repeating this process several times eventually covers the tape with hBN flakes of various sizes, which can then be transferred onto a 90-nm-thick $SiO_2$ substrate by pressing the tape against it. Examples of mechanically exfoliated hBN flakes deposited on a $SiO_2$ substrate are shown in Figure 1.14(b). The exact same technique is employed for

the vdW magnet $CrTe_2$. Finally, a hBN flake is picked up using a polymer stamp and deposited on top of a $CrTe_2$ flake, forming the sensor–sample heterostructure. An optical image of the resulting structure is shown in Figure 1.14(c): a yellow hBN flake of 85 nm thickness covers a $CrTe_2$ flake of 64 nm thickness. The corresponding atomic force microscopy (AFM) characterization, used to determine the flake thicknesses, is shown in Figure 1.14(d) and confirms the excellent thickness uniformity of the $CrTe_2$ flake.

## Experimental apparatus

This section provides a good opportunity to describe the experimental apparatus used throughout this PhD work. Depicted in Figure 1.15, it consists of a scanning confocal microscope with green laser excitation (532 nm) and a high–numerical-aperture objective (typically NA = 0.7) that focus the laser beam on a $\sim 1\ \mu m^2$ spot. The PL signal emitted by an ensemble of $V_B^-$ centers is collected with the same objective, discriminated from the excitation laser by a dichroic mirror, filtered through a confocal pinhole and a bandpass filter before being detected by avalanche photodiodes (APD). A homemade RF antenna, consisting of a metallic wire loop, was positioned in close proximity to the sample. The microscope objective is further mounted on a piezoelectric scanner, allowing the laser beam to be scanned over a 60 $\mu m^2$ area. At each position, the combination of optical excitation and RF driving enable the measurement of the ODMR spectrum of $V_B^-$ centers. Unless explicitly stated, all experiments are performed under ambient conditions.

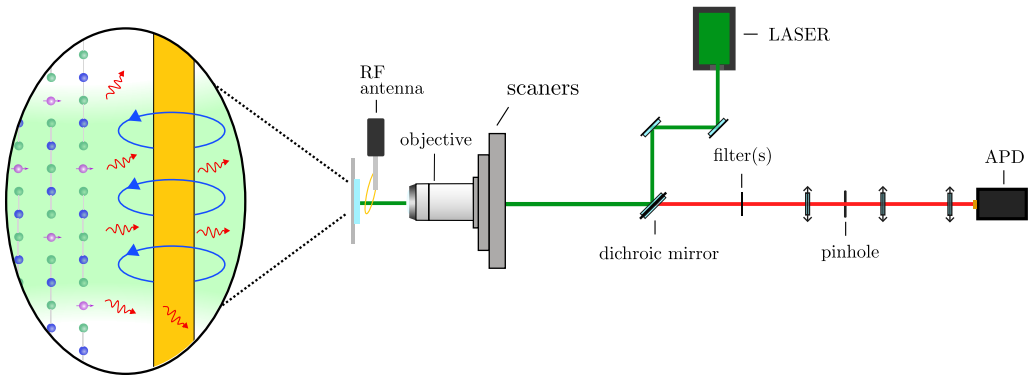


**Figure 1.15:** Simplified scheme of the experimental apparatus used in my thesis. The left panel illustrates $V_B^-$ centers (purple spins) being simultaneously excited by the laser beam (green shading) and an RF magnetic field generated by the antenna (blue arrows).

### 1.4.2 Sensitivity characterization

We begin with a PL raster scan of the $CrTe_2$/hBN heterostructure, the PL is monitored while the green laser beam scans the sample. The result is shown in Figure 2.4(a). A PL signal of few hundred of kilocounts per second (kcts/s) is observed. Notably, the signal is enhanced by a factor two on the $CrTe_2$ flake. This observation is explained by the metallic nature of $CrTe_2$ which reflects back part of the PL signal of $V_B^-$ centers .

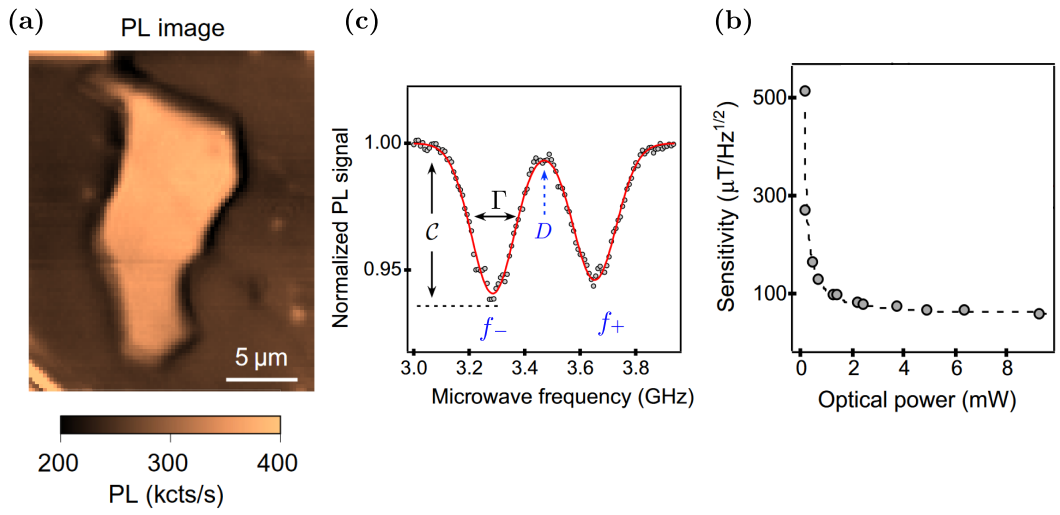


**Figure 1.16:** Sensor characterization. (a) PL image recorded across the hBN/$CrTe_2$ heterostructure. (b) ODMR spectrum recorded on the hBN flake with a bias field $B_b = 7$ mT, aligned with defect quantization axis, and with an optical power of 2.1 mW. The solid line is a fit to the data with Gaussian functions. (c) Magnetic field sensitivity $\eta_B$ as a function of the optical power. The black dashed line is a guide to the eye.

We then characterized the crucial figure of merit of the sensor: its sensitivity. To this end, ODMR spectra are recorded far from the $CrTe_2$ flake while applying a bias magnetic field $B_b = 7$ mT. A typical spectrum is shown in Figure 2.4(b). In this regime, already discussed in Section 1.2.3, the orthorombic ZFS parameter $E$ can be neglected and the ODMR frequencies are simply given by $f_\pm = D \pm \gamma_e B_b$. From such sensing scheme, based on ODMR spectroscopy the magnetic field sensitivity, $\eta_B$, can be inferred as [146]

$$\eta_B \approx 0.7 \times \frac{1}{\gamma_e} \times \frac{\Gamma}{\mathcal{C}\sqrt{\mathcal{R}}}, \tag{1.26}$$

where $\mathcal{R}$ is the PL signal count rate, $\mathcal{C}$ the contrast of the ODMR spectrum, and $\Gamma$ its linewidth. This important quantity, expressed in $T/\sqrt{Hz}$, gives the minimal magnetic field our sensor can resolve within a one second acquisition time. It is optimal when it is the lowest, i.e, for a sharp ODMR linewidth, a high ODMR contrast and a high PL signal count rate. To estimate the best working regime we measures ODMR spectra at different optical powers. From the parameters $\{\mathcal{R}, \mathcal{C}, \Gamma\}$, we extract the optical power dependence of the magnetic field sensitivity. As shown in Figure 2.4(c), $\eta_B$ improves with increasing laser power and achieves an optimal value around $\sim 60$ $\mu T/\sqrt{Hz}$, for a $\sim 1$ $\mu m^2$ laser spot. This saturation behavior results from a competition between the increasing count rate and a contrast reduction at high optical power, a well known behavior [146]. This sensitivity is approximately one order of magnitude worse than that achieved in single-defect scanning $NV^-$ microscopy and ensemble-based widefield $NV^-$ microscopy, which both reaching sensitivities of $1$ $\mu T/\sqrt{Hz}$ when the $NV^-$center is probed through confocal microscopy and continuous ODMR spectroscopy [24, 26, 147, 148]. However, the key advantages of our vdW magnetic sensor lie in its ease of use, high flexibility, and, more importantly, its ability to be placed in close proximity to the target sample. In this first proof-of-concept experiment, the hBN flake is relatively thick (about 80 nm), but later in this manuscript we will show that the sensor thickness can be reduced down to a few atomic layers.

### 1.4.3 Magnetic imaging

We now perform the magnetic field imaging of the $CrTe_2$ flake. An ODMR spectrum is recorded at each point of the scan, from which the Zeeman shift of the lower ODMR frequency $f_-$ is extracted. Here, we only track one magnetic resonance of the $V_B^-$ center to reduce data acquisition time. After subtracting the offset linked to the bias magnetic field $B_b$, the Zeeman shift is simply given by $\Delta_Z = \gamma_e B_z$, where $B_z$ is the magnetic field projection along the $V_B^-$ quantization axis. Note that working with defect ensemble limits the spatial resolution of the imaging process to the size of the focused laser beam, $\sim 1$ µm.

The map of the magnetic field component $B_z$ produced by the $CrTe_2$ flake is shown in Figure 1.17(a). The magnetic field is mainly generated at the edges of the flake as expected for a uniformly magnetized flake with homogeneous thickness [131]. Furthermore, the recorded magnetic field distribution directly confirms that

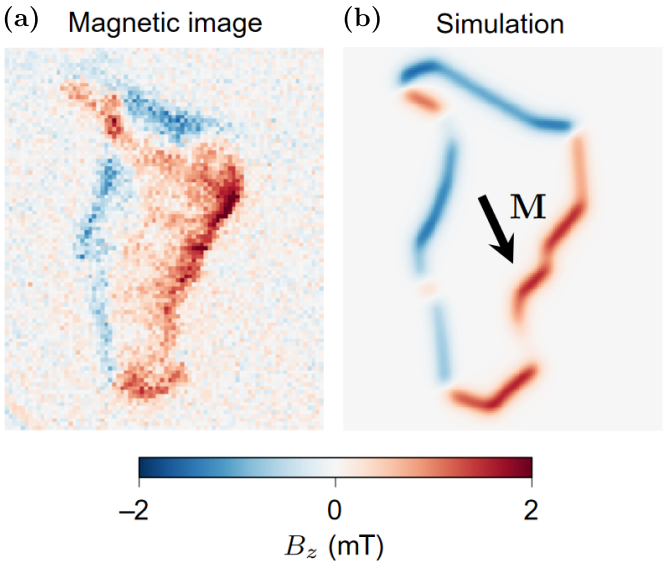


**Figure 1.17:** Magnetic-field imaging with $V_B^-$ centers in hBN. (a) Map of the magnetic field component $B_z$ produced by the $CrTe_2$ flake, obtained by measuring the Zeeman shift of the lower ODMR frequency of the $V_B^-$ centers. Experiments are carried out with a bias magnetic field $B_b = 7$ mT and an optical power of 0.6 mW. The acquisition time per pixel is 4.2 s. (e) Simulated map of the magnetic field component $B_z$ for a uniform in-plane magnetization M (black arrow) with an azimuthal angle $\phi_M = 297°$ and a norm M = 60 kA/m.

the $CrTe_2$ flake features an in-plane magnetization. Indeed, considering a uniform out-of-plane magnetization, the magnetic field component $B_z$ would be identical at all edges of the flake.

To perform a quantitative analysis of the recorded magnetic field map, Florentin Fabre, former PhD student of the team, simulated the distribution of the magnetic field component $B_z$ produced by a $CrTe_2$ flake with constant thickness and uniform in-plane magnetization $M$. The details of the simulation can be found in his PhD thesis [149]. The simulated magnetic field map, presented in Figure 1.17(b), shows very good agreement with the experimental measurement.

In this work, we successfully demonstrated that $V_B^-$ centers embedded in an hBN flake can operate as a quantum magnetic-field sensor, capable of mapping the stray magnetic field produced by a van der Waals magnet with micrometer-scale spatial resolution. This result constitutes one of the first experimental validations of quantum sensing with a vdW sensor, marking a significant step toward the development of atomically thin quantum sensors. Such a sensing unit will likely find numerous applications in 2D materials research by offering a simple way to probe in situ the

physics of van der Waals heterostructure. The study was published in 2022 [150], coinciding with two other independent reports that achieved similar demonstrations [113, 151], thereby establishing the foundation of this emerging research field.

## 1.5 Conclusion

The $V_B^-$ center is an atomic-like system embedded in a van der Waals material. Its spin can be monitored through optical and RF excitations, enabling ODMR spectroscopy. Furthermore, its ground-state spin couples to various perturbations, magnetic and electric fields, temperature, and strain, making this defect a promising versatile quantum sensor. After presenting this general picture, we concluded this first chapter by moving from promise to practice and demonstrating magnetic field imaging of a vdW magnet using $V_B^-$ centers embedded in an hBN flake. Yet, while this first chapter highlights the potential of the $V_B^-$ center, it also reveals two major limitations: (i) its weak optical emission, which necessitates ensemble measurements and thus limits the spatial resolution to the micrometer scale, and (ii) its nuclear-spin-rich environment, which constrains its sensitivity by producing a broad ODMR spectrum linewidth. Furthermore, to claim any advantage over existing quantum sensors, one must demonstrate sensing with an atomically thin hBN flake, which relies on the assumption that the defect remains optically and magnetically active in the few-layer limit. These considerations defines the starting point of my PhD work.

# 2 Spin-dependent photodynamics of the $V_B^-$ center

## Outline


**1.1 Optical and spin properties of the $V_B^-$ center in hBN . . 21**

1.1.1 From the electronic structure to the optical properties . . 21

1.1.2 Optically-detected magnetic resonance . . . . . 26

**1.2 Spin Hamiltonian . . . . . 29**

1.2.1 Electron spin-spin interaction . . . . . 30

1.2.2 Stress and electric-field couplings . . . . . 32

1.2.3 Zeeman effect . . . . . 36

1.2.4 Hyperfine interaction . . . . . 37

**1.3 Coherent control and spin relaxation times . . . . . 40**

1.3.1 Initialization and readout . . . . . 41

1.3.2 Coherent spin control and rabi Sequence . . . . . 42

1.3.3 Longitudinal spin relaxation time $T_1$ . . . . . 45

1.3.4 Inhomogeneous coherence time $T_2^*$ . . . . . 47

1.3.5 Spin echo coherence time $T_2$ . . . . . 49

**1.4 Magnetic imaging with $V_B^-$ centers in hBN: proof of concept . . . . . 51**

1.4.1 Sensor engineering . . . . . 52

1.4.2 Sensitivity characterization . . . . . 55

1.4.3 Magnetic imaging . . . . . 56

**1.5 Conclusion . . . . . 58**


All the experiments conducted on the $V_B^-$ center in this manuscript rely, directly or indirectly, on its spin-dependent photodynamics. It is the spin-dependent photodynamics which enables spin initialization through optical pumping, spin-state readout through photoluminescence (PL) detection, and ultimately, optically detected

magnetic resonance (ODMR) spectroscopy. While the basic mechanisms underlying ODMR spectroscopy were introduced in Chapter 1, the present Chapter is dedicated to a detailed investigation of the $V_B^-$ center's spin-dependent photodynamics. Although the general principles are well established, thanks to seminal works on the $NV^-$ center in diamond [14, 152–155], each defect exhibits its own specificities. In the process of developing a new quantum sensor based on $V_B^-$ centers, it is therefore essential to carry out a dedicated study of this particular system.

In the first part [§ 2.1], we introduce the seven-level used to describe the photodynamics of the $V_B^-$ center. The performances of the model will be illustrated through the simulation of the optically-induced spin polarization and spin-dependent PL signal. In the second part [§ 2.2], we develop and conduct an experimental procedure to determine all the parameters of the model at room temperature. This includes excited-state lifetime measurements and PL time traces under continuous optical power. Since most sensing applications operate at cryogenic temperatures, the third part [§ 2.3] extends the study to liquid-helium conditions. Finally, taking advantage of the cryogenic setup, we perform a systematic study of the PL signal as a function of magnetic field [§ 2.4], which offers both an excellent opportunity to test our seven-level model and to get valuable physical insight on the properties of the $V_B^-$ center.

## 2.1 Photodynamics modelling

### 2.1.1 Seven-level model

As mentioned in Chapter 1, the photodynamics of the $V_B^-$ center involves a spin triplet ground state, $^3A_2'$, at least two spin triplet excited states, $^3E''$ and $^3E'$, and an intermediate spin singlet state, $^1E'$. To capture the essential features of the spin-dependent photodynamics, while keeping the model as simple as possible, we simplify the picture and retain only a single triplet excited state, neglecting the higher-lying $^3E'$ state. This approximation is motivated by (i) the ultrafast non-radiative relaxation within the excited-state (ES) triplet manifold, predicted to be much shorter than the time resolution of the experimental apparatus ($\ll$ 200 ps), and (ii) the assumption that this relaxation is essentially spin-conserving ($\Delta m_s = 0$), rendering the internal dynamics of the ES triplet manifold non-critical for understanding the spin-dependent photodynamics. We thus consider the seven-

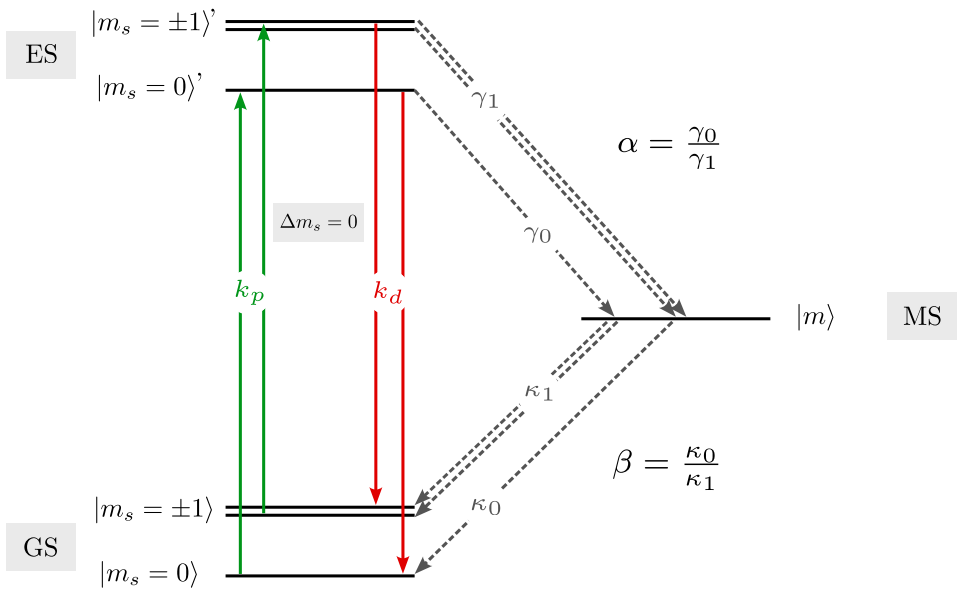


**Figure 2.1:** Schematic of the seven-level model describing the spin-dependent photodynamics of the $V_B^-$ center. All notations are defined in the main text.

level model shown in Figure 2.1, comprising three spin sublevels in the ground state (GS) $\{|m_s = 0\rangle, |m_s = -1\rangle, |m_s = +1\rangle\}$, three spin sublevels in the excited state (ES) $\{|m_s = 0\rangle', |m_s = -1\rangle', |m_s = +1\rangle'\}$, where the prime (') distinguishes them from the GS states, and one singlet state $|m\rangle$, referred to as the metastable state.

Each level has a certain probability of occupation, referred to as its population. Because the optical excitation and ISC processes couple the levels, populations can be transfered from one level to another. We assume that these transitions are purely incoherent. This assumption is motivated by the very broad nature of all the levels involved in the $V_B^-$ photodynamics which resemble more to a quasi-continuum than discrete levels. In this regime, populations do not evolve coherently through Rabi oscillations but instead undergo random jumps between states. The transition probability per unit time, or *rate*, from state $|i\rangle$ to state $|f\rangle$ can be expressed using Fermi's golden rule:

$$\Gamma_{if} = C|\langle f|\hat{W}|i\rangle|^2 \rho(E), \tag{2.1}$$

where $C$ is a constant, $\rho(E)$ is the density of states and $\hat{W}$ is the interaction operator, representing either the electric dipole interaction or the ISC process. The rates included in the model are the followings:

- Optical pumping $k_p$: Depicted with green arrows in Figure 2.1, it transfers

population from the GS to the ES while conserving the spin projection ($\Delta m_s = 0$). We assume that the oscillator strength is independent of the spin projection.

- Radiative decay $k_d$: Depicted with red arrows in Figure 2.1, it transfers population from the ES to the GS while conserving $m_s$ ($\Delta m_s = 0$). We assume that the oscillator strength is independent of the spin projection.

- ISC from the ES to the metastable state: Depicted with dashed grey arrows, with two distinct rates depending on the initial spin state: $\gamma_0$ from $|m_s = 0\rangle'$ and $\gamma_1$ from $|m_s = \pm 1\rangle'$. We define their ratio as $\alpha = \gamma_0/\gamma_1$.

- ISC from the metastable state to the GS: Also depicted with dashed grey arrows, with two distinct rates depending on the final spin state: $\kappa_0$ to $|m_s = 0\rangle$ and $\kappa_1$ to $|m_s = \pm 1\rangle$. We define their ratio as $\beta = \kappa_0/\kappa_1$.

In this model, we have neglected the longitudinal spin relaxation rate, $\Gamma_1 = 1/T_1$, which couples $|m_s = 0\rangle$ and $|m_s = \pm 1\rangle$. We assume that under optical pumping, $\Gamma_1$ is significantly slower than the pumping rate $k_p$, so the defect is optically excited before the relaxation of the spin populations occurs ($\Gamma_1 \ll k_p$). Since our later characterization will only involve optical excitation, we also do not include any RF pumping rate. Finally, we assume that the seven-level system is closed, with no rates coupling the defect to any external degree of freedom.

The time evolution of the population in state $|i\rangle$, denoted $n_i$, then results from a competition between some incoming rates, bringing new populations to the state, and some outgoing rates taking away some populations. Formally, this competition can be expressed with the rate equation :

$$\frac{dn_i}{dt} = \sum_j \Gamma_{ji} n_j - \sum_j \Gamma_{ij} n_i. \tag{2.2}$$

Applying this equation to our model, we obtain a set of seven coupled equations:

$$\frac{dn_0}{dt}(t) = \kappa_0 n^*(t) - k_p n_0(t) + k_d n'_0(t), \tag{2.3}$$

$$\frac{dn_{-1}}{dt}(t) = \kappa_1 n^*(t) - k_p n_{-1}(t) + k_d n'_{-1}(t), \tag{2.4}$$

$$\frac{dn_{+1}}{dt}(t) = \kappa_1 n^*(t) - k_p n_{+1}(t) + k_d n'_{+1}(t), \tag{2.5}$$

$$\frac{dn'_0}{dt}(t) = k_p n_0(t) - \gamma_0 n'_0(t) - k_d n'_0(t), \tag{2.6}$$

$$\frac{dn'_{-1}}{dt}(t) = k_p n_{-1}(t) - \gamma_1 n'_{-1}(t) - k_d n'_{-1}(t), \tag{2.7}$$

$$\frac{dn'_{+1}}{dt}(t) = k_p n_{+1}(t) - \gamma_1 n'_{+1}(t) - k_d n'_{+1}(t), \tag{2.8}$$

$$\frac{dn^*}{dt}(t) = \gamma_0 n'_0(t) + \gamma_1 (n'_{+1}(t) + n'_{-1}(t)) - (\kappa_0 + 2\kappa_1) n^*(t). \tag{2.9}$$

As for the states, we denoted the ES populations with a prime ($'$), while the metastable-state population is denoted with an asterisk ($*$). As one could have anticipated from the model, $|m_s = +1\rangle^{(')}$ and $|m_s = -1\rangle^{(')}$ undergo identical dynamics. One could therefore question the necessity of a seven-level model compared to a simpler five-level model, in which the $|m_s = \pm 1\rangle$ sublevels would be merged. This choice will become justified later in this chapter, when a magnetic field will be applied, lifting the degeneracy between $|m_s = -1\rangle$ and $|m_s = +1\rangle$.

To compute the time-evolution of the population one can write the previous system of differential equations in a matrix form:

$$\frac{du}{dt} = Mu, \tag{2.10}$$

with :

$$u = \begin{bmatrix} n_0 \\ n_{-1} \\ n_{+1} \\ n'_0 \\ n'_{-1} \\ n'_{+1} \\ n^* \end{bmatrix} \quad , \quad M = \begin{bmatrix} -k_p & 0 & 0 & +k_d & 0 & 0 & \kappa_0 \\ 0 & -k_p & 0 & 0 & +k_d & 0 & \kappa_1 \\ 0 & 0 & -k_p & 0 & 0 & +k_d & \kappa_1 \\ +k_p & 0 & 0 & -\gamma_0 - k_d & 0 & 0 & 0 \\ 0 & +k_p & 0 & 0 & -\gamma_1 - k_d & 0 & 0 \\ 0 & 0 & +k_p & 0 & 0 & -\gamma_1 - k_d & 0 \\ 0 & 0 & 0 & \gamma_0 & \gamma_1 & \gamma_1 & -(\kappa_0 + 2\kappa_1) \end{bmatrix}. \tag{2.11}$$

By diagonalizing $M$, one obtains a new basis in which the time evolution is trivial, each component following an exponential law $ae^{\lambda_i t}$, with $\lambda_i$ the eigenvalues of $M$. If the rates are time-independent, the physical populations at time $t$ can be directly obtained by transforming back to the population basis. If the rates are time-dependent, an iterative calculation can instead be performed, updating the rates at each step $dt$, with $dt$ chosen much smaller than the shortest timescale in the model.

### 2.1.2 Practical examples

To illustrate the capability of this simple model, I present basic simulations of the two essential processes underlying ODMR: optically-induced spin polarization and spin-dependent PL emission.

#### Optically-induced spin polarization

I begin by computing the time evolution of the **GS** populations under constant optical pumping, starting from a thermal distribution of the spin populations: $n_0(t=0) = n_{+1}(t=0) = n_{-1}(t=0) = \frac{1}{3}$. To give an example, I fix arbitrarily the values of $k_p$, $k_d$, $\gamma_0$, $\alpha$, and $\kappa_0$, but explore three different values of the ratio $\beta$ between the ISC rates $\kappa_0$ and $\kappa_1$. The results are displayed in Figure 2.2 (a-c).

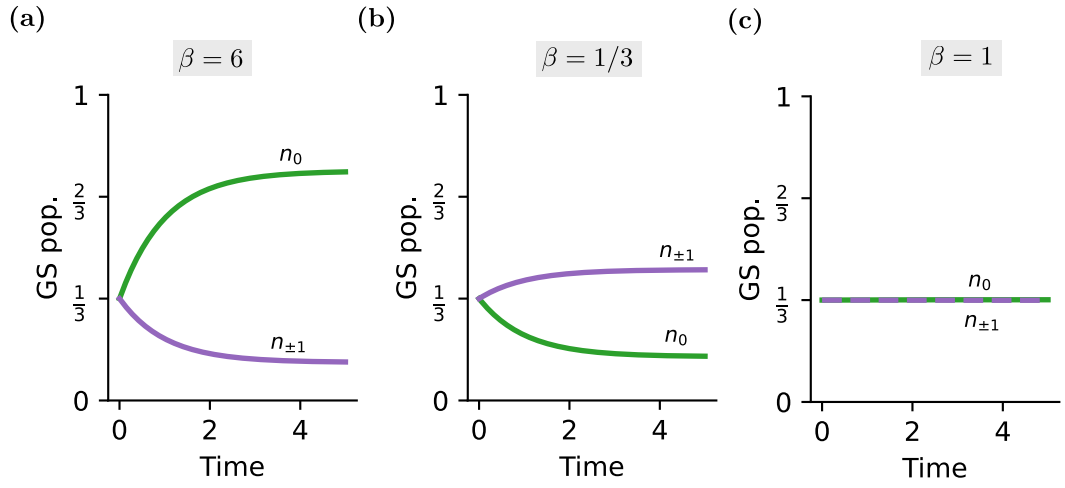


**Figure 2.2:** Simulations of the GS populations under constant optical pumping, starting from a thermal spin distribution. The rates are set to $(k_p = 1 \quad , \quad k_d = 1 \quad , \quad \kappa_0 = 500 \quad , \quad \alpha = 1/2 \quad , \quad \gamma_0 = 1000)$, while (a) $\beta = 6$, (b) $\beta = 1/2$, and (c) $\beta = 1$.

When $\beta > 1$, i.e $\kappa_0 > \kappa_1$, an optically-induced polarization builds up in $|m_s = 0\rangle$, whereas for $\beta < 1$, the polarization is in favor of $|m_s = \pm 1\rangle$ [Fig. 2.2(a,b)]. Lastly, if $\beta = 1$, no polarization occurs [Fig. 2.2(c)]. This behavior is readily understood: as the populations pass through the metastable state, the branching ratio $\beta$ determines whether they preferentially decay into $|m_s = 0\rangle$ or $|m_s = \pm 1\rangle$. In all cases, the system eventually reaches a steady state in which the populations no longer evolve in time. Hence, one can define a steady-state polarization $\mathcal{P}$ in $|m_s = 0\rangle$. To derive its expression, we take the steady-state limit of the rate equations by setting $\frac{dn_i}{dt} = 0$, which yields:

$$\mathcal{P} = \frac{n_0}{n_0 + n_{-1} + n_{+1}} = \frac{1}{1 + \frac{2\alpha}{\beta} \times \frac{k_d + \gamma_1}{k_d + \gamma_0}}. \tag{2.12}$$

It may seem surprising that the pumping rate $k_p$ does not appear in this expression. This is a direct consequence of one of our assumptions. By neglecting the longitudinal spin relaxation rate $\Gamma_1$, we effectively removed the only process opposing the spin polarization process. As a result, even the weakest pumping rate can drive the system to maximum polarization, provided one waits long enough. As expected, nonetheless, the polarization depends on the ratio $\beta$. In the limit where the direct decay $k_d$ is negligible compared to the ISC rates $k_d \ll (\gamma_0, \gamma_1)$, the relationship between the spin polarization and $\beta$ becomes even more direct:

$$\lim_{k_d \ll (\gamma_0, \gamma_1)} \mathcal{P} = \frac{1}{1 + \frac{2}{\beta}}. \tag{2.13}$$

In this regime, the GS polarization is only determined by the branching ratio $\beta$, between the ISC rates from the metastable state to the GS.

## Spin-dependent PL emission

In practice, we never directly access the GS populations. To compare our the simulations with experimental data, we must therefore relate the populations to the only directly measurable physical quantity: the PL signal. Since one PL photon is emitted per radiative decay, the detected PL signal, $S(t)$, can be written as:

$$S(t) = \eta k_d \left( n'_0(t) + n'_{+1}(t) + n'_{-1}(t) \right). \tag{2.14}$$

Here, $\eta$ accounts for the imperfect collection and detection efficiency of the experimental apparatus. Regardless of the exact values of $\eta$ or $k_d$, the main result is

that the PL signal is proportional to the ES populations. To predict the time evolution of the PL signal one therefore just need to compute the ES populations. As an example, I set arbitrarily $\beta = 6$ and compute the ES populations under continuous optical excitation starting from a thermal spin distribution in the GS. This time, I explore three different regimes: $\alpha < 1$, $\alpha > 1$ and $\alpha = 1$. The three resulting curves are plotted in Figure 2.3 (d-f).

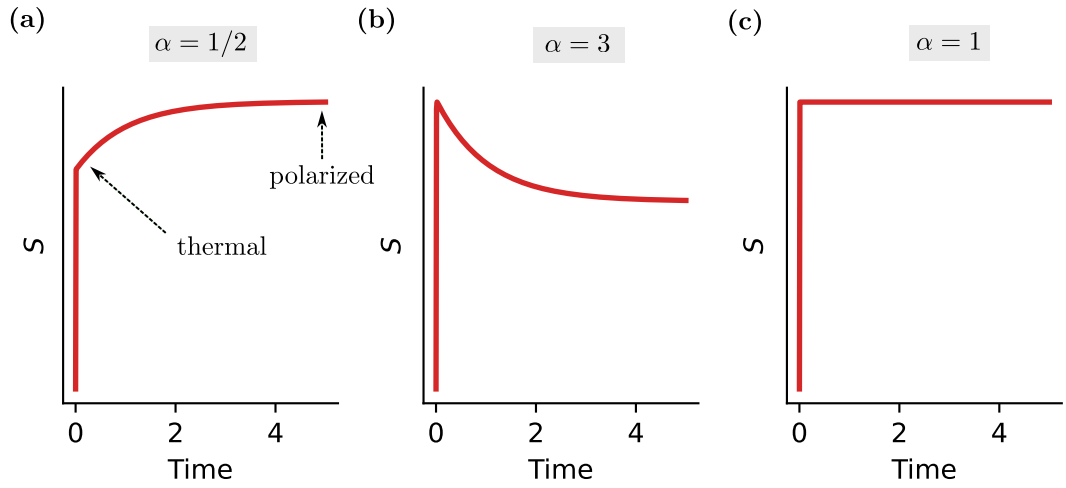


**Figure 2.3:** Simulated time-evolution of the PL signal, $S$, under constant optical pumping, starting from a thermal spin distribution in the GS. The rates were set to $(k_p = 1 \quad , \quad k_d = 1 \quad , \quad \kappa_0 = 500 \quad , \quad \beta = 6 \quad , \quad \gamma_0 = 1000)$, while three regimes of $\alpha$ are explored: (a) $\alpha = 1/2$, (b) $\alpha = 3$, and (c) $\alpha = 1$.

When $\alpha < 1$, optically-induced polarization into $|m_s = 0\rangle$ is accompanied by an increase in PL signal because the populations are pumped into the spin state with the longest ES lifetime ($\gamma_0 \ll \gamma_1$). In this regime, $|m_s = 0\rangle$ is a bright state, while $|m_s = \pm 1\rangle$ correspond to dark states. This is precisely the situation observed for $V_B^-$ centers. Conversely, when $\alpha > 1$, $|m_s = 0\rangle$ becomes a dark state, and the polarization process leads to a drop in PL. Finally, if $\alpha = 1$, all spin states share the same ES lifetime, and the optical pumping has no effect on the PL.

In summary, if $\beta$ is the parameter governing the spin polarization, $\alpha$ is the one determining the spin dependent PL contrast. Deriving the exact expression of the ODMR contrast is, however, not straightforward, since in our model we did not include a RF driving rate. Nevertheless, one can still give an upper bound by assuming a perfect populations reversal by the RF drive. In this case, the off-resonance PL signal, $S_{\text{off}}$, can be expressed as

$$S_{\text{off}} = \eta k_d k_p \left[ \frac{\mathcal{P}}{\gamma_0 + k_d} + \frac{1-\mathcal{P}}{\gamma_1 + k_d} \right],$$

while the on-resonance signal, $S$, is given by

$$S_{\text{on}} = \eta k_d k_p \left[ \frac{1-\mathcal{P}}{\gamma_0 + k_d} + \frac{\mathcal{P}}{\gamma_1 + k_d} \right].$$

The ODMR contrast can then be defined as the relative difference between the off- and on-resonance PL signals:

$$\mathcal{C}_{\text{Max}} = \frac{S_{\text{off}} - S_{\text{on}}}{S_{\text{off}}} \times 100.$$

Once again, taking the limit $k_d \ll (\gamma_0, \gamma_1)$ proves insightful, yielding:

$$\lim_{k_d \ll (\gamma_0, \gamma_1)} \mathcal{C}_{\text{Max}} = \frac{2\mathcal{P}(1-\alpha) + \alpha - 1}{\mathcal{P}(1-\alpha) + \alpha} \times 100. \tag{2.15}$$

With this last expression, one can easily verify that the maximum ODMR contrast is reached in the limit $\alpha \to 0$, i.e, when $|m_s = \pm 1\rangle$ are maximally coupled to the ISC channel. Conversely, for $\alpha = 1$, both spin states exhibit identical ES lifetimes, and the contrast vanishes.

In conclusion, our seven-level model successfully reproduces both the optically induced spin polarization and the spin-dependent PL signals. In the limit where the radiative decay rate is negligible compared to the ISC rates $\gamma_0$ and $\gamma_1$, the model further provides a direct relation between the efficiency of these mechanisms and the parameters $\alpha$ and $\beta$. The relation (2.13) between the GS spin polarization and the ratio $\beta$ will prove particularly essential in the following.

## 2.2 Photodynamics at room temperature

We now start the experimental investigation with room temperature measurements. Our goal is to extract all the parameters of the seven-level model introduced in the previous section. To this end, we rely on time-resolved PL measurements to

probe both the ES lifetime [§ 2.2.1] and the PL response under continuous optical pumping [§ 2.2.2].

The sample consists of hBN flakes, mechanically exfoliated from a bulk crystal grown by James H. Edgar's group at Kansas state university. The exfoliation is done at the LPCNO in Toulouse by Jules Fraunié and Cédric Robert. It is worth mentioning that Jules, who started his PhD at the same time as I did, systematically carried out the exfoliation of the flakes studied in this work. The hBN flakes are few tens of nanometers thick and deposited on a $SiO_2$ substrate. The $V_B^-$ centers were then created via nitrogen-ion implantation at 30 keV energy with a dose of $10^{14}$ ions/cm$^2$. This step was performed by Gregory Seine at CEMES, Toulouse. A PL raster scan of a typical nitrogen-implanted hBN flake is shown in Figure 2.4(a). It exhibits a homogeneous PL signal with distinct plateaus that reflect the topography of the flake. A PL spectrum further confirms the origin of the emission, showing the broad near-IR spectrum characteristic of the $V_B^-$ center.

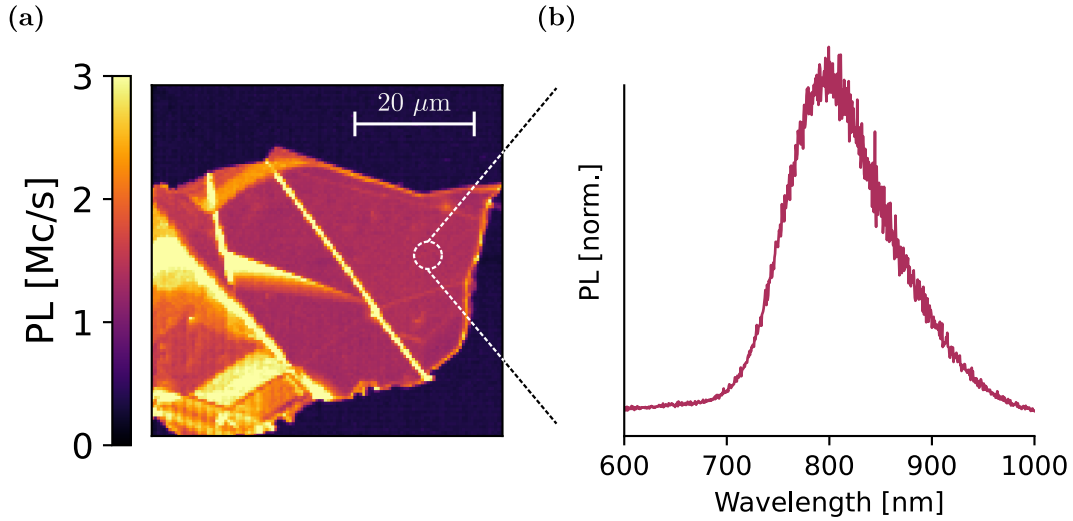


**Figure 2.4:** hBN flake implanted with nitrogen ions. (a) PL raster scan at an optical power of 500 µW. (b) PL spectrum.

The properties of the $V_B^-$ centers are studied through the same homemade confocal microscope presented in Section 1.4.1. The $V_B^-$ centers are excited with a green laser at 532 nm, combined with an acousto-optic modulator (AOM) to generate microsecond-long laser pulses. To measure the ES lifetime, we additionally employ a pulsed laser source at the same wavelength, with a pulse duration of 60 ps. The PL signal is detected by an avalanche photodiode (APD) and recorded on a photon-counting card with a temporal resolution of 200 ps. The measurements performed in

this section were performed with the assistance of Mu Zhao and Carolin Schrader, respectively postdoctoral researcher and PhD student in the team.

### 2.2.1 Excited state lifetime measurements

One of the most common experimental methods used in photodynamics studies is the measurement of PL decay. The principle is to abruptly switch off the optical excitation and monitor the induced PL decay. As the PL signal mirrors the ES populations, the characteristic time of the PL decay directly yield the ES lifetime. According to our model, if the pumping term vanishes at $t = 0$, the time evolution of the ES populations is governed by the following equations:

$$\frac{dn'_0}{dt}(t) = -\left(k_d + \gamma_0\right) n'_0(t)$$

$$\frac{dn'_{-1}}{dt}(t) = -\left(k_d + \gamma_1\right) n'_{-1}(t)$$

$$\frac{dn'_{+1}}{dt}(t) = -\left(k_d + \gamma_1\right) n'_{+1}(t).$$

Upon straightforward integration, the time evolution of the PL signal can be expressed as:

$$S(t) \propto \left[n'_0(t=0)e^{-\frac{t}{\tau_0}} + \left(n'_{-1}(t=0) + n'_{+1}(t=0)\right) e^{-\frac{t}{\tau_1}}\right], \tag{2.16}$$

where we have defined the characteristic spin-dependent ES lifetimes:

$$\tau_0 = (\gamma_0 + k_d)^{-1}, \quad \text{and} \quad \tau_1 = (\gamma_1 + k_d)^{-1}. \tag{2.17}$$

In addition, the amplitudes of the exponentials functions yield the state populations and, consequently, the spin polarization. Strictly speaking, the amplitudes gives the spin polarization in the ES,

$$\mathcal{P}' = \frac{n'_0}{n'_0 + n'_{-1} + n'_{+1}}.$$

However, because the picosecond excitation pulses are much shorter than the ISC rates, $\gamma_0$ and $\gamma_1$, the GS and ES polarizations do not have time to diverge, so that $\mathcal{P} = \mathcal{P}'$ [1]. Consequently, Equation (2.16) can be rewritten as:

[1] Since we assumed the oscillator strength of the pumping and radiative rates to be spin-

$$S(t) \propto \mathcal{P} e^{-\frac{t}{\tau_0}} + (1-\mathcal{P}) e^{-\frac{t}{\tau_1}}. \tag{2.18}$$

In summary, within our seven-level model framework, a single PL decay measurement grants access to three key quantities: $\tau_0$, $\tau_1$, and $\mathcal{P}$. These quantities are themselves directly related to the parameters of the model, namely the ISC rates $\gamma_0$, $\gamma_1$, the radiative rate $k_d$ and the ratio $\beta$ between the ISC rates $\kappa_0$ and $\kappa_1$. However, fitting a PL decay with a bi-exponential function is always challenging since different sets of amplitudes and lifetimes can sometimes produce comparably good fits. To mitigate this issue we developed a an original fitting procedure in two independent steps.

## ES lifetimes of thermal and polarized spin distributions

The measurements are carried out using the experimental pulsed sequence depicted in Figure 2.5(a). A first microsecond-long pulse, generated with the AOM, polarizes the $V_B^-$ center into the bright state $|m_s = 0\rangle$. After a short delay $\delta_p = 200$ ns, ensuring that all populations of the ES and metastable state have relax to the GS, a first picosecond laser pulse probes the PL decay. Since $\delta_p$ is much shorter than the longitudinal spin relaxation time $T_1$, this measurement probes the PL decay of a polarized spin distribution. Then, within the same experimental sequence, a second picosecond laser pulse is applied after a delay $\delta_t = 200$ µs. This time $\delta_t$ is much longer than $T_1$ at room temperature [cf. Chap. 1 § 1.3.3]. Therefore this second PL decay is associated with $V_B^-$ centers prepared in a thermal spin distribution. PL decays recorded on a first hBN flake, for a polarized and thermal spin distribution, are shown in Figure 2.5(b). A faster decay is observed for the thermal state, even though the lifetimes are identical in both cases. This difference arises solely from the spin populations: in the thermal state, 2/3 of the spin population decays with the shortest lifetime.

We first fit the PL decay associated with the thermal spin distribution [red data points in Fig. 2.5(b)], with the biexponential function expressed in Equation (2.18), convoluted with the measured instrumental response function (IRF). Importantly, since the spin are prepared in a thermal distribution, the polarization is fixed at $\mathcal{P} = 1/3$. We obtain $\tau_1 = 0.57(3)$ ns and $\tau_0 = 1.26(3)$ ns. We then hold these

independent, only the ISC rates $\gamma_0$ and $\gamma_1$ can induce $\mathcal{P} \neq \mathcal{P}'$ .

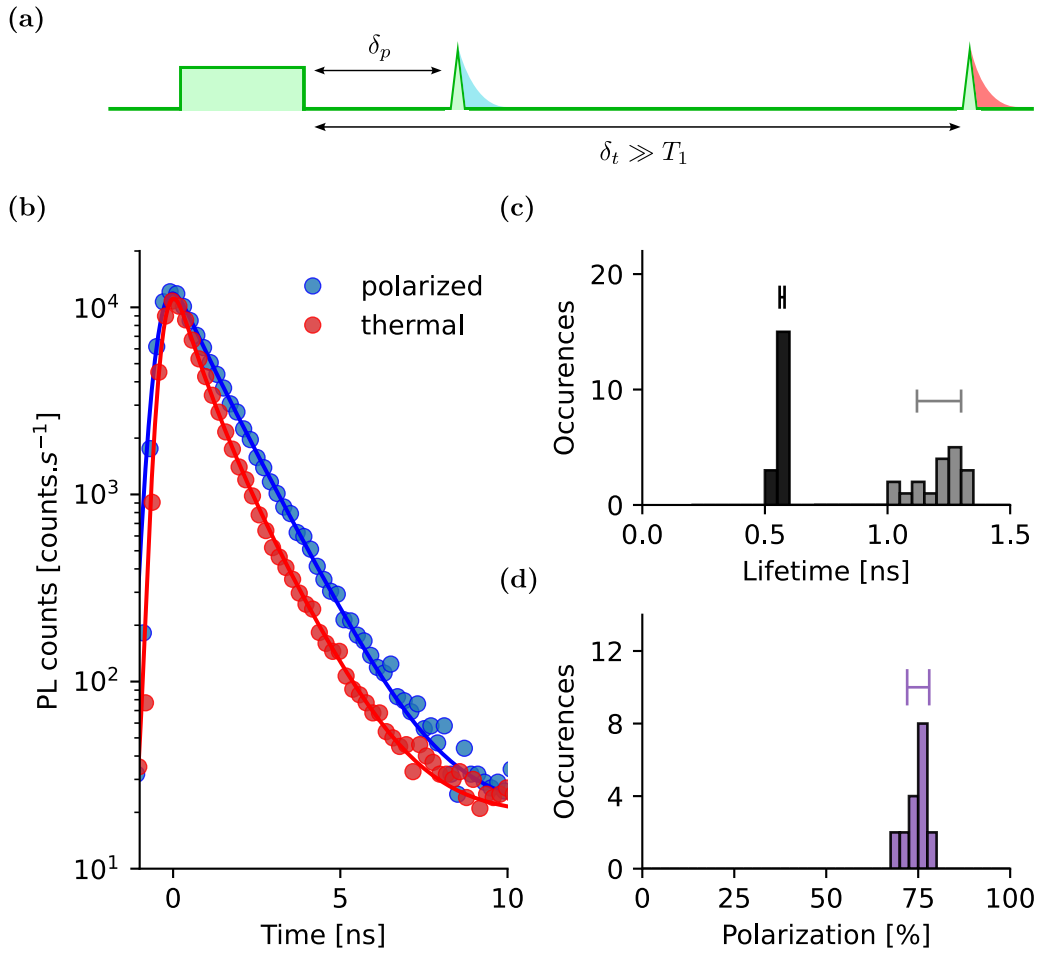


**Figure 2.5:** PL decays measurement. (a) Sequence used to measured the PL decays of a polarized and thermal spin distribution. (b) Typical PL decays for a polarized and a thermal spin distribution. The thermal state data has been shifted to facilitate comparison. The data are fitted with the biexponential decay of Eq. (2.18) convoluted with the measured IRF (solid lines). The IRF has been itself fitted with a Gaussian function prior to the measurement, yielding a width of $\sim 300$ ps. (c) Histograms obtained for both short (black) and long (grey) lifetimes. Each bin corresponds to 50 picoseconds. The horizontal lines are centered on the mean values and extend over one standard deviation. (d) Statistical distribution of the GS polarization extracted from the fitted exponential amplitudes. Each bin corresponds to 2.5%.

lifetimes fixed and fit the PL decay associated with a polarized state with the polarization $\mathcal{P}$ as single free parameter [blue data points in Fig. 2.5(b)]. We extract a spin polarization in $|m_s = 0\rangle$: $\mathcal{P} = 80(2)\%$.

To further validate this result, we performed the measurement on 16 hBN flakes. The resulting histograms are shown in Figure 2.5(c–d), all exhibiting the same trend. From these measurements, we extract mean values of $\tau_0 = 0.53(6)$ ns, $\tau_1 = 1.22(9)$ ns, and $\mathcal{P} = 75(7)\%$, with uncertainties given as one standard deviation across

the flake statistics. The narrow spread highlights both the reproducibility of the behavior and the limited flake-to-flake variability.

### Determination of the model parameters

We can now infer the values of three parameters of our seven-level model. To this end, we make one crucial postulate: the direct decay $k_d$ can be neglected. As discussed in Chapter 1, ab-initio works predicts a symmetry forbidden optical transition [80, 106, 107], yielding a slow radiative lifetimes of $\sim$ 10 µs [107]. We therefore assume here that the ES lifetimes are completely dominated by the ISC process: $k_d \ll (\gamma_0, \gamma_1)$. In this case the expressions of the lifetimes given in Equation (2.17) simply become:

$$\tau_0 = \gamma_0^{-1}, \quad \text{and} \quad \tau_1 = \gamma_1^{-1}. \tag{2.19}$$

It may seem counterintuitive that a PL decay can be dominated by a non-radiative process. This is in fact a direct consequence of Equation (2.14): any process acting on the ES population, radiative or not, also affects the PL signal. Within this assumption, we obtain $\gamma_0 = 820 \pm 60$ MHz and $\gamma_1 = 1.75 \pm 0.06$ GHz, corresponding to a ratio $\alpha = 0.47(5)$. Moreover, a negligible direct decay also implies that the polarization $\mathcal{P}$ depends only on the ratio $\beta$ between the ISC rates $\kappa_0$ and $\kappa_1$ [cf. Eq. (2.13)]. We can thus further infer $\beta = 6 \pm 1$.

These values capture the essential features of the $V_B^-$ photodynamics: $\alpha < 1$ confirms that $|m_s = 0\rangle$ acts as the bright state, while $\beta > 1$ drives its polarization though optical pumping. To complete the model, two parameters remain however to be determined: the pumping rate $k_p$ and one ISC rate, $\kappa_0$.

## 2.2.2 PL time traces under continuous optical excitation

After analyzing the PL response under picosecond laser excitation, we now turn to time-resolved PL measurements under continuous optical pumping.

## Pumping rate $k_p$ and polarization dynamics

In Section 2.1.1, we have shown that the parameter of the model determining the spin polarization is the branching ratio $\beta$. However, we did not discuss yet the timescale of the polarization process. Since polarization builds up over an optical cycle, its timescale is limited by the slowest transition of the model. We already know that the ISC rates $\gamma_0$ and $\gamma_1$ are fast, on the order of $ns^{-1}$, so the optical cycle duration is limited either by the ISC rates $\kappa_0$ and $\kappa_1$ or by the pumping rate $k_p$. Empirically, the polarization process accelerates with increasing optical power, indicating that under most experimental conditions, the slowest rate is the pumping rate $k_p$. This behavior is readily reproduced by our model: starting from a thermal spin distribution, we switch on $k_p$ at $t = 0$ with $\kappa_0$ and $\gamma_0$ set one and three orders of magnitude higher than the pumping rate, respectively. The simulated PL traces, shown in Figure 2.6(a), clearly indicate that polarization grows exponentially with a characteristic rate increasing with $k_p$. We conclude that analyzing the polarization dynamics under varying optical power with simulations from our seven-level model provides a direct way to extract the pumping rate $k_p$.

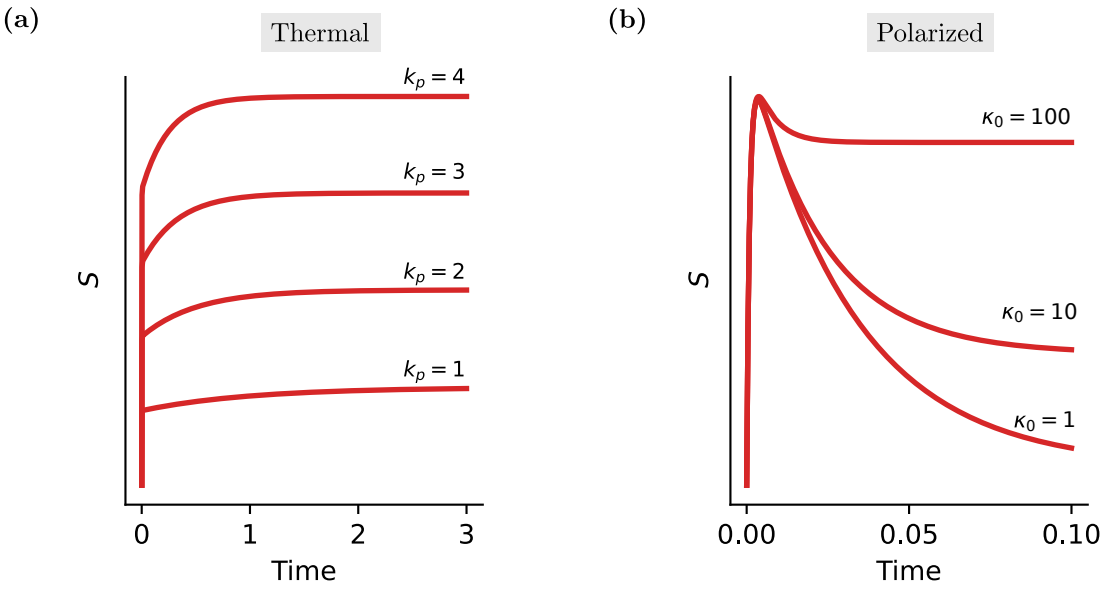


**Figure 2.6:** Simulated time-evolution of the PL signal, $S$, under continuous optical pumping for (a) a thermal spin distribution under various pumping rate $k_p$ and (b) a polarized spin distribution for various ISC rate $\kappa_0$.

## ISC rate $\kappa_0$ and PL overshoot

We now simulate PL time traces under continuous optical pumping starting from a polarized spin distribution. One might naively expect a flat PL response, since the polarization is already maximized. However, as shown by the simulation in Figure 2.6(b), this is not the case. The PL exhibits a sharp maximum before reaching its steady-state value. This well-known behavior, commonly referred to as PL overshoot, is a direct signature of the metastable level [154]. The mechanism is the following: initially, all populations are available for excitation to the ES, yielding maximal PL signal. As the system evolves toward steady state, a fraction of the population becomes trapped in the metastable state and is therefore no longer available for excitation, leading to a PL reduction. Importantly both the amplitude and decay time of the peak depend on $\kappa_0$ [Fig. 2.6(b)]. Analysing the PL time traces of a polarized spin distribution thus provides a means to access the remaining ISC rate $\kappa_0$.

## Thermal and polarized states PL time traces

Based on the previous discussion, our strategy is as follows: measure the PL time trace under continuous optical pumping for both a polarized and a thermal spin distribution, and fit the data with simulations from our model to extract the pumping rate $k_p$ and the ISC rate $\kappa_0$. The experimental sequence is shown in Figure 2.7(a). It is similar to the one developed for the PL decays measurements, except that this time we only consider microsecond-long laser pulses, generated by the AOM. A first pulse laser pulse probes the thermal spin distribution, while after a delay $\delta_p = 200$ ns, a second laser pulse probes the polarized spin distribution. Finally a delay $\delta_t = 200$ µs is respected to ensure the relaxation toward a thermal spin distribution. The sequence is repeated for seven different optical powers, ranging from 1 to 30 mW.

In this study, all measurements were performed below the saturation of the optical transition. This is confirmed by the linear increase of the steady-state PL signal with optical power, plotted in Figure 2.7(b). In this regime, the pumping rate can be assumed to scale linearly with the laser power,

$$k_p = k_p^0 \times P_{opt},$$

where $k_p^0$ is a proportionality factor expressed in MHz/mW and $P_{opt}$ is the op-

tical excitation power in mW. Accordingly, during the fit procedure, the coefficient $k_p^0$, rather than $k_p$, is treated as the free parameter. To further improve the accuracy of the simulations, the temporal profile of $k_p^0$ was weighted by the shape of the laser pulse, measured via reflection and displayed in Figure 2.7(c). Finally, the entire dataset is fitted simultaneously with only two free parameters: $k_p^0$ and $\kappa_0$. The parameters $\gamma_0$, $\gamma_1$, and $\beta$ are constrained to their previously measured values, while the direct decay is fixed at the value predicted ab initio $k_d = \frac{1}{10}$ µs$^{-1}$ [107], to ensure consistency with our earlier analysis. The experimental data and corresponding simulation fits are shown in Figure 2.7(d,e).

An overall good agreement is obtained between the data and the simulations. The PL overshoot of the polarized spin distribution is very well reproduced, and the polarization dynamics is reasonably well fitted, although a slight discrepancy appears at high optical power. From the fit, we extract $k_p^0 = 1 \pm 0.4$ MHz/mW. This implies that the lowest pumping rate used in this experiment was $k_p \approx 1$ MHz. Given that $1/T_1 \approx 100$ kHz, we can conclude that neglecting $T_1$ was a justified assumption. For the ISC rate $\kappa_0$, we find $\kappa_0 = 41(8)$ MHz. Using the previously determined ratio $\beta$, we further deduce $\kappa_1 = 7(2)$ MHz. With $\kappa_0$ and $\kappa_1$ known, we can also infer the metastable state lifetime, defined as:

$$\tau^* = \frac{1}{\kappa_0 + 2\kappa_1}. \tag{2.20}$$

We obtain $\tau^* = 18(3)$ ns. Lastly, we evaluate the upper bond of the ODMR contrast using Equation (2.15), yielding $\mathcal{C}_{\text{Max}} \approx 30\%$. Tables 2.1 summarizes the results.

### 2.2.3 Discussion

Our ES lifetime measurements are in very good agreement with the work of Baber et al. [156], who reported $\tau_0 = 0.49$ ns and $\tau_1 = 1$ ns, as well as with the more recent study of Lee et al. [157], which found $\tau_0 = 0.47(5)$ ns and $\tau_1 = 1.18(9)$ ns. The pumping rate $k_p$ is more difficult to compare to other studies, as it strongly depends on the experimental setup. Nonetheless, it is worth noting that a recent work by Escalante et al. estimated $k_p^0 = 2.98(4)$ MHz/mW [158], comparable to our value. The metastable lifetime is also in good agreement with the literature. Using a similar approach, Whitefield et al. [159] and Lee et al. [157] reported $\tau^* = 30(1)$

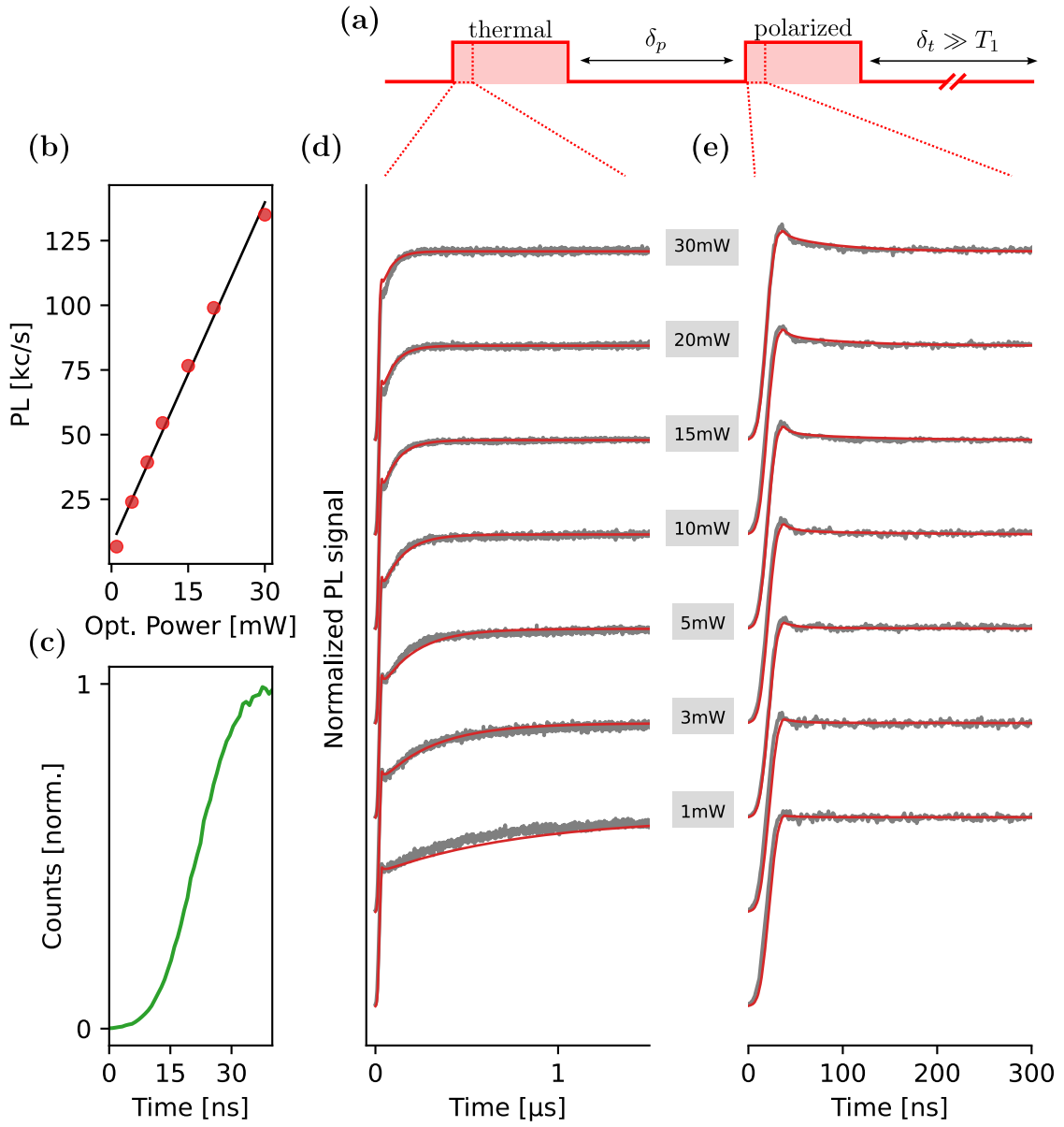


**Figure 2.7:** Constant optical pumping of a thermal and a polarized spin distribution. (a) Pulse sequence scheme, $\delta_p = 200$ns and $\delta_t = 200$ µs. (b) Steady state PL signal as a function of the optical power. The data are fitted with a linear function (solid black line). (c) Laser pulse shape, measured by reflection. Data are rebinned to avoid noise in the simulation. PL signal time traces for (d) the thermal and (e) the polarized spin distribution. Data are shown in grey, while the solid red lines represent the simulation fits.

ns and $\tau^* = 31.5$ ns, respectively. More recently, two groups directly measured $\tau^*$ with the so-called PL recovery method: Konrad et al. obtained $\tau^* = 24.0(3)$ ns [160], while Escalante et al. reported $\tau^* = 15(3)$ ns [158]. Both values are in very close agreement with our inferred result. In summary, our results are consistently aligned with those reported in the literature, both prior to and following this work, underscoring the robustness and reproducibility of the extracted values. However, if

| Parameter of the model | Inferred value |
|---|---|
| $k_p^0$ | 1.0(4) MHz/mW |
| $\gamma_0$ | 0.82(6) GHz |
| $\alpha$ | 0.47(5) |
| $\kappa_0$ | 41(8) MHz |
| $\beta$ | 6(1) |
| **Additional parameter** | |
| $\tau^*$ | 18(3) ns |
| $\mathcal{P}$ | 75(3) % |
| $\mathcal{C}_{\text{Max}}$ | $\approx 30\%$ |

**Table 2.1:** Overview of all extracted parameters characterizing the $V_B^-$ center photodynamics at room temperature.

the values are indeed reproduced by many, all do not agree on their interpretation. In particular, the hypothesis of a negligible direct decay ($k_d \ll \gamma_0, \gamma_1$) remains a matter of debate.

## Direct decay: an alternative scenario

Instead of assuming a weak direct decay, some reports choose to retain it as a free parameter. In this alternative framework, the measurement of $\tau_0$ and $\tau_1$ no longer provides a direct estimation of the ISC rates, $\gamma_0$ and $\gamma_1$ [cf. Eq. (2.17)]. The same holds for the polarization, which now depends not only on the ratio $\beta$, but as well on the direct decay rate $k_d$ and on the ISC rates $\gamma_0$ and $\gamma_1$ [cf. Eq. (2.12)]. As a result, analyzing the exact same dataset may lead to completely different estimates of the ISC rates. To illustrate this, I re-analyze the data presented in the previous section. The fits remain constrained by the measured ES lifetimes, but an additional degree of freedom is introduced through the direct spin-conserving decay $k_d$. This second fit procedure is shown in Figure 2.8.

Once again, a good agreement is observed between the data and the simulation. Aside from minor variations, the obtained set of parameters is in good agreement with the two literature reports relying on a direct decay model, as shown in Table 2.2.

Two features stand out: (i) a strong direct decay on the order of GHz, and (ii) an extremely low value of the ratio $\alpha$ ($\gamma_0 \ll \gamma_1$). In this new scenario, the polarization mechanism is fundamentally different. Since the population of $|m_s = 0\rangle'$ is largely

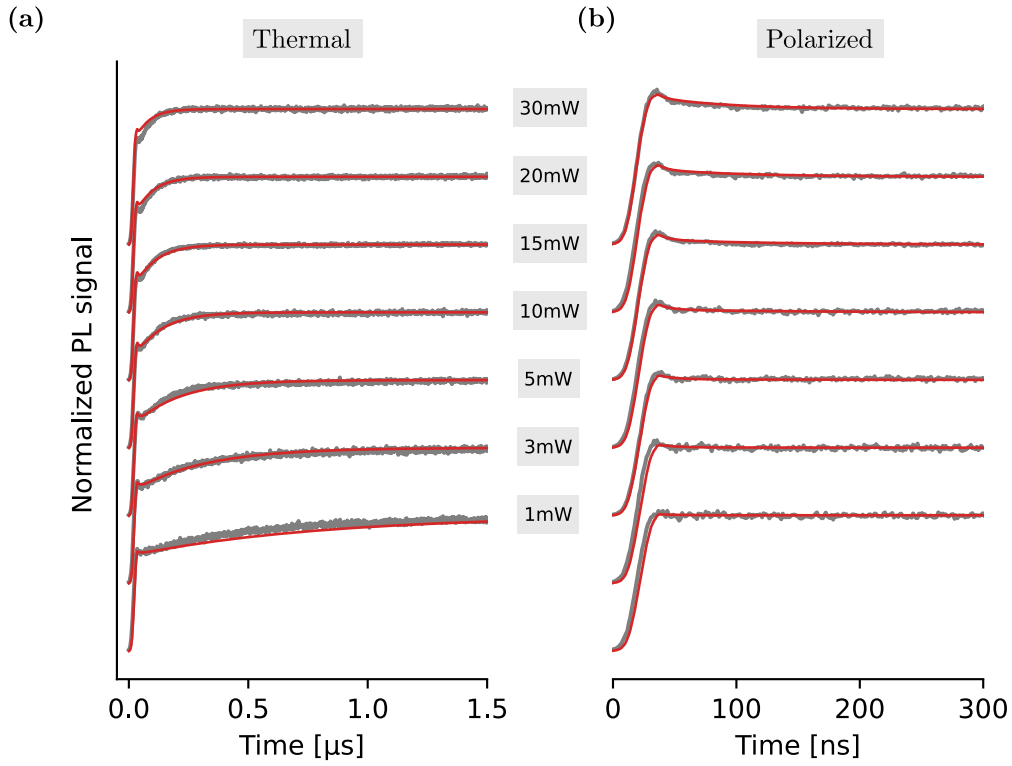


**Figure 2.8:** Analysis incorporating a direct decay. Simulation fits (red solid lines) and recorded PL time traces (grey lines) for (a) the thermal and (b) the polarized spin distribution. the dataset is the same than in the previous section.

| Parameter | Present work | Whitefield *et al.* [159] | Lee *et al.* [157] |
|---|---|---|---|
| $k_p$ | 10(2) MHz/mW | / | / |
| $k_d$ | 0.8(1) GHz | 0.88(3) GHz | 0.849 MHz |
| $\gamma_0$ | 0.03(2) GHz | 0.13(3) GHz | $< 0.2$ GHz |
| $\gamma_1$ | 1.1(3) GHz | 1.15(3) GHz | 1.286 GHz |
| $\kappa_0$ | 9(2) MHz | 13(1) MHz | 22.7 MHz |
| $\kappa_1$ | 20(10) MHz | 10(1) MHz | 4.54 MHz |
| **Additional parameter** | | | |
| $\tau^*$ | 20(10) ns | 30(1) ns | 31.5 ns |
| $\mathcal{P}$ | 78% | 74% | 96% |
| $\mathcal{C}_{\text{Max}}$ | $\sim 36\%$ | $\sim 28\%$ | $\sim 55\%$ |

**Table 2.2:** Rates extracted from a seven-level model including a direct decay $k_d$.

unaffected by the ISC rate, the precise value of the ratio $\beta$ becomes less critical, and even $\beta \leq 1$ can still result in polarization into $|m_s = 0\rangle$. Notably, the rates $\kappa_0$ and $\kappa_1$ remain unchanged compared to the previous model. This model nonetheless raises a critical question: how can such a strong direct decay be reconciled with the notoriously weak emission of the defect?

Whitefield *et al.* propose to attribute this decay to a non-radiative process such as internal conversion [159]. However, no theoretical work supports yet this hypothesis. Lee *et al.*, on the other hand, suggest that the low brightness of $V_B^-$ ensembles may not stem from an intrinsically low radiative decay rate, but rather from a charge-state stabilization issue, arguing that most boron vacancies may not be converted into optically-active $V_B^-$ centers [157]. As we will see later in Chapter 4, we dot not align with this hypothesis and instead believe that our samples contain a high density of $V_B^-$ centers.

Since we demonstrated that our data can be fairly well reproduced by neglecting this additional parameter, which moreover lacks theoretical support, we conclude that ab initio reports are correct and that the emission of the $V_B^-$ center is, unfortunately, intrinsically weak. Consequently, the no-direct-decay assumption will be maintained in the following.

## 2.3 Photodynamics at liquid-helium temperature

Even though our model is now complete, most future sensing applications will likely not operate at room temperature. Indeed, many target systems of interest, such as vdW magnets and superconductors, only unveil their characteristic properties under cryogenic conditions. ODMR spectroscopy of $V_B^-$ centers at cryogenic temperature has already been demonstrated, first by Liu et al. [109] and later by Mathur et al. [161]. However, no comprehensive photodynamic studies have yet been reported under these conditions. We therefore extended our investigation down to liquid-helium temperature, assuming that our seven-level model remains valid in this regime. The measurements were conducted with a setup similar to that used at room temperature, and were carried out by the same team of investigators, Mu Zhao, Carolin Schrader, and myself.

### 2.3.1 Measurements

We cooled down the sample in a liquid-helium cryostat to 4 K and begin with the measurement of the ES lifetimes. The sequence is the same as the one presented in Figure 2.5, except that the delay $\delta_t$ , applied to reach a thermal spin distribution, must be extended to account for the $T_1$ elongation at low temperature. Since $T_1$ reached the millisecond at 4 K, we set $\delta_t = 20$ ms such that the sequence becomes

long and requires significant acquisition time. Therefore, we did not carry out a statistical study and instead measure the spin-dependent ES lifetimes on a single hBN flake. The resulting PL decay curves, from a thermal and polarized spin distribution, are shown in Figure 2.9(a).

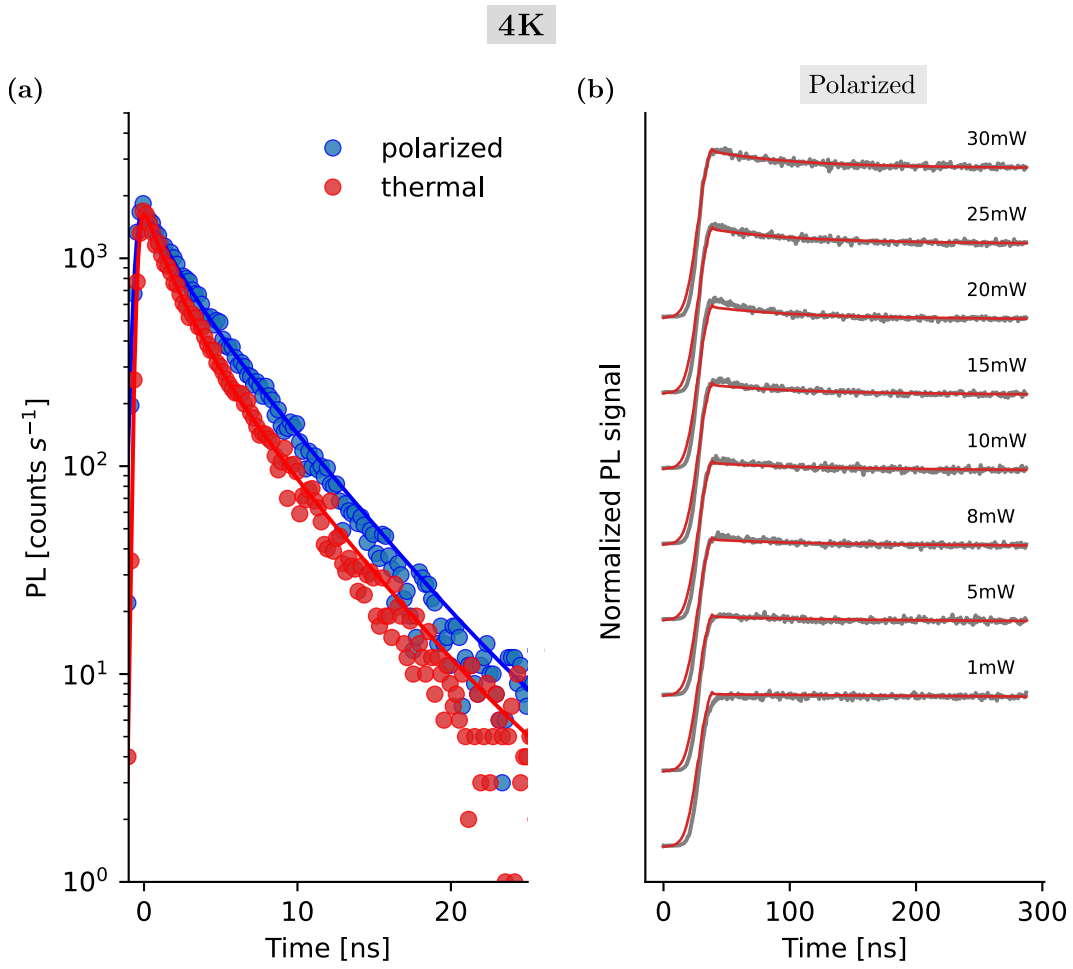


**Figure 2.9:** Photodynamics of the $V_B^-$ center at 4 K. (a) PL decays under picosecond excitation for a thermal (red) and a polarized (blue) spin distribution. The solid lines represent fits made with a bi-exponential function convoluted with the IRF. (b) PL time traces of the polarized spin distribution under continuous optical pumping at eight different optical powers. The experimental data are fitted with the seven-level model (solid red line).

Using the two-step analysis procedure described in Section 2.2.1, we extract $\tau_0 = 4.46(7)$ ns and $\tau_1 = 1.50(5)$ ns. The ES lifetimes are thus slightly longer at 4 K. However, both the short and long components increase by a similar factor, yielding a ratio $\alpha = 0.34(2)$, close to the room-temperature value. For the polarization in $|m_s = 0\rangle$, we obtain $\mathcal{P} = 71(1)\%$, thereby yielding a ratio $\beta = 4.9(2)$, as well nearly unchanged compared to the result obtained at room temperature

We next measure the PL time traces under continuous optical pumping [Fig. 2.9(b)]. Since the measurement sequence must be repeated for different optical powers, we reduced the acquisition time by omitting the measurement of the thermal state, which requires a delay $\delta_t \gg T_1$. With $\gamma_0$, $\gamma_1$, and $\beta$ fixed, the PL overshoot of the polarized spin distribution is fitted by adjusting $k_p^0$ and $\kappa_0$ in the simulation. The procedure yields $k_p^0 = 0.44(3)$ MHz/mW and $\kappa_0 = 24(2)$ MHz. With all the parameters of the model extracted we can finally infer the value of the metastable lifetime, $\tau^* = 18(3)$ ns, as well as the upper bond of the ODMR contrast, $\mathcal{C}_{\text{Max}} \approx 34\%$.

### 2.3.2 Comments

All the low-temperature rates and parameters are summarized in Table 2.3, together with the room-temperature values for comparison. While a three-fold elongation of the ES lifetime had already been reported by Mu et al. [162], our bi-exponential analysis further reveals that all ISC rates increase by nearly the same factor, so that the ratios $\alpha$ and $\beta$ remain essentially unchanged. In consequence, both spin polarization and ODMR contrast remain very close to the values extracted at room temperature. It is worth noting that the three-fold increase in ES lifetime is also in excellent agreement with the temperature dependence of the ISC rate, predicted by Reimers et al. [107], supporting the claim that the ES lifetime is entirely dominated by the ISC process.

| Parameter of the model | 300 K | 4 K |
|---|---|---|
| $k_p^0$ | 1.0(4) MHz/mW | 0.44(3) MHz/mW |
| $\gamma_0$ | 0.82(6) GHz | 0.22(1) GHz |
| $\alpha$ | 0.47(5) | 0.34(2) |
| $\kappa_0$ | 41(8) MHz | 24(2) MHz |
| $\beta$ | 6(1) | 4.9(2) |
| **Additional parameter** | | |
| $\tau^*$ | 18(3) ns | 30(3) ns |
| $\mathcal{P}$ | 75(3) % | 71(1) % |
| $\mathcal{C}_{\text{Max}}$ | $\approx 30\%$ | $\approx 34\%$ |

**Table 2.3:** Low temperature versus room temperature parameters of the seven-level model.

These results provide a nuanced picture. On the one hand, the photodynamics is not altered at 4 K, on the other hand, it is not improved either. Especially, the increase in ISC rates remains insufficient to significantly improve the quantum efficiency of the $V_B^-$ center. Nonetheless, we now have a complete and consistent model that describes the photodynamics of the $V_B^-$ center at 4 K. In the next section, we test this model with a practical example.

## 2.4 Photodynamics in an external magnetic field

During sensing experiments, the defect is always subjected to a magnetic field, whether from an external bias magnet or from the magnetic sample itself. By shifting and mixing the spin states, such fields can drastically alter the photodynamics of the $V_B^-$ center. Thanks to the low-temperature conditions, we are now able to use a vectorial magnet capable of generating magnetic fields of up to 3.5 T along an arbitrary axis. Taking advantage of this opportunity, we conclude this chapter by examining the impact of an external magnetic field on the $V_B^-$ center photodynamics. These last sets of measurements were carried out by Jodok Happacher and Juanita Bocquel from Professor Maletinsky's group at the University of Basel, together with myself during a visit to their laboratory.

### 2.4.1 Seven-level model in a magnetic field

In presence of a magnetic field, the spin Hamiltonian reads :

$$H = D\hat{S}_z^2 + \gamma_e \mathbf{B}\hat{\mathbf{S}}, \tag{2.21}$$

where we neglect the orthorhombic zero-field-splitting (ZFS) parameter $E$. This is because this term mixes $|m_s = -1\rangle$ with $|m_s = +1\rangle$ sublevels, i.e., two dark states with identical photodynamics. It therefore plays no role here. The situation is, however, different for the Zeeman term. If a field aligned with the defect quantization axis $z$ merely shifts the degeneracy between $|m_s = \pm 1\rangle$ [see Sec.1.2.3], an off-axis field component can mix $|m_s = -1\rangle$ with $|m_s = 0\rangle$. This originates from the Zeeman terms $\propto \hat{S}_x$ and $\propto \hat{S}_y$, which do not commute with $\hat{S}_z$. As a consequence of this mixing, the spin-dependent photodynamics can be drastically modified under a magnetic-field.

To express the rates at a given magnetic field in terms of the zero-field rates, measured in the previous section, we follow the seminal approach of Tetienne et al., originally developed for the $NV^-$ center in diamond [163, 164]. The principle is to expand the new eigenstates in the initial unmixed basis, i.e.,

$$|i\rangle = \sum_{n=1}^{7} c_n^i(\mathbf{B})\,|n\rangle\,, \tag{2.22}$$

where $|i\rangle$ is one of the seven state of the model states under a given magnetic field $\mathbf{B}$, $c_n^i(\mathbf{B})$ are complex field-dependent coefficients, and $|n\rangle$ denotes the initial basis states: $\{|1\rangle = |m_s = 0\rangle\,, |2\rangle = |m_s = -1\rangle\,, |3\rangle = |m_s = +1\rangle\,, |4\rangle = |m_s = 0\rangle'\,, |5\rangle = |m_s = -1\rangle'\,, |6\rangle = |m_s = +1\rangle'\,, |7\rangle = |m\rangle\}$. Then, one injects these new states in the Fermi's golden rule [Eq. (2.1)]. With some algebra, and once again neglecting coherences, the rate $\Gamma_{if}(B)$ coupling the mixed states $|i\rangle$ and $|f\rangle$ can be expressed as

$$\Gamma_{if}(\mathbf{B}) = \sum_{n=0}^{6}\sum_{m=0}^{6} |c_m^f(\mathbf{B})|^2 |c_n^i(\mathbf{B})|^2 \Gamma_{n,m}(0), \tag{2.23}$$

where $\Gamma_{nm}(0)$ is the zero-field rate coupling $|n\rangle$ and $|m\rangle$ of the unmixed basis. This complex expression in fact has an intuitive meaning. Suppose the magnetic field mixes the zero-field excited states $|m_s = 0\rangle'$ and $|m_s = -1\rangle'$, to form a new state:

$$|i\rangle = \frac{|m_s = 0\rangle' + |m_s = -1\rangle'}{\sqrt{2}}. \tag{2.24}$$

Then, according to Equation 2.23, the new ISC rate coupling the state $|i\rangle$ with the metastable state is not $\gamma_0$ or $\gamma_1$, but rather

$$\Gamma_{if} = \frac{\gamma_0 + \gamma_1}{2}. \tag{2.25}$$

Hence, the mixed initial state decays with a rate that is itself a weighted combination of the zero-field rates. Crucially, this means that knowledge of the zero-field rates is sufficient to predict the photodynamics at any applied magnetic field $\mathbf{B}$. The key quantities are now the coefficients $c(\mathbf{B})$, which encode the spin-state mixing. They can be obtained by diagonalizing both the GS and ES spin Hamiltonians. The metastable state, by contrast, remains unperturbed due to its singlet nature. For both the GS and ES Hamiltonians we use the form given by Equation (2.21), with the only subtlety being the need to update the ZFS parameters $D$ at low temperature. We take $D(4K) = 3.63$ GHz for the GS and $D'(4K) = 2.2$ GHz for the ES, following literature reports [109, 111, 161, 162].

### 2.4.2 Dependence on magnetic field orientation

We begin by simulating the impact of magnetic-field misalignment. The field magnitude is fixed to $|\mathbf{B}| = 100$ mT, and the new eigenstates are computed for a tilt angle $\theta$ with respect to the $z$ axis. Since the spin projection along the $z$ axis is no longer a good quantum number, the states are now labeled $|a\rangle$, $|b\rangle$, and $|c\rangle$. Accordingly the ISC rates are now denoted as $\gamma_a, \gamma_b, \gamma_c$ and $\kappa_a, \kappa_b, \kappa_c$. The change of labels is summarized in Figure 2.10(a).

To visualize spin-state mixing in the ES, we compute in Figure 2.10(b) the expectation value of the $\hat{S}_z$ operator as a function of $\theta$ for each of the three ES eigenstates. The results show that $|a\rangle'$ and $|b\rangle'$ (initially $|m_s = 0\rangle'$ and $|m_s = -1\rangle'$) become strongly mixed as $\theta$ increases. By contrast, $|c\rangle'$ (initially $|m_s = +1\rangle'$) remains almost unaffected, owing to its large energy separation from $|a\rangle'$. According to Equation (2.23), this mixing alters the ISC rates from the ES. The new ISC rates from the ES are plotted in Figure 2.10(c). As expected, the rates mirror the spin mixing: $\gamma_c$ remains nearly constant, while $\gamma_b$ and $\gamma_a$ converge and even invert their order. As a direct consequence, the brightness of $|a\rangle$ is drastically reduced.

After analyzing the ES, we now evaluate spin mixing in the GS [Fig. 2.10(d)]. The behavior is qualitatively similar to that of the ES, but with a weaker mixing

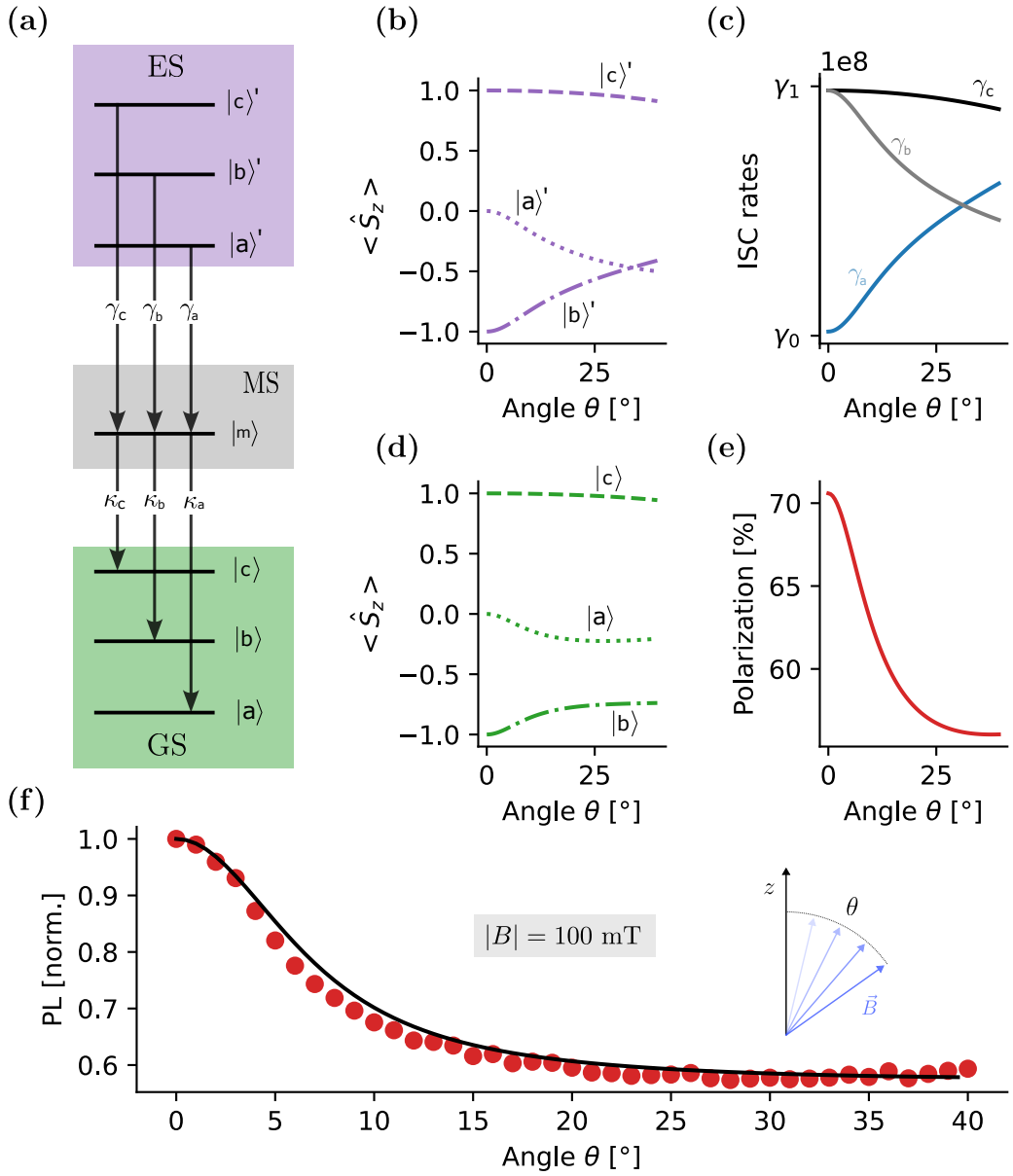


**Figure 2.10:** Impact of off-axis magnetic-field on spin-dependent photodynamics of the $V_B^-$ center. The magnetic field norm is fixed at $|B| = 100$ mT in both experimental data and simulations. (a) Seven-level model with the new state and rate labels. (b) Expectation value of the $\hat{S}z$ operator for the three ES eigenstates. (c) Simulated evolution of the ISC rates from the ES as a function of the magnetic-field angle $\theta$ with respect to the $z$ axis. (d) Expectation value of the $\hat{S}z$ operator for the three GS eigenstates. (e) Simulation of the spin polarization in $|0\rangle$ as a function of $\theta$, defined as $\mathcal{P} = \frac{1}{1+\frac{\kappa_+}{\kappa_0}+\frac{\kappa_-}{\kappa_0}}$.(f) Steady-state PL signal as a function of the angle $\theta$. Experimental data are shown as red dots, and the simulation as a solid black line. The simulation is normalized by the maximum of the experimental data.

owing to the larger axial ZFS parameter. Instead of plotting the evolution of the ISC rates, we directly compute the spin polarization in $|a\rangle$, defined as

$$\mathcal{P} = \frac{1}{1 + \frac{\kappa_c}{\kappa_a} + \frac{\kappa_b}{\kappa_a}}. \tag{2.26}$$

The result is displayed in Figure 2.10(e). Starting from $\mathcal{P} \approx 70\%$ at zero field, the steady-state spin polarization gradually decreases to only $\mathcal{P} \approx 55\%$ at $\theta = 45°$. In summary, a misaligned magnetic field reduces both the brightness of $|a\rangle$ and its polarization, which directly translates into a reduction of the PL signal. We now confront this prediction with experimental data. Thanks to the pre-calibrated superconducting magnet, both the magnitude and orientation of the field can be tuned without the need for ODMR spectra. We fix $|\mathbf{B}| = 100$ mT, as in the simulation, and monitor the PL signal under continuous optical pumping while gradually misaligning the magnet. The resulting PL signal versus angle $\theta$ curve is shown in Figure 2.10(f), together with the simulated signal. As expected, a pronounced PL signal drop is observed. Furthermore, the agreement with the simulation is remarkable. In particular the observed $\sim 40\%$ attenuation is very well reproduced by the simulation. Importantly, no fitting procedure is performed: the PL signal evolution is computed directly from the zero-field rates measured in the previous section and from the diagonalization of the GS and ES Hamiltonians. Only a single normalization is applied to match the simulated PL to the experimental value at $\theta = 0°$, since the absolute scaling factor between ES populations and PL signal remains undetermined.

### 2.4.3 Level anti-crossings

After this first encouraging result, we now perform a complementary experiment. This time, the magnetic field is aligned with the defect's quantization axis $z$, but its magnitude is increased up to the maximum available value of 3.5 T. In the absence of misalignment, one might naively expect a trivial, flat PL response, since no spin mixing should be induced by the bias field. However, as shown in Figure 2.11(a), two sharp PL drops are observed at $B_z = 79$ mT and $B_z = 129$ mT. These values are not arbitrary: they correspond precisely to the ground- and excited-state level anticrossings (GSLAC, ESLAC), which occur when the Zeeman shift cancels the axial ZFS parameter [Fig. 2.11(b)],

$$B_{\mathrm{LAC}} = \frac{D^{(\prime)}}{\gamma_e}. \tag{2.27}$$

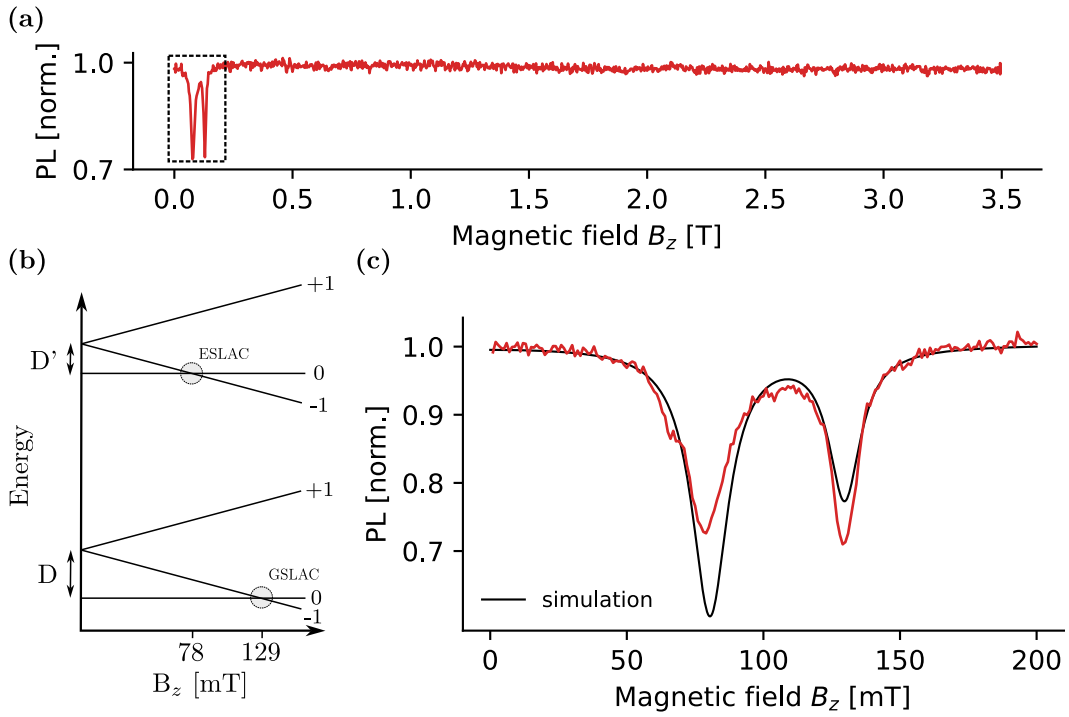


**Figure 2.11:** PL signal under an axial magnetic field. (a) PL signal as a function of a magnetic field $B_z$. (b) Illustration of the level anticrossings in the ES and GS. (c) Zoom on the low-field region of figure (a). Experimental data (red dots) are compared with the simulation (black solid line). The two dips occur at $B_{ESLAC} \approx 78$ mT and $B_{GSLAC} \approx 129$ mT, respectively.

At these specific fields, $|m_s = -1\rangle$ is no more protected by the $D$ parameter, and becomes highly sensitive to any off-axis magnetic field components. In particular those generated by the surrounding nitrogen nuclear spins. In more formal terms, the secular approximation introduced in Chapter 1 is no longer valid, and the full hyperfine tensor must be taken into account. The most rigorous way to model the LAC would thus be to include the hyperfine interaction explicitly in the Hamiltonian. However, this would drastically increase the number of states (with $^{14}$N isotope, each electron state is subdivided in 27 hyperfine states), making simulations drastically more complex. Instead, we adopt a simpler approach by treating the hyperfine interaction as an effective transverse magnetic field $B_\perp$, which can be estimated to first order from the two dominant non-secular components of the hyperfine tensor, $A$,

$$B_\perp \approx \frac{1}{4\gamma_e} \sum_i^3 \left( A^i_{xx} + A^i_{yy} \right), \tag{2.28}$$

where the sum runs over the three nearest-neighbor nitrogen atoms. Using the ab-initio values of the hyperfine tensor from Ref.[80], we estimate $B_\perp \approx 5$ mT. With

this additional term, the Hamiltonians now reads:

$$H = D^{(')}\hat{S}_z^2 + \gamma_e B_z \hat{S}_z + \gamma_e B_\perp \hat{S}_x. \tag{2.29}$$

With this new Hamiltonian, we simulate the PL evolution as a function of the bias magnetic field and compare it with the experimental data in Figure 2.11(c). Once again, the simulation reproduces well the experimental trends. Building on the discussion developed in the previous section, we can now fully interpret the origin of these features: the ESLAC enhances the non-radiative pathway, while the GSLAC degrades the GS spin polarization, both effects leading to a PL drop. Some discrepancy in the dip amplitudes is nonetheless observed, most likely due to our transverse magnetic field approximation. As will become evident in the next chapter, level anticrossings induced by hyperfine interactions are rich in physics and cannot be fully captured within such a simplified framework. Still, the overall agreement remains satisfactory, and we retain this approximation as it considerably simplifies the simulations. Notably, the fact that no additional PL signal drops are observed at higher fields, confirms that the spin-dependent photodynamics of the $V_B^-$ center is primarily governed by a single ES, as assumed throughout this work.

### 2.4.4 PL versus magnetic-field: the complete picture

We now combine both types of measurements and record a two-dimensional PL map as a function of the magnetic-field magnitude $|\mathbf{B}|$ and the misalignment angle $\theta$. The resulting experimental data, together with the corresponding simulation, are shown in Figure 2.12(a,b). An excellent overall agreement is observed, both qualitatively and quantitatively.

Let us emphasize one last time: apart from a global scaling factor, no free parameters are involved, everything is computed from the zero-field rate measurements. This demonstrates that, despite the complex photodynamics involving many levels and rates, the $V_B^-$ center photodynamics can ultimately be captured by a relatively simple seven-level model that, moreover, neglects direct radiative decay.

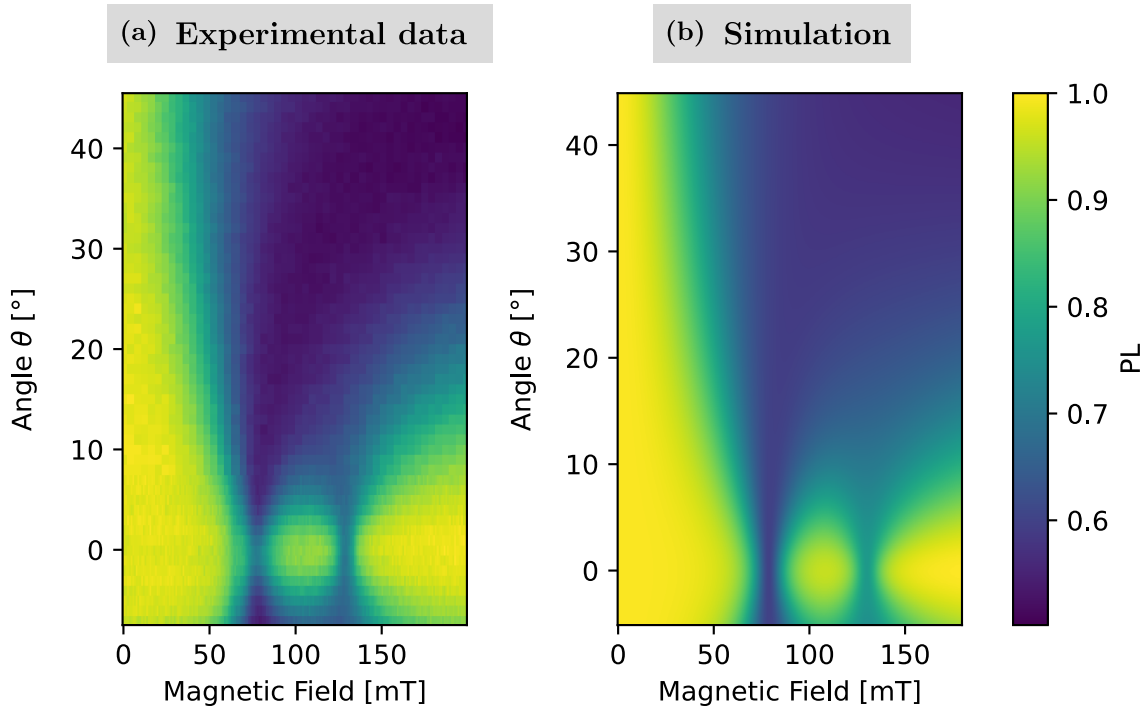


**Figure 2.12:** Steady state PL signal of the $V_B^-$ center as a function of a magnetic field $\mathbf{B}$. (a) Experimental data and (b) simulation, both normalized by their respective maximums.

## 2.5 Conclusion

In this work, we have performed a comprehensive characterization and analysis of the spin-dependent photodynamics of the $V_B^-$ center, at both room and cryogenic temperatures, together with an in-depth investigation of its PL signal magnetic field dependence. Our results demonstrate that the essential photodynamic properties of the defect can be accurately reproduced and understood within a seven-level model that neglects direct radiative decay. This conclusion lends strong support to earlier theoretical predictions suggesting that the radiative transition is symmetry-forbidden [80, 106, 107].

### Slow direct decay

The confirmation of a negligible radiative decay rate naturally raises the question of how it could be enhanced. One possible pathway is to apply perturbations to the hBN lattice in order to induce favorable symmetry changes. This idea has been investigated in our group by Mu Zhao, who characterized the evolution of

the photodynamics under hydrostatic pressure [115]. While the study did reveal pressure-induced modifications of the ISC rates, it also showed a significant reduction of PL signal and ODMR contrast beyond a few GPa.

An alternative approach is to apply strain to the crystal, for instance through substrate patterning, polymer encapsulation, or piezoelectric strain cells [165–167]. Our group has already explored the latter method, again through the efforts of Mu Zhao, but no measurable impact on PL signal was observed. It should be noted, however, that only uniaxial strain was tested, leaving room for further exploration.

A third possibility is to consider different hBN polytypes, i.e., stacking sequences of the layers. Although the defect symmetry itself is defined within a single layer and is therefore not expected to depend directly on stacking, recent work predicts modifications of the spin–phonon coupling in rhombohedral boron nitride (r-BN) [118]. While this study only addressed spin properties, one could imagine that the phonon-mediated radiative decay could also be stacking dependent.

## PL signal quenching as a tool

The PL signal quenching induced by magnetic-field misalignment has several implications. Most importantly, it limits the ability to sense quantitatively strongly misaligned fields, as both the PL signal and the spin-state contrast decrease to the point where ODMR measurements become unfeasible. On the other hand, this effect can also be turned into a resource: magnetic-field-induced PL signal quenching can be exploited to qualitatively image misaligned fields, as previously demonstrated for the $NV^-$ center in diamond, which displays a similar PL signal dependence on field orientation [163]. This technique has, for example, been used for the magnetic imaging of skyrmions [168]. Finally, PL quenching offers a practical means to align the magnetic field with the defect's quantization axis, by simply monitoring the PL response, provided that the bias field lies in the appropriate range.

## ODMR contrast

The reader may have noticed a striking discrepancy between the estimated maximum ODMR contrast, on the order of $\sim 30\%$, and the typical contrast observed in the spectra presented in Chapter 1, which barely reaches a few percent. The

first and most obvious reason lies in the non-optimized RF excitation. In most experimental setups, including ours, the RF drive is applied via an external antenna with a non-ideal field orientation with respect to the defect's quantization axis. Interestingly, however, a recent study reported a contrast as high as $\approx 40\%$ at zero field by employing a gold waveguide [169], a value not too far from our estimate.

The second contributing factor is, unfortunately, more intrinsic: the very broad magnetic resonance of the $V_B^-$ center. The hyperfine interaction splits the electron spin states into multiple hyperfine sublevels, which distributes the spin population across several transitions. Consequently, the microwave excitation cannot simultaneously address all spin states, leading to a reduced effective ODMR contrast. A possible strategy to mitigate this issue is to engineer the hyperfine structure, either through isotopic purification or by optically pumping the population into a specific hyperfine state. These approaches will be discussed in detail in the next chapter.

# 3 Engineering the $V_B^-$ center nuclear spin environment

## Outline


**2.1 Photodynamics modelling . . . . . 62**

2.1.1 Seven-level model . . . . . 62

2.1.2 Practical examples . . . . . 66

**2.2 Photodynamics at room temperature . . . . . 69**

2.2.1 Excited state lifetime measurements . . . . . 71

2.2.2 PL time traces under continuous optical excitation . . . . 74

2.2.3 Discussion . . . . . 77

**2.3 Photodynamics at liquid-helium temperature . . . . . 81**

2.3.1 Measurements . . . . . 81

2.3.2 Comments . . . . . 83

**2.4 Photodynamics in an external magnetic field . . . . . 84**

2.4.1 Seven-level model in a magnetic field . . . . . 84

2.4.2 Dependence on magnetic field orientation . . . . . 86

2.4.3 Level anti-crossings . . . . . 88

2.4.4 PL versus magnetic-field: the complete picture . . . . . 90

**2.5 Conclusion . . . . . 91**


The $V_B^-$ center resides within a crystal lattice densely populated with nuclear spins. As illustrated in Figure 3.1, its first neigboring shell consists of three nitrogen atoms, which within natural isotopic abundance, are almost exclusively $^{14}N$ (99.64 %), carrying a nuclear spin $I = 1$. The second shell is formed by six boron atoms, which may host either $^{11}B$ (80 %, $I = 3/2$) or $^{10}B$ (20 %, $I = 3$) nuclei. Beyond this, nitrogen atoms reappear in the third shell, followed by successive shells of boron and nitrogen. This very dense nuclear-spin environment gives rise to the broad ODMR spectrum linewidth of $V_B^-$ centers, presented in Chapter 1. For sensing scheme based on ODMR spectroscocy, this has a detrimental impact on the

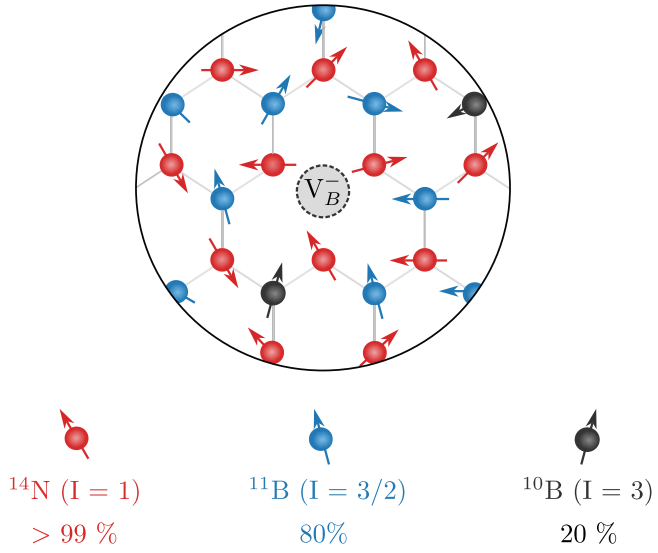


**Figure 3.1:** Illustration of the dense nuclear spin environment surrounding a $V_B^-$ center in hBN with natural isotopic content.

sensitivity, which scales inversely with the magnetic resonance linewidth. In this chapter, we explore two pathways to mitigate this strong limitation.

## Isotopic purification

While the atomic lattice is fixed by nature, one degree of freedom remains at our disposal: isotopes. On the one hand, isotopes share the same number of protons and electrons and therefore exhibit nearly identical chemical behavior. On the other hand, differences in neutron number modify both the nuclear spin and the gyromagnetic ratio of the nuclei, which respectively determine the number of hyperfine states and the energy splitting between them. By controling the isotopic composition of the lattice, it may thus be possible to engineer a configuration more favorable for the spin properties of the $V_B^-$ center.

The ideal scenario would be to completely eliminate isotopes with non-zero nuclear spin, thereby suppressing hyperfine interaction-induced ODMR broadening. This strategy has already yielded spectacular results for the $NV^-$ center in diamond, which, in a $^{13}$C-depleted carbon lattice, exhibits ultra-long millisecond-scale coherence times [17, 170, 171]. Similar improvements have been reported for phosphorus donors in silicon purified from $^{29}$Si [172].

Unfortunately, the situation is more complex in hBN. Both stable isotopes of boron carry non-zero nuclear spins: $^{11}$B ($I = 3/2$) and $^{10}$B ($I = 3$) and the same holds for nitrogen, with $^{14}$N ($I = 1$) and $^{15}$N ($I = 1/2$). The margin for improvement is therefore more limited, yet it remains essential and cannot be overlooked.

## Nuclear spin polarization

A broad hyperfine structure is not, in itself, detrimental. The linewidth of the ODMR spectrum becomes large only because the entire hyperfine manifold is populated. Conversely, if one could polarize the nuclear spins into a single state of the hyperfine manifold, a sharp linewidth, accompanied by enhanced magnetic resonance contrast, could in principle be recovered. Owing to their low gyromagnetic ratio, however, nuclear spins are not so easily polarized. A well-known strategy consists in exploiting the hyperfine interaction to transfer polarization from the electronic spins to the surrounding nuclei. Initially demonstrated in metals with conduction electronsn in EPR experiments [173, 174], this technique, known as dynamic nuclear polarization (DNP), was later adapted to color centers through optical pumping schemes, achieving room-temperature nuclear-spin polarization of first-neighbor nuclear spin as high as 100% [175–177]. This is the second pathway that we chose to explore in this chapter.

## Outline

In what follows, we provide a detailed account of the hBN crystal growth and isotopic purification process [§ 3.1]. Since isotopic purification is achieved during hBN growth, it is worth elaborating further on the growth method as well as the subsequent characterization of the samples quality. We then examine the impact of isotopic purification on the hyperfine structure of the $V_B^-$ center and identify the isotopic configuration best suited for sensing applications [§ 3.2]. Finally, we build on these improvements to investigate dynamic nuclear polarization and assess its potential to enhance sensitivity [§ 3.3].

## 3.1 Isotopic purification of hBN

Each atomic species exhibits a characteristic natural isotopic abundance. Unless specific precautions are taken during growth, the material's composition will simply reflect this natural isotopic content. The challenge of isotopic purification therefore lies in developing a growth technique capable of producing material with an almost pure content of the desired isotopes. For hBN, four possible monoisotopic configurations are possible: $h^{11}B^{14}N$, $h^{10}B^{14}N$, $h^{11}B^{15}N$, and $h^{10}B^{15}N$. The aim of this section is to expand on the sample preparation process introduced in Chapter 1, by providing more details about the crystal growth, isotopic purification, and subsequent characterization.

### 3.1.1 Metal-flux growth of bulk monoisotopic hBN crystals

The hBN crystals were synthesized by the group of James H. Edgar at Kansas State University, using the metal-flux growth technique illustrated in Figure 3.2(a). A commercial boron powder is placed in an alumina crucible together with a mixture of metallic precursors, nickel and chromium. The crucible is then placed in a furnace continuously supplied with $N_2$ and $H_2$ gases. The temperature of the furnace over time is plotted in Figure 3.2(b) (red solid line). After a rapid warm-up, the furnace is maintained at 1500 °C for 24 hours, before being slowly cooled down at a rate of 0.5 °C per hour over 50 hours. While the hydrogen gas minimizes impurities by reacting with residual carbon and oxygen atoms, the nitrogen and boron atoms bond to form bulk millimeter-sized hBN crystals that precipitate on the surface of the nickel–chromium ingot. Finally, the furnace is brought back to room temperature within 20 hours. All the process is carried out under atmospheric pressure.

Notably, by simply replacing the natural-abundance boron powder with commercially available isotopically purified boron powders (*Ceradyne Inc.*), one can grow $h^{10}B^{14}N$ or $h^{11}B^{14}N$ crystals with a boron isotope purity beyond 99% [133]. In these crystals, the nitrogen content can be considered naturally purified, as $^{14}N$ already dominates the natural nitrogen isotopic composition ($> 99\%$).

Purifying the nitrogen isotope requires more ingenuity. Because $^{15}N$ is very rare, it is an expensive resource that cannot be continuously injected into the furnace as previously. To address this practical constraint, James Edgar and colleagues

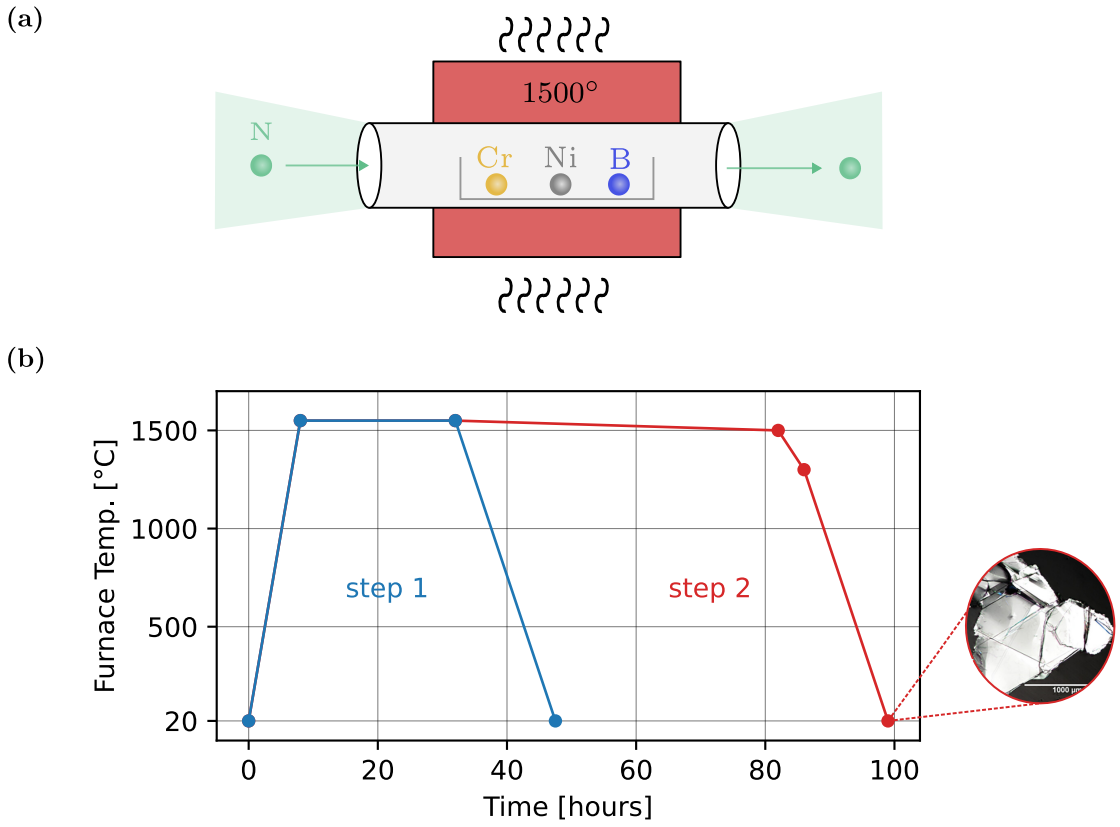


**Figure 3.2:** Growth of isotopically purified hBN crystals. (a) Schematic of the growth process involving an alumina crucible, metallic precursors, boron powder, and a nitrogen flux, all placed inside a furnace heated to 1500 °C. (b) Furnace temperature profile over time. for the $^{15}$N isotope purification a first heating cycle (blue) is realized prior to the main heating cycle (red). Figure reproduced from Ref. [134]. Right panel: photograph of a typical bulk hBN crystal obtained by the metal-flux growth method.

developed an adapted procedure with two heating cycles [134]. The furnace is first heated under an argon and hydrogen flow only, to ensure a homogeneous mixture of the precursors and low impurity concentration [solid blue line in Fig. 3.2(b)]. Only then is the furnace sealed with $^{15}$N gas and subjected to the heating cycle described in the previous paragraph (red line). Since the $^{15}N_2$ gas is isotopically enriched above 99%, the remaining two isotopic configurations, h$^{11}$B$^{15}$N and h$^{10}$B$^{15}$N, can finally be obtained.

### 3.1.2 Raman characterization

Once growth is completed, it is essential to verify the crystal quality and confirm that the isotopic purification has been successful. To this end, Raman spectroscopy was performed. These measurements were carried out by Juliette Plo, a PhD student in the team working on optical spectroscopy of hBN, assisted by Thierry Michel.

Raman spectroscopy consists in measuring the energy difference between an incident laser beam and the light inelastically scattered by the sample. In this process, part of the photon energy is transferred to excite a vibration of the crystal lattice. By collecting the scattered light with a high-resolution spectrometer, one can therefore infer the energy of the Raman-active phonon modes. Within a simple harmonic oscillator model, the frequency $\omega$ of a phonon mode scales as $\omega \propto \sqrt{k/\mu}$, where $k$ is the effective spring constant and $\mu$ is the reduced mass of the vibrating atomic pair, boron and nitrogen in our case. As the reduced mass $\mu$ increases (decreases), a redshift (blueshift) of the phonon frequency is expected [178]. Since isotopes differ in their masses, a shift of the phonon mode energy can be observed when the isotopic content is modified. Raman spectroscopy is therefore a well-suited tool to probe isotopic purification.

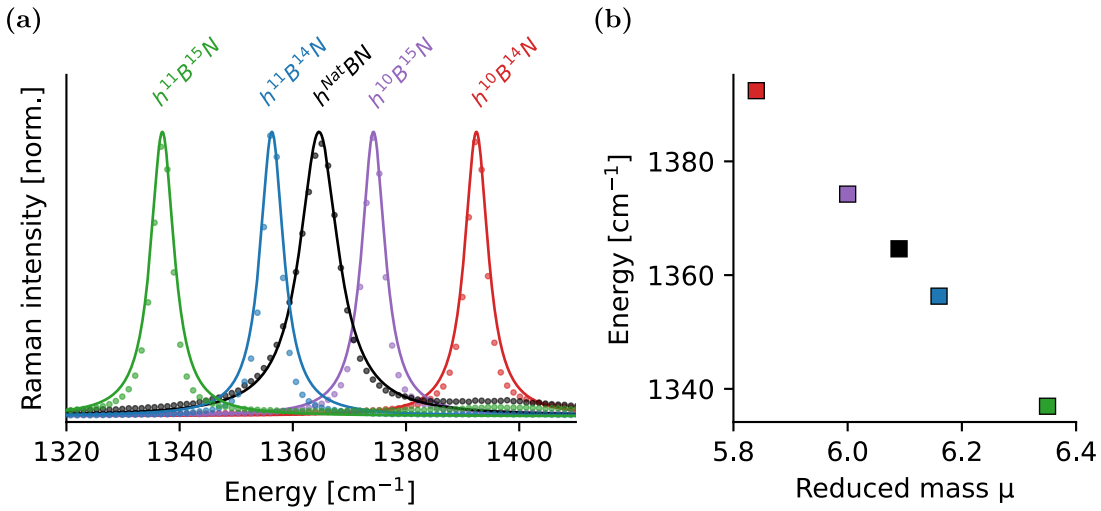


**Figure 3.3:** Raman spectroscopy characterization of the isotopically purified hBN crystals. (a) Raman spectra of the $E_{2g}$ phonon mode of hBN for the four differentisotopic configurations, along with natural hBN. (b) Position of the $E_{2g}$ phonon mode as a function of the reduced mass of the boron-nitrogen pair. Both figures are reproduced from Ref. [134].

Raman spectroscopy was performed on the four isotopically purified samples, together with a reference hBN crystal with natural isotopic composition. The resulting spectra, shown in Figure 3.3(a), are centered around the high-energy $E_{2g}$ phonon mode of hBN. This mode corresponds to an in-plane vibration, where boron and nitrogen atoms oscillate in opposite directions within the same hexagonal layer. It is characteristic of the hexagonal symmetry and represents the most prominent feature in the Raman spectrum of hBN [179].

As expected, the $E_{2g}$ phonon mode shifts to higher energies when the reduced mass decreases, following a linear scaling, in excellent agreement with DFT calculations [134] [Fig. 3.3(b)]. Note that the shift appears linear because the small difference between the isotopic masses masks the $1/\sqrt{\mu}$ dependence. In addition, the Raman peaks of all isotopically purified samples exhibit linewidths nearly twice as narrow as the one of the natural-abundance sample, indicating a significant reduction in isotopic disorder, which otherwise cause inhomogeneous broadening of the phonon line. These Raman spectra therefore attest the success of the isotopic purification as well as the high crystalline quality of the samples. At the date these crystals were grown, they represented the first isotopically purified hBN crystals ever reported.

### 3.1.3 Nitrogen ion implantation

To introduce $V_B^-$ centers into the crystal, we follow the same approach as in Chapter 2. Bulk crystals are first mechanically exfoliated in Toulouse by Jules Fraunié and Cédric Robert from LPCNO, Toulouse. The hBN flakes, typically a few tens of nanometers thick, are then deposited on a $SiO_2$ substrate. The samples are subsequently irradiated with a nitrogen ion dose of $10^{14}$ ions/cm$^2$ at 30 keV. This step was once again carried out at CEMES in Toulouse by Gregory Seine. It should be noted that the nitrogen beam used for the implantation is not isotopically purified with $^{15}$N and could, in principle, introduce isotopic disorder. However, simulations performed by our collaborator Alain Claverie, based on the well-established SRIM software, indicate that at 30 keV the nitrogen ions stop within the $SiO_2$ substrate and therefore do not affect the nitrogen content of the hBN flakes.

## 3.2 ODMR spectroscopy of the $V_B^-$ center in isotopically purified hBN flakes

We now study the impact of the isotopic purification on the hyperfine structure of the $V_B^-$ center. As introduced in Chapter 1 § 1.2.4, the ground-state (GS) spin Hamiltonian of a $V_B^-$ center, under a magnetic field $B_z$, is given by:

$$\hat{\mathcal{H}} = D\hat{S}_z^2 + |\gamma_e|\hat{S}_z B_z + \sum_{i=0}^{N} \hat{\mathbf{S}} A^i \hat{\mathbf{I}}^i. \tag{3.1}$$

Under most conditions, the first two terms largely dominate the Hamiltonian. In this case, one can apply the secular approximation and retain only the longitudinal component of each hyperfine tensor:

$$\hat{\mathcal{H}} = D\hat{S}_z^2 + |\gamma_e|\hat{S}_z B_z + \sum_{i=0}^{N} A_{zz}^i \hat{S}_z \hat{I}_z. \tag{3.2}$$

This expression clearly illustrates the detrimental role of the nuclear-spin bath. Each nuclear spin produces a subdivision of the electronic state into $2I+1$ sub-states, split by the axial hyperfine coupling $A_{zz}$. When summed over the successive surrounding atomic shells, the hyperfine interaction gives rise to a quasi-continuum of states, deleterious for the sensor's sensitivity.

Isotopic purification, by modifying the nuclear spin and the gyromagnetic ratio, affects both the number of hyperfine states and their energy spacing, leaving room for some improvement. Intuitively, low nuclear spin and low gyromagnetic ratio should lead to a sharper magnetic resonance linewidth. Yet these two properties are not always combined in a single isotope, as shown in Table 3.1. Identifying the optimal isotopic configuration is precisely the objective of this section.

| | $^{10}B$ | $^{11}B$ | $^{14}N$ | $^{15}N$ |
|---|---|---|---|---|
| Nuclear spin | 3 | 3/2 | 1 | 1/2 |
| Gyromagnetic ratio [MHz/T] | 4.6 | 13.7 | 3.07 | −4.3 |
| Natural abundance | 20% | 80% | 99.6% | 0.4% |

**Table 3.1:** Stable isotopes of boron and nitrogen.

Through ODMR spectroscopy we begin the investigation by examining the impact of the boron isotope, going from $^{11}$B to $^{10}$B [§ 3.2.4]. We then address the nitrogen isotope, starting from $^{14}$N, as in natural hBN, and moving to $^{15}$N [§ 3.2.1]. Next, we demonstrate that the observed behavior is fully reproduced by a simple Hamiltonian simulation [§ 3.2.3].

The measurements, conducted by myself, are performed with the same home-made confocal microscope described in the previous chapter. A green excitation laser is focused onto a $\sim$1 µm$^3$ volume, while the PL signal is detected by an avalanche photodiode (APD) and recorded with a data acquisition device

(DAQ). To deliver the RF excitation, a homemade antenna, consisting of a simple metallic wire, is placed in close proximity to the sample. Figure 3.4 illustrates this configuration. On a longitudinal (along the $z$ axis) confocal PL raster scan, one can distinguish the hBN flake, which owing to its nanometric thickness, appears as a single plane. Approximately 20 µm above the flake lies the RF antenna.

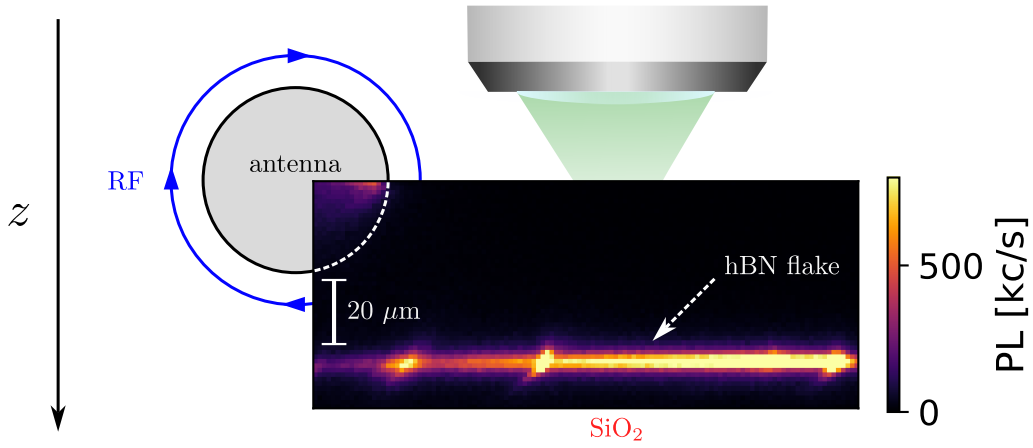


**Figure 3.4:** Confocal PL raster scan along the $z$ axis of a nitrogen-implanted hBN flake, overlaid by the RF antenna and the microscope objective. The position of the microscope objective is not at scale.

### 3.2.1 From $^{14}$N to $^{15}$N isotope

Being the closest neighbors, the nitrogen atoms are the only ones coupled strongly enough to the electron spin to produce a hyperfine structure distinguishable in the ODMR spectrum. Natural hBN is almost exclusively composed of $^{14}$N, which carries a nuclear spin $I = 1$. In this case, the first shell, made of three equivalent nitrogen atoms, yields an effective total nuclear spin of $I_{\text{eff}} = 3 \times 1 = 3$, and therefore $2I_{\text{eff}} + 1 = 7$ hyperfine peaks [cf. Chap.1 § 1.2.4]. In contrast, $^{15}$N has a lower nuclear spin of $I = 1/2$, resulting in a reduced effective nuclear spin of $I_{\text{eff}} = 3/2$. With this isotope, one would therefore expect only 4 hyperfine states. Additionally, the gyromagnetic ratio of $^{15}$N is approximately 1.4 times larger (in absolute value) than that of $^{14}$N [see Tab. 3.1]. Since the hyperfine coupling scales linearly with the nuclear gyromagnetic ratio, the axial hyperfine splitting $A_{zz}$ should increase accordingly. In summary, isotopic purification with $^{15}$N should result in fewer hyperfine states with a larger frequency spacing.

We now verify this prediction. I begin with the $h^{11}B^{14}N$ sample, which closely ressembles natural hBN. A magnetic field of a few mT is first applied to split the two electron spin resonances and we focus on a single one. The resulting ODMR spectrum, shown in Figure 3.5(a), unsurprisingly exhibits a broad linewidth of $\sim$ 200 MHz. Within this resonance, the hyperfine structure resulting from the interaction with the first nitrogen shell is barely visible. Nonetheless, by fitting the data with seven equally spaced Gaussians functions, I obtain a FWHM of $\Gamma = 54(2)$ MHz as well as an hyperfine splitting $A_{zz} = 47.5(3)$ MHz.

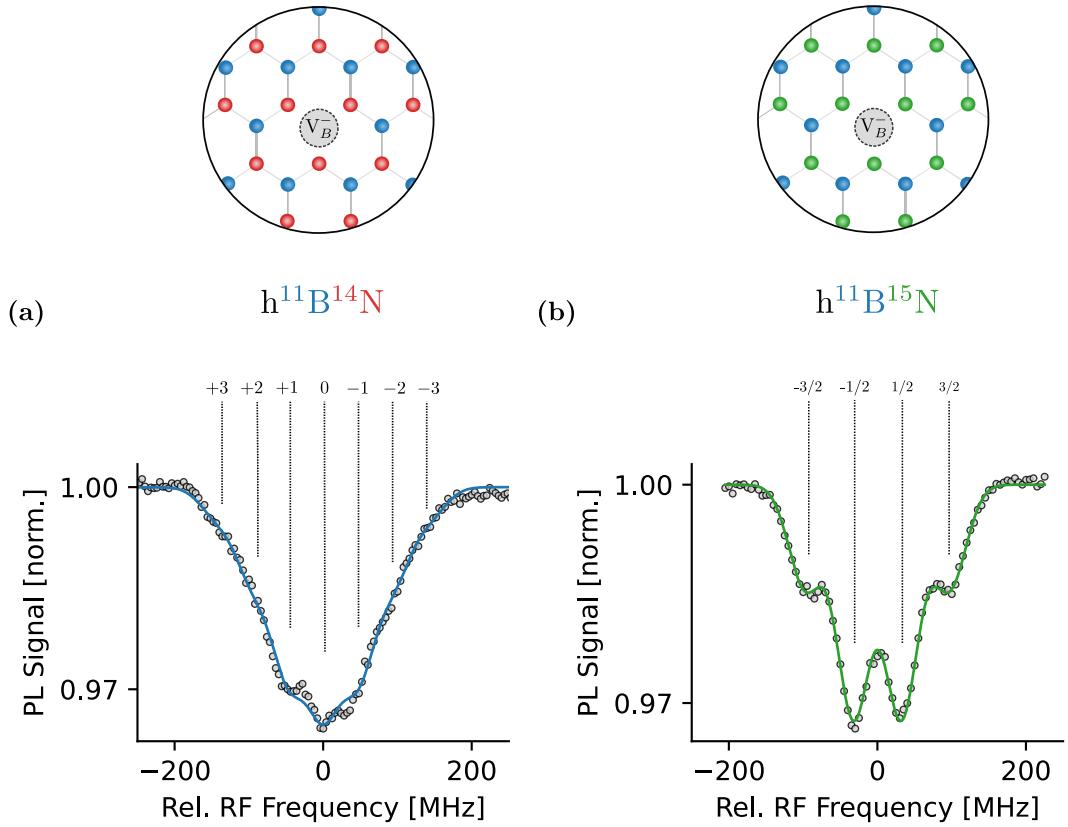


**Figure 3.5:** Hyperfine structure of the $V_B^-$ center in hBN crystals with a monoisotopic nitrogen content. (a,b) ODMR spectra focus on the $|m_s = -1\rangle$ electron spin resonance in (a) $h^{11}B^{14}N$ and (b) $h^{11}B^{15}N$ flakes. A magnetic field of few mT is applied along the $z$ axis. The optical and RF power are $P_{opt} = 500$ µw and $P_{RF} = 25$ dBm respectively.

I then proceed in the same way with the freshly prepared $h^{11}B^{15}N$ sample [Fig. 3.5(b)]. The difference is striking: instead of seven closely spaced hyperfine peaks, we now observe four well-separated peaks in the ODMR spectrum. They correspond to the four projections of the effective nitrogen nuclear spin, $m_I = \{-3/2, -1/2, +1/2, +3/2\}$. The relative amplitudes of the hyperfines resonances is further consistent with the degeneracy of each $\{1, 3, 3, 1\}$. Note

that due to the negative gyromagnetic ratio, the hyperfine state ordering is reversed compared to $^{14}$N. Fitting these peaks with four Gaussians functions yields $A_{zz} = 64.4(2)$ MHz, which gives a ratio $\frac{A_{zz}(^{15}\mathrm{N})}{A_{zz}(^{14}\mathrm{N})} = 1.36(2)$, in excellent agreement with the ratio $\frac{\gamma_N(^{15}\mathrm{N})}{\gamma_N(^{14}\mathrm{N})}$ [cf. Table 3.1].

Although the hyperfine structure is now much better resolved, the linewidth of the hyperfine lines remains unchanged, $\Gamma = 52.9(4)$ MHz. To obtain an improvement in this regard, one needs to turn to the purification of the boron isotope.

### 3.2.2 From $^{11}$B to $^{10}$B isotope

Boron atoms constitute the second neighboring shell of a boron vacancy. Too far to be strongly coupled to the central electron spin and properly resolved in the ODMR spectrum, but close enough to broaden the hyperfine lines. Since $^{10}$B possesses a higher nuclear spin one could reasonably expect a broader linewidth in a hBN crystal purified with $^{10}$B. However, the gyromagnetic ratio is threefold smaller for $^{10}$B than $^{11}$B [see Tab. 3.1]. Hence, if the number of nuclear spin states is more important with $^{10}$B, the spacing between the states is also reduced. In the end, it is not obvious to predict which effect dominates.

I now measure the hyperfine structure of the two remaining isotopic configurations, h$^{10}$B$^{14}$N and h$^{10}$B$^{15}$N. The corresponding spectra are displayed in Figure 3.6. A clear linewidth reduction is observed compared to the $^{11}$B samples. We obtain $\Gamma = 46(1)$ MHz for h$^{10}$B$^{14}$N and $\Gamma = 44.1(3)$ MHz for h$^{10}$B$^{15}$N, corresponding to a linewidth improvement of nearly 15%. Before commenting further on these promising results, we verify that they are fully reproduced by a simple Hamiltonian simulation.

### 3.2.3 Simulations of the $V_B^-$ center hyperfine Structure

I follow the approach of Alrik Durand and Florentin Fabre, former PhD students of the team, who previously carried out such calculations for h$^{11}$B$^{14}$N and h$^{10}$B$^{14}$N [124, 149]. Once again, we adopt the secular approximation, retaining only the $A_{zz}$ component of each hyperfine tensor. Our calculation includes three nitrogen atoms from the first shell, six boron atoms from the second shell, and six nitrogen atoms from the third shell. The third shell is added because the $V_B^-$ center couples almost

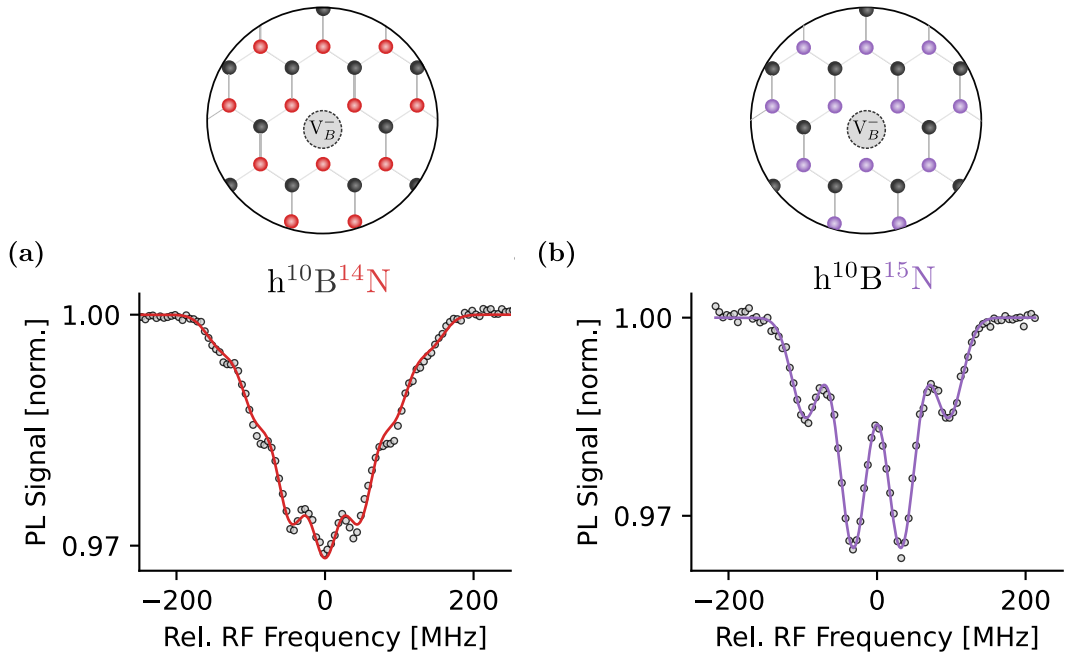


**Figure 3.6:** Hyperfine structure of the $V_B^-$ center in hBN crystals with a monoisotopic boron content. (a,b) ODMR spectra focus on the $|m_s = -1\rangle$ electron spin resonance in (a) h$^{10}$B$^{14}$N and (b) h$^{10}$B$^{15}$N flakes. A magnetic field of few mT is applied along the $z$ axis. The optical and RF power are $P_{opt} = 500$ µw and $P_{RF} = 25$ dBm respectively.

as strongly to it as to the second shell [80]. Assuming perfect $D_{3h}$ symmetry, all nuclear spins within a given shell are equivalent, allowing us to consider only three distinct values of $A_{zz}$. The values of the hyperfine coupling are extracted from the supplementary information of Ref. [80], where they have been calculated by DFT.

Within the secular approximation, the total Hamiltonian remains diagonal, so that the energy splittings induced by each nuclear spin can simply be added algebraically. An energy (or frequency) histogram is then constructed with a bin size of 5 MHz. To provide better intuition, an ODMR spectrum is reconstructed by assigning a Gaussian function to each level prior to binning. The amplitude of the Gaussian function is determined by degeneracy and its linewidth is empirically set to 30 MHz. The histograms are shown in Figure 3.7, with the simulated spectra plotted as solid lines. The simulations perfectly reproduce the trend observed in the data. From the fits, I obtain a linewidth improvement of $\sim 13\%$ in $^{10}$B samples, in excellent agreement with the experimental observations.

Notably, according to the simulation, the purification with $^{15}$N samples also yield a thinner linewidth. This arises because nitrogen atoms from the third shell also

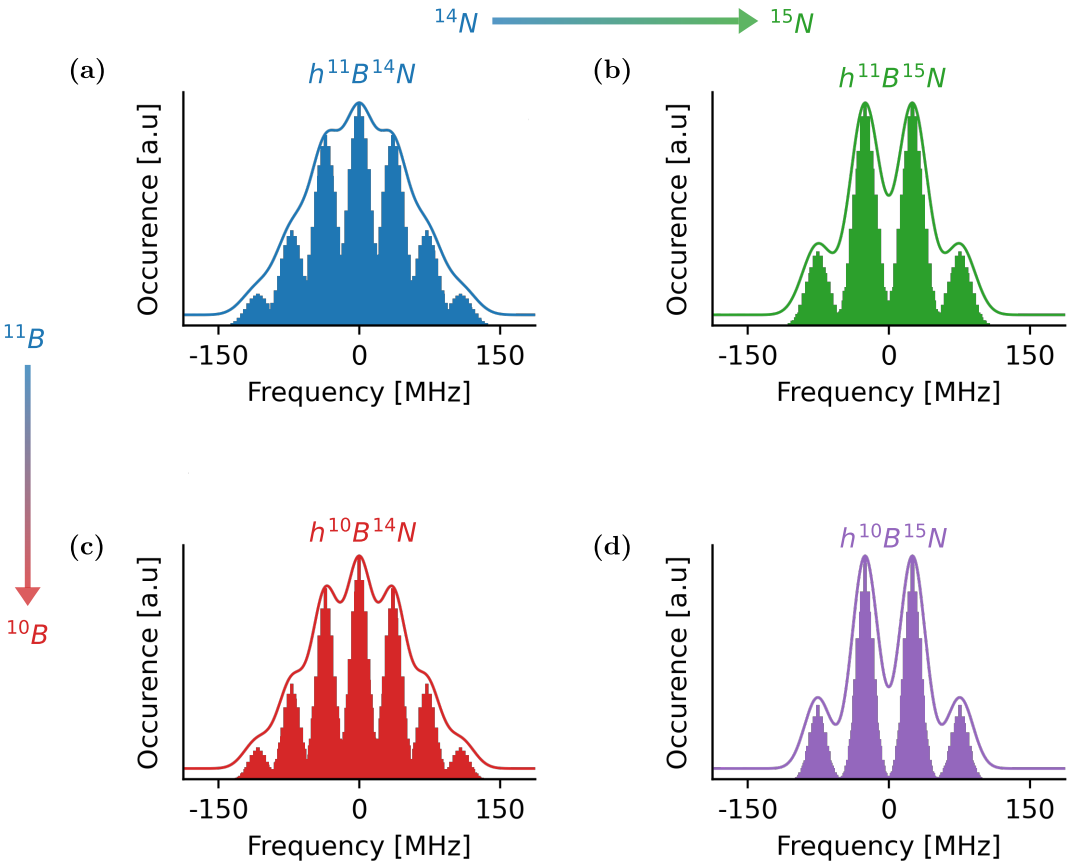


**Figure 3.7:** Simulations of the $V_B^-$ center hyperfine structure in the four isotopic configurations. (a-d) Histograms of the hyperfine levels in a given electronic spin resonance ($m_s \neq 0$). The simulation details are given in the main text.

contribute to the unresolved hyperfine manifold. Unlike the boron case, the reduced number of nuclear spin states in $^{15}$N compensates for its larger gyromagnetic ratio, resulting in a slightly more compact hyperfine structure. However, this effect is weak, less than 4%, and therefore difficult to demonstrate experimentally.

### 3.2.4 Discussion

Starting from a broad and unresolved hyperfine structure in $h^{11}B^{14}N$, we have engineered the nuclear spin environment of the $V_B^-$ centers to produce a far simpler ODMR spectrum, reduced to just four well-resolved peaks in $h^{10}B^{15}N$. This outcome carries direct and concrete implications for sensing experiments.

In basic sensing experiments based on continuous ODMR spectroscopy, the sensitivity scales inversely with the linewidth $\Gamma$: a narrower resonance line yields

improved sensitivity [cf. Eq. (1.26)]. This can be intuitively understood by noting that a sharper ODMR line produces a larger PL signal drop for a given magnetic-field variation, i.e., a larger derivative with respect to magnetic field. With natural hBN, the hyperfine structure cannot be properly resolved within a reasonable acquisition time, as a consequence the ODMR spectrum is typically fitted with a single Gaussian function, yielding a broad linewidth of $\Gamma \approx 200$ MHz [113, 150, 151]. In contrast, with $h^{10}B^{15}N$ the hyperfine peaks are well resolved, and each electronic branch can now be fitted with four individual Gaussian functions. In this case, one can reasonably argue that the relevant linewidth for the sensitivity is that of a single hyperfine peak, only $\Gamma \approx 45$ MHz. This corresponds to a static magnetic-field sensitivity enhancement by nearly a factor of four.

Furthermore, if purification with $^{10}B$ and $^{15}N$ yields a narrower inhomogeneous broadening, one can readily expect the spin-echo coherence time to be enhanced as well. This is precisely what ab initio calculations predict: an improvement factor of 1.25 when going from $^{11}B$ to $^{10}B$, and a factor of 2 when going from $^{14}N$ to $^{15}N$, resulting in a nuclear-spin-limited $T_2$ of nearly 200 ns in $h^{10}B^{15}N$ [124, 180]. These predictions have already been verified experimentally [124, 181]. In this manuscript, I postpone $T_2$ measurements of $V_B^-$ centers in $h^{10}B^{15}N$ crystals to the next chapter.

## 3.3 Optically-induced nuclear spin polarization

Now that we have pushed the hBN lattice to its limits, no further improvement can be expected from the material side. It is therefore up to us to explore alternative paths to further optimize the sensitivity. One appealing strategy in this regard is nuclear spin polarization. Indeed, polarizing the first nitrogen shell into a single hyperfine state would concentrate the population into one hyperfine line of the ODMR spectrum, thereby increasing the contrast. Polarizing the second boron shell, although more ambitious, would additionally result in a narrowing of the linewidth.

A previous study by Gao et al. demonstrated optically-induced nuclear spin polarization, also referred to as dynamic nuclear polarization (DNP), with $V_B^-$ centers and reported a polarization of nearly 50% of the first nitrogen shell [182]. However, their sample was not isotopically purified, making the quantitative estimation

of nuclear polarization uncertain. In this section, we therefore take advantage of the well-resolved hyperfine structure of $h^{10}B^{15}N$ to refine the analysis, yielding a more modest estimate of the nuclear spin polarization ($\sim 30\%$)[§ 3.3.1]. To account for the observed behavior, we then introduce a toy model of the optically-induced nuclear spin polarization process. Already rich in physical insight, this simplified approach allows us to tentatively identify the origin of the modest nuclear spin polarization efficiency [§ 3.3.2]. Finally, we examine the magnetic-field dependence of the polarization, comparing experimental data with a simulation, and gain further understanding of its underlying driving mechanism[§ 3.3.3]. The experimental work was carried out by myself and Théo Rastoin, a Master's intern. The Lindblad-based simulations, shown in the last section, was performed by Alrik Durand, a former postdoctoral fellow of the team.

### 3.3.1 Experimental observation

Optically pumped nuclear spin polarization is relatively straightforward to implement experimentally. One only needs a magnetic field aligned with the defect's quantization axis and sufficiently strong optical power. To begin, we fix the magnetic field at $B_z = 90$ mT and record a series of ODMR spectra on the $|m_s = +1\rangle$ electronic branch while progressively increasing the optical power. Representative examples are shown in Figures 3.8(a–d).

In these data, one readily observes a distortion of the ODMR lineshape as the optical power increases. More precisely, the hyperfine peaks associated with positive nuclear spin projections ($m_I = +1/2$ and $m_I = +3/2$) become more pronounced, while those associated with negative projections appear less contrasted. This is a clear signature of the optical pumping of the first nitrogen shell. We also note the absence of linewidth narrowing, indicating that the boron shell remains unpolarized.

A reader familiar with the literature may notice that the pumping appears to occur on the opposite hyperfine peaks compared to the previous work of Gao et al. [182]. This difference simply arises from the negative sign of the $^{15}N$ gyromagnetic ratio, which reverses the hyperfine state ordering within a given electron spin resonance. Ultimately, however, both cases correspond to polarization into the nuclear spin with higher spin projection.

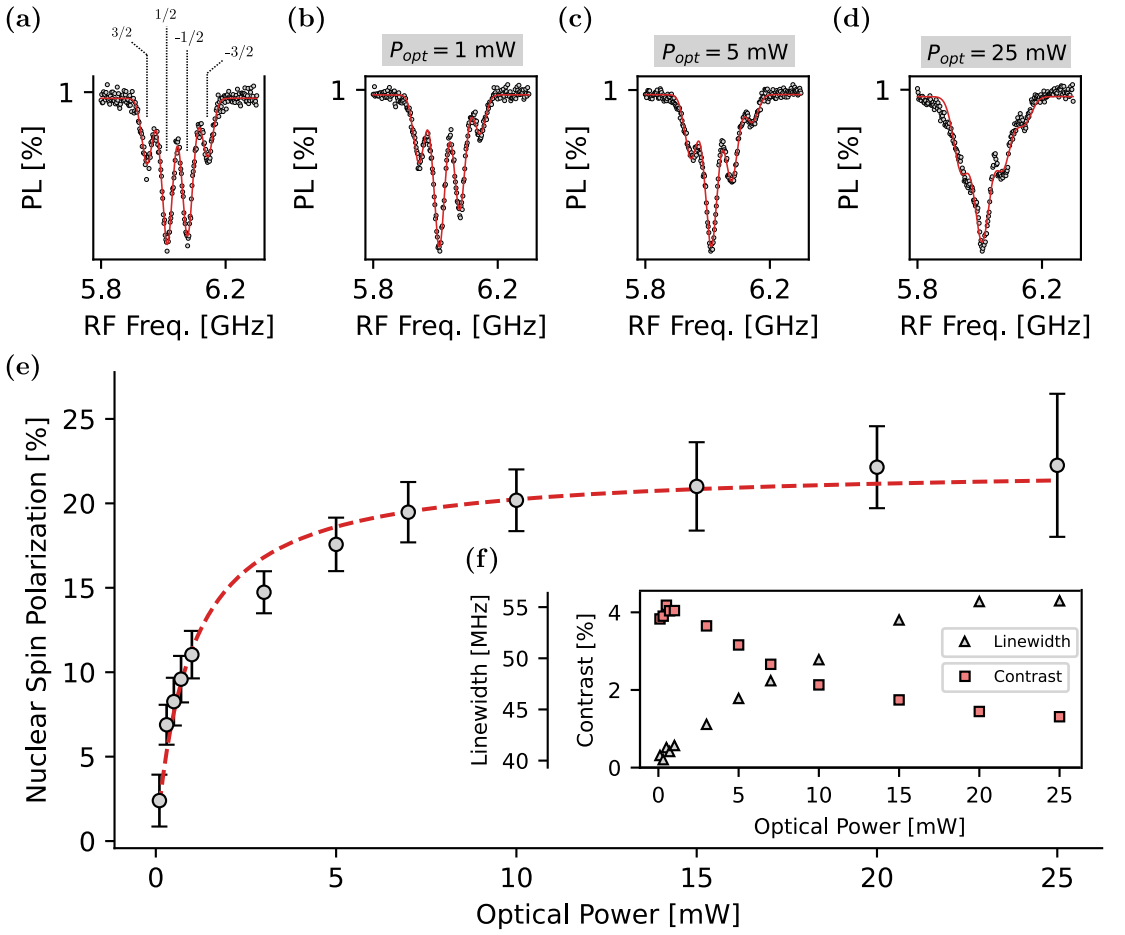


**Figure 3.8:** Optically-induced nuclear spin polarization. (a–d) ODMR spectra of the $|m_s = +1\rangle$ electron spin resonance recorded under a magnetic field of $B_z$ =90 mT and optical powers of (a) 500 µW, (b) 1 mW, (c) 5 mW, and (d) 25 mW. (e) Nuclear spin polarization as a function of optical power, extracted by fitting each ODMR spectrum with four Gaussian functions and applying Equation (3.3). The uncertainty of each data point is obtained by propagating the fitting errors on the Gaussian amplitudes. The red dotted line represents a fit using the saturation model of Equation (3.10), yielding $\mathcal{P}\text{max} = 22.1(6)\%$ and $\mathcal{P}\text{sat} = 0.96(1)$ mW. (f) ODMR spectrum linewidth (grey triangles) and contrast (red squares) as a function of the optical power.

To be quantitative, each ODMR spectrum is fitted with four Gaussians functions in order to extract the relative amplitudes of the hyperfine transitions, $\mathcal{A}_{m_I}$, which, to first approximation, are proportional to the populations of the corresponding nuclear spin states. The nuclear polarization is then defined as [182]:

$$\mathcal{P}_{DNP} = \frac{\sum m_I \mathcal{A}_{mI}}{3/2 \sum \mathcal{A}_{mI}} \times 100 \tag{3.3}$$

With this definition, the polarization is 0% when there is as much population in $m_I = +3/2$ ($m_I = +1/2$) than in $m_I = -3/2$ ($m_I = -1/2$), and reaches 100% when all the population resides in the $m_I = +3/2$ hyperfine state. The evolution

of $\mathcal{P}_{DNP}$ with optical power, $P_{opt}$, is shown in Figure 3.8(e). Starting near 0% at low power, the polarization gradually increases and appears to saturate at around 20%. Interestingly, the data are well described by a saturation-like equation,

$$\mathcal{P}_{DNP}(P_{opt}) = \mathcal{P}_{DNP}^{max} \frac{1}{1 + \frac{P_{sat}}{P_{opt}}}, \tag{3.4}$$

with $\mathcal{P}_{DNP}^{max}$ the nuclear spin polarization at saturation and $P_{sat}$ the characteristic saturation power. We obtain $\mathcal{P}_{DNP}^{max} = 22.1(6)\%$ and $P_{sat} = 0.96(1)$ mW. These results are in good agreement with the behavior observed by Gao et al., though our polarization efficiency is weaker (10 % less for this given field). In any cases, a nuclear spin polarization of $\sim 20 - 30\%$ lies far from the $\sim 100\%$ obtained with the exact same technique with the $NV^-$ center in diamond [176, 183, 184] or divacancies in SiC [177]. The potential gain in sensitivity is further tempered by an overall degradation of the ODMR spectrum quality with increasing optical power. As shown in Figure 3.8(f), the contrast decreases by more than 50%, while the linewidth of an individual hyperfine resonance broadens by $\sim 15$ MHz. These effects are well known in the community of optically active spin defects [146]. In continuous ODMR spectroscopy, RF and optical excitations compete: the laser polarizes the spin in $|m_s = 0\rangle$ while the RF drive transfer the populations toward $|m_s = \pm 1\rangle$ . As a result, an excessive optical pumping rate hampers RF-driven transitions and reduces the contrast. In addition, a high pumping rate reduces the effective lifetime of the ground state. Once this lifetime becomes shorter than the inhomogeneous coherence time $T_2^*$, the ODMR linewidth becomes lifetime-limited and exhibits power broadening. It is worth noting, though, that a pulsed ODMR scheme, in which optical and RF excitations are temporally separated, could be employed to mitigate both issues. Nonetheless, given the modest level of nuclear spin polarization, one could only expect an improvement in sensitivity of a few tens of percent.

### 3.3.2 Toy model

To understand the mechanism behind DNP, we now introduce a simple toy model, initially developed for the $NV^-$ center in diamond [176]. We consider a $V_B^-$ center coupled to a single $^{15}N$ nuclear spin $I = \frac{1}{2}$ through the hyperfine interaction, yielding the Hamiltonian:

$$\hat{\mathcal{H}} = D\hat{S}_z^2 + |\gamma_e|\hat{S}_z B_z + \hat{\mathbf{S}} A \hat{\mathbf{I}}. \tag{3.5}$$

So far, we have worked within the secular regime, where the Zeeman and zero-field-splitting (ZFS) terms dominate over the hyperfine interaction. To understand the mechanism behind DNP, it is however necessary to go beyond this approximation. This can be achieved by applying a magnetic field $B_z$ such that the Zeeman and ZFS terms compensate each other, that is, by reaching a level anticrossing (LAC) [cf. Chap. 2]. Near these specific points, the secular approximation no longer holds, and the full hyperfine tensor must be taken into account. The hyperfine tensor $A$ is a $3 \times 3$ matrix, but in our case, the $x, y$ plane can be defined such that $A$ becomes diagonal [80]. Under this condition, the hyperfine Hamiltonian reduces to three distinct terms:

$$\mathcal{H}_{\text{hyp}} = \hat{\mathbf{S}} A \hat{\mathbf{I}} \tag{3.6}$$

$$= A_{xx}\hat{S}_x\hat{I}_x + A_{yy}\hat{S}_y\hat{I}_y + A_{zz}\hat{S}_z\hat{I}_z. \tag{3.7}$$

While the last term is our familiar secular term, producing the hyperfine structure, the first two terms do not commute with $\hat{S}_z$ or $\hat{I}_z$ and thus do not preserve the $z$-axis as either the electronic or nuclear quantization axis. As a result, they can drive electron–nuclear spin flip-flops. This becomes clearer when one express Equation (3.7) as a function of the electronic and nuclear spin ladder operators,

$$\hat{S}_\pm = \frac{1}{\sqrt{2}}(\hat{S}_x \pm i\hat{S}_y),$$

$$\hat{I}_\pm = \frac{1}{\sqrt{2}}(\hat{I}_x \pm i\hat{I}_y).$$

In this case, one obtain

$$A_{xx}\hat{S}_x\hat{I}_x + A_{yy}\hat{S}_y\hat{I}_y = (\frac{A_{xx}+A_{yy}}{4})[\hat{S}_+\hat{I}_- + \hat{S}_-\hat{I}_+] + (\frac{A_{xx}-A_{yy}}{4})[\hat{S}_+\hat{I}_+ + \hat{S}_-\hat{I}_-] \tag{3.8}$$

$$= A_+[\hat{S}_+\hat{I}_- + \hat{S}_-\hat{I}_+] + A_-[\hat{S}_+\hat{I}_+ + \hat{S}_-\hat{I}_-], \tag{3.9}$$

where we have defined $A_+ = \frac{A_{xx}+A_{yy}}{4}$ and $A_- = \frac{A_{xx}-A_{yy}}{4}$. In this form, one can readily see that the non-secular hyperfine terms generate two distinct processes:

electron-nuclear spin flip-flop through $A_+$, and electron-nuclear spin flip-flip through $A_-$. Thanks to these terms it becomes possible to transfer the electron spin polarization, obtained by optical pumping, to the nuclear spin. This is the principle of optically-induced nuclear spin polarization.

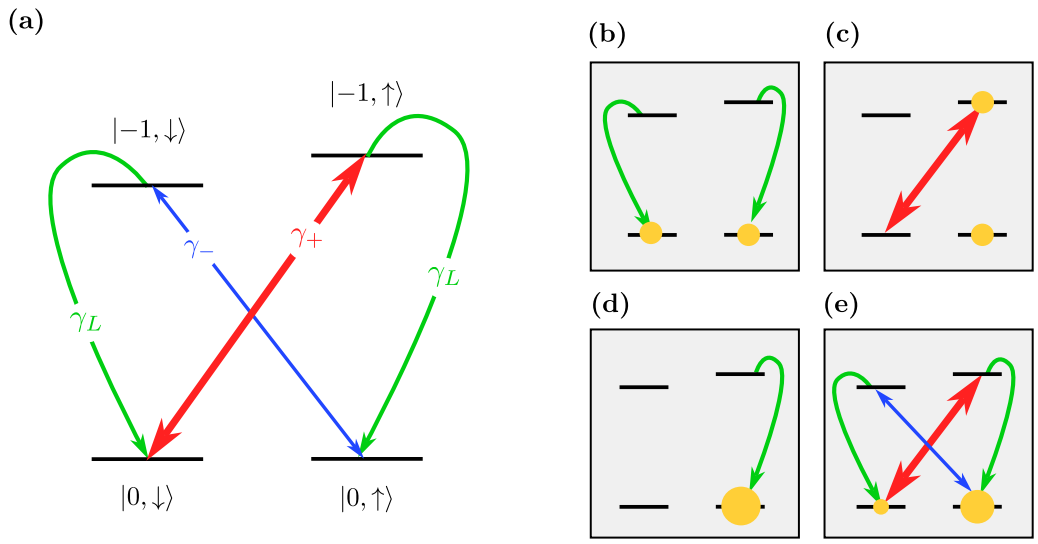


**Figure 3.9:** Model of optically-induced nuclear spin polarization. (a) Four-level model. All notations are defined in the main text. (b-e) Step-by-step illustrations of the nuclear spin polarization.

Since the non-secular regime is reached only for the lower electronic resonance $|m_s = -1\rangle$, the $|m_s = +1\rangle$ resonance remaining far from the LAC, one can reduce the system to an effective four-dimensional Hilbert space:

$$\{|0,\uparrow\rangle, |0,\downarrow\rangle\ , |-1,\uparrow\rangle\ , |-1,\downarrow\rangle\},$$

where the number $\{0, 1\}$ denotes the electron spin projection and the arrow the nuclear spin projection. These four levels are illustrated in Figure 3.9. Because of the hyperfine interaction, these states are not eigenstates of the Hamiltonian given in Equation (3.5). As a result, the hyperfine coupling can mediate transitions between them. The first mechanism corresponds to an electron–nuclear spin flip-flop, therefore it couples $|0,\downarrow\rangle$ with $|-1,\uparrow\rangle$. We describe this process by a bidirectional rate $\gamma_+$, proportional to $A_+$. The second mechanism is an electron–nuclear spin flip-flip, coupling $|0,\uparrow\rangle$ with $|-1,\downarrow\rangle$. It is represented by a bidirectional rate $\gamma_-$, proportional to $A_-$. Finally, we include the optical pumping process, on which the entire mechanism relies. Since the excited state is not explicitly included in

this simplified model, we consider an effective pumping rate $\gamma_L$, which transfers population from the $|-1\rangle$ to the $|0\rangle$ electron spin manifold, while preserving the nuclear spin projection.

With this model, we can now understand the principle of optically induced nuclear spin polarization. The first step is achieved by the optical pumping rate, which polarizes the electron spin in $|0\rangle$ [Fig. 3.9(b)]. Then the hyperfine-mediated flip-flop rate $\gamma_+$ transfers the populations from $|0,\downarrow\rangle$ into $|-1,\uparrow\rangle$ [Fig. 3.9(c)]. The latter are then bring back to the $|0\rangle$ electron spin manifold through the optical pumping rate $\gamma_L$ [Fig. 3.9(d)]. Starting from an unpolarized nuclear spin, we successfully polarized it into the state $|\uparrow\rangle$. At this stage, the reader may argue that the electron–nuclear spin flip-flip process, mediated by $\gamma_-$, acts as a depolarization channel [Fig. 3.9(e)]. This is indeed correct. However, in general, $A_+ \gg A_-$ (and consequently $\gamma_+ \gg \gamma_-$), so that a nuclear spin polarization can still build when the optical pumping rate $\gamma_L$ compensates the depolarizing rate $\gamma_-$.

More formally, one can solve the steady-state rate equations associated with the four-level model of Figure 3.9 to obtain the nuclear spin polarization $\mathcal{P}_\uparrow$ in $|0,\uparrow\rangle$:

$$\mathcal{P}_\uparrow = \mathcal{P}_{max} \cdot \frac{1}{1+\frac{\mathcal{P}_{sat}}{\gamma_L}}, \tag{3.10}$$

with,

$$\mathcal{P}_{max} = \frac{|\gamma_+ - \gamma_-|}{|\gamma_+ + \gamma_-|} = \frac{|A_+ - A_-|}{|A_+ + A_-|}. \tag{3.11}$$

Hence, as observed experimentally [cf. Fig. 3.8], the nuclear spin polarization is predicted to follow a saturation law. Furthermore, the model reveals an interesting insight: as soon as $A_- \neq 0$ ($\gamma_- \neq 0$), the maximum achievable nuclear spin polarization can never reach 100 %. Taking the ab-initio values of the hyperfine tensors, extracted from Ref. [80], Equation (3.11) predicts a maximum polarization $\mathcal{P}_{max} \approx 50\%$. Although the prediction remains higher than the measured value, it gives us an explanation to account for the modest nuclear spin polarization obtained. While other spin defects in 3D materials commonly verify $A_- = 0$ [185], the hyperfine tensor of the $V_B^-$ center does not, directly yielding a lower nuclear spin polarization efficiency.

## Tentative Explanation

We now tentatively propose an explanation by comparing the $V_B^-$ center in hBN with the $NV^-$ center in diamond. The components of the hyperfine tensor directly reflect the symmetry of the system. Achieving $A_- = 0$, i.e., $A_{xx} = A_{yy}$, requires axial symmetry around the $z$ axis, which corresponds to a rotational symmetry of at least $\frac{2\pi}{3}$. Both defects nominally satisfy this condition. However, for the hyperfine tensor, not only the electronic spin density but also the nuclear positions contribute. Figure 3.10 illustrates the difference between the two defects at this specific regard. In the $NV^-$ center, the nitrogen atom lies along the defect's main symmetry axis, resulting in an axially symmetric hyperfine tensor that fulfills $A_{xx} = A_{yy}$. In contrast, for the $V_B^-$ center, the neighboring nitrogen atoms are located in-plane and displaced from the main symmetry axis, which breaks the condition and leads to $A_{xx} \neq A_{yy}$.

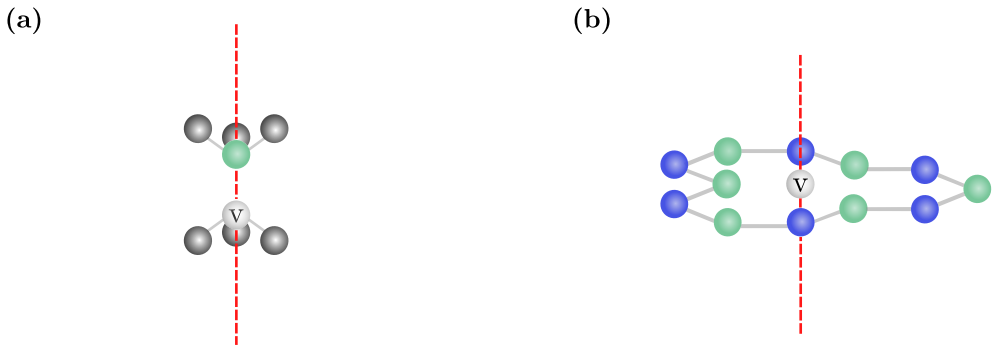


**Figure 3.10:** Axial symmetry of the $V_B^-$ center in hBN and $NV^-$ center in diamond. Illustration of the $NV^-$ center (a) and $V_B^-$ center (b). The main symmetry axis of each defect is indicated by a red dashed line.

Nonetheless, it should be noted that in a three-dimensional crystal, the hyperfine tensor of a nucleus located off the main symmetry axis of the defect can still exhibit axial symmetry along another local axis and therefore satisfy $A_{xx} = A_{yy}$. This is the case, for instance, for $^{13}C$ nuclei in diamond for which one can as well reach a high polarization through DNP mediated by the $NV^-$ center [186]. In contrast, a lamellar crystal such as hBN exhibits lower overall symmetry, and apart from the out-of-plane $z$ axis, no other axial symmetry can be found. Importantly, this argument suggests that all spin defects hosted in van der Waals materials are likely to suffer from the same intrinsic limitation.

### 3.3.3 Magnetic field dependence

As the non-secular hyperfine terms become effective only in the vicinity of level anti-crossings (LACs), the DNP process is inherently sensitive to the magnetic field. It remains, nonetheless, unclear whether the ground-state LAC (GSLAC) or the excited-state LAC (ESLAC) plays the dominant role. While it would be reasonable to expect that most of the nuclear spin polarization occurs in the ground state due to its longer lifetime, the report by Gao et al. instead suggests that the ESLAC governs the DNP over a wide range of magnetic fields [182]. To clarify this point, the final subsection of this chapter is dedicated to investigating the magnetic-field dependence of the DNP mechanism.

#### Magnetic Field Alignment

For this study, it is crucial to ensure proper alignment of the magnetic field along the $z$ axis. Any misalignment introduces Zeeman terms $\propto \hat{S}_x, \hat{S}_y$, which contribute to the depolarizing rate and reduce the achievable nuclear spin polarization. To demonstrate this effect, I intentionally misalign the field and measure the nuclear spin polarization as a function of the angle $\theta$ between the field and the $z$ axis. To do so, I keep the distance between the sample and the magnet fixed, and laterally displace the magnet. For each displacement, I first record ODMR spectra of both electronic branches. From their central frequencies, $f_-$ and $f_+$, the magnetic field angle $\theta$ can be extracted using the relations given in Refs. [163, 164]. Then, I set the optical power to 10 mW and measure the resulting nuclear spin polarization. The corresponding data are plotted in Figure 3.11.

After only a few degrees of misalignment, the nuclear spin polarization vanishes, and the ODMR spectrum recovers a symmetric lineshape [Fig. 3.11(b,c)]. Consequently, for all subsequent field-dependent measurements, we systematically start by measuring $f_-$ and $f_+$ and verify that $\theta = 0$ within the errorbars. Near the GSLAC, however, $f_-$ cannot be extracted. In that case, the magnet position is instead optimized by maximizing the PL signal, leveraging the PL magnetic-field dependence discussed in Chapter 2.

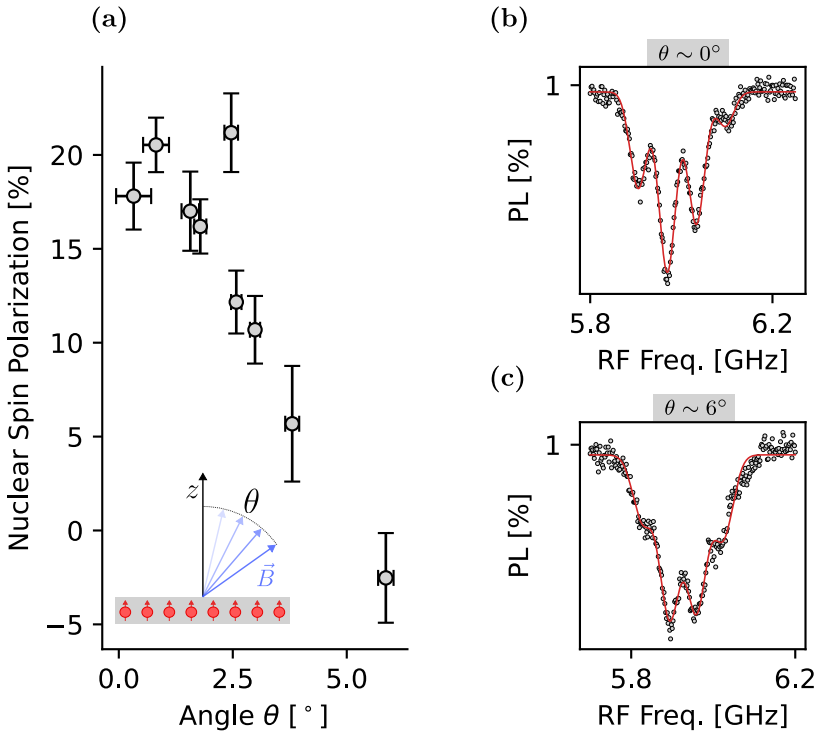


**Figure 3.11:** Magnetic-field alignment and nuclear spin polarization. (a) Nuclear spin polarization as a function of the angle $\theta$ between the defect quantization axis and the magnetic field. The angle $\theta$ is extracted from the upper and lower resonance frequencies of the $V_B^-$ center ODMR spectrum (see main text). (b,c) ODMR spectra of the upper electronic branch recorded at $|B| = 90$ mT under an optical power of 10 mW for (b) $\theta \approx 0°$ and (c) $\theta \approx 6°$.

## DNP versus Magnetic Field

We set the optical power to 10 mW in order to saturate the nuclear spin polarization, while minimizing the degradation of both the ODMR spectrum contrast and linewidth [cf. Fig. 3.8(f)]. The nuclear spin polarization is then measured as the magnet is gradually brought closer to the sample. The resulting dataset is plotted in Figure 3.12.

As expected, the DNP remains low far from the LACs and gradually builds up as the magnetic field increases. At the ESLAC, a polarization of nearly 17% is obtained, while it reaches approximately 30% at the GSLAC. These results confirm that the nuclear spin polarization mechanism is driven by non-secular hyperfine terms, which become effective only near the LACs. Moreover, they suggest that the GSLAC exerts a stronger influence than the ESLAC. To gain further insight into this behavior, we now turn to simulations.

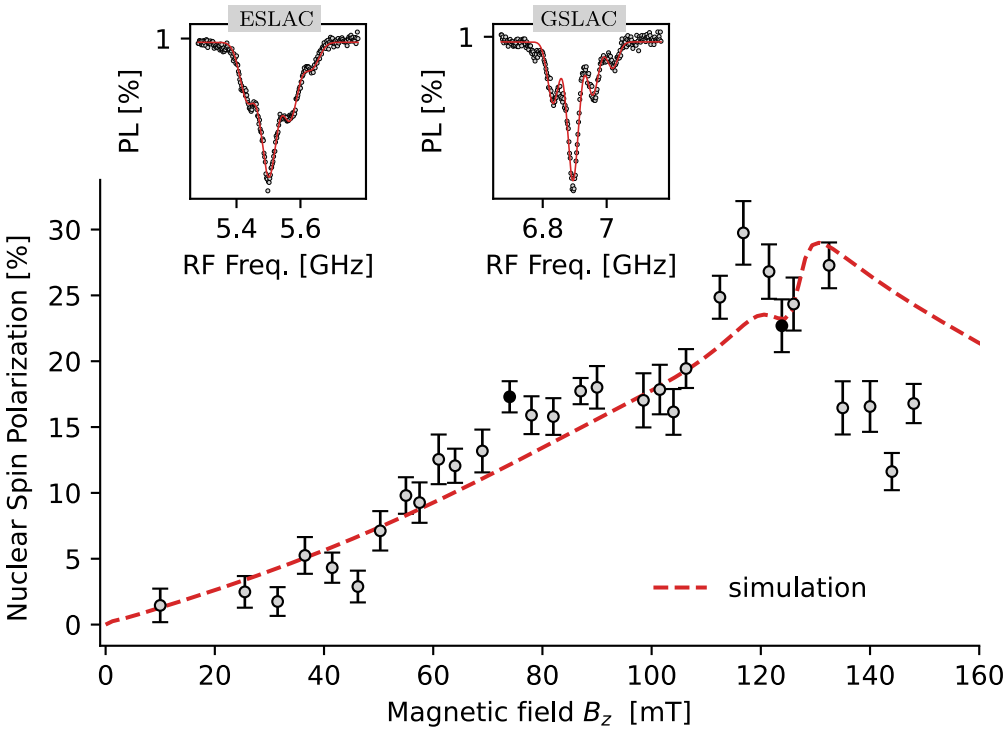


**Figure 3.12:** Magnetic-field dependence of optically-induced nuclear spin polarization. Nuclear spin polarization as a function of the magnetic field $B_z$. For each field value, an ODMR spectrum of the upper electron spin resoanance is recorded under an optical power of 10 mW. The nuclear spin polarization is extracted by fitting the data with four Gaussian functions and applying the definition given in Equation (3.3). The two black dots indicate the ESLAC and GSLAC field values, for which the corresponding ODMR spectra are shown in the insets. The red dashed line represents the Lindbladian simulation.

A first option would be to adopt a rate-equation model similar to the one presented in Chapter 2, but extended to include the hyperfine states. Unfortunately, the Python code I developed was not designed to scale efficiently to such a high-dimensional Hilbert space. Instead, Alrik Durand, a former PhD student and postdoctoral fellow of the team, implemented a simulation based on the widely used Lindblad master-equation formalism. The Lindblad master equation can be viewed as a generalization of the Schrödinger equation that incorporates relaxation and decoherence processes through so-called jump operators. It can be written as:

$$\frac{d\rho}{dt} = -\frac{i}{\hbar}\left[\hat{\mathcal{H}}, \rho\right] + \sum_k \left(\hat{L}_k \rho \hat{L}_k^\dagger - \frac{1}{2}\left\{\hat{L}_k^\dagger \hat{L}_k, \rho\right\}\right) \tag{3.12}$$

where $\rho$ is the density matrix, $\hat{\mathcal{H}}$ the Hamiltonian, and $\hat{L}_k$ the jump operators. The Hamiltonian includes the axial ZFS, the electronic and nuclear Zeeman terms, as well as the hyperfine interaction with the three nearest-neighbor nitrogen atoms,

for both the GS and ES. The hyperfine tensors are taken from Ref. [182]. The three subspaces are connected through optical pumping and intersystem crossing (ISC) rates, both included as jump operators. Since this work preceded the study of the photodynamics presented in Chapter 2, we adopted parameter values from the literature [107, 156, 182]. Additionally, we account for a spin relaxation time of $T_1 = 15$ µs and a coherence time of $T_2 = 50$ ns in the GS, while both are neglected in the ES due to its short lifetime. It is worth noting that the computational cost is significantly reduced when working with $^{15}$N, owing to the smaller Hilbert space, $2^3 = 8$ states per electron spi resonance for $^{15}$N, compared to $3^3 = 27$ for $^{14}$N. The resulting simulated curve is plotted alongside the experimental data as a red dashed line.

An overall good agreement is obtained between the simulation and the experimental data, with the maximum polarization of approximately 30% being especially well reproduced. Interestingly, the simulation reveals that most of the polarization originates from the GSLAC, even well away from the exact crossing field at 124 mT. Enhancing the contribution from the ESLAC would require optical powers beyond a reasonable range. This behavior can be readily explained by the short lifetime of the ES, which limits the number of nuclear spin flip-flops occurring in that state. This is somewhat unfortunate, since the hyperfine components are actually more favorable in the ES, i.e., the $A_-$ term is smaller. Importantly, even near the GSLAC, the DNP does not exceed 30%, whereas Gao et al. reported values up to 60%. This discrepancy cannot arise, at least directly, from the isotopic content difference, since the hyperfine tensor scales linearly with the nuclear gyromagnetic ratio, making the $A_+$ and $A_-$ terms isotope-independent. Instead, we conclude that isotopic purification in h$^{10}$B$^{15}$N simply improves the resolvability of the hyperfine structure, allowing a more accurate Gaussian fit and, consequently, a lower, yet more reliable, estimate of the nuclear spin polarization.

## 3.4 Conclusion

In this work, we explored strategies to mitigate the impact of the dense lattice nuclear spin bath on the magnetic field sensitivity of the $V_B^-$ center. We first investigated isotopic engineering by characterizing the four possible isotopic configurations of hBN: h$^{11}$B$^{14}$N, h$^{10}$B$^{14}$N, h$^{11}$B$^{15}$N, and h$^{10}$B$^{15}$N. By examining

the hyperfine structure through ODMR spectroscopy, we unambiguously identified $h^{10}B^{15}N$ as the most favorable configuration for sensing applications, owing to its well-isolated and sharper hyperfine lines. We estimated the gain in sensitivity to be roughly a factor of four. This study thus completed a key line of investigation initiated by Angela Haykal and Rana Tanos, former PhD students of the team, who first examined the influence of boron isotopes in 2022 [124].

Taking advantage of the well-resolved hyperfine structure of $h^{10}B^{15}N$, we then investigated optically-induced nuclear spin polarization. Previously demonstrated in natural hBN, we reproduced these results while refining the analysis. Our measurements reveal a modest nuclear spin polarization of up to 30%, implying a limited potential gain in magnetic-field sensitivity. We further identified the origin of this limited polarization as a symmetry constraint, likely to affect all spin defects in van der Waals materials. Lastly, by characterizing the magnetic-field dependence of the DNP process, and identified the GSLAC as the main source of nuclear spin polarization at room temperature.

## Literature

Two other groups studied isotopic purification in parallel with us and reached the same conclusions [181, 187]. Furthermore, working on the exact same sample as ours, Gong et al. demonstrated that purification with $^{10}B$ and $^{15}N$ not only leads to sharper ODMR lines but also enhances the spin-echo coherence time [181], in agreement with theoretical predictions [180].

Regarding DNP, Ru *et al.*, working with natural hBN, also reported a maximum polarization of about 30%. Their use of a pulsed-ODMR scheme may have improved the accuracy of the quantitative estimate. More recently, Nakamura *et al.* conducted an in-depth investigation of DNP and reached conclusions consistent with ours, particularly concerning the limitations of the process and the predominant role of the GSLAC [188].

## Prospects

This work could pave the way for several future investigations. One immediate direction would be to explore DNP at cryogenic temperatures. With the slightly

longer ES lifetime expected at low temperature, the ESLAC could, in principle, contribute more significantly to nuclear spin polarization than at room temperature. A recent study, however, reported preliminary DNP measurements at 4K and observed no improvement [110].

Alternatively, one could explore other nuclear spin polarization techniques, such as selective RF pulses [175], Hartmann–Hahn cross-polarization [189, 190], double-resonance–mediated nuclear spin polarization [191], RF-driven relaxation–assisted polarization transfer [192–194], or cross-polarization–induced polarization [195], among others. It should be noted, however, that most of these schemes are not compatible with continuous ODMR spectroscopy.

# 4 Neutron irradiation for $V_B^-$ centers generation

## Outline


**3.1 Isotopic purification of hBN . . . . . 98**

3.1.1 Metal-flux growth of bulk monoisotopic hBN crystals . . . 98

3.1.2 Raman characterization . . . . . 99

3.1.3 Nitrogen ion implantation . . . . . 101

**3.2 ODMR spectroscopy of the $V_B^-$ center in isotopically purified hBN flakes . . . . . 101**

3.2.1 From $^{14}$N to $^{15}$N isotope . . . . . 103

3.2.2 From $^{11}$B to $^{10}$B isotope . . . . . 105

3.2.3 Simulations of the $V_B^-$ center hyperfine Structure . . . . . 105

3.2.4 Discussion . . . . . 107

**3.3 Optically-induced nuclear spin polarization . . . . . 108**

3.3.1 Experimental observation . . . . . 109

3.3.2 Toy model . . . . . 111

3.3.3 Magnetic field dependence . . . . . 116

**3.4 Conclusion . . . . . 119**


After optimizing the material properties in the previous chapter, the next step is to optimize the defect engineering process. In the developing process of our sensor, identifying the irradiation conditions that maximize sensitivity is crucial. Yet, our objective is not merely to create $V_B^-$ centers, but to do so within *atomically-thin* hBN flakes, i.e few-layer thick, where proximity to the sample could offer a distinct advantage. Starting from a bulk crystal, as in our case, two different strategies can be envisioned.

The first approach is the one we have followed so far: exfoliate the bulk crystal first, and then perform ion implantation. Although effective, this method presents

several challenges. Once irradiated, the flakes become difficult to handle, for reasons that remain unclear, which complicates the assembly of vdW heterostructures. Furthermore, irradiating atomically thin samples represents a new frontier for the ion implantation community, and the optimal parameters for vacancy creation in an atomically-thin material are still unknown. Most likely for this reason, the formation of $V_B^-$ centers in atomically thin flakes, through ion implantation, has not been reported yet. While we continue to regard ion implantation as a promising technique, we explored in parallel an alternative route: neutron irradiation.

In contrast to ion implantation, neutron irradiation produces a homogeneous defect distribution throughout the crystal depth, allowing the process to be performed directly on bulk crystal. The irradiated crystal can then be exfoliated at will to obtain thin flakes containing $V_B^-$ centers already embedded within the lattice. By creating the defects prior to exfoliation, this approach circumvents the aforementioned challenges encountered with ion implantation. In this chapter, we investigate this strategy in detail.

We begin this chapter by introducing the basic principles of neutron irradiation [§ 4.1]. In contrast to ion implantation, which relies on ballistic scattering, neutron irradiation also involves a more exotic mechanism: nuclear transmutation, which deserves to be discussed. We then present a first batch of neutron-irradiated samples, demonstrate the occurrence of nuclear transmutation, and examine the evolution of the orthorhombic zero-field splitting parameter $E$ with irradiation time. In a second batch [§ 4.2]. we characterize the optical and spin properties of the $V_B^-$ centers as a function of irradiation time, identifying the sample that offers the best compromise for sensing applications [§ 4.3]. Finally, we investigate whether neutron irradiation can be used to embed $V_B^-$ centers in atomically thin hBN flakes [§ 4.4].

## 4.1 Working principle of neutron irradiation: a $^{10}$B advantage

When discussing neutron irradiation, it is important to distinguish between thermal and fast neutrons. The distinction between both lies in their respective kinetic energies. The exact boundary is not well defined in the literature, here, we consider neutrons with an energy lower than 0.5 eV as thermal neutrons, and the rest as

high-energy (fast) neutrons. Because of this kinetic energy difference, both do not interact with the hBN lattice through the same mechanisms. Indeed, the energy required to displace an atom from its lattice site in hBN, the so-called displacement threshold, lies on the order of a few tens of electronvolts [196–198]. Therefore, in contrast to high energy neutrons or to the 30 keV nitrogen ions used so far, thermal neutrons are not energetic enough to create vacancies through direct knock-on collisions. Instead, they interact with the crystal lattice through another mechanism: nuclear transmutation.

Nuclear transmutation occurs when a nucleus captures a neutron and transmutes into another nuclear specie. The probability for a given nucleus to capture a thermal neutron is determined by its cross section $\sigma$, expressed in barns. On one hand, the thermal neutron capture cross sections of $^{14}$N and $^{11}$B are relatively modest, about 5 millibarns and 1.8 barns, respectively. On the other hand, the cross section of $^{10}$B is colossal, $\sigma \sim 3890$ barns, ranking among the largest in the periodic table [199, 200]. This exceptional value even makes $^{10}$B one of the most promising constituents for neutron-detector fabrication [201–203].

When a $^{10}$B atom captures a neutron, it transmutes into a $^{7}$Li atom and an alpha particle ($^{4}$He). Two reaction channels can occur:

$$^{10}\mathrm{B} + \mathrm{n} \rightarrow {}^{7}\mathrm{Li}(1.01\mathrm{MeV}) + {}^{4}\mathrm{He}(1.78\mathrm{MeV}), \tag{4.1}$$

$$^{10}\mathrm{B} + \mathrm{n} \rightarrow {}^{7}\mathrm{Li}(0.84\mathrm{MeV}) + {}^{4}\mathrm{He}(1.47\mathrm{MeV}) + \gamma(0.48\mathrm{MeV}). \tag{4.2}$$

In practice, the second channel dominates with a branching ratio of $\sim 94\%$ [145, 201]. Nonetheless, in both channels the kinetic energies of the Li and He fragments are more than sufficient to knock lattice nuclei out of their sites and initiate collision cascades. Thus, in the end, the defect-creation process is not so different from ion implantation, except that here, each cascade is triggered by a neutron-capture event.

The second main difference compared to ion implantation lies in the penetration depth. It is well known that ions create defects only within a narrow region whose depth is determined by the ion species and its kinetic energy. In contrast, neutrons are electrically neutral, therefore the neutron flux is not attenuated by ionization but only by scattering with the lattice and neutron capture. As a result, neutrons

can cross samples over much larger distances. Let us make a short order of magnitude estimate. Considering the large cross-section difference among lattice nuclei, we consider only $^{10}$B atoms. Given an atomic density $N_{^{10}\mathrm{B}}$, one can define a characteristic penetration depth $\Lambda = (N_{^{10}\mathrm{B}}\sigma_{^{10}\mathrm{B}})^{-1}$. The probability of neutron capture in an infinitesimal slice $\delta z$ is then independent of depth, $P = \frac{\delta z}{\Lambda}$, so that the neutron flux $\phi(z)$ follows a Beer–Lambert law:

$$\phi(z) = \phi_0\, e^{-\frac{z}{\Lambda}}, \tag{4.3}$$

with $\phi_0$ the incident neutron flux at the sample surface [201]. Taking $N_{^{10}\mathrm{B}} = 5.25 \times 10^{22}\,\mathrm{boron.cm}^{-3}$, $\sigma_{^{10}\,\mathrm{B}} = 3890\,\mathrm{barns} = 3.89 \times 10^{-21}\,\mathrm{cm}^2$, and $z = 10\mu\mathrm{m} = 10^{-3}\,\mathrm{cm}$ (the typical thickness of our bulk crystal), one obtains a transmitted fraction $\frac{\phi(10\mu\mathrm{m})}{\phi_0} \approx e^{-0.205} \approx 0.81$, i.e., an attenuation of only $\sim 19\%$. The neutron flux is thus only weakly attenuated over a 10 µm path, which means that irradiation can be performed directly on the bulk material before exfoliation. Moreover, the defect distribution can reasonably be considered homogeneous through the bulk crystal depth, so that every flake resulting from exfoliation should contain similar defects density, regardless of their thicknesses.

## 4.2 First iteration: early steps with neutron irradiation

We began this study in 2021, when isotopic purification was still limited to the boron isotope. The first batch of samples therefore consisted of h$^{11}$B$^{14}$N and h$^{10}$B$^{14}$N crystals. The neutron irradiation was carried out at the Ohio State University Research Reactor, following the procedure described in Ref. [145]. The crystals were irradiated at a reactor power of 300 kW, with a neutron flux composed of 48 % thermal neutrons ($E \lesssim 0.5$ eV) and 52 % fast neutrons ($E > 0.5$ eV). Two neutron fluences were applied to the samples: $2.6 \times 10^{16}$ n.cm$^{-2}$ and $2.6 \times 10^{17}$ n.cm$^{-2}$, where n denotes neutron. For reasons that remain unclear, the $^{11}$B sample with lowest neutron fluence proved unusable, reducing the total to three samples. Table 4.1 summarizes these three samples, indicating their isotopic composition, neutron fluence, and corresponding labels.

| Samples | Isotopic content | Neutron fluence [n/cm$^2$] |
|---|---|---|
| $S_{11}^b$ | $h^{11}B^{14}N$ | $2.6e17$ |
| $S_{10}^a$ | $h^{10}B^{14}N$ | $2.6e16$ |
| $S_{10}^b$ | $h^{10}B^{14}N$ | $2.6e17$ |

**Table 4.1:** $1st$ batch of neutron irradiated samples

Figure 4.1 shows a photograph of a pristine hBN crystal alongside a neutron-irradiated one. A clear color change can be observed, induced by the formation of color centers.

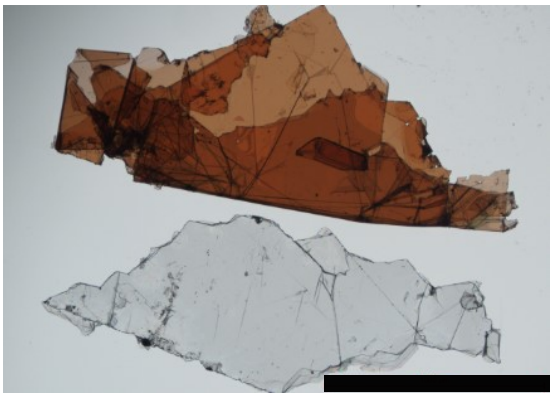


**Figure 4.1:** Photograph of pristine (bottom) and neutron-irradiated hBN (top) crystals.

The measurements presented in this section were realized by myself and Alrik Durand, while the simulations performed on the second part were once again realized by our colleagues Adam Gali and Péter Udvarhelyi, computational physicists at the Wigner Research Centre for Physics in Budapest.

### 4.2.1 Optical characterization: $^{10}$B versus $^{11}$B isotopes

As a first step, we perform photoluminescence (PL) raster scans, in which the PL signal is recorded while a 1 mW green laser spot is scanned across the sample surface. Owing to the high PL count rate, an optical density filter is inserted to attenuate the signal and protect the APDs. Figure 4.2(a) shows such a scan on the $S_{10}^a$ sample. A spatially homogeneous PL intensity is observed, confirming that neutron irradiation produces a dense ensemble of color centers. To identify the

origin of this emission, the PL signal is subsequently analyzed using a spectrometer. The spectra measured on the three samples are plotted in Figure 4.2(b). They consistently exhibit the characteristic broad emission band of the $V_B^-$ center centered around 800 nm. Apart from a small shoulder at shorter wavelengths and the $E_{2g}$ Raman peak of hBN at 573 nm [cf. Chapter 2], no additional features are observed, indicating that the PL emission is largely dominated by $V_B^-$ centers.

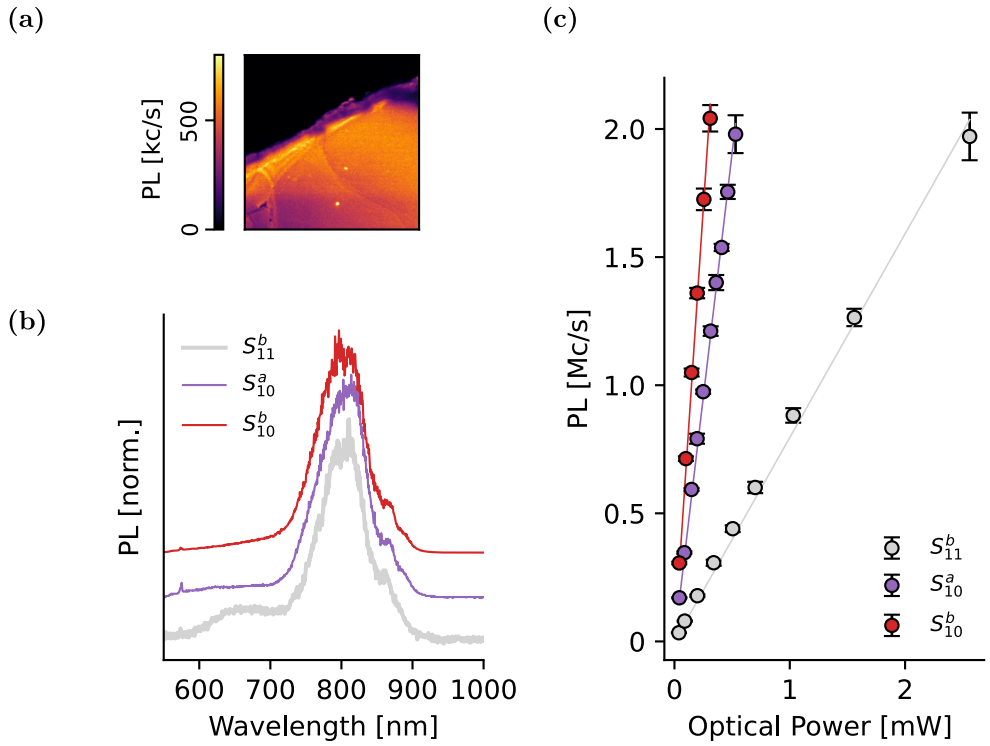


**Figure 4.2:** Optical characterization of neutron irradiated $h^{11}B^{14}N$ and $h^{10}B^{14}N$ bulk crystals. (a) PL raster scan of $S_{10}^a$ sample. (b) PL spectrums of the three neutron irradiated samples. Each PL spectrums is normalized by its maximum and artificially shifted in $y$ for an easier comparison. (c) PL signal as a function of optical power for the three neutron irradiated samples. The solid lines represent a linear fit. An optical density is used to not damage the detectors.

We now quantitatively compare the PL count rates between the three samples by measuring the PL as a function of the optical excitation power. For each power, the PL signal is measured at five different locations, and the mean value and standard deviation are taken as the PL signal estimate and its uncertainty, respectively. The resulting plots are displayed in Figure 4.2(c). For all three samples, a linear increase of the PL signal is observed, as expected in a low optical power regime [cf. Chapter 2]. Notably, the slope exhibits a strong sample dependence. To be quantitative, we fit the data with a linear function. In between $S_{11}^b$ and $S_{10}^b$ samples, which were

exposed to the same neutron fluence and differ only by the boron isotope, a ratio of 8.5 in favor of $S_{10}^b$ sample is extracted. This result confirms the involvement of neutron transmutation in the defect creation process. At the same time, it further demonstrates the advantage of isotopically purified $^{10}$B samples, which, in addition to optimizing the ODMR linewidth [cf. Chapter 3], lead to a more efficient creation of $V_B^-$ centers under thermal neutron irradiation. We note that the decent PL signal observed in $S_{11}^b$, despite the absence of nuclear transmutation, originates from fast neutrons, which generate vacancies through collisions, independently of the isotopic composition.

Between $S_{10}^a$ and $S_{10}^b$, a factor of approximately 1.8 is extracted, which is considerably smaller than the neutron fluence ratio between the two samples ($\times$ 10). This observation suggests that the density of $V_B^-$ centers does not increase linearly with the neutron dose. Several mechanisms could account for this nonlinearity: (i) the conversion of single boron vacancies into divacancies or larger vacancy clusters, (ii) the saturation of electron donors, which prevents full activation of all neutral boron vacancies, and (iii) a modification of the $V_B^-$ center photodynamics in highly irradiated samples. This last aspect will be further investigated using the second batch of sample in Section 4.3.

### 4.2.2 Orthorhombic splitting $E$ and charge model

In Chapter 1, we have seen that an orthorhombic zero-field-splitting (ZFS) parameter $E$ is systematically observed in zero-field ODMR spectra of $V_B^-$ center, leading to the following fine-structure Hamiltonian:

$$\hat{\mathcal{H}}_{\mathrm{FS}} = D\hat{S}_z^2 + E\left(\hat{S}_x^2 - \hat{S}_y^2\right). \tag{4.4}$$

Based on group-symmetry analysis and simulations performed by Adam Gali and Péter Udvarhelyi, we have further shown that this orthorhombic term can only be attributed to the coupling of the $V_B^-$ center with a local transverse electric field. In close analogy with the $NV^-$ center in diamond, we attributed this electric field to a local distribution of charges surrounding the spin defect. From the previous optical characterization, it is clear that our three samples exhibit different $V_B^-$ center densities. Since the defect carries a negative charge, such variations should also be accompanied by corresponding changes in the local charge density. This batch of samples is therefore well suited to test our understanding of the orthorhombic

parameter $E$.

To probe the ZFS parameter $E$, we perform zero-field ODMR spectroscopy on the three samples. The corresponding spectra are shown in Figure 4.3(a). Unambiguously, the orthorhombic ZFS parameter follows the same trend as the $V_B^-$ center density, increasing monotonically from $S_{11}^b$ to $S_{10}^b$.

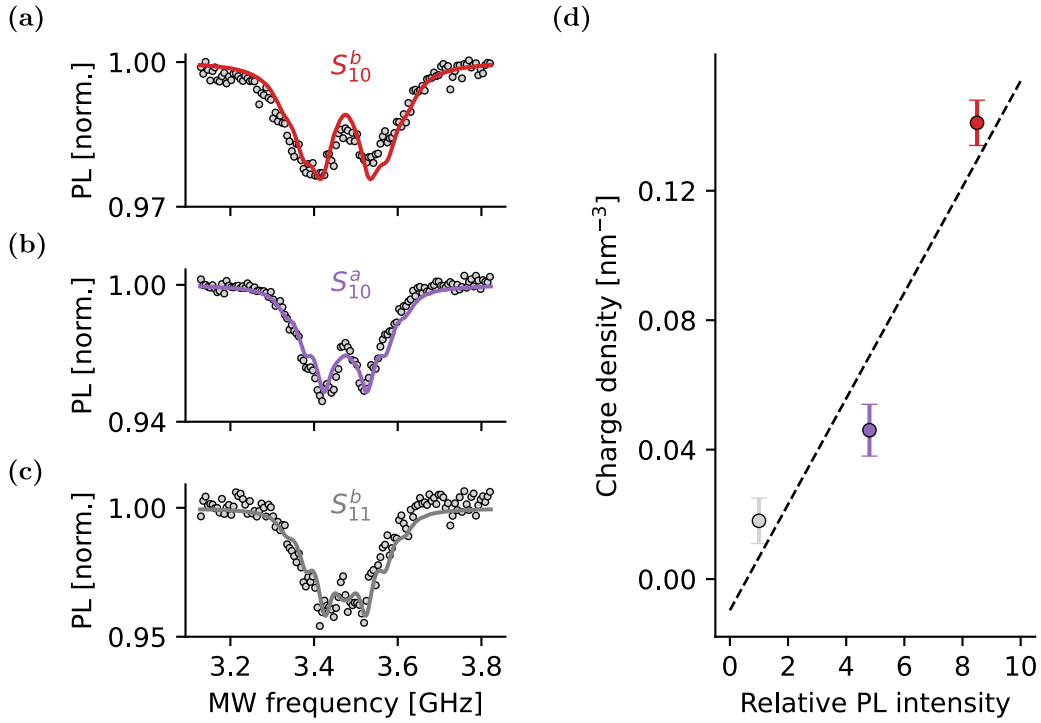


**Figure 4.3:** Orthorhombic parameter E and charge model in neutron irradiated hBN crystals. Zero-field ODMR spectra for sample (a) $S_{11}^b$ (b) $S_{10}^a$ and (c) $S_{10}^b$. The solid colored lines depicted the charge model simulations described in the main text. (d) Extracted charged densities as a function of the relative PL intensities, measured in the previous section. The dashed line is a linear data fit to guide the eyes.

To further analyze the data, our colleagues Adam Gali and Péter Udvarhelyi fit the experimental spectra using a charge model originally developed for the $NV^-$ center in diamond [116]. In this model, a single $V_B^-$ center is placed at the center of a sphere with a radius of 10 nm. Within this sphere, a fixed number of positive and negative charges are randomly distributed, defining a charge density $\rho_c$. Physically, the negative charges can be associated with other $V_B^-$ centers, while the positive ones represent the unknown electron donors. Both species are included in equal numbers to ensure overall charge neutrality. This charge distribution generates a local electric field at the position of the central $V_B^-$ center, which is then

incorporated into the spin Hamiltonian described in Equation (4.4). The hyperfine interaction with the three nearest $^{14}$N nuclei is also included for improved accuracy. For a given value of the charge density $\rho_c$, $10^4$ random charge configurations are simulated, yielding $10^4$ different local electric fields and, consequently, $10^4$ corresponding sets of eigenenergies. By adding an empirical fixed linewidth to each transition, an ODMR spectrum is reconstructed. Finally, for each sample, both the charge density and the ODMR contrast are optimized in order to find the best agreement with the experimental data. The resulting simulation fits are shown as solid colored lines over the data in Figures 4.3(a-c).

A very good agreement is reached. We extract $\rho_c(S_{11}^b) = 0.018(3)$ nm$^{-3}$, $\rho_c(S_{10}^a) = 0.046(4)$ nm$^{-3}$, and $\rho_c(S_{10}^b) = 0.141(8)$ nm$^{-3}$. According to our understanding, these charge densities should scale proportionally with the $V_B^-$ center densities in the three samples. Unfortunately, we lack an accurate independent measurement of the absolute defect density to make a direct comparison. Instead, we rely on the relative PL intensities measured in the previous section, which to first approximation, should reflect the relative $V_B^-$ center densities across the samples. Therefore, in Figure 4.3(d), we plot the extracted charge densities as a function of the measured relative PL intensities. As expected, a clear correlation emerges. Although this does not constitute rigorous evidence, this demonstrates that the orthorhombic parameter $E$ increases with the density of charged defects, as expected for an orthorhombic parameter $E$ arising from the coupling of the $V_B^-$ electron spin with a local electric-field.

Furthermore, by assuming that the charges originate solely from $V_B^-$ centers and their positive counterparts, one can directly estimate the $V_B^-$ center density as $\rho_{V_B^-} \approx \frac{\rho_c}{2}$. We find $\rho_{V_B^-}(S_{11}^b) \approx 80$ ppm, $\rho_{V_B^-}(S_{10}^a) \approx 205$ ppm, and $\rho_{V_B^-}(S_{10}^b) \approx 630$ ppm, where the defect densities have been converted into parts per million (ppm). These estimates compare well with $V_B^-$ centers densities inferred in ion-implanted samples [125, 137, 140]. More broadly, in the context of the NV$^-$ center literature, these values correspond to very high defect-densites [204]. These high $V_B^-$ densities could account for the strong PL signal observed despite the very low quantum efficiency of the defect.

## 4.3 Second iteration: optimizing the sensitivity

In Chapter 3, we identified $h^{10}B^{15}N$ as the most promising isotopic configuration for sensing, owing to its sharper hyperfine lines. Based on this conclusion, we therefore initiated a second neutron irradiation run exclusively on $h^{10}B^{15}N$ crystals, dedicated to the optimization of the magnetic-field sensitivity. As a reminder, the latter reads:

$$\eta_B \approx 0.7 \times \frac{1}{\gamma_e} \times \frac{\Gamma}{\mathcal{C}\sqrt{\mathcal{R}}}. \tag{4.5}$$

Following this expression, we begin this section by characterizing the PL count rates $\mathcal{R}$ [§ 4.3.1]. We then carry out ODMR spectroscopy under magnetic field to estimate the optimal neutron fluence for the ODMR spectrum contrast $\mathcal{C}$ and linewidth $\Gamma$ [§ 4.3.2]. Next, we investigate the impact of neutron fluence on the spin relaxation times, revealing the presence of a noise source whose density increases with irradiation time. [§ 4.3.3]. Finally, we perform cross-relaxation spectroscopy and attribute the noise to a bath of electron spin-1/2 [§ 4.3.4].

| **Sample** | **Picture** | **Neutron fluence [n/cm$^2$]** |
|---|---|---|
| $S_1$ |  | $1.4e16$ |
| $S_{10}$ |  | $1.4e17$ |
| $S_{60}$ |  | $8.6e17$ |

**Table 4.2:** Sample batch of neutron irradiated $h^{10}B^{15}N$ crystals. The size of the crystals is typically one milimeter.

This time, three irradiation durations were tested: 1 hour, 10 hours, and 60 hours, corresponding to neutron fluences of $1.4 \times 10^{16}$, $1.4 \times 10^{17}$, and $8.6 \times 10^{17}$

n.cm$^{-2}$, respectively. To avoid confusion with the previous batch, we label these new samples according to their respective irradiation times. This second batch of samples is summarized in Table 4.2.

This second set of measurements was conducted by myself and Jessica Tournaud, a first-year PhD student. I would also like to acknowledge the involvement of Clément Charbonnier and Lucas Moreau-Lalaux, master's interns.

### 4.3.1 PL signal optimization

The PL signal intensity is a first important parameter involved in the sensivity [Eq. (4.5)]. As with the first batch, we begin with a simple measurement of PL signal as a function of the optical power. The resulting curves are displayed in Figure 4.4(a).

Although the absolute count rates cannot be directly compared with those of the first sample batch, owing to differences in the collection path configuration, one can again observe a linear increase of the PL signal with optical power with a typical intensity of a few Mc/s. However, surprisingly, the most irradiated sample ($S_{60}$) appears less bright than the second most irradiated one ($S_{10}$). To highlight this behavior, I fit the PL signal as a function of optical power curves with a linear function and plot, in Figure 4.4(b), the slope $\alpha$ as a function of neutron fluence. While the PL signal increases by a factor of $\approx 3$ between the $S_1$ and $S_{10}$ samples, a drop of almost 50 % is observed between the $S_{10}$ and $S_{60}$ samples. We note that a similar behavior has already been observed for ion-implanted hBN samples [135]. More generally, a drop in PL at high irradiation doses has already been reported in the color-center literature, for instance for the $NV^-$ and SiV centers in diamond [205, 206], or silicon vacancy in silicon carbide [207]. The mechanisms usually invoked are the ones already mentioned in § 4.2.1. Namely, (i) an accumulation of lattice damage leading to vacancy clustering, and (ii) an accumulation of charges in the defect environment, driving its conversion into a non-optically-active charge state. Alternatively, we wonder if this effect might not arise from a modification of the defect photodynamics. To investigate this additional possibility, we now turn to excited-state (ES) lifetime measurement.

As in Chapter 2, we employ a pulsed laser with picosecond pulses to probe the ES lifetime. To simplify the measurement scheme and reduce the acquisition time, we

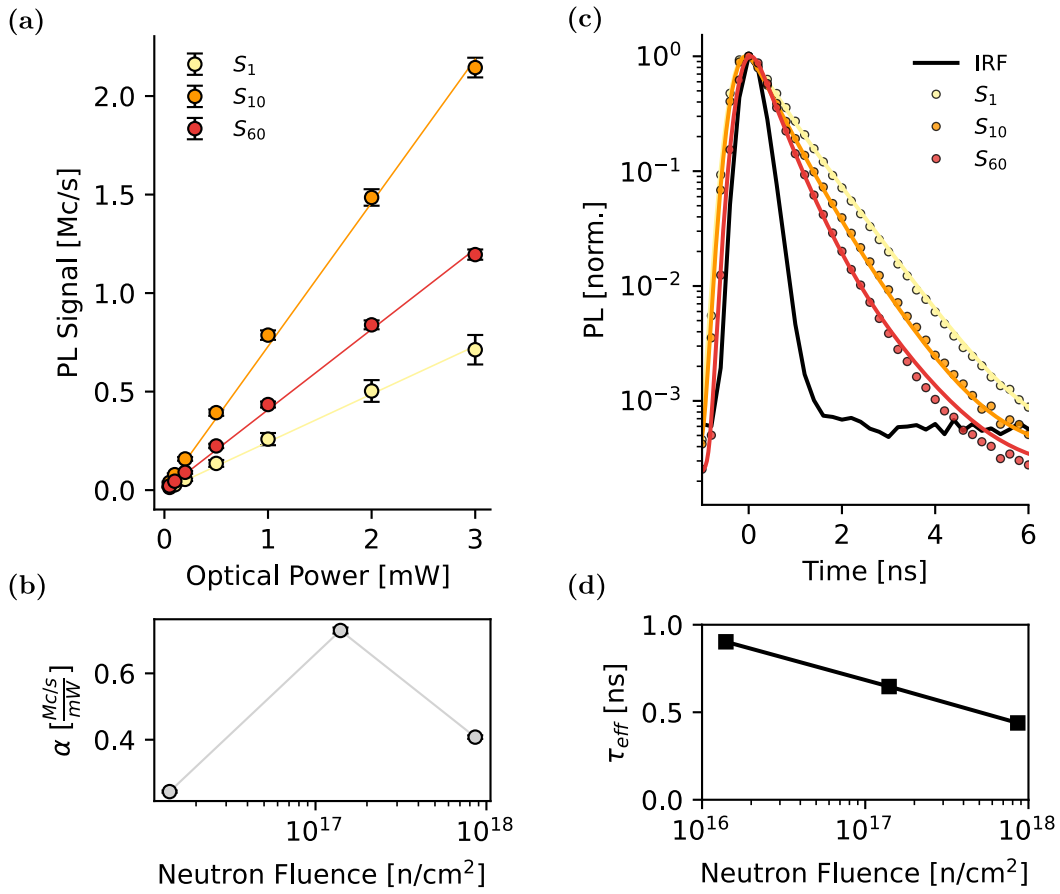


**Figure 4.4:** Optical characterization of neutron irradiated h$^{10}$B$^{15}$N crystals. (a) PL count rate as a function of optical power, $P_{opt}$, for the three samples. The solid lines represent linear fits, $f(P_{opt}) = \alpha P_{opt}$. (b) Slope parameters $\alpha$ extracted from the fits. (c) PL decays under picosecond excitation. The solid black line shows the instrumental response function (IRF), while the solid colored lines are fits using a convolution between a biexponential decay and a Gaussian function. (d) Effective excited-state lifetimes as a function of neutron fluence. The effective lifetime is estimated by tacking the sum of the short and long lifetimes weighted by their respective amplitudes.

measure only the lifetime associated with the polarized spin distribution, obtained after a microsecond-long AOM pulse. The PL decays induced by the picosecond pulses are shown in Figure 4.4(c). A clear impact of neutron fluence is observed, with faster decays observed for the most irradiated samples. As a reminder, we concluded in Chapter 2 that the ES lifetime is largely governed by the non-radiative intersystem-crossing (ISC) rate toward the metastable state. Consequently, the present measurements indicate an enhancement of this non-radiative channel with increasing neutron fluence. This effect is definitely among the causes of the PL signal drop observed in the $S_{60}$ sample. However, caution is required: both a decrease in the lifetime and a reduction in the spin polarization can lead to faster decays. Since we do not measure the thermal state, we cannot distinguish between

these two contributions. For this reason, we prefer to define an effective lifetime, $\tau_{\text{eff}}$, as the sum of the short and long components weighted by their respective amplitudes. The extracted $\tau_{\text{eff}}$ are plotted in Figure 4.4(d). A monotonic decrease of $\tau_{\text{eff}}$ is observed with increasing neutron fluence, from approximately 1 ns in the $S_1$ sample to less than 0.5 ns in the $S_{60}$ sample.

Although this remains to be confirmed, it is tempting to attribute the modification of the ISC rate to irradiation-induced strain in the hBN lattice. Indeed, ISC rates depend on both spin–orbit coupling and local phonon modes, and are therefore highly sensitive to changes in the crystal structure. This interpretation is further supported by recent high-pressure experiments. which also revealed a shortening of the effective ES lifetime when the hBN lattice is subjected to hydrostatic stress [115].

These results therefore reveal one contribution to the PL signal drop observed with increasing neutron fluence: a direct modification of the defect's photodynamics. Vacancy clustering and charge-state effects remain potential additional contributing factors. We thus conclude that the optimal PL signal is not achieved at the highest irradiation time but rather for the intermediate one, 10 hours. To properly identify the best sample for constructing our sensor, however, we must now measure the two remaining key parameters: the ODMR spectrum contrast and linewidth.

### 4.3.2 ODMR spectroscopy of neutron irradiated $h^{10}B^{15}N$ crystals

Magnetometry experiments are typically carried out under a small bias magnetic field to both avoid the non-linear regime at zero field and distinguish between positive and negative field values [cf. Chapter 1]. We therefore apply a small magnetic field of a few mT along the $z$-axis and perform ODMR spectroscopy measurements, focusing on a single electronic resonance. To extract the linewidth and contrast, we then fit each spectrum with four Gaussian functions. The three resulting spectra are displayed in Figure 4.5(a), while the linewidth and contrast are plotted in Figures 4.5(b,c) as a function of the neutron fluence.

In the $S_1$ sample, a well-resolved hyperfine structure, characteristic of isotopically purified $h^{10}B^{15}N$ crystals, appears. We obtain $\Gamma(S_1) = 40.1(5)$MHz and $C(S_1) = 4.3(1)\%$, where $\Gamma$ denotes the linewidth of a single hyperfine line and $C$ the contrast of the most pronounced line [Fig. 4.5(a)]. These values are fully

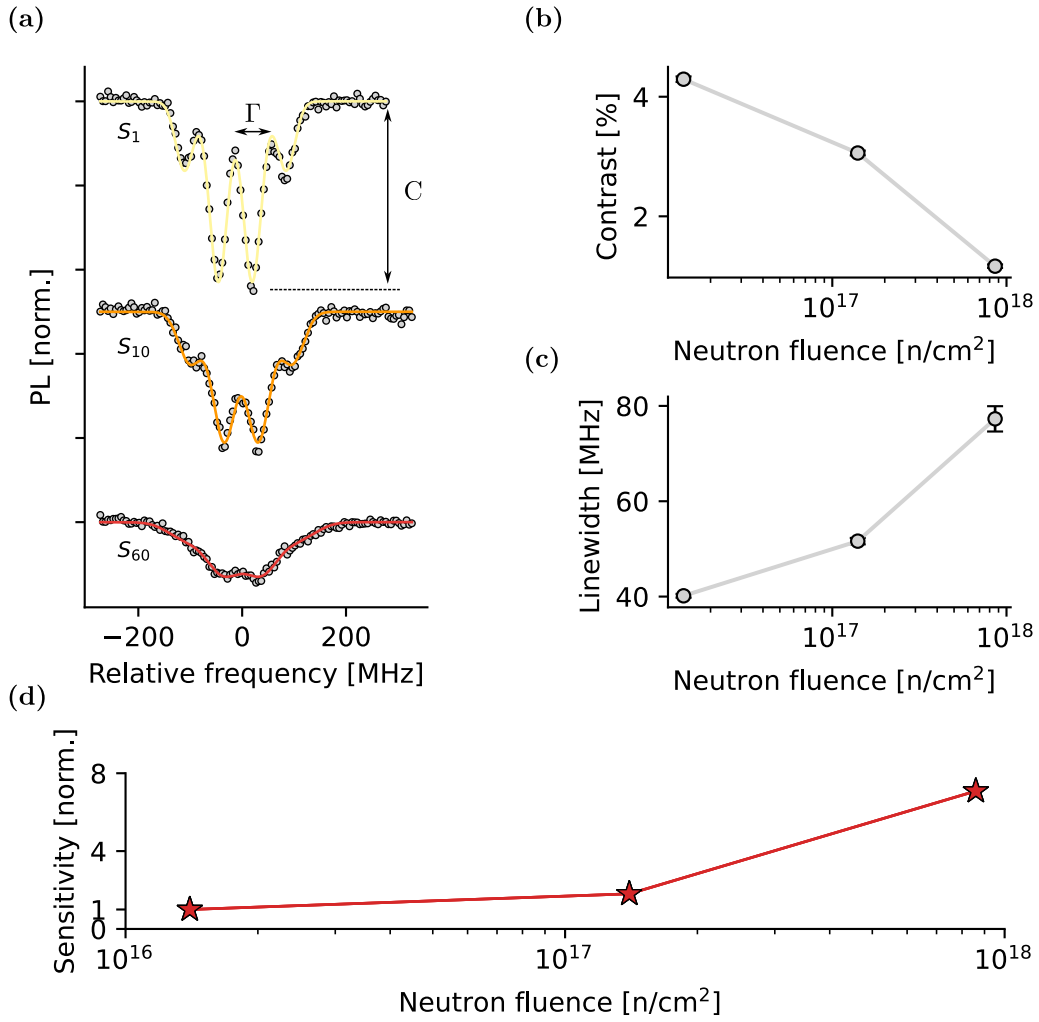


**Figure 4.5:** ODMR spectroscopy on $h^{10}B^{15}N$ neutron irradiated bulk crystals. (a) ODMR spectra of the three samples under a bias magnetic field of a few mT along the $z$-axis. The spectra focus on a single electron spin resonance. Optical power: $P_{opt} = 500\mu$W, RF power: $P_{\mathrm{RF}} = 25$ dBm. The solid colored lines are fits using four equally spaced Gaussians functions with a common linewidth. (b) ODMR spectrum contrast as a function of neutron fluence. (c) Linewidth of a single hyperfine line as a function of neutron fluence. (d) Evolution of the DC magnetic-field sensitivity with neutron fluence. All values are normalized to the sensitivity of the $S_1$ sample to emphasize relative changes rather than absolute values.

consistent with those reported in Chapter 3 for He-implanted samples. Since we established in that chapter that $\Gamma \approx 40$MHz is limited by hyperfine coupling with boron nuclei, we conclude that the ODMR spectrum quality of the $S_1$ sample is state of the art.

The $S_{10}$ and $S_{60}$ samples, however, clearly exhibit degraded ODMR properties, with broader linewidth, $\Gamma(S_{10}) = 52(1)$MHz and $\Gamma(S_{60}) = 77(3)$MHz, and lower contrasts, $C(S_{10}) = 3.0(1)\%$ and $C(S_{60}) = 1.2(1)\%$. In the $S_{60}$ sample, the

degradation is particularly severe, and the hyperfine structure becomes almost indistinguishable. This behavior has a drastic impact on the DC magnetic field sensitivity.

Giving the absolute sensitivity would be misleading because these samples are bulk, and thus emit significantly more signal than the intended sensor, ideally a thin flake, would. Consequently, I compute only the relative scaling, $\eta \propto \frac{\Gamma}{C\sqrt{R}}$, using the previously extracted linewidth $\Gamma$, contrast $C$, and taking $R$, as the relative PL intensity measured in the previous section. All sensitivity values are then normalized to that of the $S_1$ sample. The normalized sensitivity evolution with neutron fluence is plotted in Figure 4.5(d). Interestingly, the sensitivities of the $S_1$ and $S_{10}$ samples are nearly identical. Although the $S_{10}$ sample exhibits a worse ODMR spectrum, this is compensated by its higher PL count rate. In contrast, the $S_{60}$ sample suffers both from severe ODMR degradation and only a modest PL increase, resulting in a much poorer sensitivity. We conclude that the optimal neutron fluence should lie between $1 \times 10^{16}$ n.cm$^{-2}$ and $1 \times 10^{17}$ n $\cdot$ cm$^{-2}$. Below this range, the signal intensity decreases without improving the hyperfine-limited linewidth, while above it, the PL signal gain is insufficient to compensate for the drastically broadened linewidth and reduced contrast. We are currently refining the analysis by investigating a third batch of samples with neutron fluences lying precisely within this range. These results, however, are left for a future PhD thesis.

To explain the overall degradation of the ODMR spectra with increasing irradiation time, strain can once again be invoked. On the one hand, the drop in contrast could result from the previously observed modification of the ISC rate, attributed to lattice damage. On the other hand, the linewidth broadening could arise from strain-induced random shifts of the axial ZFS parameter $D$ [cf. Chap. 1 § 1.2.2]. However, another possibility can be considered for the linewidth, an inhomogeneous broadening limited by electron spin–spin interactions between $V_B^-$ centers and surrounding electron spins. Such a regime would be reached only in samples with very high spin density, which seems plausible according to our charge density estimates from the first section.

### 4.3.3 Impact of neutron irradiation on spin relaxation times

We now turn to pulsed measurement and investigate the impact of the neutron fluence on the spin relaxation times.

#### Longitudinal Spin relaxation Time $T_1$

We begin with the longitudinal spin relaxation time $T_1$. To measure it, we rely on the fully optical sequence depicted in Figure 4.6(a). The readout PL signal is monitored as a function of the delay $\tau$ between two laser pulses. The data, displayed in Figure 4.6(b), reveal a pronounced effect: the longitudinal spin relaxation, i.e, the characteristic time to reach a thermal spin distribution from a polarized state, becomes significantly faster as the neutron fluence increases. We fit the decay with a monoexponential function to extract its dependence on neutron fluence, further plotted in Figure 4.6(c).

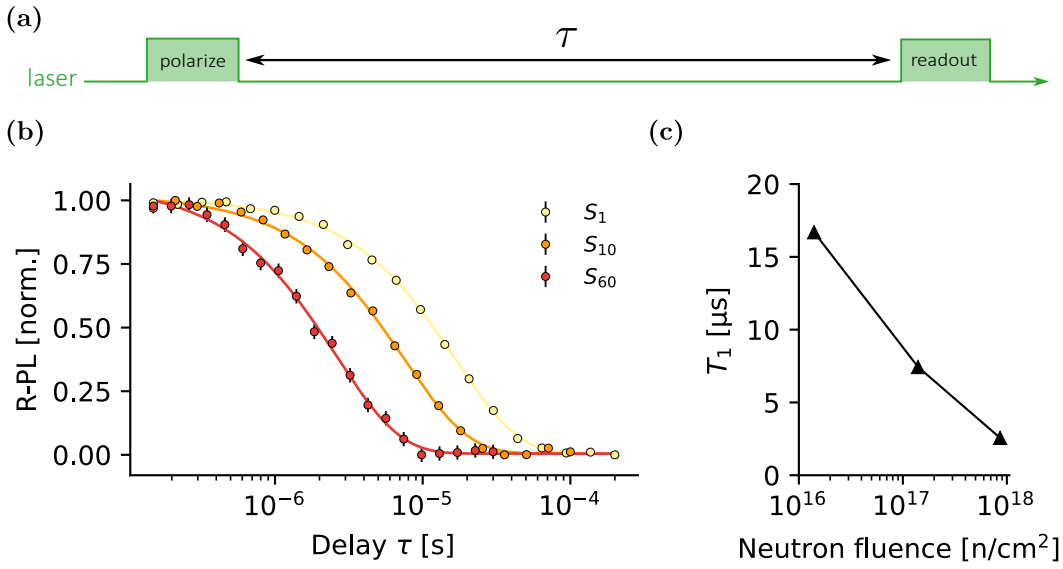


**Figure 4.6:** Longitudinal spin relaxation time $T_1$ in neutron-irradiated hBN bulk crystals.(a) Sketch of the $T_1$ optical sequence .(b) Readout PL signal as a function of the interpulse delay $\tau$. All sequences are normalized to their respective maximum for easier comparison. For reference, the contrast between the fully polarized state and the thermal equilibrium is about 15% in the $S_1$ sample.(c) Extracted $T_1$ values as a function of the neutron fluence.

Between the $S_1$ and $S_{10}$ samples, $T_1$ is already reduced by more than a factor of two ($T_1(S_1) = 16.7(3)$ µs and $T_1(S_{10}) = 7.4(2)$ µs), while in the $S_{60}$ sample it decreases further, down to $T_1(S_{60}) = 2.6(1)$ µs. Once again, this trend mirrors observations in ion-implanted hBN flakes [135]. Yet no well-established explanation

has been reached. Since the $T_1$ value of approximately 15–20 $\mu$s is known to be phonon-limited, as evidenced by its temperature dependence [cf. Chapter 1], it is tempting to suggest that high neutron irradiation perturbs either the phonon modes or the spin–phonon coupling through lattice damage. Another possibility would be broadband magnetic noise produced by a dense spin bath, as observed for $NV^-$ centers in highly doped diamond samples [119, 208, 209]. A systematic temperature-dependent study could resolve this question, but it is left for future work.

## Spin Echo Coherence Time $T_2$

To further characterize the spin dynamics, we now turn to spin-echo measurements and probe the coherence time $T_2$. We apply a small magnetic field of a few mT along the $z$ axis, target the most pronounced line of the hyperfine structure, and perform a differential echo sequence to ensure reliability [Fig. 4.7(a)]. The echo signals for the three samples are plotted in Figure 4.7(b).

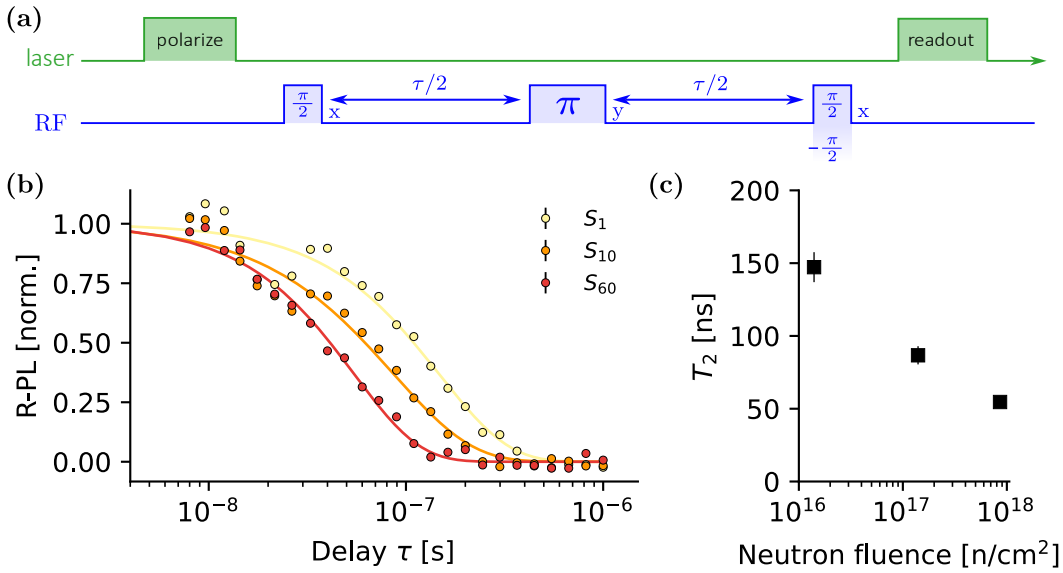


**Figure 4.7:** Spin echo coherence time $T_2$ in neutron-irradiated $h^{10}B^{15}N$ bulk crystals. (a) Sketch of the $T_2$ sequence. (b) Readout PL signal as a function of the interpulse delay $\tau$. (c) Extracted $T_2$ values as a function of the neutron fluence.

Fitting the echo signal of the $S_1$ sample with a stretched-exponential decay, we extract $T_2(S_1) = 150(10)$ns. Notably, this value lies very close to the predicted value of $\sim$ 200 ns for a $T_2$ limited by the nuclear-spin-bath in $h^{10}B^{15}N$ [124, 180]. Alongside the narrow ODMR linewidth, this result confirms that the coherence

properties of the $S_1$ sample are state-of-the-art. Nonetheless, as the neutron fluence increases, a trend similar to that observed for $T_1$ emerges: the coherence time $T_2$ decreases. We extract $T_2(S_{10}) = 87(6)$ ns and $T_2(S_{60}) = 54(2)$ ns [Fig. 4.7(c)]. Spin coherence is most often limited by magnetic noise, and in samples with defect densities as high as ours, this noise most likely originates from a bath of surrounding electron spins.

### 4.3.4 Cross-relaxation relaxometry

Previous studies have highlighted the presence of electron spin $S = 1/2$ centers in neutron-irradiated samples, possibly associated with $N_\mathrm{B}V_\mathrm{N}$ and $C_\mathrm{N}V_\mathrm{B}$ defects [104, 124, 210, 211]. To verify the presence of these parasitic spins in our samples, we turn to cross-relaxation relaxometry.

#### Principle

Cross-relaxation relaxometry relies on the same mechanism that underlies dynamical nuclear polarization [cf. Chap.3]. The idea is to activate the non-secular terms of the dipolar interaction tensor, which couple the defect spin to another spin species, thereby enabling spin flip-flop transitions between the two. The difference lies in the nature of the partner spins: instead of a few strongly coupled nuclear spins, we now probe a dilute bath of electronic spins. Accordingly, in place of probing the bath polarization via the ODMR spectrum as we did in Chapter 3, we now measure its impact on the longitudinal relaxation time $T_1$ of the $\mathrm{V}_\mathrm{B}^-$ center.

The procedure is sketched in Figure 4.8. A bias magnetic field is tuned to bring the $|m_s = 0\rangle \leftrightarrow |m_s = -1\rangle$ transition of the $\mathrm{V}_\mathrm{B}^-$ center ground state into resonance with the $|m_s = -1/2\rangle \leftrightarrow |m_s = +1/2\rangle$ transition of the electron spin-1/2 bath. This condition reads:

$$\gamma_e B_z = D - \gamma_e B_z. \tag{4.6}$$

It yields $B_z \approx 62$ mT at room temperature. At this field, the flip-flop terms of the dipolar interaction become active between the two spin species and enhance the $\mathrm{V}_\mathrm{B}^-$ center population relaxation rate, thereby reducing $T_1$. As a result, by measuring $T_1$ as a function of the magnetic field, one can detect the presence of the parasitic spin specie.

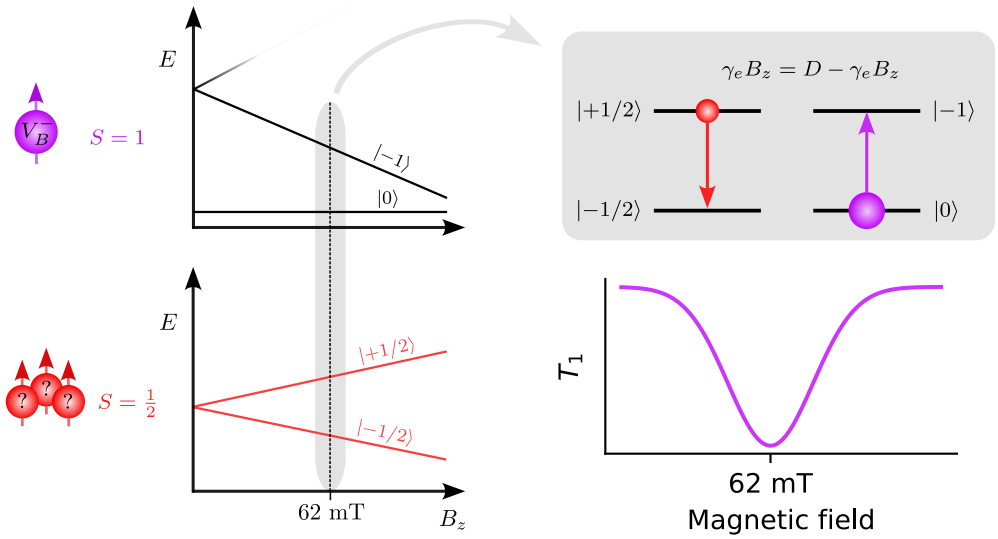


**Figure 4.8:** Cross-relaxation relaxometry principle. A bias magnetic field $B_z$ brings the $V_B^-$ center and electron spin-1/2 bath spin transitions into resonance ($B_z = \frac{D}{2\gamma_e}$). Spin flip-flops then accelerate $V_B^-$ depolarization, yielding a dip in $T_1$ at this specific magnetic field.

## Measurements

A permanent magnet is mounted on piezoelectric stages, themselves fixed on manual translation stages. Using the manual translation, we first position the magnet at the appropriate distance from the sample to reach the resonance condition $B_z \approx 62$ mT. The magnetic field value and its alignment are inferred by measuring a full ODMR spectrum of both electronic branches [cf. Sec. 3.3.3]. We then remotely control the piezo stages to perform a high-resolution scan over a magnetic-field range of approximately 15 mT. For each magnet position, we first record an ODMR spectrum to extract the bias field $B_z$ from the Zeeman shift. We then perform a $T_1$ sequence and fit the PL decay with a stretched-exponential function to extract the corresponding $T_1$ value. For such bulk samples, the signal is strong enough that a single $T_1$ measurement takes only a few minutes, however, the entire procedure typically requires few days to be completed.

In Figure 4.9(a), I plot the $T_1$-versus-magnetic-field data for the three samples. In the $S_1$ and $S_{10}$ samples, a clear $T_1$ drop is observed at $B_z \approx 62$ mT. The hypothesis is confirmed, electron spin-1/2 do coeexist with $V_B^-$ centers in our neutron-irradiated samples. Furthermore, it is usually assume that the $1/T_1$ value at resonance scales with the density of the bath [212]. Hence, we conclude that the spin-1/2 density also increases with irradiation, not surprising for vacancy-related defects.

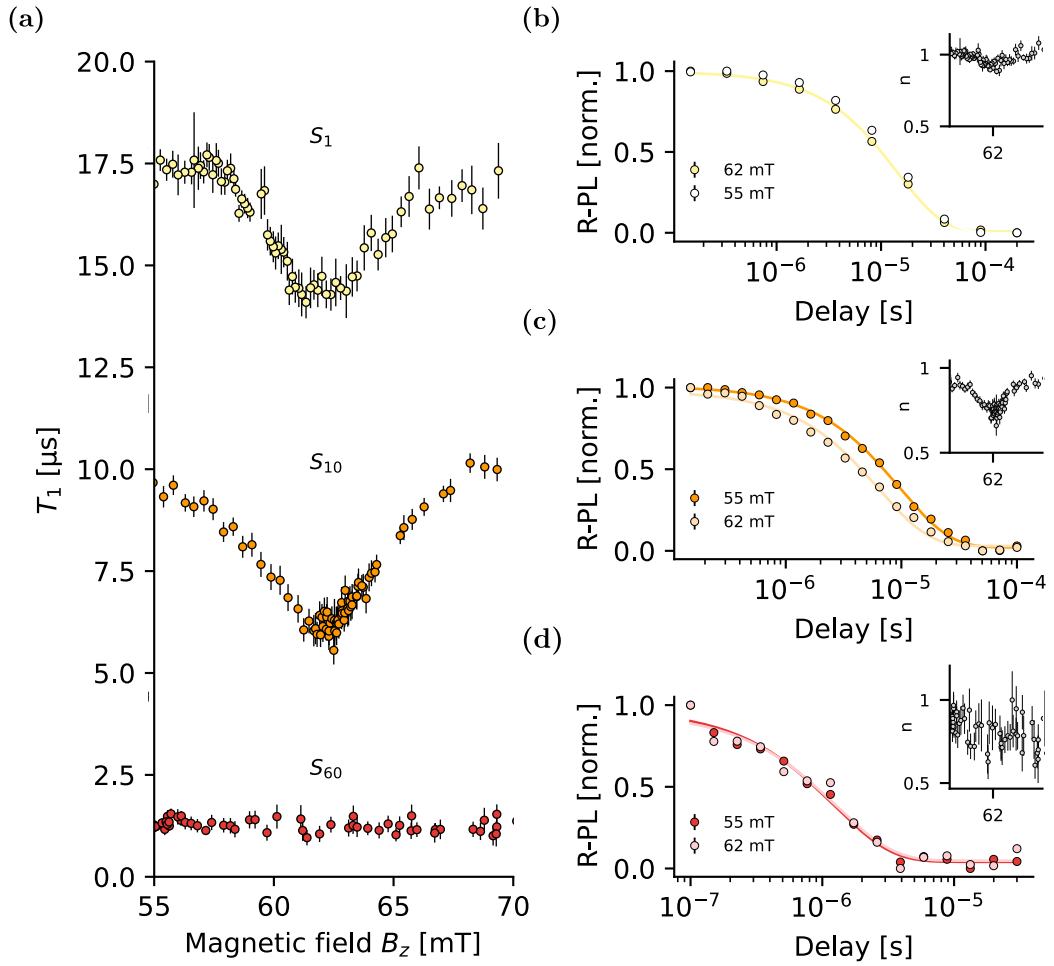


**Figure 4.9:** Cross-relaxation $T_1$ relaxometry in neutron-irradiated hBN. (a) $T_1$ as a function of the bias magnetic field $B_z$ for the $S_1$, $S_{10}$, and $S_{60}$ samples at $T \approx 300$ K. (b–d) Representative $T_1$ curves for the same samples, recorded off resonance with the electron spin-1/2 bath and at resonance ($B_z = 62$ mT). Solid lines: fits with stretch exponential decays. Insets: fitted stretch exponent $n$.

Surprisingly, the most irradiated sample shows no clear reduction of $T_1$ at the resonant field. It is unlikely that the spin-1/2 bath has vanished, since the coherence time is shorter in the $S_{60}$ sample than in the $S_{10}$ sample. Instead, this may be because the off-resonant $T_1$ is already too short to be sensitive to additional dipolar coupling with the spin-1/2 bath, or conversely, the spin-1/2 bath may be strong enough to dominate $T_1$ even away from resonance.

It is also worth discussing the stretch exponent $n$ of the decay, which I deliberately allowed to deviate from unity during the fits. For this purpose, in Figures 4.9(b-d), I plot two representative examples per sample. A $T_1$ sequence measured off-

resonance and one at resonance with the electron spin-1/2 bath. The magnetic-field dependence of the stretch exponent, $n$, is plotted in inset panels. In both the $S_1$ and $S_{10}$ samples, the $T_1$ reduction is associated with a stretch exponent lower than 1. Such a departure from monoexponential behavior is expected when $T_1$ is limited by dipolar coupling [119, 208, 209, 213–217]. Intuitively, when dipolar interactions dominate, the ensemble of $V_B^-$ centers becomes highly heterogeneous: some defects lie closer to, and are more strongly coupled with, spin-1/2 defects than others, and therefore decay faster. Averaging over this distribution of decay rates naturally yields a stretched exponential with $n < 1$. By contrast, when the relaxation is phonon-limited, all $V_B^-$ centers couple to the same well-defined phonon mode and decay at the same rate, leading to $n = 1$. Interestingly, although the stretch exponent $n$ of the $S_{60}$ sample shows no clear field dependence, within the substantial error bars, its value remains clearly below 1. Additionally, the off-resonant stretch exponent of the $S_{10}$ sample is also slightly below 1. These trends could indicate that the irradiation-induced drop in $T_1$, characterized in the previous section, is driven more by coupling to a growing spin bath than by strain. However, such a claim would require temperature-dependent $T_1$ measurements, which I was unfortunately unable to perform at this time.

## Conclusion

These final characterizations unambiguously confirm the presence of an electron spin-1/2 bath generated by neutron irradiation. This information allows us to better interpret the drop in the spin-echo coherence time $T_2$ observed in the previous section. In the $S_1$ sample, $T_2$ lies very close to the nuclear-spin-limited value of approximately 200 ns. We therefore conclude that the spin-1/2 bath is not dense enough at this neutron fluence to become the dominant decoherence mechanism over the nuclear spin bath. Conversely, in the $S_{10}$ and $S_{60}$ samples, $T_2$ is significantly lower than the expected nuclear spin limit. Furthermore, it appears dependent on the neutron fluence with lower $T_2$ in samples exposed to higher neutron fluences. We conclude that the electronic spin bath dominates the spin-echo coherence time of $V_B^-$ centers in samples $S_{10}$ and $S_{60}$ . We note that, in addition to spin-1/2, the $V_B^-$ centers themselves may also contribute to the electronic spin bath. These two distinct decoherence regime, nuclear-spin-limited and electron-spin-limited, are illustrated in Figure 4.10. They will be of primary importance when probing the coherence of these samples in the few-layer limit in Chapter 5.

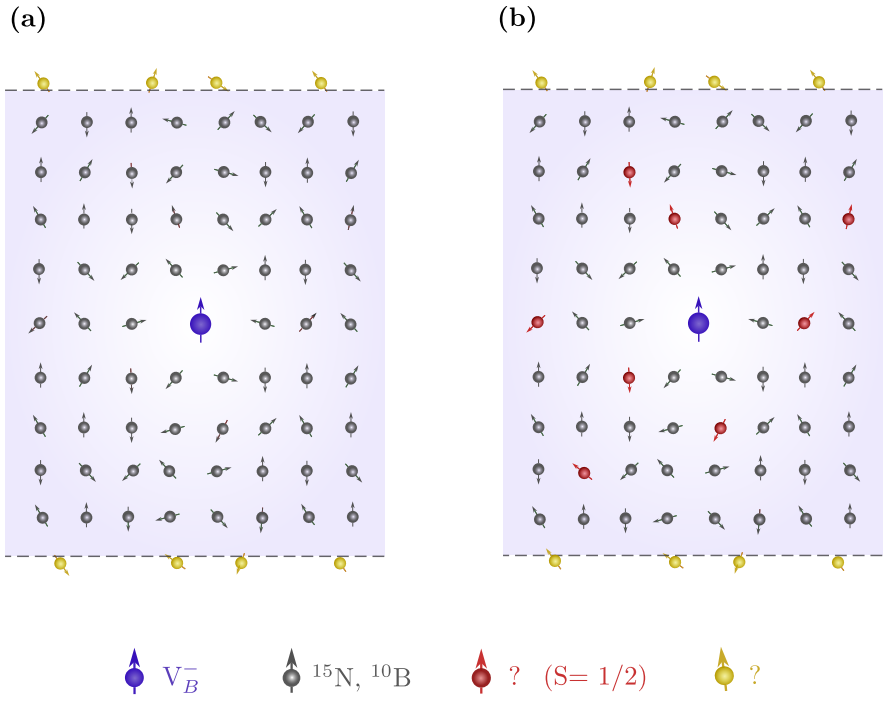


**Figure 4.10:** Schematic illustration of the two distinct coherence regimes observed in the neutron irradiated hBN samples: (a) nuclear-spin-limited $T_2$, and (b) electron-spin-limited $T_2$.

## 4.4 Toward an atomically-thin sensor

All this characterization is motivated by the supposed advantage of neutron irradiation to engineer $V_B^-$ centers in ultra-thin hBN flakes. However, a crucial question lies underneath: are $V_B^-$ centers stable down to the few-layer limit? In fact, it is the proximity to the surface, rather than the thickness itself, that is of concern. Surfaces are known to be highly perturbative environments, being in direct contact with the ambient, they readily accumulate charges and impurities that can be detrimental to point defects. Moreover, surface-induced band bending in the host's electronic structure has emerged as a possible obstacle to stabilizing a given charge state. For example, stabilizing the negatively charged $NV^-$ center close to the diamond surface has been a long-standing challenge and remains an active area of research [43, 44, 50, 51]. Despite being a central motivation of much of the $V_B^-$ center literature, this question remains unanswered. All prior work has been performed either on bulk crystals or on flakes with thicknesses of a few tens of nanometers. We are now in a position to address this crucial question.

In Toulouse, the mechanical exfoliation of bulk $h^{10}B^{14}N$ crystals was first carried

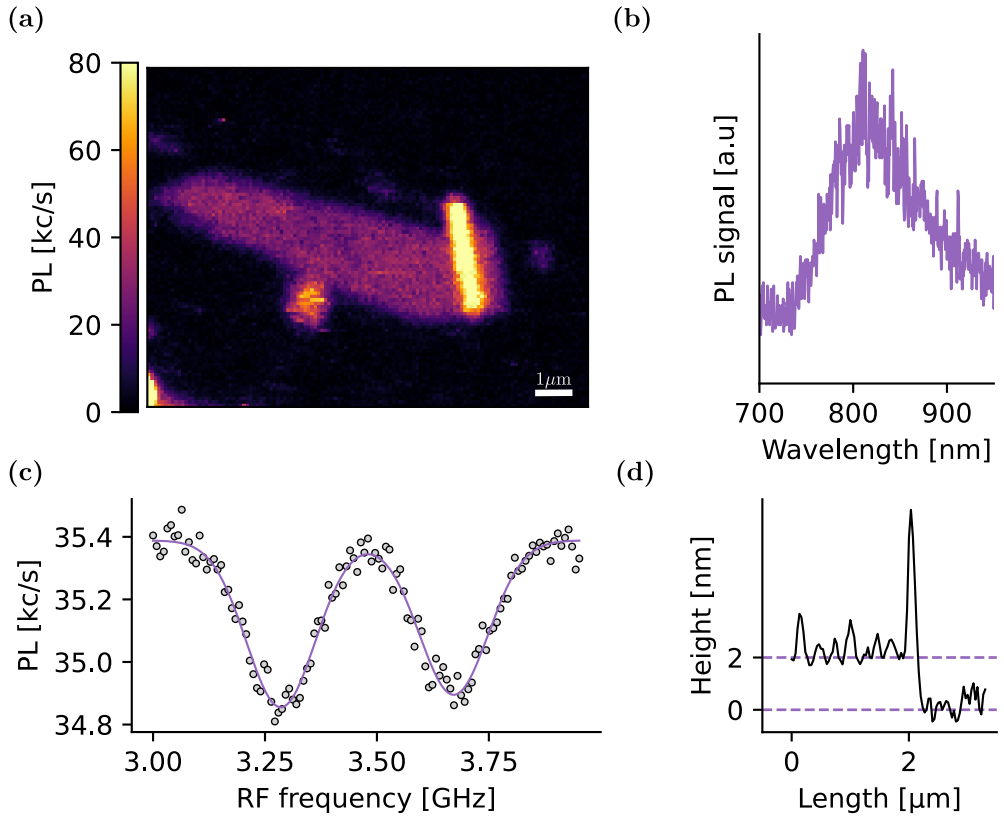


**Figure 4.11:** $V_B^-$ centers in few-layer thick $h^{10}B^{14}N$ flake. (a) PL raster scan recorded at $P_{opt} = 500\mu W$. (b) Normalized PL spectrum. (b) ODMR spectrum under a bias magnetic field $B_z \approx 3.5$ mT. (d) AFM line profile across the flake, dashed lines are guides to the eye.

out by Cédric Robert and Jules Fraunié. The samples were then carefully examined under an optical microscope to locate candidate for thin hBN flakes. One flake with very low optical contrast was marked as a potential few-layer flake. Once the sample back to Montpellier, I examined this promising flake in detail. I began with a PL raster scan: a signal of a few tens of kc/s traced an elongated feature in the scan [Fig. 4.11(a)]. The flake emits a PL signal! To ensure its origin, I recorded a PL spectrum: the familiar broad emission of the $V_B^-$ center appeared [Fig. 4.11(b)]. The information is confirmed, the thin flake hosts optically active $V_B^-$ centers. As a last but not least verification, I recorded an ODMR spectrum. Two broad electron spin resonances, centered at 3.47 GHz, concluded the identification [Fig. 4.11(c)]. To verify its thickness, we immediately performed atomic force microscopy (AFM) measurements, which revealed an apparent step height of 2 nm [Fig. 4.11(d)]. For comparison, the height of a single hBN layer on $SiO_2$ substrate is commonly measured at $\sim 1$ nm, because of the presence of an interfacial water layer [52, 64]. Given an interlayer spacing of $\sim 0.33$ nm, we therefore estimate the flake to be only 3-5 layers thick. This simple result may be the most important of this manuscript:

even when atomically close to the surface, the $V_B^-$ centers remain optically active and can still be operated as sensors. Simultaneously, this demonstrates the value of neutron irradiation, which, to date, is the only technique that has enabled this important step forward.

When the $h^{10}B^{15}N$ crystals arrived, we repeated the procedure and confirmed our previous conclusions. On a $\sim$ 3 nm-thick flake, we measured a robust PL signal of $\sim$ 60 kc/s and resolved the clear hyperfine structure characteristic of a $h^{10}B^{15}N$ crystal [Fig. 4.12]. Notably, the linewidth of an individual hyperfine line is measured to be $\Gamma = 44.6(6)$ MHz, identical to that observed in bulk. As a figure of merit, we extracted the DC magnetic sensitivity and obtained $\eta = 104(3)\ \mu T/\sqrt{Hz}$, similar to the one measured on a 80 nm thick flake at the end of the first Chapter [cf. Chap. 1 § 1.4.2], except that here the flake is only few-layer thick. This improvement mainly results from the isotopic purification with $^{10}B$ and $^{15}N$, as well as an improved collection efficiency achieved through the use of a new microscope objective.

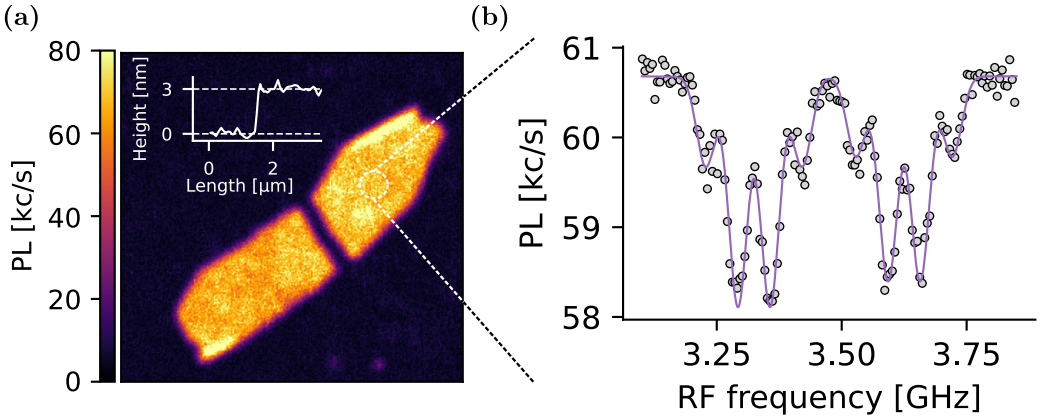


**Figure 4.12:** $V_B^-$ centers in few-layer thick $h^{10}B^{15}N$ flake. (a) PL raster scan recorded at $P_{opt} = 500\,\mu W$, inset: AFM profile. (b) ODMR spectrum under a bias magnetic field $B_z \approx 3$ mT.

## 4.5 Conclusion

In this chapter, we established neutron irradiation as a viable route to engineer ensembles of $V_B^-$ centers in hBN. With a first sample batch, we demonstrated that thanks to nuclear transmutation, neutron irradiation is particularly efficient to engineer a dense and homogeneous distribution of $V_B^-$ centers in hBN crystals purified with $^{10}B$. Additionally, we verified that the orthorhombic splitting $E$ increases with the defect density, strengthening our claim that it originates from

the coupling of the defect's electron spin with a local electric field. In a second sample batch with the ideal isotopic configuration, $h^{10}B^{15}N$, we then initiated an optimization of the neutron fluence for sensor sensitivity. Systematic measurements at three irradiation doses revealed a consistent evolution of both optical and spin properties. While the non-radiative ISC rates are clearly enhanced with irradiation time, the ODMR spectrum linewidth broadens, its contrast decreases, and the spin-relaxation times $T_1$ and $T_2$ shorten with increasing neutron fluence. We attribute these changes to irradiation-induced strain and to dipolar coupling with a spin-1/2 bath, detected via cross-relaxation $T_1$ relaxometry. Finally, we demonstrated the potential of neutron irradiation to engineer $V_B^-$ centers in atomically thin hBN flakes, simultaneously showing that $V_B^-$ centers remain optically active and operable as sensors down to the few-layer limit, an important milestone for our project.

If the operability of the $V_B^-$ center in few-layer flakes is now asserted, this does not necessarily mean that reducing the thickness has no impact on the defect's properties. This question will be addressed in the following and final chapter.

# 5 Optical and spin properties of $V_B^-$ centers in atomically-thin hBN flakes

## Outline


**4.1 Working principle of neutron irradiation: a $^{10}$B advantage . . . . . 124**

**4.2 First iteration: early steps with neutron irradiation . . 126**

4.2.1 Optical characterization: **$^{10}$B** versus **$^{11}$B** isotopes . . . . 127

4.2.2 Orthorhombic splitting $E$ and charge model . . . . . 129

**4.3 Second iteration: optimizing the sensitivity . . . . . 132**

4.3.1 PL signal optimization . . . . . 133

4.3.2 ODMR spectroscopy of neutron irradiated h$^{10}$B$^{15}$N crystals 135

4.3.3 Impact of neutron irradiation on spin relaxation times . . 138

4.3.4 Cross-relaxation relaxometry . . . . . 140

**4.4 Toward an atomically-thin sensor . . . . . 144**

**4.5 Conclusion . . . . . 146**


At the end of the previous chapter, we described a procedure to obtain few-layer hBN flakes with $V_B^-$ centers embedded within. At the same time, we demonstrated that the $V_B^-$ centers remain optically active and that their spin transitions can still be interrogated by ODMR spectroscopy in this limit. However, even if the defect remains stable, its properties could be drastically modified by proximity to interfaces or by the reduced dimensionality. Understanding how the thickness reduction affects the properties of the defect is crucial to assess its potential as a nanoscale quantum sensor. In this final Chapter, we address this issue by systematically investigating how thickness reduction, from bulk-like to atomically thin flakes, impacts both the optical and spin properties of the $V_B^-$ center.

In the first section [§ 5.1], we focus on the optical properties. By combining systematic measurements on flakes of various thicknesses with numerical simulations,

we highlight the important role of nanophotonic effects in shaping the optical response of the $V_B^-$ centers. In the second section [§ 5.2], we extend our previous analysis of the orthorhombic splitting parameter $E$ to few-layer hBN flakes, revealing that this splitting vanishes in this limit. This observation is further interpreted within our local electric-field framework. In the following section [§ 5.3], we initiate pulsed experiments with a systematic study of the thickness dependence of the longitudinal spin relaxation time $T_1$. Once again, a clear influence of the thickness reduction is observed, manifesting as a faster spin relaxation in thinner flakes. Finally, we conclude this chapter by investigating the impact of surface proximity on spin coherence [§ 5.4]. Surprisingly, we show that the $V_B^-$ center's spin coherence is remarkably resilient to surface proximity, and that reduced dimensionality may even enhance coherence depending on the nature of the spin bath limiting the spin coherence.

## 5.1 Flake thickness-dependent optical response of a $V_B^-$ centers

In this first section, we begin by investigating the dependence of the PL signal on the hBN flake thickness. To this end, flakes were exfoliated from the $h^{10}B^{14}N$ crystal, denoted $S_{10}^a$ in Chapter 4 §4.2. As usual, the hBN flakes are then deposited onto a 90 nm-thick SiO2 substrate. The optical response of the embedded $V_B^-$ centers was then studied using the same experimental apparatus as in the previous chapters, namely a scanning confocal microscope operating under ambient conditions. Optical excitation was provided by a laser at $\lambda_L = 532$ nm, focused onto the sample through a high-numerical-aperture objective (NA = 0.95). The PL emitted by the $V_B^-$ centers was collected by the same objective, spectrally filtered from the excitation laser, and directed to a silicon avalanche photodiode (APD) operating in the single-photon-counting regime. The measurements were carried out by myself and Alrik Durand, while the simulations were performed by Guillaume Cassabois, from our team, and Jean-Michel Gérard from CEA Grenoble.

We start by showing an illustrative example. In Figure 5.1(a) is displayed a PL raster scan of a typical neutron-irradiated hBN flake deposited on $SiO_2$. It is not especially thin and appears completely ordinary at first glance. However, a closer look reveals a step-by-step variation of the PL signal along one of its edges [Fig.5.1(b)]. In

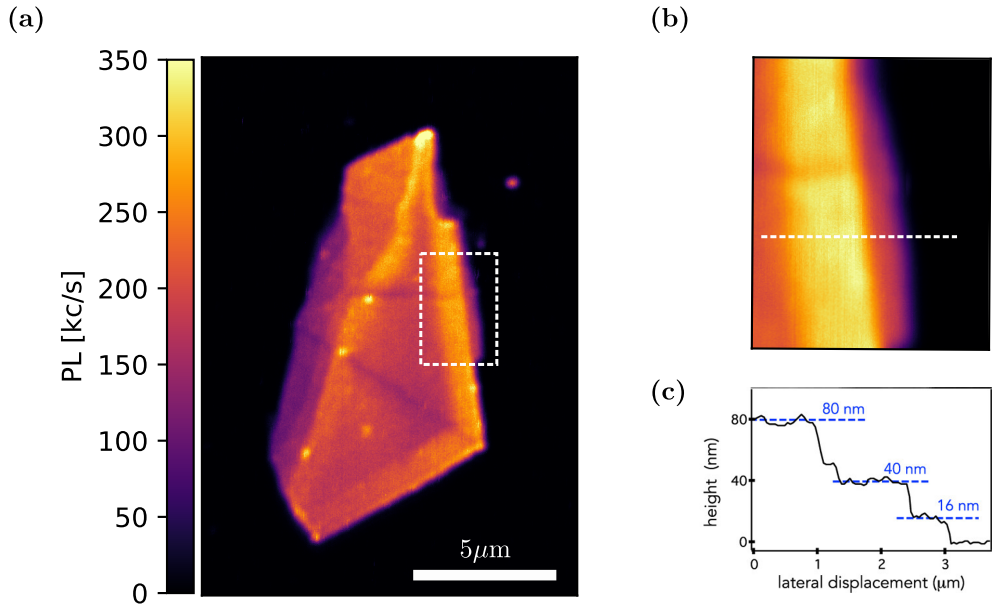


**Figure 5.1:** PL signal of $V_B^-$ centers embedded in a staircase-like hBN flake. (a) PL scan of the flake in the plane parallel to the surface, the region of interest is marked by a white dashed square. (b) Zoom on the region of interest, showing a staircase-like PL signal. The white dashed line indicates the AFM profile location. (c) AFM profile across the edge.

Figure 5.1(c), we plot the corresponding topography profile, measured with atomic force microscopy (AFM). The profile reveals a staircase-like topography, with a first plateau at $\sim$ 16 nm, a second at $\sim$ 40 nm, and a final one at $\sim$ 80 nm. Considering that neutron irradiation produces defects uniformly distributed throughout the hBN flake, the number of $V_B^-$ centers and thus the PL intensity are expected to increase with the thickness. Surprisingly, we instead observe that the PL signal significantly weakens when the thickness increases from $t = 40$ to $t = 80$ nm. From this observation, one conclude that the PL signal does not scale linearly with flake thickness. The aim of this section is to identify the physical mechanisms underlying this behavior.

### 5.1.1 Modelling of the PL signal thickness-dependence

Building on the photodynamics model developed in Chapter 2, the PL signal, $S$, emitted by a $V_B^-$ center can be expressed as :

$$S = \eta k_p k_d \left( \frac{\mathcal{P}}{\gamma_0 + k_d} + \frac{(1-\mathcal{P})}{\gamma_1 + k_d} \right).$$

Here, $\eta$ denotes the detection efficiency, $k_p$ the pumping rate, $k_d$ the direct radiative decay, $\gamma_0$ and $\gamma_1$ the intersystem-crossing (ISC) rates from the excited state to the

metastable state, and $\mathcal{P}$ the spin polarization in $|m_s = 0\rangle$ in the ground state. As argued throughout this manuscript, the excited-state lifetime of the $V_B^-$ center is dominated by the non-radiative ISC rates $\gamma_0$ and $\gamma_1$ ($k_d \ll \gamma_0, \gamma_1$). In this limit the PL signal becomes

$$S \approx \eta k_p k_d \left( \frac{\mathcal{P}}{\gamma_0} + \frac{(1-\mathcal{P})}{\gamma_1} \right). \tag{5.1}$$

We now assume that the ISC rates are thickness independent and that the $V_B^-$ center concentration is homogeneous along the depth. In this case, the thickness-dependence of the PL signal can only arise from the first three factors, $\eta$, $k_p$ and $k_d$. Formally, one can express the PL signal emitted by a $V_B^-$ center at a depth $z$ in a hBN flake of thickness $t$ as

$$S(t,z) \propto \eta(t,z) k_p(t,z) k_d(t,z).$$

We now link each of these factors to a thickness-dependent quantity.

- Pumping rate $k_p$.
  Considering a flux $\Phi$ of excitation photons, the pumping rate can be written as
  $$k_p = \alpha\, \Phi,$$
  where $\alpha$ is a dimensionless factor referred to as the absorption. Furthermore, the excitation photon flux $\Phi$ can be directly related to the optical power $P_{opt}$ by
  $$\Phi = \frac{P_{opt}}{E_p},$$
  with $E_\mathrm{p}$ the energy of an excitation photon, $E_\mathrm{p} \sim 2.33$ eV for a laser wavelength of 532 nm. Hence, one can write
  $$k_p = k_p^0\, P_{opt}, \qquad \text{with} \qquad k_p^0 = \frac{\alpha}{E_\mathrm{p}}. \tag{5.2}$$
  Here we just recovered a linear scaling of the pumping rate with the optical power, as already argued in Chapter 2. What matters for our present concern is that the pumping rate $k_p$ is directly proportional to the absorption. Because of Fabry-Perot interferences at the laser wavelength $\lambda_L$, one can expect the absorption to exhibit a thickness dependence so that $\mathbf{k_p(t,z)} \propto \boldsymbol{\alpha(t,z)}$ [1].

[1] In practice, when the excitation volume and its non-uniform illumination are taken into ac-

- Radiative decay rate $k_d$.
  Because of the nanometric size of the flakes one can also expect an enhancement of the radiative decay rate thorough the Purcell effect. We define the Purcell factor at a depth $z$ in a flake of thickness $t$ as the ratio between the radiative decay at a depth $z$ in a flake of thickness $t$ with the radiative decay in bulk hBN $\mathcal{F}(t,z) = \frac{k_d(t,z)}{k_d(t\to\infty,z)}$. Therefore, through the Purcell factor the radiative decay can exhibit a thickness dependence $\mathbf{k_d(t,z)} \propto \boldsymbol{\mathcal{F}(t,z)}$.

- The detection efficiency $\eta$. The factor $\eta$ encompasses all the losses along the collection path. As will become clear in the following, one of these contributions is thickness-dependent: the collection efficiency of the microscope objective, $\mathcal{C}(t,z)$. The latter is defined as the fraction of the PL signal emitted at depth $z$ in a flake of thickness $t$ that is captured by the objective. Hence, $\boldsymbol{\eta(t,z) \propto \mathcal{C}(t,z)}$.

Finally, the PL signal emitted by $V_B^-$ centers buried at a depth $z$ within a hBN flake of thickness $t$ verifies:

$$\mathcal{S}(t,z) \propto \mathcal{C}(t,z)\,\mathcal{F}(t,z)\,\alpha(t,z). \tag{5.3}$$

The individual impact of these three distinct contributions on the PL signal is now examined one by one.

### 5.1.2 Optical absorption

Notably, optical absorption is the only contribution that can be easily probed experimentally, independently of the other two. Hence, for this one, we performed not only simulations but also measurements.

#### Pumping rate measurements

In Chapter 2, we showed that the pumping rate can be extracted by analyzing the spin polarization dynamics under continuous optical excitation [cf. Sec. 2.2.2]. The argument is straightforward: since spin polarization is achieved by cycling

count, the proportionality constant is rescaled by a geometric factor, but the proportional relationship still holds.

the population between the ground and excited states, the speed of this process is limited by the slowest rate in the photodynamics, which, under most excitation conditions, is the pumping rate $k_p$. Since $k_p$ is proportional to the absorption $\alpha$ [cf Eq. (5.2)], it is possible to access the latter by measuring the dynamics of the optically induced spin polarization process. To make the measurement more robust, we record $k_p$ for different optical powers and extract the proportionality coefficient $k_p^0$, which is itself proportional to the absorption [cf Eq. (5.2)].

To this end, we use the simple pulse sequence depicted in Figure 5.2(a). A laser pulse, generated by the AOM, probes the spin polarization dynamics, after which a delay $\delta_t = 200\,\mu s \gg T_1$, is applied to allow the spin population to relax back to thermal equilibrium. We then fit the polarization dynamics occurring at the beginning of the PL pulse with a monoexponential function to extract the pumping rate $k_p$. This procedure is repeated for various optical powers to obtain the power dependence of $k_p$. As expected the optically-induced polarization in the bright spin state accelerates when the optical power increases [Fig. 5.2(b)].

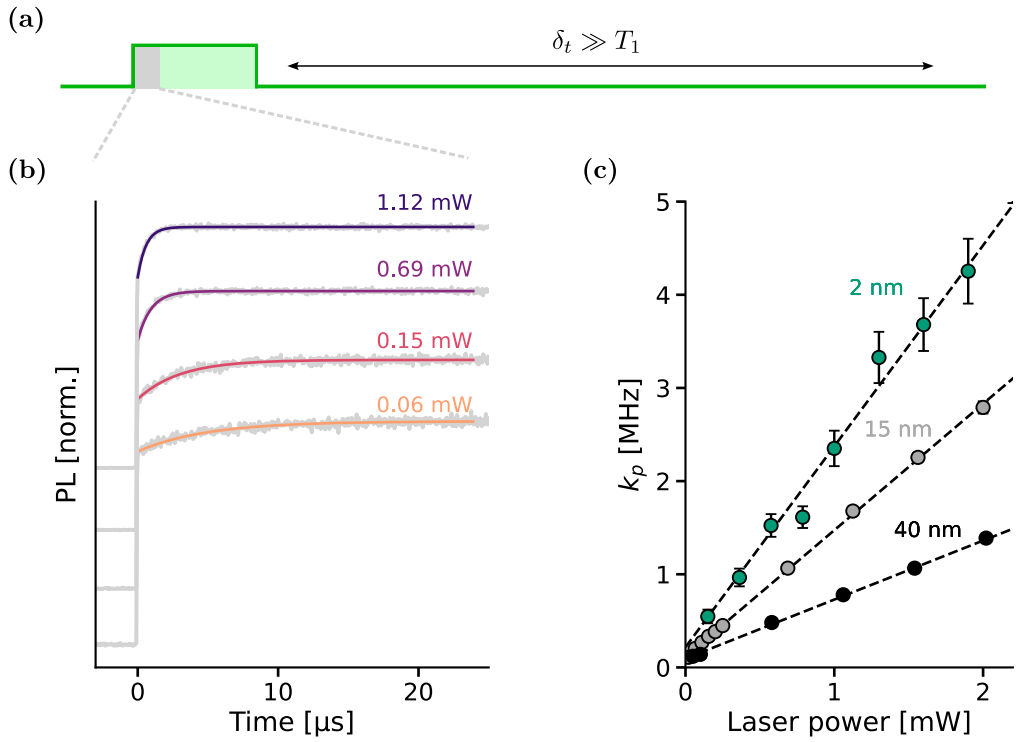


**Figure 5.2:** Polarization rate versus optical power for various flake thicknesses. (a) PL time trace versus optical powers on a 15 nm thick flake. Before the laser pulse, the defect is at thermal equilibrium. The solid colored lines are exponential fits. (b) Polarisation rates as a function of optical power for three different hBN flakes.

The pumping rates as a function of optical power are plotted for three flakes with different thicknesses in Figure 5.2(c). A clear thickness dependence is observed, with stronger pumping rates in thinner flakes for identical optical power. By fitting the curves with a linear scaling, we extract $k_p^0 = 2.1(1)$ MHz/mW for the 2 nm-thick flake, $k_p^0 = 1.33(1)$ MHz/mW for the 15 nm-thick flake, and $k_p^0 = 0.633(7)$ MHz/mW for the thickest flake of 40 nm. Through Equation (5.2), these results directly indicates a stronger optical absorption in thin flakes. To understand this behavior, we now turn to simulations.

## Simulations of Absorption Depth Profiles

To simulate the optical absorption profile through a flake of given thickness $t$, Guillaume Cassabois used the model illustrated in Figure 5.3(a). The sample is described as a multilayer stack, air/hBN($t$)/SiO2(90 nm)/Si. We therefore consider four optical media: air ($n_{\text{air}} = 1$), hBN ($n_{hBN} = 2.3$), SiO2 ($n_{SiO_2} = 1.45$), and Si ($n_{Si} = 4.3$), with refractive indices taken at the excitation wavelength $\lambda_L = 532$ nm. The air and bottom silicon layers are assumed to be semi-infinite, such that no light is reflected back from these regions. The structure is treated as purely one-dimensional and discretized into slices of thickness $\delta z$, where $\delta z$ is adapted to the flake thickness.

The time-averaged Poynting vector, $\Pi(t, z)$, is then computed using a transfer-matrix approach. This quantity encodes the direction and magnitude of the laser electromagnetic flux at the depth $z$ for a hBN flake of thickness $t$. The $V_B^-$ centers are modeled by a linear complex susceptibility that is set arbitrarily small, such that the presence of the defects does not affect the field distribution but allows us to extract an absorption profile. Specifically, we first compute the transmittance, $T(t, z)$ from the ratio between the incident and transmitted pointing vectors across a hBN slice $\delta z$:

$$T(t, z) = \frac{\Pi(t, z)}{\Pi(t, z - \delta z)}. \tag{5.4}$$

The absorption per unit length, $\alpha(t, z)$, is then given by:

$$\alpha(t, z) = \frac{T(t, z) - T(t, z - \delta z)}{\delta z}. \tag{5.5}$$

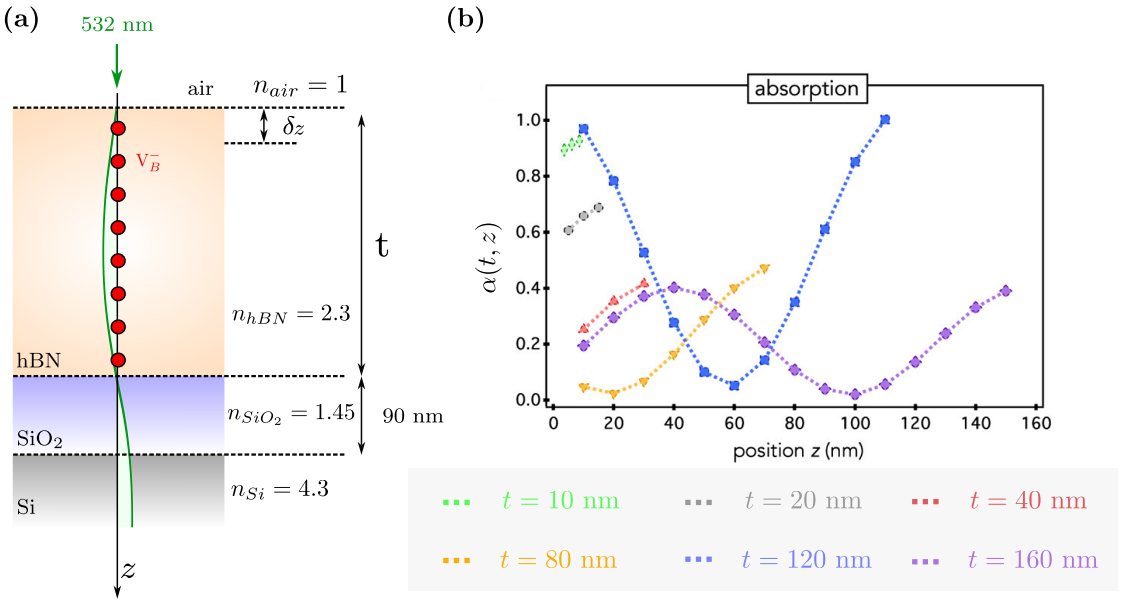


**Figure 5.3:** $V_B^-$ centers optical absorption in a hBN/$SiO_2$/Si structure. (a) Scheme of the model. (b) Computed optical absorption profiles for six hBN flake thickness: $t = 10$nm ($\delta z = 2.5$ nm), $t = 20$nm ($\delta z = 5$ nm), $t = 40$nm ($\delta z = 5$ nm), $t = 80$nm ($\delta z = 10$ nm), $t = 120$nm ($\delta z = 10$ nm) and $t = 160$nm ($\delta z = 10$ nm).

In Figure 5.3(b) we plot six simulated absorption depth profiles, corresponding to six hBN flake thicknesses, ranging from 10 nm to 160 nm. Interestingly, the simulations demonstrate that, due to Fabry–Pérot interferences, flakes with a thickness equal to a multiple of the laser wavelength $\lambda_L/2n_{\mathrm{hBN}} \approx 120$ nm exhibit maximum absorption near the optical interfaces. Remarkably, this behavior also holds for thin flakes ($t \ll \lambda_L$).

## Optical Absorption Thickness Dependence

Since the flakes are all thinner than the laser Gaussian beam waist, the detected signal in the experiment corresponds to an average over the entire flake thickness. To obtain the thickness-dependence of the absorption, $\alpha(t)$, the previous absorption profiles must therefore be integrated over the hBN flake thickness $t$:

$$\alpha(t) = \int_0^t \alpha(t, z)\, \delta z. \tag{5.6}$$

For a better comparison with the simulation, we expanded the dataset and measured, using the method described in Section 5.1.2, the coefficient $k_p^0$ for eight

additional flakes with thicknesses ranging from ∼60 to ∼120 nm. The extracted coefficients $k_p^0$ are plotted as a function of flake thickness in Figure 5.4, together with the simulated absorption thickness dependence $\alpha(t)$.

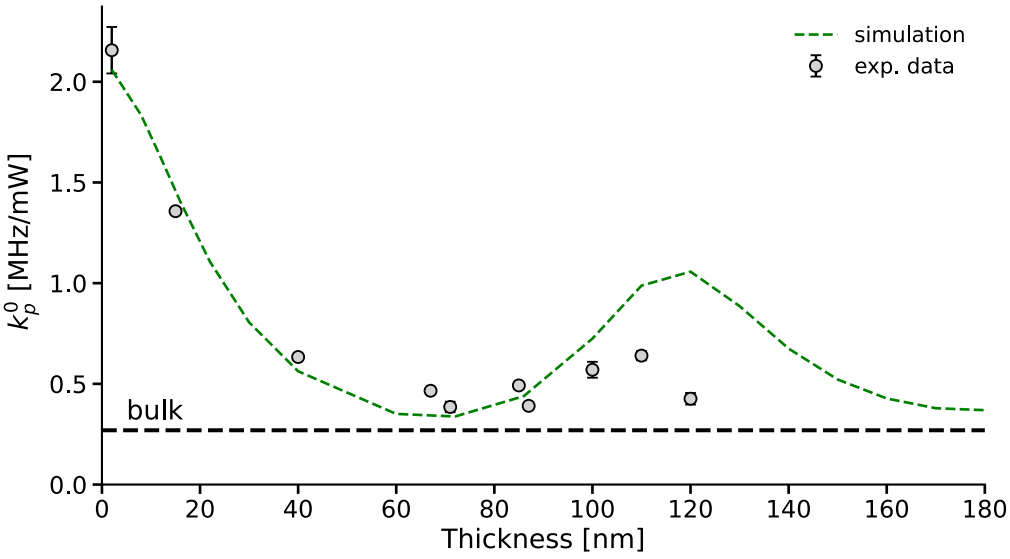


**Figure 5.4:** Factor $k_p^0$ (pumping rate per unit optical power) as a function of hBN flake thickness. Experimental data are compared with the simulated optical absorption thickness-dependence (green dotted line). The simulation curve is rescaled to match the experiment. The bulk value of $k_p^0$ is represented as a black dashed line.

A simple rescaling has been applied to the simulation to match the experimental values. A very good agreement is obtained. In particular, the model successfully reproduces the observed enhanced absorption in thin flakes. It also predicts an absorption increase at resonance: $t \approx \lambda_L / 2n_{\mathrm{hBN}} \approx 120$ nm, although additional data points are required to verify this feature. This first result confirms a first contribution to the observed non-linear thickness dependence of the PL signal: Fabry-Perot interference of the excitation laser beam within the hBN/$SiO_2$/Si nanostructure.

### 5.1.3 Emission thickness-dependence

In quantum optics, the radiative rate is not an intrinsic property of the emitter, but rather depends on its local electromagnetic environment. The dielectric environment, by reshaping the density of electromagnetic modes, can enhance or inhibit an optical transition [218]. When the dielectric environment takes the form of a resonant cavity, this effect is referred to as the Purcell effect. In the following, and by a slight abuse of terminology, we will also refer to any thickness

induced modification of the emission rate as a Purcell effect. Additionally, the proximity to the two optical interfaces can affect the radiation pattern of the emitters, thereby modifying the balance between PL emitted vertically, toward the objective, and PL coupled into guided modes, i.e, laterally within the hBN flake.

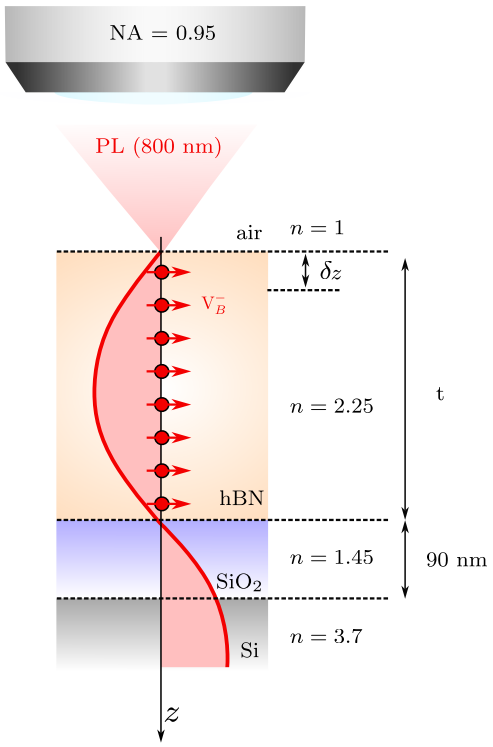


**Figure 5.5:** Scheme of the model used for the PL thickness dependence simulations.

To compute the relative contributions of both mechanisms to the detected PL signal, we collaborated with Jean-Michel Gérard from CEA Grenoble. The model, depicted in Figure 5.5, is almost identical to the one developed for the absorption, except that we now focus solely on the emission. The $V_B^-$ centers are modeled as in-plane electric dipoles emitting at $\lambda_e = 800$ nm. All refractive indices are adapted accordingly. The collection efficiency is defined for normal incidence with the numerical aperture of the objective used in this experiment, NA = 0.95. Since our goal is now to compute the radiation pattern and collection efficiency, a purely one-dimensional approach is no longer sufficient. Jean-Michel Gérard therefore opts to finite-difference time-domain (FDTD) simulations using the RSoft software suite from Synopsys.

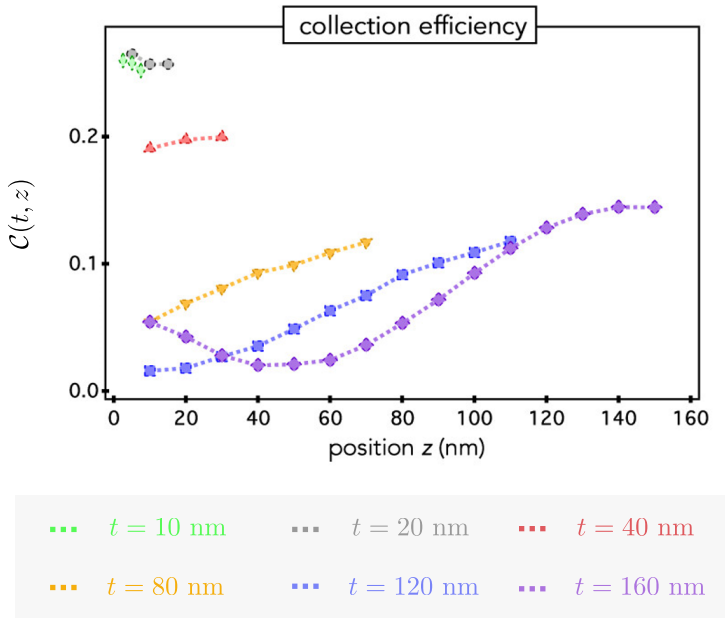


**Figure 5.6:** Computed collection efficiency depth profiles, $\mathcal{C}(t, z)$, for six hBN flake thicknesses: $t = 10$ nm ($\delta z = 2.5$ nm), $t = 20$ nm ($\delta z = 5$ nm), $t = 40$ nm ($\delta z = 5$ nm), $t = 80$ nm ($\delta z = 10$ nm), $t = 120$ nm ($\delta z = 10$ nm), and $t = 160$ nm ($\delta z = 10$ nm). The collection is calculated at normal incidence with NA $= 0.95$.

## Collection Efficiency

The collection efficiency $\mathcal{C}(t, z)$ calculated for some representative hBN thicknesses are shown in Figure 5.6. Interestingly, $\mathcal{C}(t, z)$ reaches its maximum ($\sim 25\%$) for very thin hBN layers. This is because in this regime the emission is exclusively distributed between the upper (air) and lower (silica) hemispheres, with preferential emission toward silica due to its higher refractive index. On the other hand, $\mathcal{C}(t, z)$ drops to much smaller values (down to 2%), when the hBN layer is thick enough to sustain a guided electromagnetic mode within the hBN flake. In this case, spontaneous emission is preferentially funneled into the guided mode and does not escape toward the microscope objective. Additionally, when $t$ approaches $\lambda_e/2n_{\mathrm{hBN}} \approx 180$ nm, Fabry–Pérot interferences reappear and give rise to revivals of the collection efficiency.

## Purcell Factor

We then simulated the depth profiles of the Purcell factor, $\mathcal{F}(t, z)$, which are shown in Figure 5.7. Only modest variations of $\mathcal{F}(t, z)$ are obtained, ranging from 0.67 to 1.05 over the full range of parameters $(z, t)$ under consideration. The Purcell factor

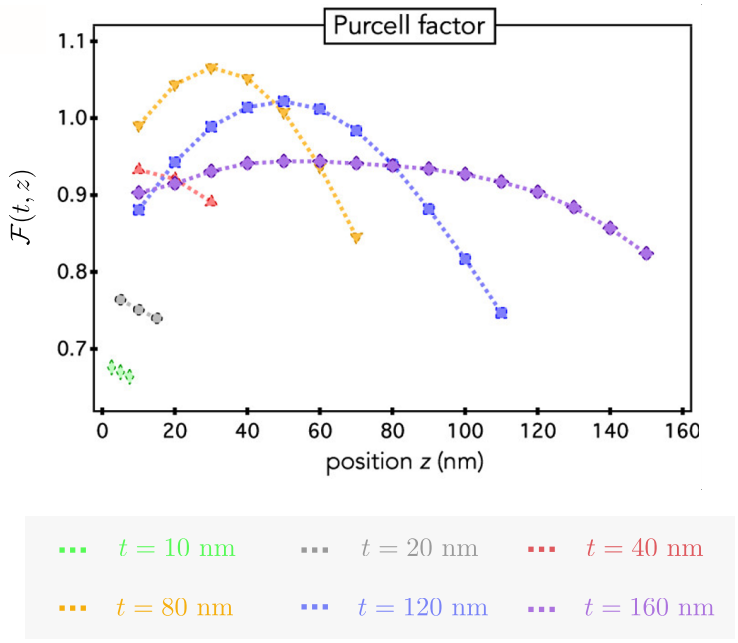


**Figure 5.7:** Computed Purcell factor, $\mathcal{F}(t,z)$, depth profiles for six hBN flake thickness: $t = 10$nm ($\delta z = 2.5$ nm), $t = 20$nm ($\delta z = 5$ nm), $t = 40$nm ($\delta z = 5$ nm), $t = 80$nm ($\delta z = 10$ nm), $t = 120$nm ($\delta z = 10$ nm) and $t = 160$nm ($\delta z = 10$ nm).

reaches its maximum at the center of an ∼100-nm-thick hBN flake, where the guided mode is most strongly confined [Fig. 5.7]. Conversely, it is minimized near the interfaces, where the guided mode intensity is low. In thin flakes, where the guided mode no longer exists and dielectric screening plays an important role [219], a clear inhibition of the Purcell factor is observed. Dielectric screening refers to the reduction of the effective electric field produced by a dipole due to the polarization response of its dielectric environment. In bulk hBN, the polarization induced by the radiated electric field is fully compensated within the material, but near an interface this compensation becomes incomplete, resulting in an induced field that partially opposes that of the dipole. As a consequence, thin flakes experience strong dielectric screening and an emission inhibition.

In any cases the variation of the Purcell factor remains low so that the product $\mathcal{C}(t,z)\mathcal{F}(t,z)$ is largely dominated by the variation of the collection efficiency.

### 5.1.4 Overall modelling and large scale study

Now that we have computed the depth profile of the absorption, collection efficiency and Purcell factor, we are able to compute the thickness dependence of the PL signal

through:

$$\mathcal{S}(t) = \int_0^t \mathcal{C}(t,z)\,\mathcal{F}(t,z)\,\alpha(t,z)\delta_z. \tag{5.7}$$

In parallel with the simulation work carried out by Guillaume Cassabois and Jean-Michel Gérard, we characterized the thickness of a few dozen hBN flakes using AFM and subsequently performed PL raster scans of each flake at an optical power of 1 mW. For each flake, the PL signal was then integrated over small regions, typically 5 µm ×5 µm, located near the AFM measurement sites. The averaged PL signal of each flake is plotted as a function of the flake thickness, together with the simulated curve in Figure 5.8.

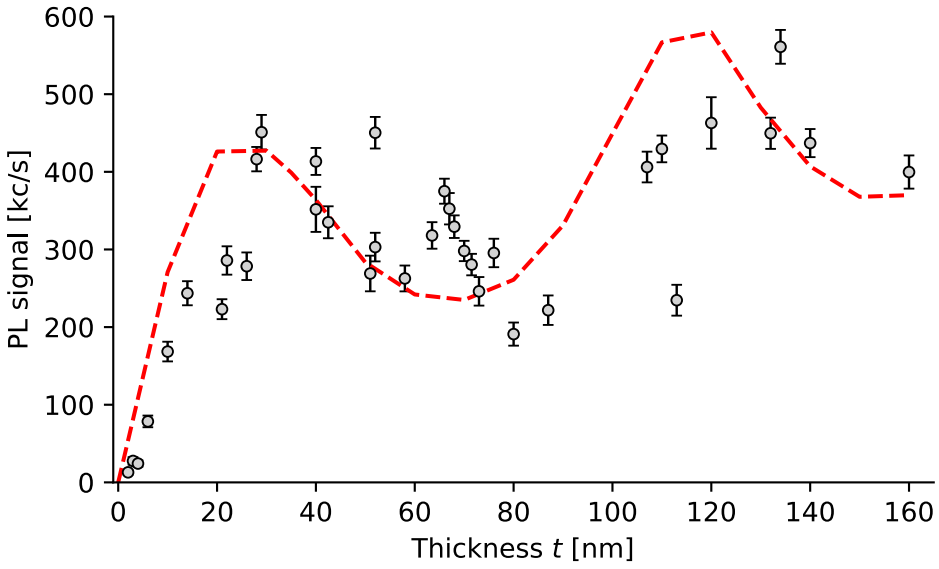


**Figure 5.8:** $V_B^-$ center PL signal dependence on hBN flake thickness. The red dashed line is the simulation, rescaled to fit the experimental data points.

A simple scaling factor is applied to the simulation to achieve the best fit with the experimental data, yielding good agreement. In particular, the simulation reproduces well the behavior observed on the staircase-like flake [Fig. 5.1], showing a local maximum around ∼40 nm and a PL signal minimum near 80 nm [Fig. 5.8].

This investigation, combining theoretical simulations and systematic analysis, demonstrates the presence of non-trivial nanophotonic effects in the optical response of $V_B^-$ centers embedded in nanometric hBN flakes. The most prominent contributions originate from a modification of the emission radiation pattern in thin flakes

and from Fabry–Pérot interference at the excitation wavelength. Although it is not surprising that a dielectric heterostructure produces such effects [52, 220], this is the first time their impact on the optical properties of a color center embedded within the van der Waals (vdW) material is reported. Notably, this study suggests that with a careful choice of thickness and refractive index, one could tailor a vdW heterostructure to optimize the optical properties of the color center. Lastly this study explains why, despite the low optical yield of $V_B^-$ centers, few-layer flakes provide a decent PL signal: enhanced absorption and the redirection of the radiation pattern toward the objective, compensate for the lower emitter density.

## 5.2 Orthorhombic splitting E in the few-layer limit

After the optical properties, we now study the spin properties of $V_B^-$ centers in few-layer hBN flakes. Based on the group-theoretical analysis of our colleagues Peter Udvarhelyi and Adam Gali, we argued in Chapter 1 that the orthorhombic splitting $E$, observed in all zero-field ODMR spectra of $V_B^-$ centers, originates from the coupling of the $V_B^-$ center's electron spin to the transverse component $\mathcal{E}_\perp$ of a local electric field. As the source of this field, we proposed a random distribution of charges within the hBN lattice, originating from $V_B^-$ centers and their positively charged counterparts. Later, in Chapter 4, we demonstrated that the orthorhombic zero-field splitting (ZFS), $E$, indeed increases with the density of $V_B^-$ centers, and that the zero-field ODMR spectra can be well reproduced using a charge model originally developed for the $NV^-$ center in diamond. In this Section, we now examine how this picture evolves as the thickness is reduced down to the few-layer limit.

### 5.2.1 Zero-field ODMR spectra in few-layer $h^{10}B^{14}N$ flakes

We begin with $h^{10}B^{14}N$ flakes, exfoliated from $S_{10}^a$ sample [cf. Sec. 4.2]. On a small area of the sample lie three flakes of interest: the 2 nm thick flake presented in Section 4.4, a second few-layer flake ($< 3$ nm), and a thicker flake of $\sim 15$ nm [Fig. 5.9(a)]. The fact that the three flakes are close to each other implies that the RF antenna does not have to be displaced from one ODMR measurement to another, and ensure similar experimental conditions for all measurements.

We start by recording a zero-field ODMR spectrum on the 15 nm thick flake. The latter, shown in Figure 5.9(b), exhibits a clear orthorhombic splitting of $E \approx 60$

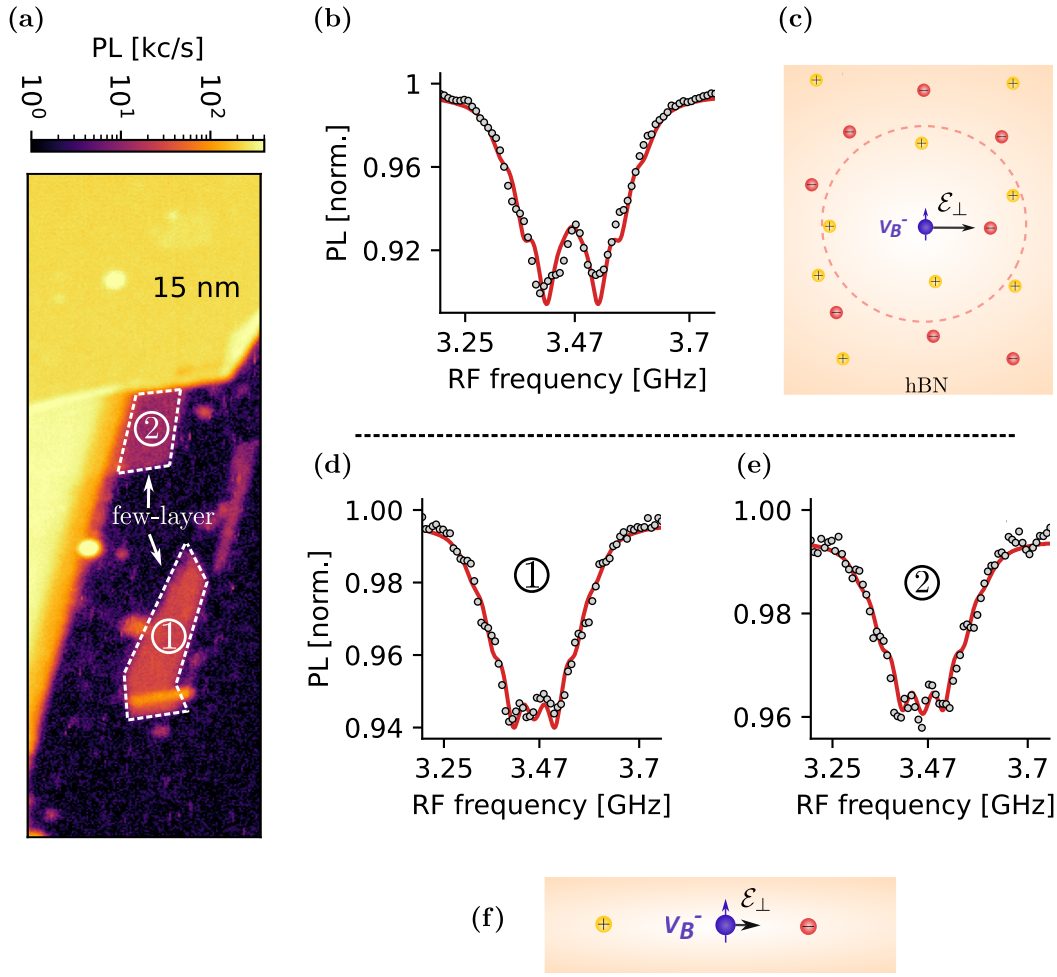


**Figure 5.9:** Orthorhombic splitting $E$ in few-layer $h^{10}B^{14}N$ flakes. (a) PL scan of the region of interest. (b) Zero-field ODMR spectrum on the 15 nm thick flake, the solid line is a fit with the charge model. (c) Illustration of a $V_B^-$ center in bulk hBN, surrounded by a charges distribution producing a transverse electric-field $\mathcal{E}_\perp$ at the $V_B^-$ center site. (d,e) Zero-field ODMR spectra of the two few-layer flakes (1) and (2), respectively. The solid line is a fit with the charge model, assuming a monolayer. (f) Illustration of a $V_B^-$ center in a few-layer hBN flake experiencing a reduced transverse electric field $\mathcal{E}_\perp$.

MHz. Using the charge model introduced in Section 4.2.2, Peter Udvarhelyi and Adam Gali, fitted the data and extracted a charge density of $\rho_c = 0.054(5)$ nm$^{-3}$. A value in excellent agreement with the one inferred on the bulk crystal $S_{10}^a$, from which these flakes have been exfoliated [cf. Sec. 4.2.2]. We therefore conclude that the $V_B^-$ centers embedded in this 15 nm-thick flake experience the same charge environment, and therefore the same transverse local electric field, $\mathcal{E}_\perp$, as that of the bulk crystal [Fig. 5.9(c)].

We now turn to the few-layer flakes. Their ODMR spectra, shown in Figures 5.9(d,e), stand in sharp contrast to that of the thick flake, showing no clear

orthorhombic splitting within the measurement precision. The characteristic hyperfine structure of $h^{10}B^{14}N$ crystals, comprising seven hyperfine peaks [cf. Chap. 3], even becomes distinctly visible [Fig. 5.9(d,e)].

This behavior is well explained by the simulations performed by Peter Udvarhelyi and Adam Gali. For this given charge density, $\rho_c = 0.054(5)$ nm$^{-3}$, their model indicates that the transverse electric field experienced by a $V_B^-$ center is predominantly generated by roughly ten nearby charges, localized within a sphere of diameter $d \sim 7$ nm. When the flake thickness $t$ becomes smaller than $d$, the number of charges contributing significantly to the transverse electric field at the $V_B^-$ center site decreases by a factor of $\sim d/t$. For hBN flakes approaching the monolayer limit, the orthorhombic parameter $E$ thus becomes too small to be resolved [Fig. 5.9(f)], leading to a single magnetic resonance in the ODMR spectrum. This effect and the emergence of a well-defined hyperfine structure are both well reproduced by the microscopic charge model applied to a monolayer hBN [red solid lines in Figs. 5.9d,e].

Notably, the orthorhombic splitting vanishing is accompanied by weak shift of the axial ZFS parameter $D$ toward lower frequency [Figs. 5.9d,e]. This prediction is fully consistent with an ab initio report which predicted a shift of the parameter $D$ by few MHz for $V_B^-$ centers embedded in monolayer hBN [80].

These results constitute a first demonstration of the impact of the reduced dimensionality on the spin properties of $V_B^-$ centers.

### 5.2.2 ODMR spectroscopy versus field in $h^{10}B^{15}N$ flakes

We now demonstrate that this result can be reproduced in a few-layer $h^{10}B^{15}N$ flake exfoliated from the $S_1$ bulk crystal [cf. Chap. 4]. The isotopic purification with $^{15}N$ , however, requires adapting our interpretation of the zero-field ODMR spectra. To illustrate this point, we express the fine-structure Hamiltonian including both the hyperfine interaction and an external magnetic field $B_z$. Within the secular approximation and considering a single nitrogen nuclear spin for simplicity, the Hamiltonian reads

$$\hat{\mathcal{H}} = D\hat{S}_z^2 + E\left(\hat{S}_x^2 - \hat{S}_y^2\right) + A_{zz}\hat{S}_z\hat{I}_z + |\gamma_e|\hat{S}_z B_z. \tag{5.8}$$

The eigenergies of this Hamiltonian are plotted in Figure 5.10 as a function of $B_z$ for a $^{14}$N and $^{15}$N isotope.

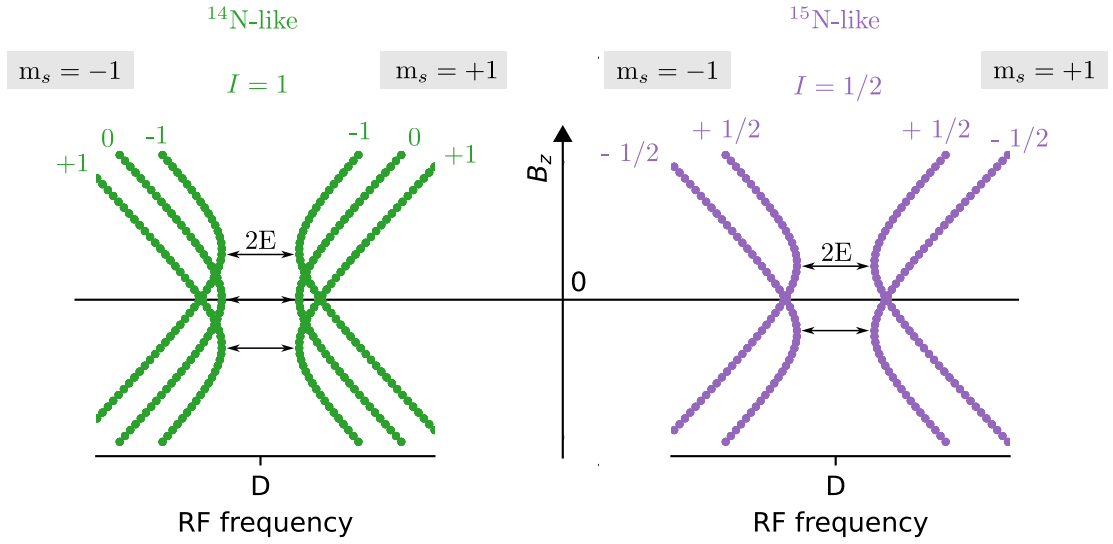


**Figure 5.10:** Othorhombic splitting $E$ and hyperfine interaction. Simulation of the othorhombic splitting near zero magnetic field with a nuclear spin $I = 1$ (left panel) and $I = 1/2$ (right panel).

When the nuclear spin multiplicity $(2I + 1)$ is odd, as with $^{14}$N which carries a nuclear spin $I = 1$, the two hyperfine states with zero nuclear spin projection ($m_I = 0$) overlap at zero-field [Fig. 5.10(a)]. As a result, the orthorhombic parameter can mixed them, yielding a splitting

$$\Delta f = 2E.$$

This is the situation we have encountered so far. In this case, the orthorhombic splitting $E$ can be directly extracted by fitting the zero-field ODMR spectrum. Conversely, when the nuclear spin multiplicity is even, such as with $^{15}$N ($I = 1/2$), no states with the same nuclear spin projection overlap at zero-field [Fig. 5.10(b)]. Consequently the orthorhombic splitting competes with the hyperfine interaction, and the splitting observed at zero bias magnetic field becomes

$$\Delta f = \sqrt{E^2 + \left(\tfrac{A_{zz}}{2}\right)^2}.$$

For $^{15}$N, which produces a large hyperfine splitting of $A_{zz} \approx 68$ MHz [cf. Chap. 3 § 3.2], the central splitting observed at zero field is therefore mostly dominated by the hyperfine interaction, making it difficult to directly extract the orthorhombic parameter $E$. This situation can nonetheless be easily circumvented by applying a

magnetic field $B_z$ that compensates the hyperfine splitting $A_{zz}$,

$$B_z = \frac{A_{zz}}{2\gamma_e} \approx 1.2\,\mathrm{mT}.$$

At this specific field, the branches corresponding to the same nuclear spin projection merge, and a simple splitting $\Delta f = 2E$ is recovered [Fig. 5.10(b)].

To probe this behavior, we replaced the permanent magnet with a calibrated coil, allowing the magnetic field to be swept simply by varying the current. We first performed the measurement on a bulk-like flake, recording an ODMR spectrum for each magnetic field value. The data are displayed as a 2D map in Figure 5.11(a). As expected, an anticrossing between the $m_I = +1/2$ hyperfine lines is observed around $B_z = 1.2$ mT. Notably, the ODMR spectra are contrasted enough to also resolve the orthorhombic splitting between the $m_I = -3/2$ lines, occurring at $B_z = \frac{3A_{zz}}{2\gamma_e} \approx 3.6$ mT. Interestingly, the splittings are accompanied by a reduction of the linewidth. This behavior, characteristic of anticrossings, results from the spin-state mixing induced by the parameter $E$, which effectively reduces the gyromagnetic ratio to zero and makes the transition insensitive to magnetic-field fluctuations [5, 221]. The improvement is nonetheless modest, suggesting that in this regime a second strong source of decoherence arises, most likely electric field noise.

To extract the orthorhombic parameter $E$, we select the ODMR spectrum recorded at $B_z = 1.2$ mT and fit it with a numerical simulation. The latter is based on the diagonalization of a Hamiltonian analogous to that given in Equation (5.8), except that it includes the hyperfine interaction with the three nearest neighbors nitrogen nuclear spins. The coil being calibrated, the magnetic field is treated as a fixed parameter. This procedure yields a good agreement with the experimental data [red solid line in Fig. 5.11(b)]. We extract an orthorhombic parameter of $E = 22(6)$ MHz, a lower value than that obtained for the $h^{10}B^{14}N$ bulk crystal. This difference can be attributed to the roughly twofold difference in neutron fluence between the two sample batches. Finally, we simulate a two-dimensional ODMR map as a function of the magnetic field with all parameters fixed [Fig. 5.11(c)]. The overall field dependence is well reproduced, except for the linewidth reduction at the anticrossings, which would require a more advanced simulation framework to be captured accurately.

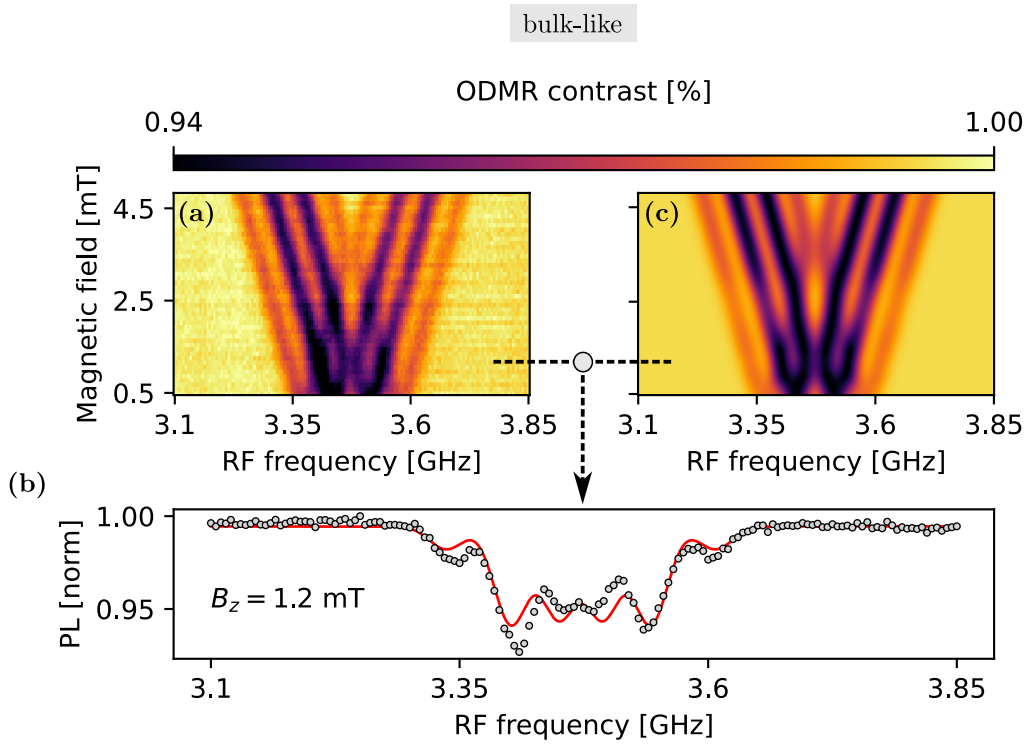


**Figure 5.11:** ODMR spectroscopy versus magnetic field in a bulk-like $h^{10}B^{15}N$ flake. (a) ODMR spectra spectroscopy as a function of the bias magnetic field $B_z$. (b) Line cut at $B_z = 1.2$ mT, the solid line is a fit using the simulation described in the main text. (c) Simulated 2D ODMR map versus field, with all parameters constrained by the fit realized at $B_z = 1.2$ mT.

We now proceed accordingly with the few-layer flake presented in Section 4.4. The two-dimensional ODMR map as a function of the magnetic field is shown in Figure 5.12(a). Notably, no orthorhombic splitting is observed within the limited signal-to-noise ratio. We follow the same procedure as for the thick flake, fitting the line cut at $B_z = 1.2$ mT before simulating the full field dependence [Fig. 5.12(b,c)]. Since no splitting appears in the data, we set $E = 0$. With this choice, a reasonable agreement is obtained.

The vanishing of the orthorhombic parameter $E$ thus appears as a robust and reproducible signature of few-layer flakes. It further highlights that our thinnest flakes are sufficiently thin to modify the local environment of the defect and impact its spin properties. This conclusion may extend well beyond the orthorhombic parameter.

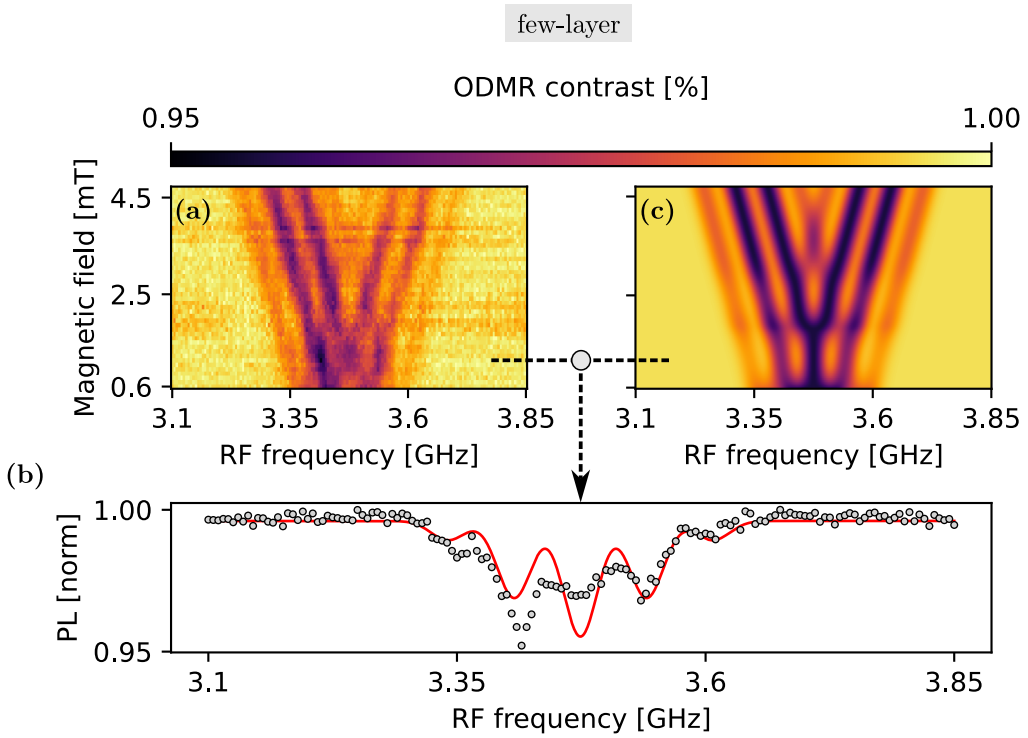


**Figure 5.12:** ODMR spectroscopy versus magnetic field in a few-layer $h^{10}B^{15}N$ flake. (a) ODMR spectra as a function of the bias magnetic field $B_z$. (b) Line cut at $B_z = 1.2$ mT, the solid line is a fit using the simulation described in the main text. (c) Simulated 2D ODMR map versus field, with all parameters constrained by the fit realized at $B_z = 1.2$ mT.

## 5.3 Thickness dependence of the longitudinal spin relaxation time $\mathbf{T_1}$

After ODMR spectroscopy, we now study the evolution of the longitudinal spin relaxation time $T_1$ of $V_B^-$ center with the hBN flake thickness. The sample is the same as the one studied in Sections 5.1, $h^{10}B^{14}N$ flakes exfoliated from $S_{10}^a$ bulk crystal [cf. Chap. 4]. As a reminder the pulsed sequence used to measure $T_1$ is depicted in Figure 5.13(a). A first laser pulse polarizes the spin in $|m_s = 0\rangle$, while after a delay $\tau$, a second laser pulse reads out the spin state. $T_1$ is then extracted by fitting the decay of the readout PL signal with an exponential decay. A relaxation curve measured at room temperature on a thick flake (80 nm) is displayed in Figure 5.13(b). From the fit we obtain $T_1 = 15.7(1)$ µs, a value similar to the one measured on the bulk crystal $S_{10}^a$ [cf. Chap. 4]. As already discussed in Chapter 1 and 4, a $T_1$ value lying around $15 - 20$ µs indicates a spin relaxation limited by spin-phonon interaction [110, 117, 118, 222]. We conclude that in regard of the longitudinal spin relaxation times $T_1$, a 80 nm flake can be considered as a bulk

crystal. We now perform the $T_1$ sequence on a few-layer flake. The resulting curve is plotted in Figure 5.13(b). A clear shortening of $T_1$ is observed. Now, the spin populations relax within only $T_1 = 1.7(1)$ µs.

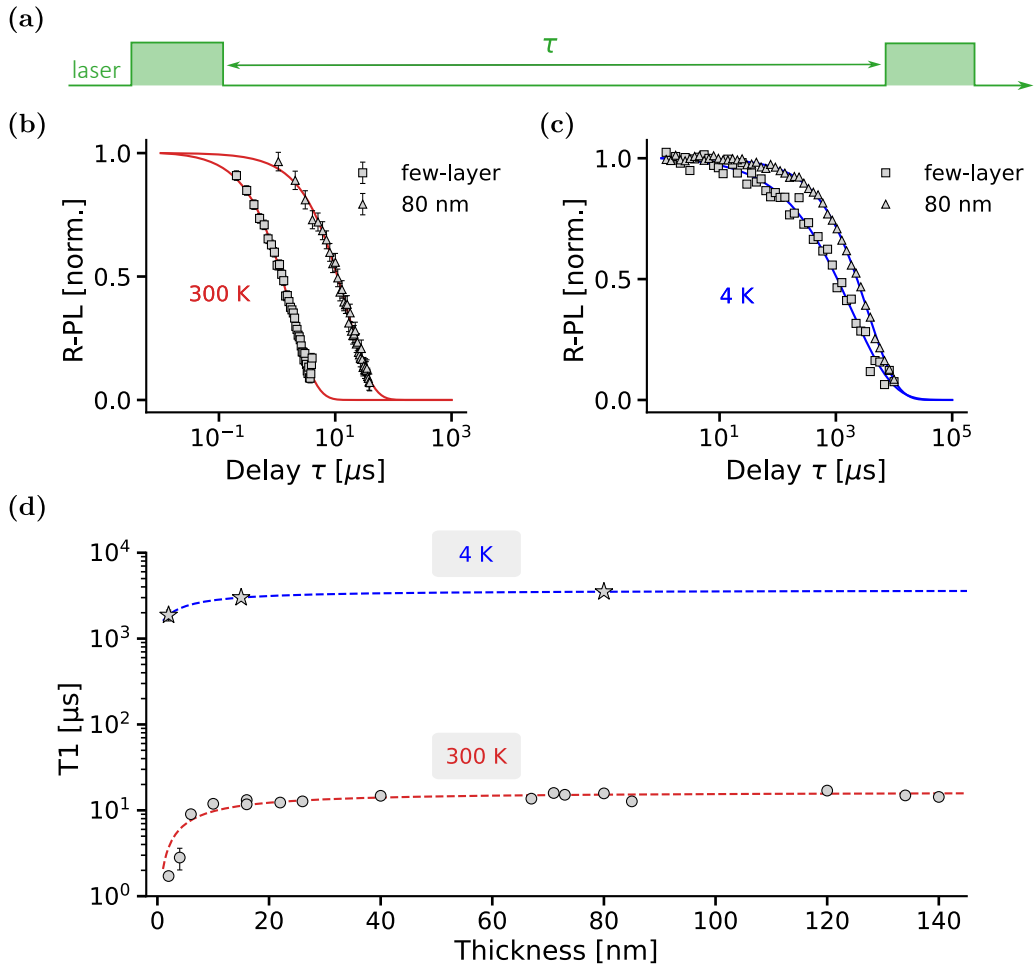


**Figure 5.13:** $T_1$ thickness dependence at room and cryogenic temperatures. (a) Scheme of the $T_1$ sequence. (b,c) Readout PL signal as a function of the delay $\tau$ for a 80 nm thick flake (triangles) and a few-layer flake (squares), measured at room temperature (b) and 4 K (c). The solild lines are stretch exponential fits. The curves are normalized between 0 and 1 to facilitate comparison. (d) $T_1$ versus thickness under both temperature conditions. The colored dashed lines are guides for the eye.

To confirm this observation, we performed systematic measurements of $T_1$ as a function of the flake thickness, with the results displayed in Figure 5.13(d). These data show that $T_1$ starts to decrease from its bulk value when the flake thickness falls below approximately 10 nm, thereby confirming that the observed $T_1$ reduction originates from the reduced thickness.

In the solid-state spin-defect literature, it is common to observe a reduction of

$T_1$ when the defect lies close to a surface or interface. This has, for instance, been reported for shallow $NV^-$ centers in bulk diamond as well as for $NV^-$ centers hosted in nanodiamonds [47, 48, 223, 224]. The origin of this phenomenon is generally attributed to surface magnetic noise, from paramagnetic impurities located at the surface. Such surface-induced noise opens an additional relaxation channel, $T_s^{-1}$, so that the total relaxation rate becomes

$$T_1^{-1} = T_p^{-1} + T_s^{-1}, \tag{5.9}$$

where $T_p^{-1}$ denotes the spin–phonon contribution. While this surface term can be neglected in bulk samples, it may dominate the spin–phonon relaxation in few-layer flakes, thereby leading to a pronounced reduction of $T_1$. Notably, if this surface magnetic noise is governed by dipolar interaction between paramagnetic impurities, no $T_1$ improvement should occur at low temperature in the thin flakes, as the dipolar interaction is in itself temperature independent. To test this hypothesis we reproduced the $T_1$ measurements on the thick and few-layer flake at 4K. The two resulting curves are plotted in Figure 5.13(c). Strikingly, the $T_1$ of both flakes scales up to the millisecond. This observation leads us to conclude that dipolar coupling is not the mechanism underlying the magnetic noise.

As an alternative, we initially proposed that the spin–phonon relaxation rate, $T_p^{-1}$, could be modified when going from bulk to the few-layer regime. However, a recent ab initio study contradicted this hypothesis by demonstrating no significant change in the spin–phonon interaction between bulk and monolayer hBN [118]. Hence, as an alternative explanation, we propose that the observed behavior could originates from thermally activated magnetic noise, such as a spin bath excited by lattice vibrations or charges hopping between traps [225, 226].

To date, the exact mechanism remains unknown. Further characterization could involve a detailed examination of the $T_1$ temperature dependence in both bulk and few-layer flakes, as well as a refined analysis of the stretch exponent of the decay. In this regard, it is worth noting that the entire room-temperature dataset is well fitted by a monoexponential function. The conclusion is less clear for the $T_1$ measured on a few-layer flake at low temperature [Fig. 5.13(c)], which clearly exhibits a decay with an exponent below unity. However, additional statistics would be required to draw a firm conclusion. Another possible approach would be to deposit few-layer

flakes on different substrates to identify the role of the hBN/substrate interface in this phenomenon.

## 5.4 Spin coherence of $V_B^-$ centers in atomically-thin hBN flakes

If the proximity to the surface is known to affect the longitudinal spin relaxation time $T_1$, it is even more established that it is detrimental to the spin coherence. Donor atoms in silicon [227], semiconductor quantum dots [228, 229], and $NV^-$ centers in diamond [45–49, 230–233], all exhibit degraded spin coherence when the spin is located within a few nanometers of the surface. In the final section of this manuscript, we therefore aim to verify whether the same conclusion holds for $V_B^-$ centers embedded in atomically thin hBN flakes.

To this end, we study two sets of $h^{10}B^{15}N$ flakes: those exfoliated from the $S_1$ crystal and those exfoliated from the $S_{10}$ crystal [cf. Sec. 4.3]. Our previous characterization of the bulk crystals, presented in Chapter 4, led us to conclude that the spin-echo coherence time $T_2$ is not limited by the same type of spin bath in the two samples [Fig. 5.14]. In the bulk crystal $S_1$, the $T_2$ lies close to the theoretical limit of $\sim 200$ ns imposed by the $^{10}B^{15}N$ nuclear spin bath, whereas in $S_{10}$ it is clearly degraded below 100 ns [cf. Sec. 4.3.3]. Through cross-relaxation relaxometry, we further attributed the origin of this noise to a bath of electron spins ($S = 1/2$) whose density increases with neutron fluence. These two regimes are illustrated in Figure 5.14. To this initial picture, we now likely need to add a contribution from surface magnetic noise, depicted as yellow spins in the figure. As the flake thickness is reduced, this additional noise source could compete with the bulk nuclear and electron spin baths, further degrading the spin coherence [Fig. 5.14]. We now verify this hypothesis by measuring the spin-echo coherence times in both samples, starting with a few-layer flake exfoliated from crystal $S_1$.

### 5.4.1 Few-layer flake from $S_1$ sample

We focus here on the few-layer flake introduced in Chapter 4, Section 4.4, for which we previously demonstrated that the ODMR linewidth remained unchanged compared to the bulk. It emits a PL signal of approximately 60 kc/s, with a signal-to-noise ratio exceeding 30 [Fig. 5.15(a)]. Its AFM profile, replotted in

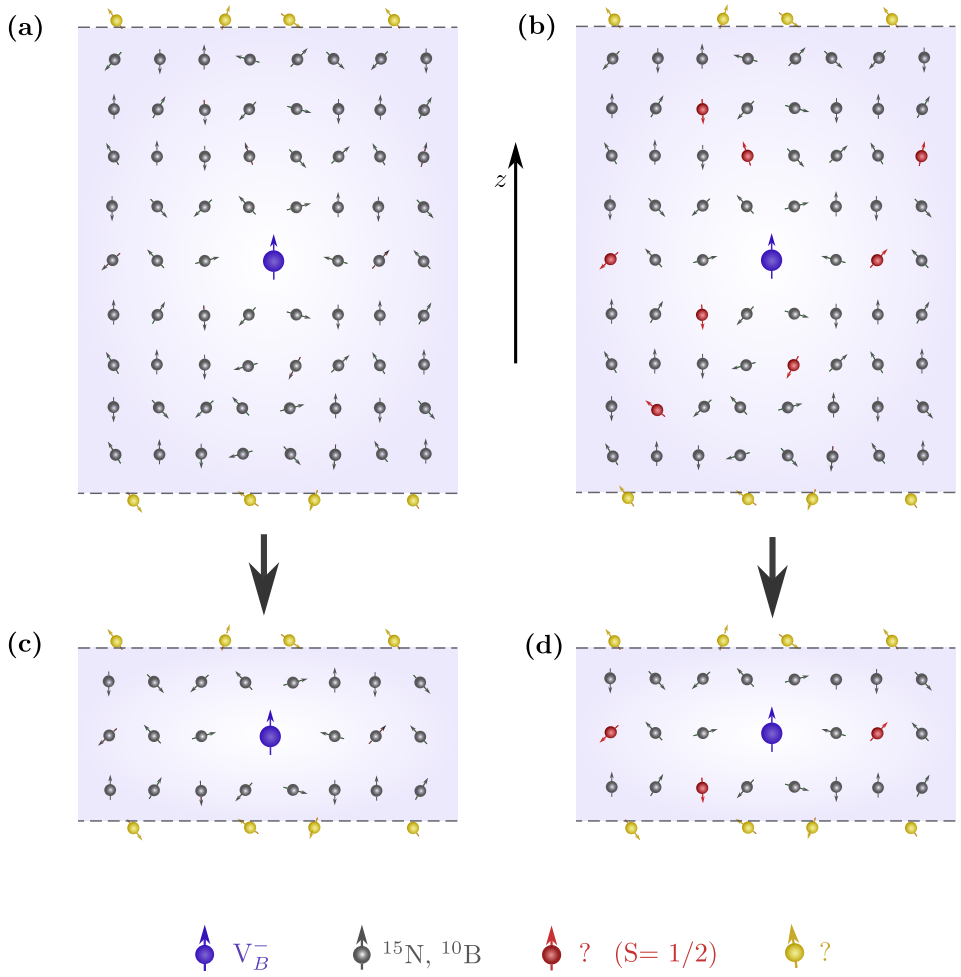


**Figure 5.14:** Illustrations or the different expected spin bath in bulk and few-layer hBN. $V_B^-$ center surrounded by (a) a nuclear spin bath and (b) both nuclear and electron spin bath. (c,d) Same in a few-layer flake. Purple: $V_B^-$ center electron spin, grey nuclear $^{10}$B $^{15}$N nuclear spins and in yellow surface spins.

Figure 5.15(b), exhibits a step height of 3 nm, which, as a reminder, corresponds to about nine layers when neglecting a potential contamination layer, or six layers when accounting for it. In both cases however, the thickness of the flake implies that $V_B^-$ centers are in average located only $\sim$ 1.5 nm away from an interface. We apply a magnetic field of a few mT along the $z$ axis, target the most contrasted hyperfine line on a given electronic branch, and perform a Rabi sequence. The result is shown in Figure 5.15(c).

Clear oscillations are observed, confirming that the $V_B^-$ center electron spin can be coherently controlled down to the few-layer limit. With a $\pi$-pulse duration of $t_\pi \sim 12$ ns, we subsequently perform a spin-echo sequence. For comparison, the

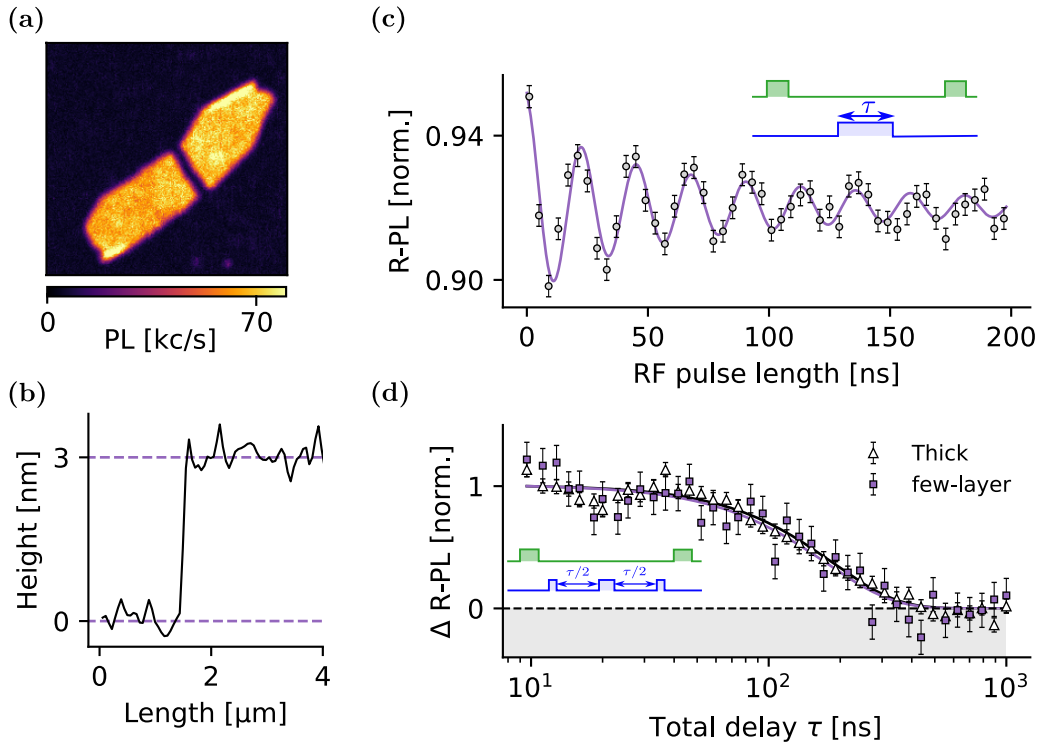


**Figure 5.15:** Spin coherence of a few-layer $h^{10}B^{15}N$ flake exfoliated from $S_1$ crystal. (a) PL scan at $P_{opt} = 0.5$ mW. (b) AFM profile. The dashed lines are guide for the eyes. (c) Readout PL signal as a function of the RF pulse length during a Rabi sequence. The sequence is illustrated in the inset. (d) Differential readout PL signal as a function of the total free precession time during a spin echo sequence for the few-layer flake (squares) and a thick flake (triangles). The solid lines are stretch exponential fits. The sequence is illustrated in the inset.

spin-echo curve obtained on this few-layer flake is plotted along with a spin echo sequence measured on a nearby thick flake in Figure 5.15(d). The result is clear: both curves decay with the same characteristic time. By fitting them with a stretched-exponential decay, we extract $T_2 = 170(15)$ ns for the few-layer flake and $T_2 = 186(8)$ ns for the thick one. Hence, in sharp contrast with $T_1$, the spin coherence time $T_2$ remains fully preserved down to atomic-scale thickness. We conclude that, surprisingly, surface magnetic noise does not play any role on the spin coherence of $V_B^-$ centers embedded in atomically-thin hBN flakes.

### 5.4.2 Few-layer flakes from $S_{10}$ sample

We now turn to a second set of thin flakes, this time exfoliated from the $S_{10}$ bulk crystal [cf. Sec. 4.3]. We begin with a simple ODMR spectroscopy characterization on three flakes with thicknesses of 15 nm, 4 nm, and 2 nm. Under a bias magnetic field $B_z$ of few mT, a single electron spin resonance is interrogated. The corresponding ODMR spectra are shown in Figure 5.16.

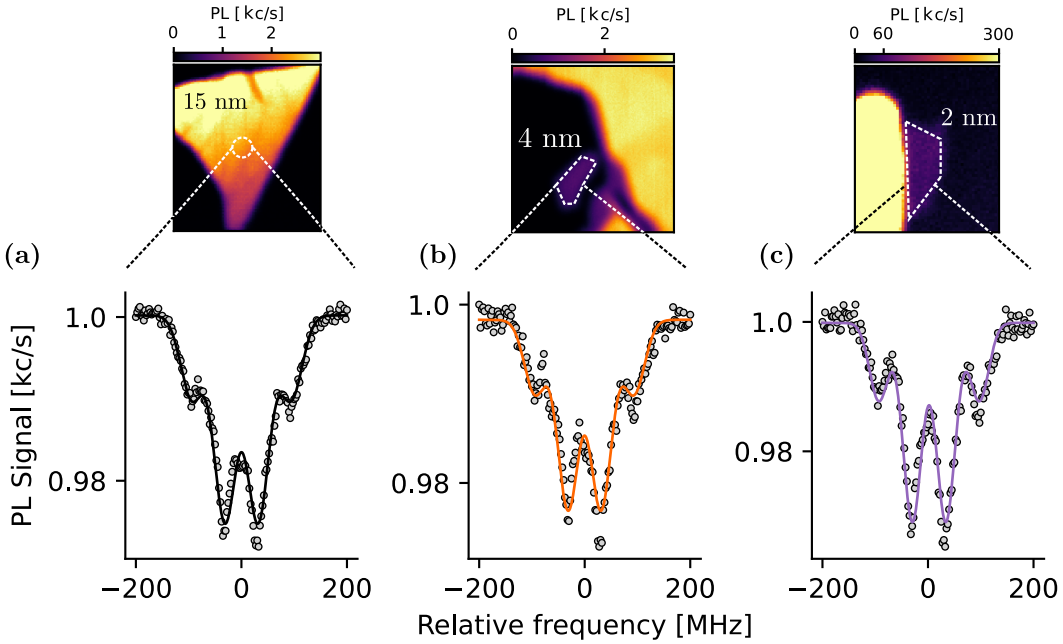


**Figure 5.16:** Inhomogeneous broadening in thin flakes exfoliated from $S_{10}$ crystal. (a–c) ODMR spectra of the three flakes. A bias magnetic field of a few mT is applied, and the spectra are focused on the lower electronic branch. The fits (colored solid lines) are made with four equaly-spaced Gaussian functions sharing the same linewidth. The top panels are the corresponding PL raster scans of the flakes.

Fitting the spectrum of the 15 nm flake with four Gaussians functions, we extract a linewidth of $\Gamma = 49.7(6)$ MHz, for an individual hyperfine line. This value, larger than that expected for a linewidth limited by the hyperfine interaction with the boron shell, is nonetheless consistent with the characterization of the bulk sample, for which neutron irradiation was found to broaden the ODMR linewidth [cf. Sec 4.3.2]. For the 4 nm-thick flake, a similar result is obtained with $\Gamma = 47.7(9)$ MHz. In contrast, a clear linewidth narrowing is observed for the thinnest 2 nm flake, with $\Gamma = 42.0(6)$ MHz, the same value as for the $S_1$ sample, which was exposed to a tenfold lower neutron fluence. Hence, thickness reduction appears surprisingly to have mitigated the inhomogeneous broadening induced by the excessively high neutron fluence and help recover a hyperfine-limited linewidth. Encouraged by this counterintuitive result, we attempted a spin-echo sequence on the 2 nm flake. Unfortunately, prolonged exposure to relatively high optical power damaged the flake, resulting in a dark region with reduced PL counts.

We eventually identified an alternative few-layer flake, consisting of a thinner region ($\sim$2 nm) adjacent to a thicker part [Fig. 5.17(a)]. Once the optical power reduced,

we perform spin-echo sequences on both the thick and thin regions. On the thick part, we obtain $T_2 = 89(6)$ ns, consistent with the $T_2$ degradation observed in the bulk crystal. Strikingly, the few-layer area exhibits a longer coherence, with $T_2 = 168(7)$ ns [Fig. 5.17(b)]. A twofold improvement compared to the thick-flake and bulk values. Intriguingly, in the $S_{10}$ sample, the spin coherence is not only preserved beside the atomic proximity with the surface but is even improved in the few-layer limit.

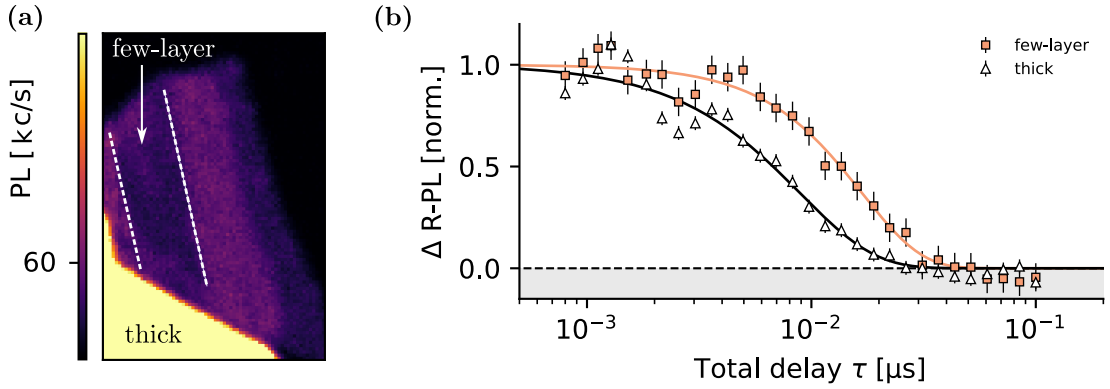


**Figure 5.17:** Spin echo coherence time in a few-layer flake exfoliated from $S_{10}$ crystal. (a) PL scan of the region of interest. the thick area is saturated. (b) Readout PL signal as a function of the total free precession time $\tau$ during an echo sequence. Orange squares are data from the few-layer area and white triangles data from the thick area. The solid lines are stretch exponential fits.

### 5.4.3 Qualitative explanation

In contrast to most of the literature on shallow spin defects, the $V_B^-$ centers spin coherence appears unaffected by proximity to the interface and can even be improved in atomically thin flakes, depending on the irradiation time. We tentatively interpret these behaviors with the qualitative picture analogue to the one proposed in Section 5.2, for the orthorhomic splitting [Fig. 5.18].

When the decoherence is governed by the lattice nuclear spin bath, as for the $S_1$ sample, the effective spin volume contributing to decoherence is limited to the nearest neighbors [Fig. 5.18(a)]. As a result, there is little difference in the defect environment between few-layer and bulk flakes, and no significant modification of the spin echo coherence time $T_2$ is observed [Fig. 5.18(b)].

Conversely, if the decoherence is dominated by an electronic spin bath, as in the $S_{10}$ sample, the effective spin volume governing the decoherence is much larger, owing

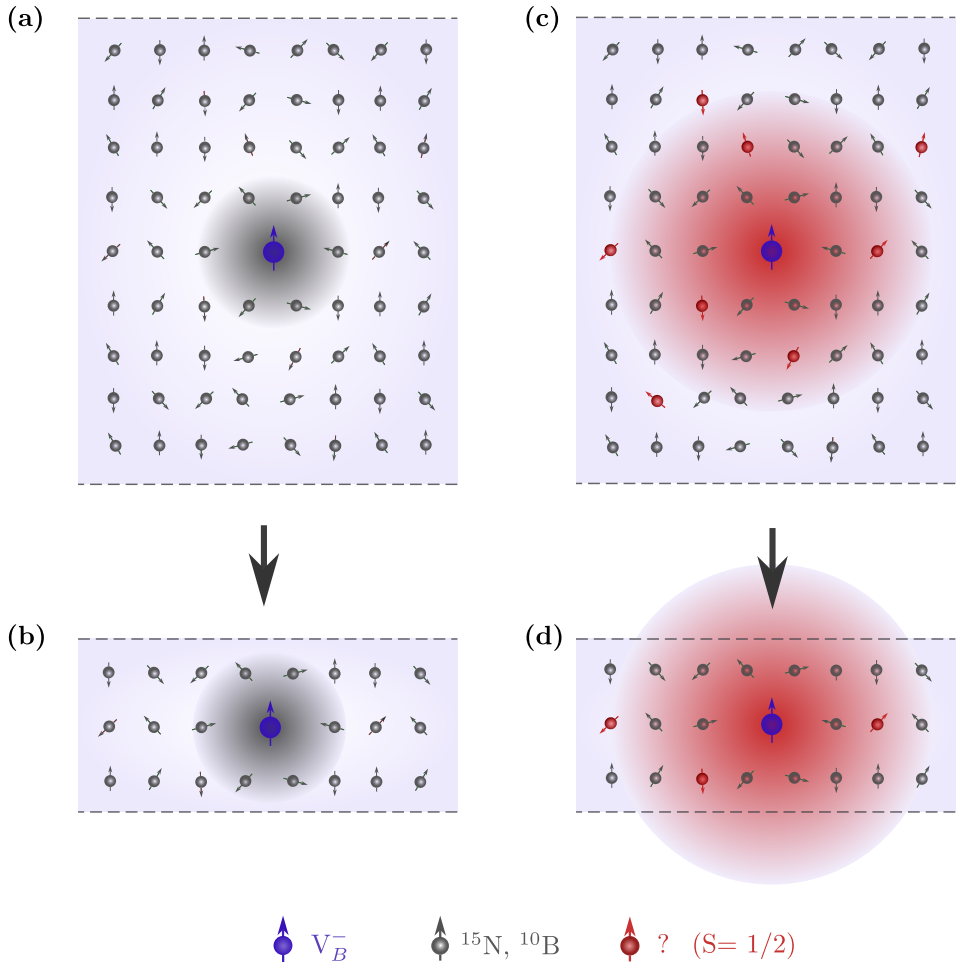


**Figure 5.18:** Illustrations of the effective spin volume surrounding a $V_B^-$ center. (a) Nuclear spin bath in bulk hBN. (b) Electron spin bath in bulk hBN. (c) Nuclear spin bath in a few-layer flake. (d) Electron spin bath in a few-layer flake. The effective spin volume is represented as a shaded sphere around the $V_B^-$ center.

to the approximately three orders of magnitude higher electron gyromagnetic ratio [Fig. 5.18(c)]. In this case, reducing the flake thickness below this characteristic volume can decrease the number of electronic spins in the defect environment and thereby improve the coherence [Fig. 5.18(d)]. In the last thin flake presented, the thickness reduction was probably sufficient to reach again the nuclear-spin-limited regime. This picture stands in stark contrast with the current state of the literature on shallow spin defects, where surface proximity is consistently reported to be detrimental to spin coherence. Instead, our results suggest that reducing the thickness down to the few-layer limit can actually help improve coherence. While for $V_B^-$ centers the spin-coherence gain is ultimately constrained by the strong nuclear spin bath, one could envision a more significant improvement in a van der

Waals material free of nuclear spins.

The second important conclusion of this work is the surprising absence of surface magnetic noise. One could legitimately argue that the spin coherence of the $V_B^-$ center is already so strongly limited by the dense nuclear spin bath that the impact of any additional surface noise remains undetectable. However, despite the intrinsically short coherence time $T_2$, it appears unlikely that an electron spin bath located only $\sim$1 nm from the defect would not be detected. Alternatively, this feature could originate from the host material of $V_B^-$ centers, hBN. As it is well known in the van der Waals materials community [57], hBN provides exceptionally clean and charge-free interfaces, which may render it particularly immune to interface-related magnetic noise.

## 5.5 Conclusion

The peculiar two-dimensional nature of van der Waals materials allows one to easily reach the few-layer limit by mechanical exfoliation, thereby unlocking, with remarkable simplicity, atomic-scale proximity between an embedded spin defect and the surface. In this final chapter, we took advantage of this property to study how reducing the thickness from bulk-like to atomic scale impacts both the optical and spin properties of the $V_B^-$ centers.

We first focused on the optical response and demonstrated the crucial role of nanophotonic effects, primarily Fabry–Pérot interference and radiation-pattern redirection, in determining the collected PL signal intensity. In few-layer flakes, both effects compensate for the small excitation volume and low quantum efficiency, yielding a decent PL signal. These findings should be considered in future sensing experiments to maximize sensitivity through tailoring sensor and substrate thicknesses.

We then studied the evolution of the orthorhombic splitting $E$ in the few-layer limit. From zero-field ODMR measurements performed on both $h^{10}B^{14}N$ and $h^{10}B^{15}N$ flakes, we observed the vanishing of the orthorhombic splitting. We demonstrated that this behavior can be accurately reproduced by a model based on a random local distribution of charges. Qualitatively, reducing the thickness below a few

nanometers decreases the number of charges surrounding the $V_B^-$ center, thereby producing a weaker transverse electric field.

Lastly, we investigated the impact of atomic-scale proximity to the interfaces on the spin relaxation times. While $T_1$ is reduced by roughly one order of magnitude in few-layer flakes, through a mechanism that remains to be identified, the coherence properties appear surprisingly insensitive to surface proximity. Even more strikingly, in a highly irradiated sample with a high defect density, reducing the thickness helped recover the nuclear-spin limited $T_2$ time. These results indicate that surface proximity is not systematically detrimental to spin coherence and even suggest that thickness reduction could become a viable strategy to enhance the coherence properties of spin defects in van der Waals materials.

# Conclusion

The rise of van der Waals materials has not only provided a wealth of new condensed matter phenomena to explore, but has also opened a promising avenue for the development of atomically thin quantum sensors. In this thesis, we contributed to this emerging research direction by investigating a first candidate for such a platform: the negatively charged boron vacancy ($V_B^-$) in hexagonal boron nitride (hBN). Hosted in a van der Waals crystal with exceptional protective capabilities, this defect exhibits a spin-dependent photodynamics reminiscent of the nitrogen-vacancy ($NV^-$) center in diamond, featuring a spin triplet ground state that can be optically initialized and read out at both room and cryogenic temperatures. Throughout this manuscript, we demonstrated that the electronic spin of the $V_B^-$ center couples to magnetic and electric fields, strain, and temperature, making this defect a potentially versatile quantum sensor. We further confirmed its sensing capabilities through the magnetic-field imaging of a van der Waals magnet, marking a proof of concept of magnetometry with spin defects embedded in a van der Waals material. However, two significant limitations were rapidly identified.

The first limitation arises from a symmetry-forbidden optical transition. Through an in-depth analysis of the spin-dependent photodynamics, we found that both room- and low-temperature behaviors can be well reproduced by assuming a negligible radiative decay rate. This result lends further support to the theoretical prediction that the $V_B^-$ center is an intrinsically dim emitter. This property is a severe limitation for sensing applications, as it prevents single-defect isolation and therefore restricts the spatial resolution of imaging to the diffraction-limited laser spot, on the micrometer scale. The second limitation originates from the dense nuclear-spin bath of the hBN lattice, which broadens the magnetic resonance and reduces the magnetic sensitivity. On this point, our work provides more encouraging results. Although the isotopic composition of hBN prevents the complete elimination of nuclear spins, we showed that isotopic purification with $^{10}B$ and $^{15}N$ yields a fourfold improvement in sensitivity by revealing a sharper and better-resolved hyperfine structure.

For such a sensor to be relevant, however, it must operate not in bulk or thick hBN flakes, but in the few-layer limit, where an advantage in sample proximity can be claimed over $NV^-$-based and other quantum sensors. To this end, we demonstrated an efficient method to engineer $V_B^-$ centers in atomically thin hBN flakes through neutron irradiation. Simultaneously we provided evidence that the $V_B^-$ center remains stable and operational for sensing even when located atomically-close to the surface.

In the last part of this manuscript, we explored the physics of $V_B^-$ centers embedded in few-layer hBN flakes, constituting a first case study of an optically active spin defect in an atomically-thin material. We demonstrated that nanophotonic effects, particularly Fabry–Pérot–like interference within the flake, play a major role in the collected photoluminescence intensity. This observation suggests that by carefully selecting the substrate or designing a suitable van der Waals heterostructure, one could significantly enhance the collection efficiency and thereby improve the overall sensitivity. Finally, we concluded this manuscript by investigating the spin-coherence evolution in the two-dimensional limit. We found that the spin-coherence time of the $V_B^-$ center is remarkably resilient to atomic-scale proximity to the surface, and can even improve when coherence is limited by an electron spin bath. We interpreted this unconventional behavior as arising from a reduction of the effective spin interaction volume surrounding $V_B^-$ centers in the few-layer limit. Although this intriguing observation cannot be fully exploited in hBN owing to the dense nuclear-spin bath that limits coherence to about 200 ns, it could lead to much more significant improvements in van der Waals materials free of nuclear spins. Such materials have indeed begun to attract attention, with recent reports of optically active spin defects in $GeS_2$ [234, 235].

The figure of merit of the improvement achieved through this thesis work is the magnetic-field sensitivity $\eta$. While we closed Chapter 1 with a sensitivity of $\sim 60$ $\mu T\sqrt{Hz}$ in a 80 nm-thick hBN flake, we closed Chapter 4, with a similar value of $\sim 100$ $\mu T\sqrt{Hz}$ in a 3 nm thick flake. Although this value is still roughly 50–100 times worse than the sensitivities achieved with state-of-the-art $NV^-$-based sensors, [24, 26, 147, 148], one must emphasize the proximity advantage. Assuming a magnetic dipolar field scaling as $1/r^3$, our defect probes magnetic fields roughly

a thousand times stronger than those sensed by a diamond tip positioned at ∼10 nm from the sample. This difference can earns additional order of magnitude when compared to ensemble-based sensors where the average distance between the $NV^-$ layer is more ∼ 100 nm. Hence, the $V_B^-$ center in hBN constitutes a competitive platform, especially in comparison with widefield $NV^-$ microscopy. While both techniques have a spatial resolution limited by optical diffraction, the atomic-scale thickness of hBN ensures much closer proximity to the sample and should not suffer from the optical aberrations that typically arise from light propagation through thick diamond sensors [42, 236].

Hence, $V_B^-$ centers embedded in thin hBN flakes hold great promise for future sensing applications, particularly for the study of other van der Waals materials and van der Waals heterostructures. One could propose for instance to use this new sensor to study van der waals superconductors. In the two-dimensional limit, superconducting magnetic vortices behave very differently than in bulk: they can arrange in a glassy state under the influence of disorder [237], or melt into a vortex liquid as the temperature approaches the superconducting critical temperature [238]. Notably, the vertical confinement also forces the vortices to expand laterally into so-called Pearl vortices [239]. The latter can reach micrometer scales in van der Waals superconductors such as $NbSe_2$ [240], such that our diffraction-limited spatial resolution should be sufficient to resolve them. In addition to static imaging, one could also perform noise spectroscopy using spin-echo or related dynamical decoupling schemes, which have recently been shown to be sensitive to the thermal motion of these superconducting magnetic vortices [240].

Alternatively, the atomic-scale proximity offered by this new platform is currently attracting attention for AC magnetic field sensing [241], particularly in the context of nuclear magnetic resonance spectroscopy [242]. Micro- and even nano-scale detection of nuclear spins has already been demonstrated using $NV^-$ centers in diamond [32, 243–245]. Interestingly, in a recent theoretical comparative study, Daly *et al.* estimate that, despite their less favorable optical and spin properties, $V_B^-$ centers could offer enhanced performance for AC magnetic-field sensing of nuclear spins compared to $NV^-$ centers in diamond, owing to their atomic-scale proximity to the target nuclei [242].

From a more fundamental perspective, strongly interacting solid-state spin ensembles can host a wealth of many-body phenomena, ranging from spin diffusion governed by hydrodynamic laws [246] to discrete time-crystal phases stabilized by periodic driving [247]. For such collective effects, the dimensionality and geometry of the spin ensemble play a primary role in determining the emergent dynamics [248]. A striking example was recently reported by Wu *et al.* [249], who demonstrated spin squeezing with a $NV^-$ centers ensemble confined in a $\sim$ 7 nm thick layer [249].

Spin defects in van der Waals materials represent a rapidly emerging platform for quantum technologies, combining the versatility of solid-state spin systems with the unique flexibility, atomic thickness, and integrability of 2D materials. The $V_B^-$ center in hBN stands as the first realization of this new generation of quantum sensors, paving the way for many others to come. We hope that the work presented in this thesis has modestly contributed to the ongoing exploration and understanding of this exciting new quantum sensing platform.

# List of Publications

The following publications are directly cited and discussed throughout this manuscript:

1. Péter Udvarhelyi, **Tristan Clua-Provost**, Alrik Durand, Jiahan Li, James H Edgar, Bernard Gil, Guillaume Cassabois, Vincent Jacques, Adam Gali *A planar defect spin sensor in a two-dimensional material susceptible to strain and electric fields*, **npj Computational Materials 9** 150 (2023) *(Derivation of the spin–electric-field and spin–stress Hamiltonians, and charge-state modeling applied to neutron-irradiated samples, discussed in Chapters 1 and 4.)*

2. Pawan Kumar, Florentin Fabre, Alrik Durand, **Tristan Clua-Provost**, Jiahan Li, James H Edgar, Nicolas Rougemaille, Johann Coraux, Xavier Marie, Pierre Renucci, Cédric Robert, Isabelle Robert-Philip, Bernard Gil, Guillaume Cassabois, Aurore Finco, Vincent Jacques *Magnetic imaging with spin defects in hexagonal boron nitride*, **Physical Review Applied 18**, L061002 (2022). *(Magnetic imaging of a van der Waals magnet with $V_B^-$ centers, discussed in Chapter 1)*

3. **T. Clua-Provost**, Z Mu, A Durand, C Schrader, J Happacher, J Bocquel, P Maletinsky, J Fraunié, X Marie, C Robert, G Seine, E Janzen, JH Edgar, B Gil, G Cassabois, V Jacques *Spin-dependent photodynamics of boron-vacancy centers in hexagonal boron nitride*, **Physical Review B 110** 014104 (2024). *(Study of the spin-dependent photodynamics of the $V_B^-$ center, discussed in Chapter 2)*

4. **T. Clua-Provost**, Alrik Durand, Z Mu, T Rastoin, Jules Fraunié, Eli Janzen, Hannah Schutte, James H Edgar, Grégory Seine, Alain Claverie, Xavier Marie, Cédric Robert, Bernard Gil, Guillaume Cassabois, Vincent Jacques *Isotopic control of the boron-vacancy spin defect in hexagonal boron nitride*, **Physical Review Letters 131** 126901 (2023) *(Isotopic purification and nuclear spin polarization, discussed in Chapter 3)*

5. **T. Clua-Provost**, Alrik Durand, Jules Fraunié, Cédric Robert, Xavier Marie,

Jiahan Li, James H Edgar, Bernard Gil, Jean-Michel Gérard, Guillaume Cassabois, Vincent Jacques *Impact of Thickness-Dependent Nanophotonic Effects on the Optical Response of Color Centers in Hexagonal Boron Nitride*, **Nano Letters 24** 12915-12920 (2024) *(Photoluminescence as a function of the hBN flake thickness, measurements and simulations ,discussed in Chapter 5)*

6. Alrik Durand, **Tristan Clua-Provost**, Florentin Fabre, Pawan Kumar, Jiahan Li, James H Edgar, Péter Udvarhelyi, Adam Gali, Xavier Marie, Cédric Robert, Jean-Michel Gérard, Bernard Gil, Guillaume Cassabois, Vincent Jacques *Optically active spin defects in few-layer thick hexagonal boron nitride*, **Physical Review Letters 131** 116902 (2023) *(Orthorhombic splitting in the few-layer limit, longitudinal spin relaxation time $T_1$ in thin flakes, discussed in Chapter 5)*

Work carried out in Toulouse by our collaborators Céric Robert and Jules Fraunié on the charge-state of the $V_B^-$ center, investigating its photoluminescence as a function of bias voltage.

4. Jules Fraunié, **Tristan Clua-Provost**, Sébastien Roux, Zhao Mu, Adrien Delpoux, Grégory Seine, Delphine Lagarde, Kenji Watanabe, Takashi Taniguchi, Xavier Marie, Thomas Poirier, James H Edgar, Jeremie Grisolia, Benjamin Lassagne, Alain Claverie, Vincent Jacques, Cedric Robert *Charge state tuning of spin defects in hexagonal boron nitride*, **Nano Letters 25** 5836-5842 (202)

# Bibliography


[1] C. L. Degen, F. Reinhard, and P. Cappellaro. "Quantum Sensing". *Reviews of Modern Physics* 89.3 (2017), p. 035002.

[2] I. K. Kominis, T. W. Kornack, J. C. Allred, and M. V. Romalis. "A Subfemtotesla Multichannel Atomic Magnetometer". *Nature* 422.6932 (2003), pp. 596–599.

[3] Achim Peters, Keng Yeow Chung, and Steven Chu. "Measurement of Gravitational Acceleration by Dropping Atoms". *Nature* 400.6747 (1999), pp. 849–852.

[4] Denis Vasyukov, Yonathan Anahory, Lior Embon, Dorri Halbertal, Jo Cuppens, Lior Neeman, Amit Finkler, Yehonathan Segev, Yuri Myasoedov, Michael L. Rappaport, Martin E. Huber, and Eli Zeldov. "A Scanning Superconducting Quantum Interference Device with Single Electron Spin Sensitivity". *Nature Nanotechnology* 8.9 (2013), pp. 639–644.

[5] F. Dolde, H. Fedder, M. W. Doherty, T. Nöbauer, F. Rempp, G. Balasubramanian, T. Wolf, F. Reinhard, L. C. L. Hollenberg, F. Jelezko, and J. Wrachtrup. "Electric-Field Sensing Using Single Diamond Spins". *Nature Physics* 7.6 (2011), pp. 459–463.

[6] P. Neumann, I. Jakobi, F. Dolde, C. Burk, R. Reuter, G. Waldherr, J. Honert, T. Wolf, A. Brunner, J. H. Shim, D. Suter, H. Sumiya, J. Isoya, and J. Wrachtrup. "High-Precision Nanoscale Temperature Sensing Using Single Defects in Diamond". *Nano Letters* 13.6 (2013), pp. 2738–2742.

[7] David M. Toyli, Charles F. de las Casas, David J. Christle, Viatcheslav V. Dobrovitski, and David D. Awschalom. "Fluorescence Thermometry Enhanced by the Quantum Coherence of Single Spins in Diamond". *Proceedings of the National Academy of Sciences* 110.21 (2013), pp. 8417–8421.

[8] H. Kraus, V. A. Soltamov, F. Fuchs, D. Simin, A. Sperlich, P. G. Baranov, G. V. Astakhov, and V. Dyakonov. "Magnetic Field and Temperature Sensing with Atomic-Scale Spin Defects in Silicon Carbide". *Scientific Reports* 4.1 (2014), p. 5303.

[9] G. Kucsko, P. C. Maurer, N. Y. Yao, M. Kubo, H. J. Noh, P. K. Lo, H. Park, and M. D. Lukin. "Nanometre-Scale Thermometry in a Living Cell". *Nature* 500.7460 (2013), pp. 54–58.

[10] L. Rondin, J.-P. Tetienne, T. Hingant, J.-F. Roch, P. Maletinsky, and V. Jacques. "Magnetometry with Nitrogen-Vacancy Defects in Diamond". *Reports on Progress in Physics* 77.5 (2014), p. 056503.

[11] Matthias Niethammer, Matthias Widmann, Sang-Yun Lee, Pontus Stenberg, Olof Kordina, Takeshi Ohshima, Nguyen Tien Son, Erik Janzén, and Jörg Wrachtrup. "Vector Magnetometry Using Silicon Vacancies in 4 H -SiC Under Ambient Conditions". *Physical Review Applied* 6.3 (2016), p. 034001.

[12] S. Hsieh, P. Bhattacharyya, C. Zu, T. Mittiga, T. J. Smart, F. Machado, B. Kobrin, T. O. Höhn, N. Z. Rui, M. Kamrani, S. Chatterjee, S. Choi, M. Zaletel, V. V. Struzhkin, J. E. Moore, V. I. Levitas, R. Jeanloz, and N. Y. Yao. "Imaging Stress and Magnetism at High Pressures Using a Nanoscale Quantum Sensor". *Science* 366.6471 (2019), pp. 1349–1354.

[13] Kihwan Kim, Jong Sung Moon, Dongkwon Lee, Jin Hee Lee, Yuhan Lee, Chanhu Park, Jugyeong Chung, Donghun Lee, and Je-Hyung Kim. "Quantum Sensing with Spin Defects: Principles, Progress, and Prospects for Use Cases". *Advanced Photonics* 7.06 (2025).

[14] Marcus W. Doherty, Neil B. Manson, Paul Delaney, Fedor Jelezko, Jörg Wrachtrup, and Lloyd C.L. Hollenberg. "The Nitrogen-Vacancy Colour Centre in Diamond". *Physics Reports* 528.1 (2013), pp. 1–45.

[15] A. Gruber, A. Dräbenstedt, C. Tietz, L. Fleury, J. Wrachtrup, and C. von Borczyskowski. "Scanning Confocal Optical Microscopy and Magnetic Resonance on Single Defect Centers". *Science* 276.5321 (1997), pp. 2012–2014.

[16] F. Jelezko, T. Gaebel, I. Popa, M. Domhan, A. Gruber, and J. Wrachtrup. "Observation of Coherent Oscillation of a Single Nuclear Spin and Realization of a Two-Qubit Conditional Quantum Gate". *Physical Review Letters* 93.13 (2004), p. 130501.

[17] Gopalakrishnan Balasubramanian, Philipp Neumann, Daniel Twitchen, Matthew Markham, Roman Kolesov, Norikazu Mizuochi, Junichi Isoya, Jocelyn Achard, Johannes Beck, Julia Tissler, Vincent Jacques, Philip R. Hemmer, Fedor Jelezko, and Jörg Wrachtrup. "Ultralong Spin Coherence Time in Isotopically Engineered Diamond". *Nature Materials* 8.5 (2009), pp. 383–387.

[18] G. D. Fuchs, V. V. Dobrovitski, D. M. Toyli, F. J. Heremans, and D. D. Awschalom. "Gigahertz Dynamics of a Strongly Driven Single Quantum Spin". *Science* 326.5959 (2009), pp. 1520–1522.

[19] Lilian Childress and Ronald Hanson. "Diamond NV Centers for Quantum Computing and Quantum Networks". *MRS Bulletin* 38.2 (2013), pp. 134–138.

[20] Rosa Brouri, Alexios Beveratos, Jean-Philippe Poizat, and Philippe Grangier. "Photon Antibunching in the Fluorescence of Individual Color Centers in Diamond". *Optics Letters* 25.17 (2000), p. 1294.

[21] Christian Kurtsiefer, Sonja Mayer, Patrick Zarda, and Harald Weinfurter. "Stable Solid-State Source of Single Photons". *Physical Review Letters* 85.2 (2000), pp. 290–293.

[22] P. Neumann, N. Mizuochi, F. Rempp, P. Hemmer, H. Watanabe, S. Yamasaki, V. Jacques, T. Gaebel, F. Jelezko, and J. Wrachtrup. "Multipartite Entanglement Among Single Spins in Diamond". *Science* 320.5881 (2008), pp. 1326–1329.

[23] E. Togan, Y. Chu, A. S. Trifonov, L. Jiang, J. Maze, L. Childress, M. V. G. Dutt, A. S. Sørensen, P. R. Hemmer, A. S. Zibrov, and M. D. Lukin. "Quantum Entanglement between an Optical Photon and a Solid-State Spin Qubit". *Nature* 466.7307 (2010), pp. 730–734.

[24] J. M. Taylor, P. Cappellaro, L. Childress, L. Jiang, D. Budker, P. R. Hemmer, A. Yacoby, R. Walsworth, and M. D. Lukin. "High-Sensitivity Diamond Magnetometer with Nanoscale Resolution". *Nature Physics* 4.10 (2008), pp. 810–816.

[25] C. L. Degen. "Scanning Magnetic Field Microscope with a Diamond Single-Spin Sensor". *Applied Physics Letters* 92.24 (2008), p. 243111.

[26] P. Maletinsky, S. Hong, M. S. Grinolds, B. Hausmann, M. D. Lukin, R. L. Walsworth, M. Loncar, and A. Yacoby. "A Robust Scanning Diamond Sensor for Nanoscale Imaging with Single Nitrogen-Vacancy Centres". *Nature Nanotechnology* 7.5 (2012), pp. 320–324.

[27] John F. Barry, Jennifer M. Schloss, Erik Bauch, Matthew J. Turner, Connor A. Hart, Linh M. Pham, and Ronald L. Walsworth. "Sensitivity Optimization for NV-diamond Magnetometry". *Reviews of Modern Physics* 92.1 (2020), p. 015004.

[28] Takuya F. Segawa and Ryuji Igarashi. “Nanoscale Quantum Sensing with Nitrogen-Vacancy Centers in Nanodiamonds – A Magnetic Resonance Perspective”. *Progress in Nuclear Magnetic Resonance Spectroscopy* 134–135 (2023), pp. 20–38.

[29] D. Le Sage, K. Arai, D. R. Glenn, S. J. DeVience, L. M. Pham, L. Rahn-Lee, M. D. Lukin, A. Yacoby, A. Komeili, and R. L. Walsworth. “Optical Magnetic Imaging of Living Cells”. *Nature* 496.7446 (2013), pp. 486–489.

[30] Romana Schirhagl, Kevin Chang, Michael Loretz, and Christian L. Degen. “Nitrogen-Vacancy Centers in Diamond: Nanoscale Sensors for Physics and Biology”. *Annual Review of Physical Chemistry* 65.1 (2014), pp. 83–105.

[31] H. J. Mamin, M. Kim, M. H. Sherwood, C. T. Rettner, K. Ohno, D. D. Awschalom, and D. Rugar. “Nanoscale Nuclear Magnetic Resonance with a Nitrogen-Vacancy Spin Sensor”. *Science* 339.6119 (2013), pp. 557–560.

[32] David R. Glenn, Dominik B. Bucher, Junghyun Lee, Mikhail D. Lukin, Hongkun Park, and Ronald L. Walsworth. “High-Resolution Magnetic Resonance Spectroscopy Using a Solid-State Spin Sensor”. *Nature* 555.7696 (2018), pp. 351–354.

[33] D. R. Glenn, R. R. Fu, P. Kehayias, D. Le Sage, E. A. Lima, B. P. Weiss, and R. L. Walsworth. “Micrometer-scale Magnetic Imaging of Geological Samples Using a Quantum Diamond Microscope”. *Geochemistry, Geophysics, Geosystems* 18.8 (2017), pp. 3254–3267.

[34] Francesco Casola, Toeno van der Sar, and Amir Yacoby. “Probing Condensed Matter Physics with Magnetometry Based on Nitrogen-Vacancy Centres in Diamond”. *Nature Reviews Materials* 3.1 (2018), p. 17088.

[35] J.-P. Tetienne, T. Hingant, J.-V. Kim, L. Herrera Diez, J.-P. Adam, K. Garcia, J.-F. Roch, S. Rohart, A. Thiaville, D. Ravelosona, and V. Jacques. “Nanoscale Imaging and Control of Domain-Wall Hopping with a Nitrogen-Vacancy Center Microscope”. *Science (New York, N.Y.)* 344.6190 (2014), pp. 1366–1369.

[36] L. Thiel, D. Rohner, M. Ganzhorn, P. Appel, E. Neu, B. Müller, R. Kleiner, D. Koelle, and P. Maletinsky. “Quantitative Nanoscale Vortex Imaging Using a Cryogenic Quantum Magnetometer”. *Nature Nanotechnology* 11.8 (2016), pp. 677–681.

[37] Yechezkel Schlussel, Till Lenz, Dominik Rohner, Yaniv Bar-Haim, Lykourgos Bougas, David Groswasser, Michael Kieschnick, Evgeny Rozenberg, Lucas Thiel, Amir Waxman, Jan Meijer, Patrick Maletinsky, Dmitry Budker, and Ron Folman. "Wide-Field Imaging of Superconductor Vortices with Electron Spins in Diamond". *Physical Review Applied* 10.3 (2018), p. 034032.

[38] I. Gross, W. Akhtar, V. Garcia, L. J. Martínez, S. Chouaieb, K. Garcia, C. Carrétéro, A. Barthélémy, P. Appel, P. Maletinsky, J.-V. Kim, J. Y. Chauleau, N. Jaouen, M. Viret, M. Bibes, S. Fusil, and V. Jacques. "Real-Space Imaging of Non-Collinear Antiferromagnetic Order with a Single Spin Magnetometer". *Nature* 549.7671 (2017), pp. 252–256.

[39] Jean-Philippe Tetienne, Nikolai Dontschuk, David A. Broadway, Alastair Stacey, David A. Simpson, and Lloyd C. L. Hollenberg. "Quantum Imaging of Current Flow in Graphene". *Science Advances* 3.4 (2017), e1602429.

[40] Zhewen Xu, Marius L. Palm, William Huxter, Konstantin Herb, John M. Abendroth, Karim Bouzehouane, Olivier Boulle, Mihai S. Gabor, Joseba Urrestarazu Larranaga, Andrea Morales, Jan Rhensius, Gabriel Puebla-Hellmann, and Christian L. Degen. "Minimizing Sensor-Sample Distances in Scanning Nitrogen-Vacancy Magnetometry". *ACS Nano* 19.8 (2025), pp. 8255–8265.

[41] L. M. Pham, N. Bar-Gill, C. Belthangady, D. Le Sage, P. Cappellaro, M. D. Lukin, A. Yacoby, and R. L. Walsworth. "Enhanced Solid-State Multi-Spin Metrology Using Dynamical Decoupling". *Physical Review B* 86.4 (2012), p. 045214.

[42] S. C. Scholten, A. J. Healey, I. O. Robertson, G. J. Abrahams, D. A. Broadway, and J.-P. Tetienne. "Widefield Quantum Microscopy with Nitrogen-Vacancy Centers in Diamond: Strengths, Limitations, and Prospects". *Journal of Applied Physics* 130.15 (2021), p. 150902.

[43] K.-M. C. Fu, C. Santori, P. E. Barclay, and R. G. Beausoleil. "Conversion of Neutral Nitrogen-Vacancy Centers to Negatively Charged Nitrogen-Vacancy Centers through Selective Oxidation". *Applied Physics Letters* 96.12 (2010), p. 121907.

[44] L. Rondin, G. Dantelle, A. Slablab, F. Grosshans, F. Treussart, P. Bergonzo, S. Perruchas, T. Gacoin, M. Chaigneau, H.-C. Chang, V. Jacques, and J.-F.

Roch. “Surface-Induced Charge State Conversion of Nitrogen-Vacancy Defects in Nanodiamonds”. *Physical Review B* 82.11 (2010), p. 115449.

[45] Kenichi Ohno, F. Joseph Heremans, Lee C. Bassett, Bryan A. Myers, David M. Toyli, Ania C. Bleszynski Jayich, Christopher J. Palmstrøm, and David D. Awschalom. “Engineering Shallow Spins in Diamond with Nitrogen Delta-Doping”. *Applied Physics Letters* 101.8 (2012), p. 082413.

[46] B. K. Ofori-Okai, S. Pezzagna, K. Chang, M. Loretz, R. Schirhagl, Y. Tao, B. A. Moores, K. Groot-Berning, J. Meijer, and C. L. Degen. “Spin Properties of Very Shallow Nitrogen Vacancy Defects in Diamond”. *Physical Review B* 86.8 (2012), p. 081406.

[47] K. Ohashi, T. Rosskopf, H. Watanabe, M. Loretz, Y. Tao, R. Hauert, S. Tomizawa, T. Ishikawa, J. Ishi-Hayase, S. Shikata, C. L. Degen, and K. M. Itoh. “Negatively Charged Nitrogen-Vacancy Centers in a 5 Nm Thin$^{12}$ C Diamond Film”. *Nano Letters* 13.10 (2013), pp. 4733–4738.

[48] T. Rosskopf, A. Dussaux, K. Ohashi, M. Loretz, R. Schirhagl, H. Watanabe, S. Shikata, K. M. Itoh, and C. L. Degen. “Investigation of Surface Magnetic Noise by Shallow Spins in Diamond”. *Physical Review Letters* 112.14 (2014), p. 147602.

[49] B. A. Myers, A. Das, M. C. Dartiailh, K. Ohno, D. D. Awschalom, and A. C. Bleszynski Jayich. “Probing Surface Noise with Depth-Calibrated Spins in Diamond”. *Physical Review Letters* 113.2 (2014), p. 027602.

[50] Arthur N. Newell, Dontray A. Dowdell, and D. H. Santamore. “Surface Effects on Nitrogen Vacancy Centers Neutralization in Diamond”. *Journal of Applied Physics* 120.18 (2016), p. 185104.

[51] Dolev Bluvstein, Zhiran Zhang, and Ania C. Bleszynski Jayich. “Identifying and Mitigating Charge Instabilities in Shallow Diamond Nitrogen-Vacancy Centers”. *Physical Review Letters* 122.7 (2019), p. 076101.

[52] K. S. Novoselov, D. Jiang, F. Schedin, T. J. Booth, V. V. Khotkevich, S. V. Morozov, and A. K. Geim. “Two-Dimensional Atomic Crystals”. *Proceedings of the National Academy of Sciences* 102.30 (2005), pp. 10451–10453.

[53] K. S. Novoselov, A. K. Geim, S. V. Morozov, D. Jiang, Y. Zhang, S. V. Dubonos, I. V. Grigorieva, and A. A. Firsov. “Electric Field Effect in Atomically Thin Carbon Films”. *Science* 306.5696 (2004), pp. 666–669.

[54] Hui Li, Shuangchen Ruan, and Yu-Jia Zeng. “Intrinsic Van Der Waals Magnetic Materials from Bulk to the 2D Limit: New Frontiers of Spintronics”. *Advanced Materials* 31.27 (2019), p. 1900065.

[55] Dong Qiu, Chuanhui Gong, SiShuang Wang, Miao Zhang, Chao Yang, Xianfu Wang, and Jie Xiong. “Recent Advances in 2D Superconductors”. *Advanced Materials* 33.18 (2021), p. 2006124.

[56] Liangzhi Kou, Yandong Ma, Ziqi Sun, Thomas Heine, and Changfeng Chen. “Two-Dimensional Topological Insulators: Progress and Prospects”. *The Journal of Physical Chemistry Letters* 8.8 (2017), pp. 1905–1919.

[57] A. K. Geim and I. V. Grigorieva. “Van Der Waals Heterostructures”. *Nature* 499.7459 (2013), pp. 419–425.

[58] Shawulienu Kezilebieke, Md Nurul Huda, Viliam Vaňo, Markus Aapro, Somesh C. Ganguli, Orlando J. Silveira, Szczepan Głodzik, Adam S. Foster, Teemu Ojanen, and Peter Liljeroth. “Topological Superconductivity in a van Der Waals Heterostructure”. *Nature* 588.7838 (2020), pp. 424–428.

[59] Yuan Cao, Valla Fatemi, Shiang Fang, Kenji Watanabe, Takashi Taniguchi, Efthimios Kaxiras, and Pablo Jarillo-Herrero. “Unconventional Superconductivity in Magic-Angle Graphene Superlattices”. *Nature* 556.7699 (2018), pp. 43–50.

[60] J.-P. Tetienne. “Quantum Sensors Go Flat”. *Nature Physics* 17.10 (2021), pp. 1074–1075.

[61] Bernard Gil, Wilfried Desrat, Adrien Rousseau, Christine Elias, Pierre Valvin, Matthieu Moret, Jiahan Li, Eli Janzen, James Howard Edgar, and Guillaume Cassabois. “Polytypes of Sp2-Bonded Boron Nitride”. *Crystals* 12.6 (2022), p. 782.

[62] Lu Hua Li, Jiri Cervenka, Kenji Watanabe, Takashi Taniguchi, and Ying Chen. “Strong Oxidation Resistance of Atomically Thin Boron Nitride Nanosheets”. *ACS nano* 8.2 (2014), pp. 1457–1462.

[63] F. Mahvash, S. Eissa, T. Bordjiba, A. C. Tavares, T. Szkopek, and M. Siaj. “Corrosion Resistance of Monolayer Hexagonal Boron Nitride on Copper”. *Scientific Reports* 7.1 (2017), p. 42139.

[64] Roman V. Gorbachev, Ibtsam Riaz, Rahul R. Nair, Rashid Jalil, Liam Britnell, Branson D. Belle, Ernie W. Hill, Kostya S. Novoselov, Kenji Watanabe, Takashi Taniguchi, Andre K. Geim, and Peter Blake. "Hunting for Monolayer Boron Nitride: Optical and Raman Signatures". *Small* 7.4 (2011), pp. 465–468.

[65] Zheng Liu, Yongji Gong, Wu Zhou, Lulu Ma, Jingjiang Yu, Juan Carlos Idrobo, Jeil Jung, Allan H. MacDonald, Robert Vajtai, Jun Lou, and Pulickel M. Ajayan. "Ultrathin High-Temperature Oxidation-Resistant Coatings of Hexagonal Boron Nitride". *Nature Communications* 4.1 (2013), p. 2541.

[66] C. R. Dean, A. F. Young, I. Meric, C. Lee, L. Wang, S. Sorgenfrei, K. Watanabe, T. Taniguchi, P. Kim, K. L. Shepard, and J. Hone. "Boron Nitride Substrates for High-Quality Graphene Electronics". *Nature Nanotechnology* 5.10 (2010), pp. 722–726.

[67] Jiamin Xue, Javier Sanchez-Yamagishi, Danny Bulmash, Philippe Jacquod, Aparna Deshpande, K. Watanabe, T. Taniguchi, Pablo Jarillo-Herrero, and Brian J. LeRoy. "Scanning Tunnelling Microscopy and Spectroscopy of Ultra-Flat Graphene on Hexagonal Boron Nitride". *Nature Materials* 10.4 (2011), pp. 282–285.

[68] A. V. Kretinin, Y. Cao, J. S. Tu, G. L. Yu, R. Jalil, K. S. Novoselov, S. J. Haigh, A. Gholinia, A. Mishchenko, M. Lozada, T. Georgiou, C. R. Woods, F. Withers, P. Blake, G. Eda, A. Wirsig, C. Hucho, K. Watanabe, T. Taniguchi, A. K. Geim, and R. V. Gorbachev. "Electronic Properties of Graphene Encapsulated with Different Two-Dimensional Atomic Crystals". *Nano Letters* 14.6 (2014), pp. 3270–3276.

[69] Simona Pace, Leonardo Martini, Domenica Convertino, Dong Hoon Keum, Stiven Forti, Sergio Pezzini, Filippo Fabbri, Vaidotas Mišeikis, and Camilla Coletti. "Synthesis of Large-Scale Monolayer 1T′-$MoTe_2$ and Its Stabilization *via* Scalable hBN Encapsulation". *ACS Nano* 15.3 (2021), pp. 4213–4225.

[70] F. Cadiz, E. Courtade, C. Robert, G. Wang, Y. Shen, H. Cai, T. Taniguchi, K. Watanabe, H. Carrere, D. Lagarde, M. Manca, T. Amand, P. Renucci, S. Tongay, X. Marie, and B. Urbaszek. "Excitonic Linewidth Approaching the Homogeneous Limit in MoS 2 -Based van Der Waals Heterostructures". *Physical Review X* 7.2 (2017), p. 021026.

[71] Obafunso A Ajayi, Jenny V Ardelean, Gabriella D Shepard, Jue Wang, Abhinandan Antony, Takeshi Taniguchi, Kenji Watanabe, Tony F Heinz, Stefan Strauf, X-Y Zhu, and James C Hone. "Approaching the Intrinsic Photoluminescence Linewidth in Transition Metal Dichalcogenide Monolayers". *2D Materials* 4.3 (2017), p. 031011.

[72] Kenji Yasuda, Xirui Wang, Kenji Watanabe, Takashi Taniguchi, and Pablo Jarillo-Herrero. "Stacking-Engineered Ferroelectricity in Bilayer Boron Nitride". *Science* 372.6549 (2021), pp. 1458–1462.

[73] J. Fraunié, R. Jamil, R. Kantelberg, S. Roux, L. Petit, E. Lepleux, L. Pacheco, K. Watanabe, T. Taniguchi, V. Jacques, L. Lombez, M. M. Glazov, B. Lassagne, X. Marie, and C. Robert. "Electron and Hole Doping of Monolayer WSe 2 Induced by Twisted Ferroelectric Hexagonal Boron Nitride". *Physical Review Materials* 7.12 (2023), p. L121002.

[74] Oleg V. Yazyev and Alfredo Pasquarello. "Magnetoresistive Junctions Based on Epitaxial Graphene and Hexagonal Boron Nitride". *Physical Review B* 80.3 (2009), p. 035408.

[75] André Dankert, M. Venkata Kamalakar, Abdul Wajid, R. S. Patel, and Saroj P. Dash. "Tunnel Magnetoresistance with Atomically Thin Two-Dimensional Hexagonal Boron Nitride Barriers". *Nano Research* 8.4 (2015), pp. 1357–1364.

[76] Sherif Abdulkader Tawfik, Sajid Ali, Marco Fronzi, Mehran Kianinia, Toan Trong Tran, Catherine Stampfl, Igor Aharonovich, Milos Toth, and Michael J. Ford. "First-Principles Investigation of Quantum Emission from hBN Defects". *Nanoscale* 9.36 (2017), pp. 13575–13582.

[77] Philipp Auburger and Adam Gali. "Towards *Ab Initio* Identification of Paramagnetic Substitutional Carbon Defects in Hexagonal Boron Nitride Acting as Quantum Bits". *Physical Review B* 104.7 (2021), p. 075410.

[78] Xingyu Gao, Sumukh Vaidya, Kejun Li, Zhun Ge, Saakshi Dikshit, Shimin Zhang, Peng Ju, Kunhong Shen, Yuanbin Jin, Yuan Ping, and Tongcang Li. "Ga". *Nature* 643.8073 (2025), pp. 943–949.

[79] Song Li and Adam Gali. "Identification of an Oxygen Defect in Hexagonal Boron Nitride". *The Journal of Physical Chemistry Letters* 13.41 (2022), pp. 9544–9551.

[80] Viktor Ivády, Gergely Barcza, Gergő Thiering, Song Li, Hanen Hamdi, Jyh-Pin Chou, Örs Legeza, and Adam Gali. "Ab Initio Theory of the Negatively Charged Boron Vacancy Qubit in Hexagonal Boron Nitride". *npj Computational Materials* 6.1 (2020), p. 41.

[81] Andreas Gottscholl, Mehran Kianinia, Victor Soltamov, Sergei Orlinskii, Georgy Mamin, Carlo Bradac, Christian Kasper, Klaus Krambrock, Andreas Sperlich, Milos Toth, Igor Aharonovich, and Vladimir Dyakonov. "Initialization and Read-out of Intrinsic Spin Defects in a van Der Waals Crystal at Room Temperature". *Nature Materials* 19.5 (2020), pp. 540–545.

[82] A. Katzir, J. T. Suss, A. Zunger, and A. Halperin. "Point Defects in Hexagonal Boron Nitride. I. EPR, Thermoluminescence, and Thermally-Stimulated-Current Measurements". *Physical Review B* 11.6 (1975), pp. 2370–2377.

[83] Luc Museur, Eduard Feldbach, and Andrei Kanaev. "Defect-Related Photoluminescence of Hexagonal Boron Nitride". *Physical Review B* 78.15 (2008), p. 155204.

[84] Toan Trong Tran, Cameron Zachreson, Amanuel Michael Berhane, Kerem Bray, Russell Guy Sandstrom, Lu Hua Li, Takashi Taniguchi, Kenji Watanabe, Igor Aharonovich, and Milos Toth. "Quantum Emission from Defects in Single-Crystalline Hexagonal Boron Nitride". *Physical Review Applied* 5.3 (2016), p. 034005.

[85] Toan Trong Tran, Christopher Elbadawi, Daniel Totonjian, Charlene J. Lobo, Gabriele Grosso, Hyowon Moon, Dirk R. Englund, Michael J. Ford, Igor Aharonovich, and Milos Toth. "Robust Multicolor Single Photon Emission from Point Defects in Hexagonal Boron Nitride". *ACS Nano* 10.8 (2016), pp. 7331–7338.

[86] L. J. Martínez, T. Pelini, V. Waselowski, J. R. Maze, B. Gil, G. Cassabois, and V. Jacques. "Efficient Single Photon Emission from a High-Purity Hexagonal Boron Nitride Crystal". *Physical Review B* 94.12 (2016), p. 121405.

[87] Nathan Chejanovsky, Mohammad Rezai, Federico Paolucci, Youngwook Kim, Torsten Rendler, Wafa Rouabeh, Felipe Fávaro de Oliveira, Patrick Herlinger, Andrej Denisenko, Sen Yang, Ilja Gerhardt, Amit Finkler, Jurgen H. Smet, and Jörg Wrachtrup. "Structural Attributes and Photodynamics of Visible Spectrum Quantum Emitters in Hexagonal Boron Nitride". *Nano Letters* 16.11 (2016), pp. 7037–7045.

[88] Sumin Choi, Toan Trong Tran, Christopher Elbadawi, Charlene Lobo, Xuewen Wang, Saulius Juodkazis, Gediminas Seniutinas, Milos Toth, and Igor Aharonovich. "Engineering and Localization of Quantum Emitters in Large Hexagonal Boron Nitride Layers". *ACS Applied Materials & Interfaces* 8.43 (2016), pp. 29642–29648.

[89] Nicholas R. Jungwirth, Brian Calderon, Yanxin Ji, Michael G. Spencer, Michael E. Flatté, and Gregory D. Fuchs. "Temperature Dependence of Wavelength Selectable Zero-Phonon Emission from Single Defects in Hexagonal Boron Nitride". *Nano Letters* 16.10 (2016), pp. 6052–6057.

[90] Romain Bourrellier, Sophie Meuret, Anna Tararan, Odile Stéphan, Mathieu Kociak, Luiz H. G. Tizei, and Alberto Zobelli. "Bright UV Single Photon Emission at Point Defects in *h* -BN". *Nano Letters* 16.7 (2016), pp. 4317–4321.

[91] Clarisse Fournier, Alexandre Plaud, Sébastien Roux, Aurélie Pierret, Michael Rosticher, Kenji Watanabe, Takashi Taniguchi, Stéphanie Buil, Xavier Quélin, Julien Barjon, Jean-Pierre Hermier, and Aymeric Delteil. "Position-Controlled Quantum Emitters with Reproducible Emission Wavelength in Hexagonal Boron Nitride". *Nature Communications* 12.1 (2021), p. 3779.

[92] Yongliang Chen, Angus Gale, Karin Yamamura, Jake Horder, Alexander Condos, Kenji Watanabe, Takashi Taniguchi, Milos Toth, and Igor Aharonovich. "Annealing of Blue Quantum Emitters in Carbon-Doped Hexagonal Boron Nitride". *Applied Physics Letters* 123.4 (2023), p. 041902.

[93] Nicholas R. Jungwirth and Gregory D. Fuchs. "Optical Absorption and Emission Mechanisms of Single Defects in Hexagonal Boron Nitride". *Physical Review Letters* 119.5 (2017), p. 057401.

[94] Hannah L. Stern, Ruizhi Wang, Ye Fan, Ryo Mizuta, James C. Stewart, Lisa-Maria Needham, Trevor D. Roberts, Rebecca Wai, Naomi S. Ginsberg, David Klenerman, Stephan Hofmann, and Steven F. Lee. "Spectrally Resolved Photodynamics of Individual Emitters in Large-Area Monolayers of Hexagonal Boron Nitride". *ACS Nano* 13.4 (2019), pp. 4538–4547.

[95] Helmi Fartas, Saïd Hassani, Jean-Pierre Hermier, Ngoc Diep Lai, Stéphanie Buil, and Aymeric Delteil. "Reproducible Generation of Green-Emitting Color Centers in hBN Using Oxygen Annealing". *Applied Physics Letters* 127.1 (2025), p. 014001.

[96] Annemarie L. Exarhos, David A. Hopper, Richard R. Grote, Audrius Alkauskas, and Lee C. Bassett. "Optical Signatures of Quantum Emitters in Suspended Hexagonal Boron Nitride". *ACS Nano* 11.3 (2017), pp. 3328–3336.

[97] Mehran Kianinia, Blake Regan, Sherif Abdulkader Tawfik, Toan Trong Tran, Michael J. Ford, Igor Aharonovich, and Milos Toth. "Robust Solid-State Quantum System Operating at 800 K". *ACS Photonics* 4.4 (2017), pp. 768–773.

[98] Xiangzhi Li, Gabriella D. Shepard, Andrew Cupo, Nicolas Camporeale, Kamran Shayan, Yue Luo, Vincent Meunier, and Stefan Strauf. "Nonmagnetic Quantum Emitters in Boron Nitride with Ultranarrow and Sideband-Free Emission Spectra". *ACS Nano* 11.7 (2017), pp. 6652–6660.

[99] A. Dietrich, M. Bürk, E. S. Steiger, L. Antoniuk, T. T. Tran, M. Nguyen, I. Aharonovich, F. Jelezko, and A. Kubanek. "Observation of Fourier Transform Limited Lines in Hexagonal Boron Nitride". *Physical Review B* 98.8 (2018), p. 081414.

[100] J. Plo, A. Pershin, S. Li, T. Poirier, E. Janzen, H. Schutte, M. Tian, M. Wynn, S. Bernard, A. Rousseau, A. Ibanez, P. Valvin, W. Desrat, T. Michel, V. Jacques, B. Gil, A. Kaminska, N. Wan, J. H. Edgar, A. Gali, and G. Cassabois. "Isotope Substitution and Polytype Control for Point Defects Identification: The Case of the Ultraviolet Color Center in Hexagonal Boron Nitride". *Physical Review X* 15.2 (2025), p. 021045.

[101] A. Sajid, Jeffrey R. Reimers, and Michael J. Ford. "Defect States in Hexagonal Boron Nitride: Assignments of Observed Properties and Prediction of Properties Relevant to Quantum Computation". *Physical Review B* 97.6 (2018), p. 064101.

[102] Noah Mendelson, Dipankar Chugh, Jeffrey R. Reimers, Tin S. Cheng, Andreas Gottscholl, Hu Long, Christopher J. Mellor, Alex Zettl, Vladimir Dyakonov, Peter H. Beton, Sergei V. Novikov, Chennupati Jagadish, Hark Hoe Tan, Michael J. Ford, Milos Toth, Carlo Bradac, and Igor Aharonovich. "Identifying Carbon as the Source of Visible Single-Photon Emission from Hexagonal Boron Nitride". *Nature Materials* 20.3 (2021), pp. 321–328.

[103] E. Y. Andrei, A. Katzir, and J. T. Suss. "Point Defects in Hexagonal Boron Nitride. III. EPR in Electron-Irradiated BN". *Physical Review B* 13.7 (1976), pp. 2831–2834.

[104] J. R. Toledo, D. B. de Jesus, M. Kianinia, A. S. Leal, C. Fantini, L. A. Cury, G. A. M. Sáfar, I. Aharonovich, and K. Krambrock. "Electron Paramagnetic Resonance Signature of Point Defects in Neutron-Irradiated Hexagonal Boron Nitride". *Physical Review B* 98.15 (2018), p. 155203.

[105] Annemarie L. Exarhos, David A. Hopper, Raj N. Patel, Marcus W. Doherty, and Lee C. Bassett. "Magnetic-Field-Dependent Quantum Emission in Hexagonal Boron Nitride at Room Temperature". *Nature Communications* 10.1 (2019), p. 222.

[106] Mehdi Abdi, Jyh-Pin Chou, Adam Gali, and Martin B. Plenio. "Color Centers in Hexagonal Boron Nitride Monolayers: A Group Theory and Ab Initio Analysis". *ACS Photonics* 5.5 (2018), pp. 1967–1976.

[107] Jeffrey R. Reimers, Jun Shen, Mehran Kianinia, Carlo Bradac, Igor Aharonovich, Michael J. Ford, and Piotr Piecuch. "Photoluminescence and Photochemistry of the VB- Defect in Hexagonal Boron Nitride". *Physical Review B* 102.14 (2020), p. 144105.

[108] Francesco Libbi, Pedro Miguel M. C. de Melo, Zeila Zanolli, Matthieu Jean Verstraete, and Nicola Marzari. "Phonon-Assisted Luminescence in Defect Centers from Many-Body Perturbation Theory". *Physical Review Letters* 128.16 (2022), p. 167401.

[109] W. Liu, Z.-P. Li, Y.-Z. Yang, S. Yu, Y. Meng, Z.-C. Li, N.-J. Guo, F.-F. Yan, Q. Li, J.-F. Wang, J.-S. Xu, Y.-T. Wang, J.-S. Tang, C.-F. Li, and G.-C. Guo. "Temperature-Dependent Energy-Level Shifts of Spin Defects in Hexagonal Boron Nitride". *ACS Photonics* 8.7 (2021), pp. 1889–1895.

[110] Zhongyuan Liu, Ruotian Gong, Benchen Huang, Yu Jin, Xinyi Du, Guanghui He, Eli Janzen, Li Yang, Erik Henriksen, James Edgar, Giulia Galli, and Chong Zu. *Temperature Dependent Spin-Phonon Coupling of Boron-Vacancy Centers in Hexagonal Boron Nitride*. 2024.

[111] Andreas Gottscholl, Matthias Diez, Victor Soltamov, Christian Kasper, Dominik Krauße, Andreas Sperlich, Mehran Kianinia, Carlo Bradac, Igor Aharonovich, and Vladimir Dyakonov. "Spin Defects in hBN as Promising Temperature, Pressure and Magnetic Field Quantum Sensors". *Nature Communications* 12.1 (2021), p. 4480.

[112] Sumukh Vaidya, Xingyu Gao, Saakshi Dikshit, Igor Aharonovich, and Tongcang Li. *Quantum Sensing and Imaging with Spin Defects in Hexagonal Boron Nitride*. 2023.

[113] A. J. Healey, S. C. Scholten, T. Yang, J. A. Scott, G. J. Abrahams, I. O. Robertson, X. F. Hou, Y. F. Guo, S. Rahman, Y. Lu, M. Kianinia, I. Aharonovich, and J.-P. Tetienne. "Quantum Microscopy with van Der Waals Heterostructures". *Nature Physics* 19.1 (2023), pp. 87–91.

[114] Péter Udvarhelyi, Tristan Clua-Provost, Alrik Durand, Jiahan Li, James H. Edgar, Bernard Gil, Guillaume Cassabois, Vincent Jacques, and Adam Gali. "A Planar Defect Spin Sensor in a Two-Dimensional Material Susceptible to Strain and Electric Fields". *npj Computational Materials* 9.1 (2023), p. 150.

[115] Z. Mu, J. Fraunié, A. Durand, S. Clément, A. Finco, J. Rouquette, A. Hadj-Azzem, N. Rougemaille, J. Coraux, J. Li, T. Poirier, J. H. Edgar, I. C. Gerber, X. Marie, B. Gil, G. Cassabois, C. Robert, and V. Jacques. *Magnetic Imaging under High Pressure with a Spin-Based Quantum Sensor Integrated in a van Der Waals Heterostructure*. 2025.

[116] T. Mittiga, S. Hsieh, C. Zu, B. Kobrin, F. Machado, P. Bhattacharyya, N. Z. Rui, A. Jarmola, S. Choi, D. Budker, and N. Y. Yao. "Imaging the Local Charge Environment of Nitrogen-Vacancy Centers in Diamond". *Physical Review Letters* 121.24 (2018), p. 246402.

[117] Andreas Gottscholl, Matthias Diez, Victor Soltamov, Christian Kasper, Andreas Sperlich, Mehran Kianinia, Carlo Bradac, Igor Aharonovich, and Vladimir Dyakonov. "Room Temperature Coherent Control of Spin Defects in Hexagonal Boron Nitride". *Science Advances* 7.14 (2021), eabf3630.

[118] Nasrin Estaji, Ismaeil Abdolhosseini Sarsari, Gergő Thiering, and Adam Gali. *Spin-Phonon Relaxation of Boron-Vacancy Centers in Two-Dimensional Boron Nitride Polytypes*. 2025.

[119] A. Jarmola, V. M. Acosta, K. Jensen, S. Chemerisov, and D. Budker. "Temperature- and Magnetic-Field-Dependent Longitudinal Spin Relaxation in Nitrogen-Vacancy Ensembles in Diamond". *Physical Review Letters* 108.19 (2012), p. 197601.

[120] Islay O. Robertson, Sam C. Scholten, Priya Singh, Alexander J. Healey, Fernando Meneses, Philipp Reineck, Hiroshi Abe, Takeshi Ohshima, Mehran Kianinia, Igor Aharonovich, and Jean-Philippe Tetienne. "Detection of Paramagnetic Spins with an Ultrathin van Der Waals Quantum Sensor". *ACS Nano* 17.14 (2023), pp. 13408–13417.

[121] Xingyu Gao, Sumukh Vaidya, Peng Ju, Saakshi Dikshit, Kunhong Shen, Yong P. Chen, and Tongcang Li. *Quantum Sensing of Paramagnetic Spins in Liquids with Spin Qubits in Hexagonal Boron Nitride*. 2023.

[122] Hao-Jie Zhou, Xiao-Wen Shen, Yu Zhou, Lei Dong, Pei-Qin Chen, Xia Chen, Guang-Wei Deng, Gang Xiang, Pei-Jie Guo, Tian-Ke Wang, Hong-Peng Wu, and Jun-Feng Wang. *Detection and Manipulation of Surface Electric Field Noise of Hexagonal Boron Nitride*. 2025.

[123] S. Meiboom and D. Gill. "Modified Spin-Echo Method for Measuring Nuclear Relaxation Times". *Review of Scientific Instruments* 29.8 (1958), pp. 688–691.

[124] A. Haykal, R. Tanos, N. Minotto, A. Durand, F. Fabre, J. Li, J. H. Edgar, V. Ivády, A. Gali, T. Michel, A. Dréau, B. Gil, G. Cassabois, and V. Jacques. "Decoherence of VB- Spin Defects in Monoisotopic Hexagonal Boron Nitride". *Nature Communications* 13.1 (2022), p. 4347.

[125] Ruotian Gong, Guanghui He, Xingyu Gao, Peng Ju, Zhongyuan Liu, Bingtian Ye, Erik A. Henriksen, Tongcang Li, and Chong Zu. *Coherent Dynamics of Strongly Interacting Electronic Spin Defects in Hexagonal Boron Nitride*. 2022.

[126] Roberto Rizzato, Martin Schalk, Stephan Mohr, Jens C. Hermann, Joachim P. Leibold, Fleming Bruckmaier, Giovanna Salvitti, Chenjiang Qian, Peirui Ji, Georgy V. Astakhov, Ulrich Kentsch, Manfred Helm, Andreas V. Stier, Jonathan J. Finley, and Dominik B. Bucher. "Extending the Coherence of Spin Defects in hBN Enables Advanced Qubit Control and Quantum Sensing". *Nature Communications* 14.1 (2023), p. 5089.

[127] Andrew J. Ramsay, Reza Hekmati, Charlie J. Patrickson, Simon Baber, David R. M. Arvidsson-Shukur, Anthony J. Bennett, and Isaac J. Luxmoore. "Coherence Protection of Spin Qubits in Hexagonal Boron Nitride". *Nature Communications* 14.1 (2023), p. 461.

[128] Daniele C. Freitas, Ruben Weht, André Sulpice, Gyorgy Remenyi, Pierre Strobel, Frédéric Gay, Jacques Marcus, and Manuel Núñez-Regueiro. "Ferromagnetism in Layered Metastable 1T-CrTe2". *Journal of Physics: Condensed Matter* 27.17 (2015), p. 176002.

[129] Anike Purbawati, Johann Coraux, Jan Vogel, Abdellali Hadj-Azzem, Nian-Jheng Wu, Nedjma Bendiab, David Jegouso, Julien Renard, Laetitia Marty, Vincent Bouchiat, André Sulpice, Lucia Aballe, Michael Foerster, Francesca Genuzio, Andrea Locatelli, Tevfik Onur Menteş, Zheng Vitto Han, Xingdan Sun, Manuel Núñez-Regueiro, and Nicolas Rougemaille. "In-Plane Magnetic Domains and Néel-like Domain Walls in Thin Flakes of the Room Temperature $CrTe_2$ Van Der Waals Ferromagnet". *ACS Applied Materials & Interfaces* 12.27 (2020), pp. 30702–30710.

[130] Xingdan Sun, Wanying Li, Xiao Wang, Qi Sui, Tongyao Zhang, Zhi Wang, Long Liu, Da Li, Shun Feng, Siyu Zhong, Hanwen Wang, Vincent Bouchiat, Manuel Nunez Regueiro, Nicolas Rougemaille, Johann Coraux, Anike Purbawati, Abdellali Hadj-Azzem, Zhenhua Wang, Baojuan Dong, Xing Wu, Teng Yang, Guoqiang Yu, Bingwu Wang, Zheng Han, Xiufeng Han, and Zhidong Zhang. "Room Temperature Ferromagnetism in Ultra-Thin van Der Waals Crystals of 1T-CrTe2". *Nano Research* 13.12 (2020), pp. 3358–3363.

[131] F. Fabre, A. Finco, A. Purbawati, A. Hadj-Azzem, N. Rougemaille, J. Coraux, I. Philip, and V. Jacques. "Characterization of Room-Temperature in-Plane Magnetization in Thin Flakes of CrTe2 with a Single-Spin Magnetometer". *Physical Review Materials* 5.3 (2021), p. 034008.

[132] Yoichi Kubota, Kenji Watanabe, Osamu Tsuda, and Takashi Taniguchi. "Hexagonal Boron Nitride Single Crystal Growth at Atmospheric Pressure Using Ni-Cr Solvent". *Chemistry of Materials* 20.5 (2008), pp. 1661–1663.

[133] Song Liu, Rui He, Lianjie Xue, Jiahan Li, Bin Liu, and James H. Edgar. "Single Crystal Growth of Millimeter-Sized Monoisotopic Hexagonal Boron Nitride". *Chemistry of Materials* 30.18 (2018), pp. 6222–6225.

[134] E. Janzen, H. Schutte, J. Plo, A. Rousseau, T. Michel, W. Desrat, P. Valvin, V. Jacques, G. Cassabois, B. Gil, and J. H. Edgar. *Boron and Nitrogen Isotope Effects on Hexagonal Boron Nitride Properties*. 2023.

[135] N.-J. Guo, W. Liu, Z.-P. Li, Y.-Z. Yang, S. Yu, Y. Meng, Z.-A. Wang, X.-D. Zeng, F.-F. Yan, Q. Li, J.-F. Wang, J.-S. Xu, Y.-T. Wang, J.-S. Tang, C.-F. Li, and G.-C. Guo. "Generation of Spin Defects by Ion Implantation in Hexagonal Boron Nitride". *ACS Omega* 7.2 (2022), pp. 1733–1739.

[136] Fei Ren, Zongwei Xu, and Yiyuan Wu. "Optimization of Carbon Irradiation Parameters for Creating Spin Defects in Hexagonal Boron Nitride". *Nanotechnology and Precision Engineering* 8.3 (2025), p. 033014.

[137] Atanu Patra, Paul Konrad, Andreas Sperlich, Timur Biktagirov, Wolf Gero Schmidt, Lesley Spencer, Igor Aharonovich, Sven Höfling, and Vladimir Dyakonov. *Quantifying Spin Defect Density in hBN via Raman and Photoluminescence Analysis*. 2025.

[138] Mehran Kianinia, Simon White, Johannes E. Fröch, Carlo Bradac, and Igor Aharonovich. *Engineering Spin Defects in Hexagonal Boron Nitride*. 2020.

[139] Madeline Hennessey, Benjamin Whitefield, John A. Scott, Mehran Kianinia, Igor Aharonovich, and Milos Toth. *Framework for Engineering of Spin Defects in Hexagonal Boron Nitride by Focused Ion Beams*. 2023.

[140] Amedeo Carbone, Ilia D. Breev, Johannes Figueiredo, Silvan Kretschmer, Leonard Geilen, Amine Ben Mhenni, Johannes Arceri, Arkady V. Krasheninnikov, Martijn Wubs, Alexander W. Holleitner, Alexander Huck, Christoph Kastl, and Nicolas Stenger. "Quantifying the Creation of Negatively Charged Boron Vacancies in He-ion Irradiated Hexagonal Boron Nitride". *Physical Review Materials* 9.5 (2025), p. 056203.

[141] Hao Gu, Moeta Tsukamoto, Yuki Nakamura, Shu Nakaharai, Takuya Iwasaki, Kenji Watanabe, Takashi Taniguchi, Shinichi Ogawa, Yukinori Morita, Kento Sasaki, and Kensuke Kobayashi. "Systematic Characterization of Nanoscale h -BN Quantum Sensor Spots Created by Helium-Ion Microscopy". *Physical Review Applied* 22.5 (2024), p. 054026.

[142] Fadis F. Murzakhanov, Boris V. Yavkin, Georgiy V. Mamin, Sergei B. Orlinskii, Ivan E. Mumdzhi, Irina N. Gracheva, Bulat F. Gabbasov, Alexander N. Smirnov, Valery Yu Davydov, and Victor A. Soltamov. "Creation of Negatively Charged Boron Vacancies in Hexagonal Boron Nitride Crystal by Electron Irradiation and Mechanism of Inhomogeneous Broadening of Boron Vacancy-Related Spin Resonance Lines". *Nanomaterials* 11.6 (2021), p. 1373.

[143] Alexander J Healey, Priya Singh, Islay O Robertson, Christopher Gavin, Sam C Scholten, David A Broadway, Philipp Reineck, Hiroshi Abe, Takeshi Ohshima, Mehran Kianinia, Igor Aharonovich, and Jean-Philippe Tetienne. "Optimisation of Electron Irradiation for Creating Spin Ensembles in Hexagonal Boron Nitride". *Materials for Quantum Technology* 4.3 (2024), p. 035701.

[144] Xingyu Gao, Siddhant Pandey, Mehran Kianinia, Jonghoon Ahn, Peng Ju, Igor Aharonovich, Niranjan Shivaram, and Tongcang Li. "Femtosecond Laser Writing of Spin Defects in Hexagonal Boron Nitride". *ACS Photonics* 8.4 (2021), pp. 994–1000.

[145] Jiahan Li, Evan R. Glaser, Christine Elias, Gaihua Ye, Dylan Evans, Lianjie Xue, Song Liu, Guillaume Cassabois, Bernard Gil, Pierre Valvin, Thomas Pelini, Andrew L. Yeats, Rui He, Bin Liu, and James H. Edgar. "Defect Engineering of Monoisotopic Hexagonal Boron Nitride Crystals *via* Neutron Transmutation Doping". *Chemistry of Materials* 33.23 (2021), pp. 9231–9239.

[146] A. Dréau, M. Lesik, L. Rondin, P. Spinicelli, O. Arcizet, J.-F. Roch, and V. Jacques. "Avoiding Power Broadening in Optically Detected Magnetic Resonance of Single NV Defects for Enhanced Dc Magnetic Field Sensitivity". *Physical Review B* 84.19 (2011), p. 195204.

[147] A. J. Healey, A. Stacey, B. C. Johnson, D. A. Broadway, T. Teraji, D. A. Simpson, J.-P. Tetienne, and L. C. L. Hollenberg. "Comparison of Different Methods of Nitrogen-Vacancy Layer Formation in Diamond for Wide-Field Quantum Microscopy". *Physical Review Materials* 4.10 (2020), p. 104605.

[148] Joseph Shaji Rebeirro, Muhib Omar, Till Lenz, Omkar Dhungel, Peter Blümler, Dmitry Budker, and Arne Wickenbrock. "Microwave-Free Wide-Field Magnetometry Using Nitrogen-Vacancy Centers". *Physical Review Applied* 21.4 (2024), p. 044039.

[149] Florentin Fabre. "Capteurs Quantiques Pour l'étude de Matériaux Magnétiques Bidimensionnels". Thesis. 2022.

[150] P. Kumar, F. Fabre, A. Durand, T. Clua-Provost, J. Li, J.H. Edgar, N. Rougemaille, J. Coraux, X. Marie, P. Renucci, C. Robert, I. Robert-Philip, B. Gil, G. Cassabois, A. Finco, and V. Jacques. "Magnetic Imaging with Spin Defects in Hexagonal Boron Nitride". *Physical Review Applied* 18.6 (2022), p. L061002.

[151] Mengqi Huang, Jingcheng Zhou, Di Chen, Hanyi Lu, Nathan J. McLaughlin, Senlei Li, Mohammed Alghamdi, Dziga Djugba, Jing Shi, Hailong Wang, and Chunhui Rita Du. "Wide Field Imaging of van Der Waals Ferromagnet Fe3GeTe2 by Spin Defects in Hexagonal Boron Nitride". *Nature Communications* 13.1 (2022), p. 5369.

[152] N. B. Manson, J. P. Harrison, and M. J. Sellars. "Nitrogen-Vacancy Center in Diamond: Model of the Electronic Structure and Associated Dynamics". *Physical Review B* 74.10 (2006), p. 104303.

[153] Ph Tamarat, N B Manson, J P Harrison, R L McMurtrie, A Nizovtsev, C Santori, R G Beausoleil, P Neumann, T Gaebel, F Jelezko, P Hemmer, and J Wrachtrup. "Spin-Flip and Spin-Conserving Optical Transitions of the Nitrogen-Vacancy Centre in Diamond". *New Journal of Physics* 10.4 (2008), p. 045004.

[154] Lucio Robledo, Hannes Bernien, Toeno van der Sar, and Ronald Hanson. "Spin Dynamics in the Optical Cycle of Single Nitrogen-Vacancy Centres in Diamond". *New Journal of Physics* 13.2 (2011), p. 025013.

[155] M. L. Goldman, A. Sipahigil, M. W. Doherty, N. Y. Yao, S. D. Bennett, M. Markham, D. J. Twitchen, N. B. Manson, A. Kubanek, and M. D. Lukin. "Phonon-Induced Population Dynamics and Intersystem Crossing in Nitrogen-Vacancy Centers". *Physical Review Letters* 114.14 (2015), p. 145502.

[156] Simon Baber, Ralph Nicholas Edward Malein, Prince Khatri, Paul Steven Keatley, Shi Guo, Freddie Withers, Andrew J. Ramsay, and Isaac J. Luxmoore. "Excited State Spectroscopy of Boron Vacancy Defects in Hexagonal Boron Nitride Using Time-Resolved Optically Detected Magnetic Resonance". *Nano Letters* 22.1 (2022), pp. 461–467.

[157] Wonjae Lee, Vincent S. Liu, Zhelun Zhang, Sangha Kim, Ruotian Gong, Xinyi Du, Khanh Pham, Thomas Poirier, Zeyu Hao, James H. Edgar, Philip Kim, Chong Zu, Emily J. Davis, and Norman Y. Yao. *Intrinsic High-Fidelity Spin Polarization of Charged Vacancies in Hexagonal Boron Nitride*. 2024.

[158] Richard A. Escalante, Andrew J. Beling, Niko Reed, Justin Welter, John Blanchard, Daniel G. Ang, Cecilia Campos, Edwin Coronel, Klaus Krambrock, Alexandre S. Leal, Paras N. Prasad, and Ronald L. Walsworth. *Direct Measurement of the Singlet Lifetime and Photoexcitation Behavior of the Boron Vacancy Center in Hexagonal Boron Nitride*. 2025.

[159] Benjamin Whitefield, Milos Toth, Igor Aharonovich, Jean-Philippe Tetienne, and Mehran Kianinia. “Magnetic Field Sensitivity Optimization of Negatively Charged Boron Vacancy Defects in hBN.” *Advanced Quantum Technologies* n/a.n/a (), p. 2300118.

[160] Paul Konrad, Mehran Kianinia, Lesley Spencer, Andreas Sperlich, Lukas Hein, Selin Steinicke, Igor Aharonovich, and Vladimir Dyakonov. *Intermediate Excited State Relaxation Dynamics of Boron-Vacancy Spin Defects in Hexagonal Boron Nitride*. 2025.

[161] Nikhil Mathur, Arunabh Mukherjee, Xingyu Gao, Jialun Luo, Brendan A. McCullian, Tongcang Li, A. Nick Vamivakas, and Gregory D. Fuchs. “Excited-State Spin-Resonance Spectroscopy of VB- Defect Centers in Hexagonal Boron Nitride”. *Nature Communications* 13.1 (2022), p. 3233.

[162] Zhao Mu, Hongbing Cai, Disheng Chen, Jonathan Kenny, Zhengzhi Jiang, Shihao Ru, Xiaodan Lyu, Teck Seng Koh, Xiaogang Liu, Igor Aharonovich, and Weibo Gao. “Excited-State Optically Detected Magnetic Resonance of Spin Defects in Hexagonal Boron Nitride”. *Physical Review Letters* 128.21 (2022), p. 216402.

[163] J-P Tetienne, L Rondin, P Spinicelli, M Chipaux, T Debuisschert, J-F Roch, and V Jacques. “Magnetic-Field-Dependent Photodynamics of Single NV Defects in Diamond: An Application to Qualitative All-Optical Magnetic Imaging”. *New Journal of Physics* 14.10 (2012), p. 103033.

[164] Jean-Philippe Tetienne. “Un microscope de champ magnétique basé sur le défaut azote-lacune du diamant: réalisation et application à l’étude de couches ferromagnétiques ultraminces” ().

[165] Clifford W. Hicks, Mark E. Barber, Stephen D. Edkins, Daniel O. Brodsky, and Andrew P. Mackenzie. “Piezoelectric-Based Apparatus for Strain Tuning”. *Review of Scientific Instruments* 85.6 (2014), p. 065003.

[166] Yaping Qi, Mohammad A. Sadi, Dan Hu, Ming Zheng, Zhenping Wu, Yucheng Jiang, and Yong P. Chen. “Recent Progress in Strain Engineering on Van Der Waals 2D Materials: Tunable Electrical, Electrochemical, Magnetic, and Optical Properties”. *Advanced Materials* 35.12 (2023), p. 2205714.

[167] Kirill I. Bolotin, Arend M. van der Zande, Stephen M. Wu, and J. Scott Bunch. “Two-Dimensional Materials and Heterostructures under Strain”. *Journal of Applied Physics* 137.19 (2025), p. 190402.

[168] W. Akhtar, A. Hrabec, S. Chouaieb, A. Haykal, I. Gross, M. Belmeguenai, M.S. Gabor, B. Shields, P. Maletinsky, A. Thiaville, S. Rohart, and V. Jacques. "Current-Induced Nucleation and Dynamics of Skyrmions in a Co -Based Heusler Alloy". *Physical Review Applied* 11.3 (2019), p. 034066.

[169] Xingyu Gao, Boyang Jiang, Andres E. Llacsahuanga Allcca, Kunhong Shen, Mohammad A. Sadi, Abhishek B. Solanki, Peng Ju, Zhujing Xu, Pramey Upadhyaya, Yong P. Chen, Sunil A. Bhave, and Tongcang Li. "High-Contrast Plasmonic-Enhanced Shallow Spin Defects in Hexagonal Boron Nitride for Quantum Sensing". *Nano Letters* 21.18 (2021), pp. 7708–7714.

[170] N. Mizuochi, P. Neumann, F. Rempp, J. Beck, V. Jacques, P. Siyushev, K. Nakamura, D. J. Twitchen, H. Watanabe, S. Yamasaki, F. Jelezko, and J. Wrachtrup. "Coherence of Single Spins Coupled to a Nuclear Spin Bath of Varying Density". *Physical Review B* 80.4 (2009), p. 041201.

[171] K. D. Jahnke, B. Naydenov, T. Teraji, S. Koizumi, T. Umeda, J. Isoya, and F. Jelezko. "Long Coherence Time of Spin Qubits $In^{12}$ C Enriched Polycrystalline Chemical Vapor Deposition Diamond". *Applied Physics Letters* 101.1 (2012), p. 012405.

[172] Alexei M. Tyryshkin, Shinichi Tojo, John J. L. Morton, Helge Riemann, Nikolai V. Abrosimov, Peter Becker, Hans-Joachim Pohl, Thomas Schenkel, Michael L. W. Thewalt, Kohei M. Itoh, and S. A. Lyon. "Electron Spin Coherence Exceeding Seconds in High-Purity Silicon". *Nature Materials* 11.2 (2012), pp. 143–147.

[173] Albert W. Overhauser. "Polarization of Nuclei in Metals". *Physical Review* 92.2 (1953), pp. 411–415.

[174] Thomas R. Carver and Charles P. Slichter. "Experimental Verification of the Overhauser Nuclear Polarization Effect". *Physical Review* 102.4 (1956), pp. 975–980.

[175] M. V. Gurudev Dutt, L. Childress, L. Jiang, E. Togan, J. Maze, F. Jelezko, A. S. Zibrov, P. R. Hemmer, and M. D. Lukin. "Quantum Register Based on Individual Electronic and Nuclear Spin Qubits in Diamond". *Science* 316.5829 (2007), pp. 1312–1316.

[176] V. Jacques, P. Neumann, J. Beck, M. Markham, D. Twitchen, J. Meijer, F. Kaiser, G. Balasubramanian, F. Jelezko, and J. Wrachtrup. "Dynamic Polarization of Single Nuclear Spins by Optical Pumping of Nitrogen-Vacancy Color Centers in Diamond at Room Temperature". *Physical Review Letters* 102.5 (2009), p. 057403.

[177] Abram L. Falk, Paul V. Klimov, Viktor Ivády, Krisztián Szász, David J. Christle, William F. Koehl, Ádám Gali, and David D. Awschalom. "Optical Polarization of Nuclear Spins in Silicon Carbide". *Physical Review Letters* 114.24 (2015), p. 247603.

[178] Manuel Cardona and M. L. W. Thewalt. "Isotope Effects on the Optical Spectra of Semiconductors". *Reviews of Modern Physics* 77.4 (2005), pp. 1173–1224.

[179] T. Q. P. Vuong, S. Liu, A. Van der Lee, R. Cuscó, L. Artús, T. Michel, P. Valvin, J. H. Edgar, G. Cassabois, and B. Gil. "Isotope Engineering of van Der Waals Interactions in Hexagonal Boron Nitride". *Nature Materials* 17.2 (2018), pp. 152–158.

[180] András Tárkányi and Viktor Ivády. *Understanding Decoherence of the Boron Vacancy Center in Hexagonal Boron Nitride*. 2025.

[181] Ruotian Gong, Xinyi Du, Eli Janzen, Vincent Liu, Zhongyuan Liu, Guanghui He, Bingtian Ye, Tongcang Li, Norman Y. Yao, James H. Edgar, Erik A. Henriksen, and Chong Zu. *Isotope Engineering for Spin Defects in van Der Waals Materials*. 2023.

[182] Xingyu Gao, Sumukh Vaidya, Kejun Li, Peng Ju, Boyang Jiang, Zhujing Xu, Andres E. Llacsahuanga Allcca, Kunhong Shen, Takashi Taniguchi, Kenji Watanabe, Sunil A. Bhave, Yong P. Chen, Yuan Ping, and Tongcang Li. "Nuclear Spin Polarization and Control in Hexagonal Boron Nitride". *Nature Materials* 21.9 (2022), pp. 1024–1028.

[183] Ran Fischer, Andrey Jarmola, Pauli Kehayias, and Dmitry Budker. "Optical Polarization of Nuclear Ensembles in Diamond". *Physical Review B* 87.12 (2013), p. 125207.

[184] Laima Busaite, Reinis Lazda, Andris Berzins, Marcis Auzinsh, Ruvin Ferber, and Florian Gahbauer. "Dynamic N 14 Nuclear Spin Polarization in Nitrogen-Vacancy Centers in Diamond". *Physical Review B* 102.22 (2020), p. 224101.

[185] Viktor Ivády, Krisztián Szász, Abram L. Falk, Paul V. Klimov, David J. Christle, Erik Janzén, Igor A. Abrikosov, David D. Awschalom, and Adam Gali. "Theoretical Model of Dynamic Spin Polarization of Nuclei Coupled to Paramagnetic Point Defects in Diamond and Silicon Carbide". *Physical Review B* 92.11 (2015), p. 115206.

[186] S. Felton, A. M. Edmonds, M. E. Newton, P. M. Martineau, D. Fisher, D. J. Twitchen, and J. M. Baker. "Hyperfine Interaction in the Ground State of the Negatively Charged Nitrogen Vacancy Center in Diamond". *Physical Review B* 79.7 (2009), p. 075203.

[187] Kento Sasaki, Takashi Taniguchi, and Kensuke Kobayashi. *Nitrogen Isotope Effects on Boron Vacancy Quantum Sensors in Hexagonal Boron Nitride*. 2023.

[188] Yuki Nakamura, Shunsuke Nishimura, Takuya Iwasaki, Shu Nakaharai, Shinichi Ogawa, Yukinori Morita, Kenji Watanabe, Takashi Taniguchi, Kento Sasaki, and Kensuke Kobayashi. "Systematic Investigation of Dynamic Nuclear Polarization with Boron Vacancy in Hexagonal Boron Nitride". *Physical Review B* 111.19 (2025), p. 195404.

[189] Eduard C. Reynhardt and Grant L. High. "Dynamic Nuclear Polarization of Diamond. II. Nuclear Orientation via Electron Spin-Locking". *The Journal of Chemical Physics* 109.10 (1998), pp. 4100–4107.

[190] C. Belthangady, N. Bar-Gill, L. M. Pham, K. Arai, D. Le Sage, P. Cappellaro, and R. L. Walsworth. "Dressed-State Resonant Coupling between Bright and Dark Spins in Diamond". *Physical Review Letters* 110.15 (2013), p. 157601.

[191] P. London, J. Scheuer, J.-M. Cai, I. Schwarz, A. Retzker, M. B. Plenio, M. Katagiri, T. Teraji, S. Koizumi, J. Isoya, R. Fischer, L. P. McGuinness, B. Naydenov, and F. Jelezko. "Detecting and Polarizing Nuclear Spins with Double Resonance on a Single Electron Spin". *Physical Review Letters* 111.6 (2013), p. 067601.

[192] Ran Fischer, Christian O. Bretschneider, Paz London, Dmitry Budker, David Gershoni, and Lucio Frydman. "Bulk Nuclear Polarization Enhanced at Room Temperature by Optical Pumping". *Physical Review Letters* 111.5 (2013), p. 057601.

[193] Gonzalo A. Álvarez, Christian O. Bretschneider, Ran Fischer, Paz London, Hisao Kanda, Shinobu Onoda, Junichi Isoya, David Gershoni, and Lucio Frydman. "Local and Bulk 13C Hyperpolarization in Nitrogen-Vacancy-Centred Diamonds at Variable Fields and Orientations". *Nature Communications* 6.1 (2015), p. 8456.

[194] Ashok Ajoy, Kristina Liu, Raffi Nazaryan, Xudong Lv, Pablo R. Zangara, Benjamin Safvati, Guoqing Wang, Daniel Arnold, Grace Li, Arthur Lin, Priyanka Raghavan, Emanuel Druga, Siddharth Dhomkar, Daniela Pagliero, Jeffrey A. Reimer, Dieter Suter, Carlos A. Meriles, and Alexander Pines. "Orientation-Independent Room Temperature Optical $^{13}$ C Hyperpolarization in Powdered Diamond". *Science Advances* 4.5 (2018), eaar5492.

[195] David A. Broadway, Jean-Philippe Tetienne, Alastair Stacey, James D. A. Wood, David A. Simpson, Liam T. Hall, and Lloyd C. L. Hollenberg. "Quantum Probe Hyperpolarisation of Molecular Nuclear Spins". *Nature Communications* 9.1 (2018), p. 1246.

[196] J. Kotakoski, C. H. Jin, O. Lehtinen, K. Suenaga, and A. V. Krasheninnikov. "Electron Knock-on Damage in Hexagonal Boron Nitride Monolayers". *Physical Review B* 82.11 (2010), p. 113404.

[197] Rajesh Kumar, Avinash Parashar, and Pierre Mertiny. "Displacement Thresholds and Knock-on Cross Sections for Hydrogenated h-BN Monolayers". *Computational Materials Science* 142 (2018), pp. 82–88.

[198] Sadegh Ghaderzadeh, Silvan Kretschmer, Mahdi Ghorbani-Asl, Gregor Hlawacek, and Arkady V. Krasheninnikov. "Atomistic Simulations of Defect Production in Monolayer and Bulk Hexagonal Boron Nitride under Low- and High-Fluence Ion Irradiation". *Nanomaterials* 11.5 (2021), p. 1214.

[199] Franco Cataldo and Susana Iglesias-Groth. "Neutron Damage of Hexagonal Boron Nitride: H-BN". *Journal of Radioanalytical and Nuclear Chemistry* 313.1 (2017), pp. 261–271.

[200] Shantanu Saha, Shrivatch Sankar, and Shamsul Arafin. "Recent Advances on Neutron-Irradiated Point Defects in h-BN for Quantum Applications". *Nanotechnology* 36.31 (2025), p. 312001.

[201] T.C. Doan, S. Majety, S. Grenadier, J. Li, J.Y. Lin, and H.X. Jiang. "Fabrication and Characterization of Solid-State Thermal Neutron Detectors Based on Hexagonal Boron Nitride Epilayers". *Nuclear Instruments and Methods in Physics Research Section A: Accelerators, Spectrometers, Detectors and Associated Equipment* 748 (2014), pp. 84–90.

[202] T.C. Doan, S. Majety, S. Grenadier, J. Li, J.Y. Lin, and H.X. Jiang. "Hexagonal Boron Nitride Thin Film Thermal Neutron Detectors with High Energy Resolution of the Reaction Products". *Nuclear Instruments and Methods in Physics Research Section A: Accelerators, Spectrometers, Detectors and Associated Equipment* 783 (2015), pp. 121–127.

[203] William Chuirazzi, Aaron Craft, Burkhard Schillinger, Steven Cool, and Alessandro Tengattini. "Boron-Based Neutron Scintillator Screens for Neutron Imaging". *Journal of Imaging* 6.11 (2020), p. 124.

[204] V. M. Acosta, E. Bauch, M. P. Ledbetter, C. Santori, K.-M. C. Fu, P. E. Barclay, R. G. Beausoleil, H. Linget, J. F. Roch, F. Treussart, S. Chemerisov, W. Gawlik, and D. Budker. "Diamonds with a High Density of Nitrogen-Vacancy Centers for Magnetometry Applications". *Physical Review B* 80.11 (2009), p. 115202.

[205] J Schwartz, P Michaelides, C D Weis, and T Schenkel. "*In Situ* Optimization of Co-Implantation and Substrate Temperature Conditions for Nitrogen-Vacancy Center Formation in Single-Crystal Diamonds". *New Journal of Physics* 13.3 (2011), p. 035022.

[206] Tim Schröder, Matthew E. Trusheim, Michael Walsh, Luozhou Li, Jiabao Zheng, Marco Schukraft, Alp Sipahigil, Ruffin E. Evans, Denis D. Sukachev, Christian T. Nguyen, Jose L. Pacheco, Ryan M. Camacho, Edward S. Bielejec, Mikhail D. Lukin, and Dirk Englund. "Scalable Focused Ion Beam Creation of Nearly Lifetime-Limited Single Quantum Emitters in Diamond Nanostructures". *Nature Communications* 8.1 (2017), p. 15376.

[207] Jun-Feng Wang, Qiang Li, Fei-Fei Yan, He Liu, Guo-Ping Guo, Wei-Ping Zhang, Xiong Zhou, Li-Ping Guo, Zhi-Hai Lin, Jin-Ming Cui, Xiao-Ye Xu, Jin-Shi Xu, Chuan-Feng Li, and Guang-Can Guo. "On-Demand Generation of Single Silicon Vacancy Defects in Silicon Carbide". *ACS Photonics* 6.7 (2019), pp. 1736–1743.

[208] A. Jarmola, A. Berzins, J. Smits, K. Smits, J. Prikulis, F. Gahbauer, R. Ferber, D. Erts, M. Auzinsh, and D. Budker. "Longitudinal Spin-Relaxation in Nitrogen-Vacancy Centers in Electron Irradiated Diamond". *Applied Physics Letters* 107.24 (2015), p. 242403.

[209] J.-P. Tetienne, R. W. de Gille, D. A. Broadway, T. Teraji, S. E. Lillie, J. M. McCoey, N. Dontschuk, L. T. Hall, A. Stacey, D. A. Simpson, and L. C. L. Hollenberg. "Spin Properties of Dense Near-Surface Ensembles of Nitrogen-Vacancy Centers in Diamond". *Physical Review B* 97.8 (2018), p. 085402.

[210] Elchin M. Huseynov, Tural G. Naghiyev, Adil A. Garibov, Nijat R. Abbasov, Oqtay A. Samedov, Reshid C. Gasimov, and Mahammad A. Bayramov. "EPR Spectroscopy of Neutron Irradiated Nanocrystalline Boron Nitride (h-BN) Particles". *Ceramics International* 47.5 (2021), pp. 7218–7223.

[211] J R Toledo and K Krambrock. "Identification and Thermal Stability of Point Defects in Neutron-Irradiated Hexagonal Boron Nitride (h-BN)". *Journal of Physics D: Applied Physics* 54.6 (2021), p. 065303.

[212] James D. A. Wood, David A. Broadway, Liam T. Hall, Alastair Stacey, David A. Simpson, Jean-Philippe Tetienne, and Lloyd C. L. Hollenberg. "Wide-Band Nanoscale Magnetic Resonance Spectroscopy Using Quantum Relaxation of a Single Spin in Diamond". *Physical Review B* 94.15 (2016), p. 155402.

[213] Mariusz Mrózek, Daniel Rudnicki, Pauli Kehayias, Andrey Jarmola, Dmitry Budker, and Wojciech Gawlik. "Longitudinal Spin Relaxation in Nitrogen-Vacancy Ensembles in Diamond". *EPJ Quantum Technology* 2.1 (2015), p. 22.

[214] David A. Simpson, Robert G. Ryan, Liam T. Hall, Evgeniy Panchenko, Simon C. Drew, Steven Petrou, Paul S. Donnelly, Paul Mulvaney, and Lloyd C. L. Hollenberg. "Electron Paramagnetic Resonance Microscopy Using Spins in Diamond under Ambient Conditions". *Nature Communications* 8.1 (2017), p. 458.

[215] Joonhee Choi, Soonwon Choi, Georg Kucsko, Peter C. Maurer, Brendan J. Shields, Hitoshi Sumiya, Shinobu Onoda, Junichi Isoya, Eugene Demler, Fedor Jelezko, Norman Y. Yao, and Mikhail D. Lukin. "Depolarization Dynamics in a Strongly Interacting Solid-State Spin Ensemble". *Physical Review Letters* 118.9 (2017), p. 093601.

[216] Erik Bauch, Swati Singh, Junghyun Lee, Connor A. Hart, Jennifer M. Schloss, Matthew J. Turner, John F. Barry, Linh M. Pham, Nir Bar-Gill, Susanne F. Yelin, and Ronald L. Walsworth. "Decoherence of Ensembles of Nitrogen-Vacancy Centers in Diamond". *Physical Review B* 102.13 (2020), p. 134210.

[217] C. Pellet-Mary, M. Perdriat, P. Huillery, and G. Hétet. "Relaxation Processes in Dipole-Coupled Nitrogen-Vacancy Centers in Zero Field: Application in Magnetometry". *Physical Review Applied* 20.3 (2023), p. 034050.

[218] M. Bayer, T. L. Reinecke, F. Weidner, A. Larionov, A. McDonald, and A. Forchel. "Inhibition and Enhancement of the Spontaneous Emission of Quantum Dots in Structured Microresonators". *Physical Review Letters* 86.14 (2001), pp. 3168–3171.

[219] Julien Claudon, Niels Gregersen, Philippe Lalanne, and Jean-Michel Gérard. "Harnessing Light with Photonic Nanowires: Fundamentals and Applications to Quantum Optics". *ChemPhysChem* 14.11 (2013), pp. 2393–2402.

[220] P. Blake, E. W. Hill, A. H. Castro Neto, K. S. Novoselov, D. Jiang, R. Yang, T. J. Booth, and A. K. Geim. "Making Graphene Visible". *Applied Physics Letters* 91.6 (2007), p. 063124.

[221] P. Jamonneau, M. Lesik, J. P. Tetienne, I. Alvizu, L. Mayer, A. Dréau, S. Kosen, J.-F. Roch, S. Pezzagna, J. Meijer, T. Teraji, Y. Kubo, P. Bertet, J. R. Maze, and V. Jacques. "Competition between Electric Field and Magnetic Field Noise in the Decoherence of a Single Spin in Diamond". *Physical Review B* 93.2 (2016), p. 024305.

[222] Sourav Mondal and Alessandro Lunghi. "Spin-Phonon Decoherence in Solid-State Paramagnetic Defects from First Principles". *npj Computational Materials* 9.1 (2023), p. 120.

[223] J.-P. Tetienne, T. Hingant, L. Rondin, A. Cavaillès, L. Mayer, G. Dantelle, T. Gacoin, J. Wrachtrup, J.-F. Roch, and V. Jacques. "Spin Relaxometry of Single Nitrogen-Vacancy Defects in Diamond Nanocrystals for Magnetic Noise Sensing". *Physical Review B* 87.23 (2013), p. 235436.

[224] Sorawis Sangtawesin, Bo L. Dwyer, Srikanth Srinivasan, James J. Allred, Lila V. H. Rodgers, Kristiaan De Greve, Alastair Stacey, Nikolai Dontschuk, Kane M. O'Donnell, Di Hu, D. Andrew Evans, Cherno Jaye, Daniel A. Fischer, Matthew L. Markham, Daniel J. Twitchen, Hongkun Park, Mikhail D. Lukin, and Nathalie P. de Leon. "Origins of Diamond Surface Noise Probed by

Correlating Single-Spin Measurements with Surface Spectroscopy". *Physical Review X* 9.3 (2019), p. 031052.

[225] Rogerio de Sousa. "Dangling-Bond Spin Relaxation and Magnetic 1 / f Noise from the Amorphous-Semiconductor/Oxide Interface: Theory". *Physical Review B* 76.24 (2007), p. 245306.

[226] T. de Guillebon, B. Vindolet, J.-F. Roch, V. Jacques, and L. Rondin. "Temperature Dependence of the Longitudinal Spin Relaxation Time T1 of Single Nitrogen-Vacancy Centers in Nanodiamonds". *Physical Review B* 102.16 (2020), p. 165427.

[227] T. Schenkel, J. A. Liddle, A. Persaud, A. M. Tyryshkin, S. A. Lyon, R. de Sousa, K. B. Whaley, J. Bokor, J. Shangkuan, and I. Chakarov. "Electrical Activation and Electron Spin Coherence of Ultralow Dose Antimony Implants in Silicon". *Applied Physics Letters* 88.11 (2006), p. 112101.

[228] Blake M. Freeman, Joshua S. Schoenfield, and HongWen Jiang. "Comparison of Low Frequency Charge Noise in Identically Patterned Si/SiO2 and Si/SiGe Quantum Dots". *Applied Physics Letters* 108.25 (2016), p. 253108.

[229] Elliot J. Connors, Jj Nelson, Haifeng Qiao, Lisa F. Edge, and John M. Nichol. "Low-Frequency Charge Noise in Si/SiGe Quantum Dots". *Physical Review B* 100.16 (2019), p. 165305.

[230] Y. Romach, C. Müller, T. Unden, L. J. Rogers, T. Isoda, K. M. Itoh, M. Markham, A. Stacey, J. Meijer, S. Pezzagna, B. Naydenov, L. P. McGuinness, N. Bar-Gill, and F. Jelezko. "Spectroscopy of Surface-Induced Noise Using Shallow Spins in Diamond". *Physical Review Letters* 114.1 (2015), p. 017601.

[231] M. Kim, H. J. Mamin, M. H. Sherwood, K. Ohno, D. D. Awschalom, and D. Rugar. "Decoherence of Near-Surface Nitrogen-Vacancy Centers Due to Electric Field Noise". *Physical Review Letters* 115.8 (2015), p. 087602.

[232] Junfeng Wang, Wenlong Zhang, Jian Zhang, Jie You, Yan Li, Guoping Guo, Fupan Feng, Xuerui Song, Liren Lou, Wei Zhu, and Guanzhong Wang. "Coherence Times of Precise Depth Controlled NV Centers in Diamond". *Nanoscale* 8.10 (2016), pp. 5780–5785.

[233] B. A. Myers, A. Ariyaratne, and A. C. Bleszynski Jayich. "Double-Quantum Spin-Relaxation Limits to Coherence of Near-Surface Nitrogen-Vacancy Centers". *Physical Review Letters* 118.19 (2017), p. 197201.

[234] W. Liu, S. Li, N.-J. Guo, X.-D. Zeng, L.-K. Xie, J.-Y. Liu, Y.-H. Ma, Y.-Q. Wu, Y.-T. Wang, Z.-A. Wang, J.-M. Ren, C. Ao, J.-S. Xu, J.-S. Tang, A. Gali, C.-F. Li, and G.-C. Guo. *Experimental Observation of Spin Defects in van Der Waals Material GeS2*. 2024.

[235] Sumukh Vaidya, Xingyu Gao, Saakshi Dikshit, Zhenyao Fang, Andres E. Llacsahuanga Allcca, Yong P. Chen, Qimin Yan, and Tongcang Li. "Coherent Spins in van Der Waals Semiconductor $GeS_2$ at Ambient Conditions". *Nano Letters* 25.39 (2025), pp. 14356–14362.

[236] S. C. Scholten, I. O. Robertson, G. J. Abrahams, Priya Singh, A. J. Healey, and J.-P. Tetienne. "Aberration Control in Quantitative Widefield Quantum Microscopy". *AVS Quantum Science* 4.3 (2022), p. 034404.

[237] Daniel S. Fisher, Matthew P. A. Fisher, and David A. Huse. "Thermal Fluctuations, Quenched Disorder, Phase Transitions, and Transport in Type-II Superconductors". *Physical Review B* 43.1 (1991), pp. 130–159.

[238] B. A. Huberman and S. Doniach. "Melting of Two-Dimensional Vortex Lattices". *Physical Review Letters* 43.13 (1979), pp. 950–952.

[239] J. Pearl. "Current Distribution in Superconducting Films Carrying Quantized Fluxoids". *Applied Physics Letters* 5.4 (1964), pp. 65–66.

[240] Sreehari Jayaram, Malik Lenger, Dong Zhao, Lucas Pupim, Takashi Taniguchi, Kenji Watanabe, Ruoming Peng, Marc Scheffler, Rainer Stöhr, Mathias S. Scheurer, Jurgen Smet, and Jörg Wrachtrup. "Probing Vortex Dynamics in 2D Superconductors with Scanning Quantum Microscope". *Physical Review Letters* 135.12 (2025), p. 126001.

[241] Souvik Biswas, Giovanni Scuri, Noah Huffman, Eric I. Rosenthal, Ruotian Gong, Thomas Poirier, Xingyu Gao, Sumukh Vaidya, Abigail J. Stein, Tsachy Weissman, James H. Edgar, Tongcang Li, Chong Zu, Jelena Vučković, and Joonhee Choi. *Quantum Sensing with a Spin Ensemble in a Two-Dimensional Material*. 2025.

[242] Declan M. Daly, Niko R. Reed, Stephen J. DeVience, Zechuan Yin, Johannes Cremer, Andrew J. Beling, John W. Blanchard, and Ronald L. Walsworth. *Prospects for Ultralow-Mass Nuclear Magnetic Resonance Using Spin Defects in Hexagonal Boron Nitride*. 2025.

[243] T. Staudacher, F. Shi, S. Pezzagna, J. Meijer, J. Du, C. A. Meriles, F. Reinhard, and J. Wrachtrup. "Nuclear Magnetic Resonance Spectroscopy on a (5-Nanometer)$^3$ Sample Volume". *Science* 339.6119 (2013), pp. 561–563.

[244] H. J. Mamin, M. Kim, M. H. Sherwood, C. T. Rettner, K. Ohno, D. D. Awschalom, and D. Rugar. "Nanoscale Nuclear Magnetic Resonance with a Nitrogen-Vacancy Spin Sensor". *Science* 339.6119 (2013), pp. 557–560.

[245] Linh M. Pham, Stephen J. DeVience, Francesco Casola, Igor Lovchinsky, Alexander O. Sushkov, Eric Bersin, Junghyun Lee, Elana Urbach, Paola Cappellaro, Hongkun Park, Amir Yacoby, Mikhail Lukin, and Ronald L. Walsworth. "NMR Technique for Determining the Depth of Shallow Nitrogen-Vacancy Centers in Diamond". *Physical Review B* 93.4 (2016), p. 045425.

[246] C. Zu, F. Machado, B. Ye, S. Choi, B. Kobrin, T. Mittiga, S. Hsieh, P. Bhattacharyya, M. Markham, D. Twitchen, A. Jarmola, D. Budker, C. R. Laumann, J. E. Moore, and N. Y. Yao. "Emergent Hydrodynamics in a Strongly Interacting Dipolar Spin Ensemble". *Nature* 597.7874 (2021), pp. 45–50.

[247] Soonwon Choi, Joonhee Choi, Renate Landig, Georg Kucsko, Hengyun Zhou, Junichi Isoya, Fedor Jelezko, Shinobu Onoda, Hitoshi Sumiya, Vedika Khemani, Curt von Keyserlingk, Norman Y. Yao, Eugene Demler, and Mikhail D. Lukin. "Observation of Discrete Time-Crystalline Order in a Disordered Dipolar Many-Body System". *Nature* 543.7644 (2017), pp. 221–225.

[248] E. J. Davis, B. Ye, F. Machado, S. A. Meynell, W. Wu, T. Mittiga, W. Schenken, M. Joos, B. Kobrin, Y. Lyu, Z. Wang, D. Bluvstein, S. Choi, C. Zu, A. C. Bleszynski Jayich, and N. Y. Yao. "Probing Many-Body Dynamics in a Two-Dimensional Dipolar Spin Ensemble". *Nature Physics* 19.6 (2023), pp. 836–844.

[249] Weijie Wu, Emily J. Davis, Lillian B. Hughes, Bingtian Ye, Zilin Wang, Dominik Kufel, Tasuku Ono, Simon A. Meynell, Maxwell Block, Che Liu, Haopu Yang, Ania C. Bleszynski Jayich, and Norman Y. Yao. *Spin Squeezing in an Ensemble of Nitrogen-Vacancy Centers in Diamond*. 2025.

# Résumé

Les capteurs quantiques à base de défauts de spin optiquement actifs, portés par le centre lacune-azote ($NV^-$) du diamant, ont déjà largement démontrés leur potentiel. Si ces derniers ont trouvé des applications en biologie et en géologie c'est surtout dans le domaine de la matière condensée qu'ils se sont démarqués avec notamment l'imagerie de texture magnétique de taille micro voir nanométriques, comme des parois de domaines dans des aimants ferromagnétiques ou des vortex magnétiques dans des supraconducteurs. La technologie, suffisamment mature, et l'intérêt de la communauté scientifique, suffisamment grand, ont même permis à des compagnies de proposer à la vente des capteurs à base de centre $NV^-$. Ces dernières années, ces capteurs ont trouvé un nouveau type d'échantillon de prédilection : les matériaux de van der Waals. Constitué de feuillés atomiques faiblement liés les uns aux autres par la faible interaction de van der Waals, ces matériaux lamellaires ont la propriété étonnante de pouvoir être exfolié jusqu'à la limite de la feuille atomique individuelle, constituant de véritables matériaux bi-dimensionnel. Après la découverte fondatrice du graphène, cette nouvelle classe de matériaux s'est rapidement élargie. On peut maintenant trouver dans ses rangs, des supraconducteurs, des aimants ferro- et antiferro-magnétiques, des isolants topologiques et plein d'autres matériaux qui constituent le bestiaire de la matière condensée. En plus de leur propriété individuelle, les matériaux de van der Waals peuvent aussi être déposé les uns sur les autres pour donner naissance à une physique encore plus riche. Supraconductivité topologique dans une structure aimant ferromagnétique-supraconducteur, supraconductivité dans des bicouches de graphènes torsadées sont des exemples de phénomènes physique originaux que ces hétérostructures peuvent produire. Pour ces raisons, et bien d'autres encore, les matériaux de van der Waals ont rapidement pris une place importante dans la recherche en physique de la matière condensée et sont donc devenu des échantillons de premier choix pour les capteurs quantique à base de centre $NV^-$. En parallèle, cependant, ils ont soulevé une question d'une autre nature : et si le capteur lui-même devenait un matériau de van der Waals ?

Passer d'un capteur tridimensionnel (3D) à un capteur bidimensionnel (2D) offrirait plusieurs avantages majeurs, le premier étant une proximité ultime entre le capteur et l'échantillon. Enfoui dans une matrice 3D, le centre $NV^-$ n'est jamais en contact direct avec l'échantillon étudié. Dans la microscopie $NV^-$ à balayage, qui représente actuellement l'état de l'art en matière d'imagerie basée sur les centres $NV^-$, cette distance atteint généralement quelques dizaines de nanomètres. À l'inverse, un capteur van der Waals de quelques couches atomiques d'épaisseur, déposé directement sur l'échantillon, pourrait atteindre une proximité atomique. Cette proximité apporte deux avantages immédiats :

- Sensibilité accrue.
  Une plus grande proximité entre le capteur et l'échantillon renforce directement le champ perçu par le défaut de spin. Par exemple, un champ magnétique dipolaire décroît avec le cube de la distance entre la source magnétique et le capteur. Une proximité à l'échelle atomique améliorerait donc considérablement la sensibilité du capteur.

- Une plus grande flexibilité.
  En tant que feuille atomique flexible, un tel capteur permettrait également son intégration dans des architectures plus complexes, notamment au sein d'hétérostructures de van der Waals. La physique riche de ces matériaux artificiels, pourrait alors être sondée in situ.

Motivée par ces promesses, une partie de la communauté a commencé à rechercher des candidats potentiels pour cette nouvelle plateforme de capteur 2D. La première étape cruciale réside dans le choix du matériau hôte, un cristal de van der Waals, bien sûr, mais lequel ?

Le critère principal est la largeur de la bande interdite : elle doit être suffisamment grande pour abriter les transitions optiques de nos défauts. La stabilité chimique à température ambiante est également essentielle afin de maintenir un dispositif de détection simple et accessible. Bien que plusieurs candidats répondent à ces exigences, un matériau se distingue clairement des autres : le nitrure de bore hexagonal (hBN). Le hBN est un matériau isolant doté d'une large bande interdite d'environ 6 eV. Presque insensible à l'oxydation et pouvant même agir comme inhibiteur

de corrosion, il est chimiquement stable jusqu'à la monocouche et conserve cette stabilité à des températures pouvant atteindre 1000 °C. Cette robustesse, combinée à ses remarquables propriétés diélectriques, a fait de l'hBN une couche protectrice incontournable dans la communauté des matériaux de van der Waals. Ainsi, du graphène déposé sur un substrat d'hBN présente une mobilité de porteurs accrue et une meilleure stabilité de charge, tandis que l'encapsulation par hBN protège les dichalcogénures de métaux de transition (TMDs) de l'oxydation pendant plusieurs mois et améliore même leurs propriétés optiques. Le hBN apparaît ainsi comme le matériau idéal pour développer un capteur bi-dimensionnel. De plus, sa large bande interdite offre amplement assez d'espace pour accueillir des défauts de spin optiquement actifs.

En 2020, un candidat est justement identifié. Gottscholl et al. démontrent l'initialisation et la lecture optiques, à température ambiante, d'un ensemble de défauts de spin dans du hBN irradié par des neutrons. Fait remarquable, cette première étude révèle également la structure microscopique des défauts : une lacune de bore ($V_B^-$), plus précisément sous sa forme chargée négativement. Non seulement ce défaut possède un spin, mais il présente également des propriétés optiques dépendantes du spin très similaires à celles du centre $NV^-$ dans le diamant, la référence en matière de défauts de spin. Cette étude pionnière a ainsi ouvert une nouvelle voie de recherche, dans laquelle s'inscrit ce travail de thèse.

L'objectif principal de cette thèse est d'évaluer le potentiel et la viabilité de la lacune de bore chargée négativement dans le hBN en tant que capteur quantique bidimensionnel. Cet objectif englobe plusieurs aspects essentiels : démontrer son utilisation en tant que capteur quantique, identifier les principaux obstacles limitant actuellement ses performances, optimiser l'environnement du défaut et son processus de création pour améliorer sa sensibilité. Toutefois, tous ces efforts reposent sur une hypothèse centrale : la possibilité d'exploiter ce capteur jusqu'à la limite des quelques couches atomiques. Loin d'être triviale, cette hypothèse doit être démontrée expérimentalement. Le manuscrit est organisé en cinq chapitres, chacun approfondissant un de ces aspects.

Dans le premier chapitre, nous présentons formellement la lacune de bore chargée négativement. À partir des prédictions ab initio issues de la littérature, nous

décrivons d'abord sa structure électronique et ses propriétés optiques avant d'introduire les principes de la spectroscopie ODMR. Nous exprimons ensuite le Hamiltonien de spin de l'état fondamental du défaut et montrons comment ce spin se couple à différents types de perturbations. Sur cette base, nous démontrons l'initialisation optique, la lecture résolue en temps et le contrôle cohérent de l'état de spin, puis nous utilisons ces outils clés pour mesurer les temps de relaxation de spin. Enfin, ce chapitre se conclut par une démonstration de principe de l'imagerie de champ magnétique avec cette nouvelle plateforme. Cette première étude, et en particulier sa dernière partie, permet d'identifier les principaux facteurs limitant actuellement la sensibilité du capteur : sa faible émission optique et son couplage avec le bain de sin nucléaire environnant.

Dans le deuxième chapitre, nous présentons une étude complète de la photodynamique dépendante du spin du défaut. Nous proposons un modèle à sept niveaux, régi par cinq paramètres indépendants. Nous réalisons ensuite une série de mesures de photoluminescence résolue en temps afin d'extraire tous les paramètres du modèle à température ambiante. La même analyse, effectuée dans des conditions cryogéniques, révèle une photodynamique pratiquement inchangée. Enfin, nous utilisons ce modèle complet pour reproduire le comportement de la photodynamique sous champ magnétique, obtenant un excellent accord avec les données expérimentales.

Dans le troisième chapitre, nous explorons deux stratégies visant à contrôler le bain de spins nucléaires et à améliorer la sensibilité du capteur : la purification isotopique et la polarisation dynamique des spins nucléaires. En purifiant le réseau d'hBN avec les isotopes $^{10}$B et $^{15}$N, nous obtenons une amélioration par un facteur quatre de la sensibilité. Nous démontrons ensuite la polarisation nucléaire par pompage optique, atteignant une polarisation modeste d'environ 30 % au maximum. Sur la base d'un modèle simplifié, nous attribuons cette limitation à une contrainte de symétrie.

Dans le quatrième chapitre, nous étudions l'irradiation neutronique comme moyen de générer des lacunes de bore. Cette technique, reposant sur la transmutation nucléaire, offre une stratégie alternative pour créer notre capteur atomiquement mince : irradier d'abord le matériau massif, puis effectuer l'exfoliation par la

suite. Sur une première série d'échantillons, nous démontrons le rôle crucial de la purification isotopique du bore pour une création efficace de défauts par irradiation de neutron. Sur une seconde série, présentant la configuration isotopique optimisée, nous identifions la durée d'irradiation optimale pour maximiser la sensibilité du capteur. Enfin, nous concluons ce chapitre par des mesures de spectroscopie ODMR réalisées sur des flocons atomiquement minces, démontrant que le spin du défaut peut encore être initialisé et lu jusqu'à la limite de quelques couches.

Dans le cinquième et dernier chapitre, nous explorons l'impacte d'une épaisseur atomiquement fine sur les propriétés du centre $V_B^-$. Nous étudions d'abord l'évolution de l'intensité du signal de photoluminescence en fonction de l'épaisseur du flocon, à la fois expérimentalement et théoriquement, et démontrons le rôle prédominant d' effets nanophotoniques. Dans la seconde partie, nous examinons l'impact de la proximité de la surface sur les temps de relaxation de spin. Nos résultats révèlent que, bien que les couches minces présentent une relaxation des populations plus rapide, la cohérence de spin y est, contre toute attente, remarquablement préservée.

Les défauts de spin dans les matériaux de van der Waals représentent une plateforme émergente pour les technologies quantiques, combinant la polyvalence des systèmes de spin à l'état solide avec l'épaisseur atomique et l'intégrabilité des matériaux 2D. Le centre $V_B^-$ dans le hBN constitue la première réalisation de cette nouvelle génération de capteurs quantiques, ouvrant la voie à des applications futures, notamment pour l'étude des matériaux de van der Waals et leurs hétérostructures, ainsi que pour la résonance magnétique nucléaire. Nous espérons que le travail présenté dans cette thèse a modestement contribué à l'exploration et à la compréhension de cette prometteuse plateforme de capteurs quantiques.